

Environmental Effects on Galaxy Evolution

Tomotsugu Goto

Department of Physics, Graduate School of Science,
The University of Tokyo

A dissertation submitted to The University of Tokyo
for the degree of Doctor of Philosophy

June 6, 2003

Acknowledgements

I am grateful to my advisers, Maki Sekiguchi, and Sadanori Okamura for their continuous encouragement and support for not only this thesis, but also for my entire graduate school life. I am indebted to Maki Sekiguchi for introducing me to an interesting field in astrophysics, galaxy evolution in clusters, and for his continuous support for my thesis project. The large amount of time I have spent with him during my graduate life has been extremely helpful to me. I wish to express my deepest gratitude to Sadanori Okamura for his guidance on this work and for careful reading of this manuscript. I owe it to Sadanori and people in his group that I was able to concentrate on my thesis project and complete it during the last four months of my graduate life.

I acknowledge Masafumi Yagi for his extensive help in solving statistical problems in this work. His brain (often called a supercomputer) is indispensable to this project. I wish to extend my sincere gratitude to Mamoru Doi for careful reading of the manuscript and many fruitful suggestions. I would like to thank Naoki Yasuda, Shinichi Ichikawa, Takashi Ichikawa, Masaru Watanabe, Masaru Hamabe, Masataka Fukugita and Kazuhiro Shimasaku for instructing me how to use the SDSS data. The monthly SDSS meeting they used to have was a precious opportunity for a graduate student like myself to learn about the SDSS. I thank Masayuki Tanaka for always chatting with me whenever I wanted to. Many discussions with him often lead to a new idea in analysis. I thank Shuichi Aoki for sharing his sharp mind with me. Not only his expertise but also his attitude to research work set an excellent example for me to learn. I thank Eiichiro and Midori Komatsu for their continuous friendship, and for teaching me a spiritual aspect to be an astronomer. I am grateful to Nell Hana Hoffman, Ricardo Colon, Emanuel Bowes, Shane Zabel, and Michael Crouch for patiently correcting my English, which significantly improved the quality of the manuscript. I thank Masami Ouchi for showing an astronomical Samurai spirit in studying 7 days without going home. The presence of such a brilliant graduate student has been a magnificent inspiration to me. I gratefully thank Takamitsu Miyaji not only for his continuous treatments to curry and rice, but also helping me to settle down in Pittsburgh. It is a privilege to make friends with a world-famous X-ray astronomer. I thank Kentaro and Michiko Nagamine for their continuous friendship, especially in visiting

us in Kashiwa. I hope to play basketball with them in the near future again. Many thanks also to Yutaka Fujita and Tomonori Totani for showing me how fun it is to be an astronomer. I thank Aya Bamba for kindly recommending me the best doughnut shop in Japan, where I sometimes hit on a good idea over a cup of coffee. I wish to thank Masatake Ohashi for his help in finishing this thesis. I thank Koji Mori, Haruyoshi Katayama and Kenji Hamaguchi for offering me the opportunity to work on X-ray astronomy. I thank our secretary, Yuri Iinuma, for handling my many impossible requests for the grant.

I wish to extend my many thanks to Christy Tremonti and Eric Peng for teaching me how to take a subway when I got lost in New York. I thank Neal A. Miller for sharing a ride in Pasadena. The discussion on radio astronomy we had in the car was quite influential to Appendix B of this work. I thank Marc Postman, Albert Conti, Sharon Busching, Alan Uomoto and Adrian C. Pope for showing me around Baltimore. I thank James E. Gunn for using my plots in his review talk, and thus encouraging me to keep studying astronomy. I thank Wataru Kawasaki and Tadayuki Kodama for showing me a variety of wonderful science that a cluster finder can do. I thank Wolfgang Voges for being kind to every young astronomers including me. His presence gave me a great relief when I got nervous in visiting the States for the first time. I thank Jeff Peterson for saying hello to me every time we met at school. I thank Ravi Sheth for being always gentle to everyone, and telling an interesting story to be a movie star. I would like to express my sincere gratitude to Toru Yamada, Yutaka Komiyama, Hisanori Furusawa, Francisco Castander, Jeff Maki, Rupert Croft, Tiziana Di Matteo, Taotao Fang, Gulab Dewangan, Kavan Ratnatunga, Douglas L. Tucker, Masanori Iye, Tadayuki Kodama, Shang-Shan Chong, Iskra Strateva, Brice Menard, Katsuko T. Nakahira, Connie Rockosi, Stefano Zibetti, Shiying Shen, Simon White, Guinevere Kauffmann and Stephane Charlot for their suggestions and discussions to improve the work. It has been a pleasure to work with them. I have been lucky to be blessed with a large number of wonderful coworkers and colleague graduate students. I thank the following for the fond memories, their kindness, their enduring friendship and a plethora of experiences together which I will remember for good: Naohisa Inada, Kayo Issya, Chiaki Hikage, Chris Miller, Percy Gomez, David Wake, Makiko Yoshida, Tomoki Saito, Eri Yamanoi, Adam Knudson, Shigeyuki Sako, Yoshihiko Yamada, Tomoaki Oyama, Fumiaki Nakata, Yasuhiro Shioya and Ichi Tanaka. I thank Tim McKay and David Weinberg for a useful discussion in the cluster working group. I thank Ching-Wa Yip and Sam Schmidt for their friendship at the University of Pittsburgh. I thank Masayuki Ohama and Katsumi Kurasawa for performing a wonderful joke on top of Mt. Wakakusa, which lubricated the communication between the U.S. and Japanese astronomers. I thank Yoshihiro Ueda for kindly teaching me how to ski. I thank Michael A. Strauss and Robert Lupton for kindly inviting me to a sushi restaurant. I thank Chisato Yamauchi and Reiko Nakajima for constructing a useful software called AstroNOMICAL

IMage Explore, or ANIME. I thank James Annis and Michael Vogeley for rescuing me at Fermilab. I thank Ivan K. Baldry for showing me around a castle. I thank J. Brinkmann for always appreciating my publications. I thank Ani Thakar, Tamas Budavari, Istvan Szapudi, Marc SubbaRao, Mariangela Bernardi, Osamu Nakamura, Erika Kamikawa for kindly feeding deer in my hometown, Nara. I thank Yeong-Shang Loh, Lei Hao, Randall Rojas and Roy Gal for making a good friend with me. I thank Rita Kim and Neta Bahcall for their hospitality during my stay in Princeton. I thank our secretary Masumi Nakaya for bringing a wonderful smile to the office. I thank David Hogg, Michael Blanton and Alex Quintero for a useful discussion on Appendix A & B. I am grateful to Sidney van den Bergh and Don York, for valuable comments on Chapter 7 of this work. I appreciate Andrew and Tony Hopkins for their friendship during my stay in Pittsburgh. I would like to extend my appreciation to A. Kathy Romer, Richard Griffiths, David A. Turnshek, Andrew Connolly, David Johnston, Erin Scheldon, Sara Hansen, Satoru Ikeuchi, Yasushi Suto, Katsuhiko Sato, John Peoples, and Sandhya Rao for their kindness. I thank Ian Smail for sending me the data that I needed before I asked. I thank Takashi Okamoto and Naoyuki Tamura for their hospitality during my visit in Durham. I thank Dajana Dzanovic for useful scientific communication through e-mail. I thank Chiaki Kobayashi for organizing the galaxy seminar.

I thank the SDSS collaboration for creating such a wonderful data set. Working with such a great data set for my four years of graduate life has been quite an experience. I thank Department of Physics of Carnegie Mellon University for its hospitality during my visit. I acknowledge financial support from the Japan Society for the Promotion of Science (JSPS) through JSPS Research Fellowships for Young Scientists. This work owes its completion to this financial support.

I thank my family, Hisako and Sayaka Goto for their continuous support for my entire life.

Lastly I deeply thank my wife Miki Goto for her continuous support and genuine affection.

With pleasure, I dedicate this work to Miki.

Tomotsugu Goto, June 6, 2003.

Contents

1 General Introduction	3
1.1 Observational Evidence for Environmental Effects	3
1.1.1 The Morphology-Density Relation	3
1.1.2 Suppression of Star Formation in Cluster Regions	5
1.1.3 Color-Magnitude Relation	5
1.1.4 Evolution of Cluster Galaxies	6
1.2 Theoretical Implications	7
1.3 Need for Larger, More Uniform Samples	9
2 The Sloan Digital Sky Survey	15
2.1 The Sloan Digital Sky Survey	15
2.1.1 The SDSS Imaging Survey	15
2.1.2 The SDSS Spectroscopic Survey	17
3 The Cut & Enhance Galaxy Cluster Catalog	30
3.1 Introduction	30
3.2 The SDSS Commissioning Data	32
3.3 The Cut & Enhance Cluster Detection Method	32
3.3.1 Color Cut	32
3.3.2 Color-color Cut	35
3.3.3 Enhancement Method	36
3.3.4 Detection	38
3.3.5 Merging	39
3.3.6 Redshift and Richness Estimation	39
3.4 Monte Carlo Simulation	40
3.4.1 Method	40
3.4.2 Monte Carlo Results	41
3.4.3 False Positive Tests	43
3.5 Visual Inspection	43
3.6 Comparison with Other Methods	44

3.6.1	Comparison of the Matched Filter and the CE Methods	45
3.6.2	Comparison of the maxBCG and the CE Methods	46
3.6.3	Comparison of the VTT and the CE Methods	46
3.7	Summary	47
4	Composite Luminosity Functions	83
4.1	Introduction	83
4.2	SDSS Data	84
4.3	Analysis and Results	85
4.3.1	Construction of the Composite Cluster LF	85
4.3.2	The Composite Cluster LF as a Function of Morphology	88
4.4	Discussion	89
4.4.1	Monte-Carlo Simulations	89
4.4.2	Check of Photometric Redshifts	90
4.4.3	Test of Cluster Centroids	91
4.4.4	Test of Background Subtraction	91
4.4.5	Test of Cluster Richness	92
4.4.6	Comparison with Other LFs	92
4.5	Summary	93
5	The Morphological Butcher-Oemler Effect	103
5.1	Introduction	103
5.2	Data	106
5.3	Analysis and Results	108
5.3.1	Fore/Background subtraction	108
5.3.2	Errors on Blue/Late Type Fractions	108
5.3.3	Blue Fraction	111
5.3.4	Late Type Fraction Using $u - r < 2.2$	112
5.3.5	Late Type Fraction Using Profile fitting	113
5.3.6	Late Type Fraction Using Concentration Parameter	114
5.3.7	On the Origin of the Scatter	115
5.4	Discussion	115
5.4.1	Morphological k -correction	115
5.4.2	Seeing Dependence	116
5.4.3	Radius, Fore/background Subtraction and Cluster Centroids	117
5.4.4	Comparison with Late-type Fraction from Spectroscopy	118
5.4.5	The Butcher-Oemler Effect: Comparison with Previous Work	118
5.4.6	The Morphological Butcher-Oemler effect	120
5.4.7	Richness Dependence	122

5.4.8	Varying Radius	124
5.5	Summary	124
6	The Morphology-Density Relation	143
6.1	Introduction	143
6.2	The SDSS Data	146
6.3	Analysis	147
6.3.1	Morphological classification	147
6.3.2	Density Measurements	149
6.4	Results	149
6.4.1	The Morphology Density Relation for the SDSS data	149
6.4.2	Morphology-Radius Relation	150
6.4.3	Physical Sizes of Galaxies	151
6.4.4	Comparison with the MORPHS Data	151
6.5	Discussion	153
6.5.1	Elliptical Fractions	153
6.5.2	The Morphology-Density Relation with C_{in}	153
6.5.3	The Morphology-Density Relation with T_{auto}	154
6.5.4	Comparison with MORPHS data	155
6.6	Summary	156
7	The Environment of Passive Spiral Galaxies	176
7.1	Introduction	176
7.2	Data	178
7.3	Selection of Passive Spiral Galaxies	179
7.3.1	Line Measurements	179
7.3.2	Selection Criteria	179
7.4	Environment of Passive Spiral Galaxies	181
7.4.1	Local Galaxy Density	181
7.4.2	Cluster Centric Radius	181
7.4.3	Photometric & Spectroscopic Properties	182
7.5	Discussion	183
7.5.1	A Transient in Galaxy Evolution	183
7.5.2	Aperture Bias	186
7.6	Summary	187
8	Fate of Infalling Galaxies	203
8.1	Summary of Our Findings	203
8.2	Circumstantial Evidence of Cluster Galaxy Evolution	206

8.3	Morphological Evolution of Cluster Galaxies	207
8.4	Possible Hypotheses	208
9	Conclusions	212
A	A Catalog of Hδ-strong Galaxies	214
A.1	Introduction	214
A.2	The SDSS Data	217
A.3	Spectral Line Measurements	218
A.3.1	H δ Equivalent Width	218
A.3.2	[OII] and H α Equivalent Widths	221
A.3.3	Emission-Filling of the H δ Line	222
A.3.4	External Errors on our Measured Equivalent Widths	224
A.4	A Catalog of HDS Galaxies	224
A.5	Discussion	227
A.5.1	Comparison with Previous Work	227
A.5.2	HDS Galaxies with Emission-lines	229
A.6	Conclusions	230
B	Merger/Interaction Origin of E+A Galaxies	252
B.1	Introduction	252
B.2	Data	256
B.3	Defining Four Subsamples of H δ -strong Galaxies	256
B.3.1	E+A	258
B.3.2	HDS+[OII]	258
B.3.3	HDS+H α	258
B.3.4	HDS+em	259
B.4	The Morphology of H δ -strong Galaxies	259
B.5	The Environment of H δ -strong Galaxies	260
B.6	Possible Star Formation Histories	262
B.7	Properties of young E+A Galaxies	267
B.8	Discussion : Origins of E+A Galaxies	268
B.8.1	Are E+As Cluster Related Phenomena?	268
B.8.2	Are E+As Dusty Star-forming Galaxies?	269
B.8.3	Merger/Interaction Origin of E+A Galaxies	271
B.9	Summary and Conclusions	272

Abstract

We investigated environmental effects on galaxy evolution using the Sloan Digital Sky Survey (SDSS) data. By developing a new, uniform galaxy cluster selection method (the Cut & Enhance method), we have created one of the largest, most uniform galaxy cluster catalog with well determined selection function. Based on this cluster catalog, we derived extensive observational evidence of cluster galaxy evolution.

Composite luminosity functions (LF) of these cluster galaxies show that cluster LFs have a brighter characteristic magnitude (M^*) and a flatter faint end slope than field LFs. We also found that early-type galaxies always have flatter slopes than late-type galaxies. These results suggest that cluster galaxies have a quite different evolutionary history from that of field galaxies.

We confirmed the existence of the Butcher-Oemler effect as an increase of fractions of blue cluster galaxies with increasing redshift. This is direct evidence of *spectral* evolution of cluster galaxies. Cluster galaxies evolve by changing their color from blue to red, perhaps reducing their star formation rate (SFR). We also found that fractions of morphologically spiral galaxies are larger in higher redshift. This “morphological Butcher-Oemler effect” is shown for the first time using an automated galaxy classification, and is direct evidence of *morphological* cluster galaxy evolution. Cluster galaxies change their morphology from spiral to early-type galaxies. In addition to the redshift evolution, we found the slight dependence of blue/spiral fractions on cluster richness, in a sense that richer clusters have smaller fractions of blue/spiral galaxies. This result has significant implication for the underlying physical mechanism since it is consistent with a theoretical prediction of a ram-pressure stripping model, where richer clusters have more effective ram-pressure.

While investigating the morphology-density relation in the SDSS, we found two characteristic environments where the morphology-density relation abruptly changes. In the sparsest regions (galaxy density below 2 galaxy Mpc $^{-2}$ or outside of 2 virial radius), the morphology-density relations become less notable, suggesting that the responsible physical mechanisms require denser environment. In the intermediate density regions, (galaxy density between 2 and 6 galaxy Mpc $^{-2}$ or virial radius between 0.3 and 2), S0 fractions increase toward denser regions, whereas late-spiral fractions decrease. Considering the median size of S0 galaxies are smaller than that of late-spiral galaxies and star formation rate radically declines in these regions, the mechanism that gradually reduces star formation might be responsible for morphological changes in these intermediate density regions (e.g., ram-pressure stripping, strangulation). In the cluster core regions (above 6 galaxy

Mpc^{-2} or inside of 0.3 virial radius), S0 fractions decreases radically and elliptical fractions increase. This is a contrasting results to that in intermediate regions and it suggests that yet another mechanism is responsible for morphological change in these regions.

Finally, we found that passive spiral galaxies preferentially live in cluster infalling regions (galaxy density $1\sim 2 \text{ Mpc}^{-2}$ and $1\sim 10$ virial radius). Thus the origins of passive spiral galaxies are likely to be cluster related. The existence of passive spiral galaxies suggest that a physical mechanism that works calmly is preferred to dynamical origins such as major merger/interaction since such a mechanism can destroy spiral arm structures.

Considering all the observational results, we propose a new evolutionary scenario of cluster infalling galaxies. Around 2 virial radius or galaxy density below 2 galaxy Mpc^{-2} , infalling field spiral galaxies quiescently stop their star formation and are transformed into passive spiral galaxies calmly. These passive spiral galaxies later become S0 galaxies. Possible responsible physical mechanisms in this region include ram-pressure stripping, strangulation, thermal evaporation and minor mergers, perhaps mainly happening in sub-clump regions around a cluster. In the cluster core regions, we speculate that S0 galaxies fade away to enhance the dominance of old bright elliptical galaxies.

Chapter 1

General Introduction

It is a remarkable feature that various properties of galaxies vary according to their environments. In 1926, Hubble classified galaxies according to their morphology along the tuning fork diagram (Figure 1.1). This is the so-called Hubble’s tuning fork diagram, and is still commonly used to understand variety in galaxy morphology. However, little is known on the origin of this variety in galaxy morphology. It has been known for a long time that galaxy cluster regions are dominated by bright elliptical galaxies, whereas star-forming spiral galaxies are more numerous in the field. Many people observed that cluster elliptical galaxies have tight correlation between their color and magnitude (so-called color-magnitude relation). This variety in galaxy properties and correlation with galaxy environments have driven many researchers to study galaxies and clusters. However, only little has been known on the origin of this variety in galaxies. The purpose of this work is to clarify observationally environment-dependent effects which affect galaxy properties causing the evolution of galaxies, in order to understand underlying physical mechanism governing this variety in properties of present day galaxies.

1.1 Observational Evidence for Environmental Effects

1.1.1 The Morphology-Density Relation

In his pioneering work, Dressler (1980) studied 55 nearby clusters and found that the fraction of elliptical galaxies are higher in the denser regions such as cluster cores. This correlation between galaxy morphology and its environment is called the morphology-density relation, and has been observed by so many people until today. Postman & Geller (1984) extended morphology study to galaxy groups (Typically a group consists of a few to dozens of galaxies.) using the data from the CfA Redshift Survey (Huchra et al. 1983). The relation was completely consistent with Dressler (1980). At low densities below galaxy density $\sim 5 \text{ Mpc}^{-3}$, population fractions seems to be independent of environment.

At high density above ~ 3000 galaxies Mpc^{-3} , the elliptical fraction increased steeply. Whitmore et al. (1993) re-analyzed the 55 nearby clusters studied by Dressler (1980) and argued that the morphology-radius relation is more fundamental; the correlation between morphology and cluster centric radius seems tighter than the morphology-density relation. Dressler et al. (1997) studied 10 high redshift clusters at $z \sim 0.5$ and found that the morphology-density relation is seen for centrally concentrated clusters. However, the relation was nearly absent for less concentrated or irregular clusters. Fasano et al. (2000) studied nine clusters at intermediate redshift ($0.1 \leq z \leq 0.25$) and found that morphology-density relation in clusters with high elliptical concentration, but not in those with low elliptical concentration. Hashimoto et al. (1999) used data from Las Campanas Redshift Survey (LCRS; Shectman et al. 1996) to study the concentration-density relation. They found that the ratio of high to low concentrated galaxies decreases smoothly with decreasing density. Dominguez et al. (2001) analyzed nearby clusters with X-ray and found that mechanisms of global nature (X-ray mass density) dominate in high density environments, namely the virialized regions of clusters, while local galaxy density is the relevant parameter in the outskirts where the influence of cluster as a whole is relatively small compared to local effects. Dominguez et al. (2002) studied groups in 2dF Galaxy Group Catalog using PCA analysis of spectra as a galaxy classification and local galaxy density from redshift space as a measure of galaxy environment. They found that both morphology-density relation and morphology-group-centric radius relation is clearly seen in high mass ($M_v \geq 10^{13.5} M_\odot$) groups, but neither relation is observed for low mass ($M_v < 10^{13.5} M_\odot$) groups.

Apparently previous studies have shown the fact that there is a correlation between galaxy morphology and environment. However, previous studies often had the following uncertainties; (i) two dimensional density estimation from the imaging data, (ii) subjective, eye-based galaxy classification, (iii) lack of the field data. Therefore, it is important to rectify these problems using a larger, more uniform data with three dimensional information, such as the SDSS data used in this work. Furthermore, to understand the underlying physical mechanism, it is of importance to specify the exact environment where galaxy morphology starts to change and the accurate amount of galaxies which undergo morphological change. We try to address these problems using the SDSS data in Chapter 6. In addition to clarify various correlations between galaxy properties as have been claimed in previous work, high quality and large quantity of the SDSS data offers us, for the first time, a chance to understand underlying physical mechanisms.

1.1.2 Suppression of Star Formation in Cluster Regions

Similarly, there have been extensive evidence that cluster galaxies have smaller amount of star formation, with redder colors than field galaxies. It has been known for a long time that cluster regions lack emission line galaxies (Osterbrook 1960; Gisler 1978; Dressler, Thompson, & Shectman 1985). Recently, many studies reported that star formation in the cores of clusters is much lower than that in the surrounding field (e.g., Balogh et al. 1997, 1998, 1999; Poggianti et al. 1999; Martin, Lotz & Ferguson 2000; Couch et al. 2001; Balogh et al. 2002).

In addition, it is becoming possible to specify the environment where star formation in galaxies starts to change. Abraham et al. (1996) reported that cluster members become progressively bluer as a function of cluster-centric distance out to 5 Mpc in A2390 ($z = 0.23$). van Dokkum et al. (1998) found S0 galaxies in the outskirts of a cluster at $z = 0.33$. These S0s show a much wider scatter in their colors and are bluer on average than those in cluster cores, providing possible evidence for recent infall of galaxies from the field. Terlevich, Caldwell & Bower (2001) reported that $U - V$ colors of early-type galaxies are systematically bluer at outside the core of Coma cluster. Pimbblet et al. (2002) studied 11 X-ray luminous clusters ($0.07 < z < 0.16$) and found that median galaxy color shifts bluewards with decreasing local galaxy density. At higher redshifts, Kodama et al. (2001) reported that colors of galaxies abruptly change at sub-clump regions surrounding a cluster at $z = 0.41$. Recently, using statistically much larger sample, Lewis et al. (2002) and Gomez et al. (2003) showed that star formation rate (SFR) of galaxies decreases toward cluster cores at around 1 virial radius. All of these results are often interpreted as the result of star-forming field disk galaxies infalling to a cluster, being transformed to passive cluster galaxies. It is of importance to observationally specify the environment where galaxy properties start to change and how much they change in order to understand the underlying physical mechanisms responsible for these differences.

1.1.3 Color-Magnitude Relation

Cluster galaxies are known to have tight color-magnitude relation. Visvanathan & Sandage (1977) noted that bright early-type galaxies in Coma and eight other local clusters have a tight correlation between their colors and magnitude, in a sense that brighter galaxies have redder colors (the color-magnitude relation; CMR). Bower, Lucey & Ellis (1992) later studied the CMR in detail using high precision photometry of early-type galaxies in Virgo and Coma clusters to find little scatter around the mean CMR. Various other studies also confirmed the existence of tight CMR in both low redshift cluster (Sandage & Visvanathan 1978; van Dokkum et al. 1998; Pimbblet et al. 2002), and high redshift clusters (Aragon-Salamanca et al. 1993; Stanford et al. 1995, 1998; Dickinson 1996;

(Ellis et al. 1997; Kodama et al. 1998; van Dokkum et al. 2000). These studies are in remarkable agreement: the slope and scatter of the CMR seem to be roughly constant with passive evolution of an old stellar population formed at high redshift. The rms of scatter about the mean CMR is typically ~ 0.04 mag, a comparable size to observational errors, implying a virtually negligible intrinsic scatter. The universality of the CMR also suggests the different star formation history between field galaxies and cluster galaxies. It is one of the purposes of this study to observationally collect the evidence for cluster galaxy evolution in order to understand the underlying physical mechanisms governing cluster galaxy evolution.

1.1.4 Evolution of Cluster Galaxies

There also have been direct evidence for cluster galaxy evolution. Butcher & Oemler (1978, 1984) found that fractions of blue galaxies are larger in the past, showing that cluster galaxies evolve from blue to red (so-called the Butcher-Oemler effect; Figure 1.2). Butcher and Oemler's work made a strong impact since it showed direct evidence for the evolution of cluster galaxies. Much work regarding the nature of these blue galaxies followed. Rakos & Schombert (1995) found that the fraction of blue galaxies increases from 20% at $z = 0.4$ to 80% at $z = 0.9$, suggesting that the evolution in clusters is even stronger than previously thought. Margoniner & De Carvalho (2000) studied 48 clusters in the redshift range of $0.03 < z < 0.38$ and detected a strong Butcher-Oemler effect consistent with that of Rakos & Schombert (1995). Despite the global trend with redshift, almost all previous work has reported a wide range of blue fraction values at respective redshifts. In particular, in a large sample of 295 Abell clusters, Margoniner et al. (2001) not only confirmed the existence of the Butcher-Oemler effect, but also found the blue fraction depends on cluster richness. Ellingson et al. (2001) studied 15 CNOC1 clusters (Yee, Ellingson, & Carlberg 1996) between $z = 0.18$ and $z = 0.55$. Since they used spectroscopically observed galaxies, they do not suffer from the fore/background contamination (but see Diaferio et al. 2001). They used galaxies brighter than $M_r = -19.0$ and found a blue fraction of ~ 0.15 at $z = 0.3$.

In addition to the color evolution of cluster galaxies, morphological evolution of cluster galaxies have been observed. Dressler et al. (1997) studied 10 high redshift clusters at $z \sim 0.5$ and found that S0 fractions are much smaller than those in nearby clusters, suggesting that S0 galaxies are created fairly recently ($z \leq 0.5$; Figure 1.3). Fasano et al. (2000) studied 9 intermediate redshift clusters and plotted morphological fraction as a function of redshift to find that S0 fraction decreases with increasing redshift, whereas spiral fraction increases with redshift. There also have been observations showing the deficit of S0 galaxies in high redshift clusters (Andrean et al. 1997; Couch et al. 1998;

Lubin et al. 1998; but also see Andreon et al. 1998; Fabricant et al. 2000). These observational results show us that cluster galaxies are likely to evolve, changing their color from red to blue, and their morphology from late-type to early-type.

However, almost all of previous work had a fundamental problem in using a heterogeneous sample of clusters. For example, one can never claim the evolution by comparing low redshift clusters observed by a ground based telescope with high redshift clusters observed by *the Hubble Space Telescope*. In such a case, high redshift clusters are much richer than low redshift clusters, and thus subjective to richness related bias. There have been many people who doubt such an evolutionary study with heterogeneous sample (Newberry, Kirshner & Boroson 1988; Allington-Smith et al. 1993; Garilli et al. 1996; Smail et al. 1998; Andreon & Ettori 1999; Balogh et al. 1999; Fairley et al. 2002). In Chapter 5, we try to rectify this problem using the largest sample of 514 clusters, uniformly selected from the same SDSS data, eliminating a richness related and redshift related bias.

1.2 Theoretical Implications

Various physical mechanisms have been proposed to explain the observational results on cluster galaxy evolution. In this section, we aim to summarize them by classifying them into three broad categories; (1) interplay between galaxies and intra-cluster medium (2) galaxy-galaxy gravitational interaction. (3) gravitational interaction between a galaxy and the cluster potential.

1. Interplay between galaxies and intra-cluster medium.

Ram-pressure stripping of cold gas in the disk of a galaxy is a candidate since the star formation loses its source due to the removal of the cold gas. (Gunn & Gott 1972; Farouki & Shapiro 1980; Kent 1981; Fujita 1998; Fujita & Nagashima 1999; Abadi, Moore & Bower 1999; Quilis, Moore & Bower 2000; Tonizzzo & Schndler 2001; Fujita 2001,2003). Ram-pressure stripping is likely to be effective in the central region of clusters where density of intra-cluster medium (ICM) is high. In fact, disk galaxies with a deficit of cold gas or a morphological sign of gas removal are often observed near cluster centers (e.g., Cayatte et al. 1990; Vollmer et al. 2000; Bravo-Alfaro et al. 2000, 2001; Solanes et al. 2001; Bureau & Carignan 2002; Vollmer 2003). Especially, Haynes & Giovanelli (1986) showed that the frequency of HI deficient galaxies projected on the sky increases close to the center of the Virgo Cluster. In addition, the ram-pressure stripping is predicted to be more effective in a richer cluster since the velocity of galaxies is larger (Bahcall 1977; Fujita et al. 1999,2001). This prediction can be observationally tested by studying fractions of blue galaxies as a function of cluster richness. We perform such an attempt in

Chapter 6.

On the other hand, star formation rates of galaxies may decrease gradually by stripping of warm halo gas that would later infall on to the galactic disks, and be the source of cold gas and stars in the galactic disks (strangulation; Larson, Tinsley & Caldwell 1980; Balogh et al. 2001; Bekki et al. 2002; Mo & Mao 2002; Oh & Benson 2002). If only warm halo gas is stripped, star formation may be allowed to continue by consuming remaining cold disk gas but, without infalling gas from halo to replenish this supply, star formation will die out on timescales of a few Gyr (Larson et al. 1980). Observationally, Finoguenov et al. (2003) found in Coma cluster the filamentary gas where strangulation is likely to be happening and they predicted quiescent star formation in galaxy disks around the filament.

Another mechanism to slow down the star formation rate of galaxies is thermal evaporation of the cold gas in disk galaxies via heat conduction from the surrounding hot ICM (Cowie & Songaila 1977; Fujita 2003). Pressure triggered star formation, in which galactic gas clouds are compressed by the ICM pressure, can temporarily increase the star formation rate (Dressler & Gunn 1983; Evrard 1991; Fujita 1998).

All of the above mechanisms need relatively high density of hot intra-cluster gas, and thus likely to happen in the central region of clusters. Although several authors indicated that these mechanisms can not explain the suppression of star formation as far as several Mpc from the center of a cluster (Balogh et al. 1997; Kodama et al. 2001; Lewis et al. 2002), Fujita et al. (2003) pointed out that these mechanisms can happen in cluster sub-clump regions (small groups around a cluster). The above mechanisms mainly affect the star formation rate of a galaxy, compared with the following dynamical mechanisms which directly affect the morphology of a galaxy.

2. Galaxy-galaxy gravitational interaction.

This category includes interaction/merging of galaxies (Icke 1985; Lavery & Henry 1988; Bekki 1998). Mergers between galaxies with compatible masses (major mergers) could create an elliptical galaxy (Toomre & Toomre 1972). However, in the semi-analytic simulation, it is known that the observed fraction of intermediate bulge-to-disk ratio galaxies can not be explained solely by major mergers (Okamoto & Nagashima 2001; Diaferio et al. 2001; Springel et al. 2001). Okamoto & Nagashima (2003) indicated that mergers between galaxies with significantly different masses (minor mergers) might play an important role in creating intermediate bulge-to-disk ratio galaxies. Galaxy harassment via high speed impulsive encounters also can affect morphology and star formation rate of cluster galaxies (Moore et al. 1996, 1998, 1999).

3. Gravitational interaction between a galaxy and the cluster potential.

Tidal compression of galactic gas via interaction with the cluster potential can increase the star formation rate of a galaxy (Byrd & Valtonen 1990, Valluri 1993; Fujita 1998).

Unfortunately, there exists little evidence demonstrating that any one of these processes is actually responsible for driving galaxy evolution. Most of these processes act over an extended period of time, while observations at a certain redshift cannot easily provide the detailed information that is needed to elucidate subtle and complicated processes. To extract useful information in comparison with the observational data, it is of importance to specify the environment where galaxy properties change. For example, stripping mechanisms (ram-pressure stripping, strangulation) and evaporation require dense hot gas, and therefore, can not happen far away from a cluster where gas density is too low. They can happen only in cluster cores or in dense sub-clumps (Fujita et al. 2003). Merging/interaction is probably difficult to happen in cluster cores since relative velocity of galaxies are too high in such regions in the present universe (Ostriker 1980; Binney & Tremaine 1987; Mamon 1992; Makino & Hut 1997). It is also important to investigate the morphology of galaxies which are currently undertaking transformation. If major merging/interaction is the responsible mechanism, galaxies should have disturbed signature (e.g., tidal tails, multiple cores) in their morphology. If minor merger is dominant, galactic bulges may become larger and larger during the evolution (Ohama 2003). If stripping or evaporation is more effective, galaxies should be transformed calmly, reducing their luminosity and sizes. In this work, we observationally try to clarify these points by examining morphology of galaxies in Sections 6 and 7.

1.3 Need for Larger, More Uniform Samples

The last two sections described various observational and theoretical implications on the evolution of cluster galaxies. However, almost all observational researches in the literature suffered from the lack of a large, uniform cluster catalog and galaxy catalog. The most commonly used cluster catalog, Abell cluster catalog (Abell 1958, Abell, Corwin and Olowin 1989) was constructed by the visual inspection of photographic plates. Although human eyes are an excellent tool to find galaxy clusters, it suffers from subjectivity. A computer based automated method is needed to create an objective cluster catalog with well understood selection function. The effects could be more severe for evolutionary study. For example, Butcher & Oemler (1984) used 10 clusters selected from the single color photographic plates to find the spectral evolution of cluster galaxies. Since higher redshift clusters are fainter due to long distance and redshifting of the flux, higher red-

shift sample could be richer clusters than the nearby sample. Thus it potentially has a malmquist type bias. As another example, Fasano et al. (2000) found morphological evolution of cluster galaxies, but their cluster sample consist of three different cluster samples observed with three different telescopes; local clusters of Dressler (1980), intermittent sample of their own and high redshift sample of Dressler (1997). It is necessary to use a large & homogeneous sample of clusters when studying evolution of cluster galaxies.

Furthermore, in many studies, the morphological classifications of galaxies have also been performed by human eyes (Dressler et al. 1980,1997; Fasano et al. 2000), and thus could have been suffered from the subjectivity. By its nature, human based classification change from person to person (Lahav et al. 1995). Even the classification by the same person can change according to the condition of the person, such as how tired he is, brightness of the display, specifications of the softwares used. Computer based automated galaxy classification is preferred since it is easier to compute completeness and contamination rate of the classification, and to apply the same method to future observational data or computer based simulations.

With the advent of the Sloan Digital Sky Survey (SDSS; see Fukugita et al. 1996; Gunn et al. 1998; Lupton et al. 1999,2001; York et al. 2000; Eisenstein et al. 2001; Hogg et al. 2001; Blanton et al. 2003a; Pier et al. 2002; Richards et al. 2002; Stoughton et al. 2002; Strauss et al. 2002; Smith et al. 2002 and Abazajian et al. 2003 for more detail of the SDSS data), which is both an imaging and spectroscopic survey of 100,000 deg² of the sky, it is now becoming possible to create a large, uniform cluster catalog and to study the evolution of cluster galaxies using a large, uniform data. The SDSS takes high quality CCD image of a quarter of the sky in 5 optical bands (u, g, r, i and z), and produce the data that enable us to classify galaxies using an automated method, without depending on human eyes. In this thesis, we take a full advantage of the SDSS data and study the environmental effects on cluster galaxy evolution using one of the largest and most uniform samples to date. The sample allows us to reveal the environmental effects on galaxy evolution in much more detail than previous study, providing us with the first opportunity to understand the underlying physical mechanisms.

In Chapter 2, we briefly describe the SDSS data. In Chapter 3, we create a new, uniform cluster catalog using the SDSS data. In Chapter 4, we study composite luminosity functions of clusters to reveal a statistical difference between cluster galaxies and field galaxies. In Chapter 5, we study the evolution of cluster galaxies and reveal that cluster galaxies evolve both spectrally and morphologically. In Chapter 6, we study the morphology-density relation and reveal the correlation between galaxy morphology and local galaxy density. In Chapter 7, we study passive spiral galaxies, which turned out to be a galaxy in transition. In Chapter 8, we discuss theoretical scenarios consistent with all the observational results. In Chapter 9, we summarize this work. Over the last decade,

the origin of post-starburst (E+A) galaxies has been actively debated, often in connection to cluster related phenomena. We present an analysis of this post-starburst phenomena in Appendix A and B, together with the reason why these chapters are not included in the main text. The cosmological parameters adopted are $H_0=75$ km s $^{-1}$ Mpc $^{-1}$, and $(\Omega_m, \Omega_\Lambda, \Omega_k)=(0.3, 0.7, 0.0)$, unless otherwise stated.

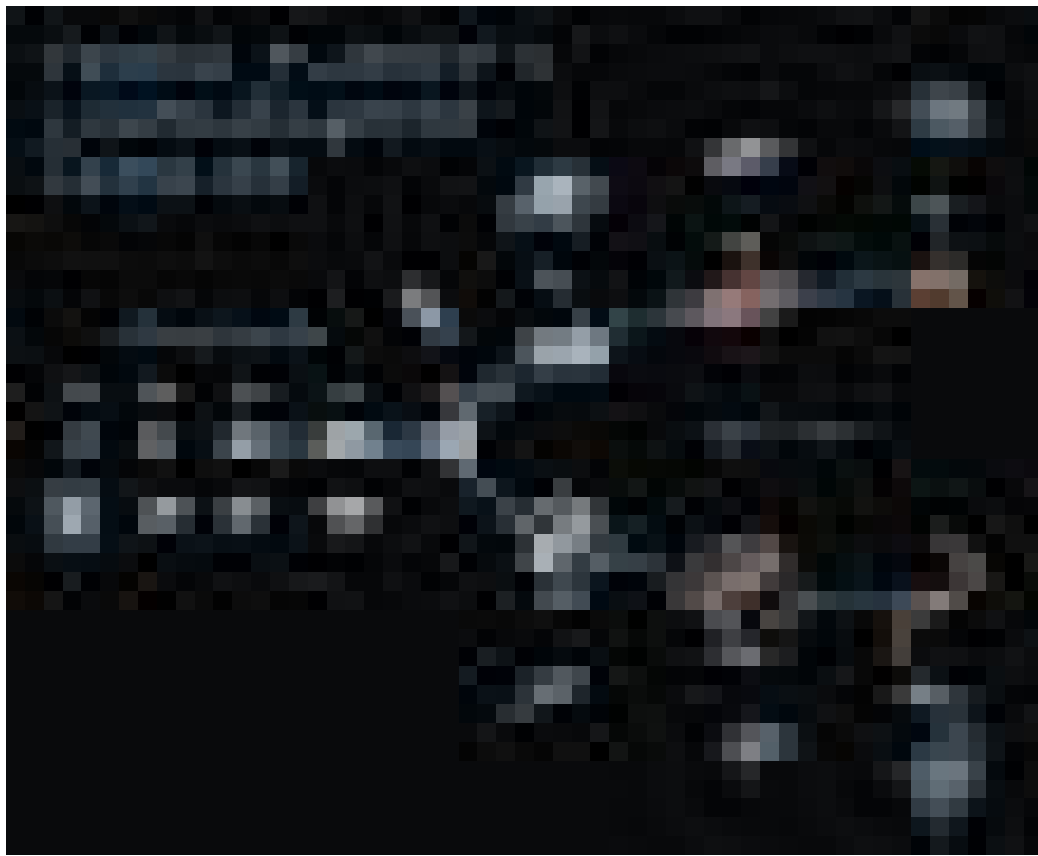


Figure 1.1: Hubble's tuning fork diagram.



Figure 1.2: Blue galaxy fraction vs. redshift. Filled circles, compact clusters ($C \geq 0.40$); open circles, irregular clusters ($C < 0.35$); dotted circles, intermediate clusters ($0.35 \leq C < 0.40$).



Figure 1.3: The S0/E fraction for clusters in the sample as a function of redshift. The open circles are the outer fields in A370 and Cl 0939+47, which are not used in the least-squares fit, shown with its 1σ errors as the solid and dotted lines. The extrapolation of this linear relation to zero redshift approximately matches the value $S0/E \sim 2$, shown by the filled square, found for 11 clusters with $0.035 < z < 0.044$ of the D80 cluster sample (Dressler et al. 1997).

Chapter 2

The Sloan Digital Sky Survey

2.1 The Sloan Digital Sky Survey

The Sloan Digital Sky Survey (SDSS; see Fukugita et al. 1996; Gunn et al. 1998; Lupton et al. 1999,2001; York et al. 2000; Eisenstein et al. 2001; Hogg et al. 2001; Blanton et al. 2003a; Pier et al. 2002; Richards et al. 2002; Stoughton et al. 2002; Strauss et al. 2002; Smith et al. 2002 and Abazajian et al. 2003 for more detail of the SDSS data.) is both an imaging and spectroscopic survey of a quarter of the sky. The SDSS began its operation in November 2000. For both imaging and spectroscopy, the SDSS uses a dedicated 2.5m telescope located at Apache Point Observatory in New Mexico, U.S.A (Figure 2.1). The SDSS telescope has a modified f/5.0 Ritchey-Chretien optical design with a large secondary and two corrector lenses below the primary mirror. The telescope has a wide (3° diameter), essentially distortion-free field of view. The SDSS telescope is shown in Figure 2.2. It is a unique feature of the SDSS that the telescope will carry out both imaging and spectroscopic surveys of the region of about π steradians centered on the north Galactic pole in five years. Imaging part of the survey obtains CCD images of $10,000 \text{ deg}^2$ of the sky in five optical bands (u, g, r, i and z ; Fukugita et al. 1996). The spectroscopic part of the survey observes one million galaxies uniformly selected from the imaging part of the survey. We use this excellent data set to tackle the long standing problems on environmental effects on galaxy evolution. In this chapter, we briefly describe the design and products of the SDSS.

2.1.1 The SDSS Imaging Survey

The imaging part of the SDSS will image $10,000$ square degrees in five bandpasses to a depth of $g \sim 23$ mag with effective wavelengths of [3561 Å, 4676 Å, 6176 Å, 7494 Å and 8873 Å] (u, g, r, i and z) spanning from the atmospheric cutoff at 300nm to the limit of CCD sensitivity at 1100nm (Fukugita et al. 1996). The imaging camera (Gunn

et al. 1998) consists of a mosaic of 30 2048×2048 SITe CCDs with $24 \mu\text{m}$ pixels as shown in Figure 2.3. A pixel in the imaging camera subtends $0.396''$ on the sky. The CCDs are arranged in six dewars (six columns) containing 5 CCDs each. The camera is mounted to the corrector plate and observes the sky through five broad band filters (u, g, r, i and z). The imaging CCDs saturate at about 14 mag, so to calibrate these data with existing astrometric catalogs, the camera contains an additional 22 CCDs, each having 2048×400 pixels, with neutral density filters that saturate at only 8 mag. The photometric calibration is carried out with a separate $20''$ photometric telescope equipped with a single-CCD camera and the SDSS filters (Uomoto et al. 2003). The photometric telescope is located near the SDSS telescope at the same site. However, at the time of writing, the calibration is still in preliminary stage. Thus we denote preliminary SDSS magnitudes as u^*, g^*, r^*, i^* and z^* , rather than the notation u, g, r, i and z that will be used for the final SDSS photometric system (and is used in this paper to refer to the SDSS filters themselves). The response functions are presented in Figure 2.4. The limiting magnitude, i.e., 5σ detection in $1''$ seeing limits, for point sources are 22.3, 23.3, 23.1, 22.3 and 20.8 in the u, g, r, i and z filters, respectively, at an airmass of 1.4. In general, the telescope is driven along a great circle on the sky in such a way that objects pass directly along a column of CCDs. This allows essentially simultaneous observations to be obtained in each of the five passbands and provides very efficient survey observing (the shutter never closes). Each object spends 5.7 mins to pass the entire CCD array. Net integration time in each filter is 54.1 sec. We show three representative bright astronomical objects observed with the SDSS camera in Figures 2.5-2.7.

The location of the survey imaging area is shown in Figure 2.8. The northern survey area is centered near the North Galactic Pole and it lies within a nearly elliptical shape 130° E-W by 110° N-S chosen to minimize Galactic foreground extinction. All scans are conducted along great circles in order to minimize the transit time differences across the camera array. There are 45 great circles (*stripes*) in the northern survey regions separated by 2.5° . The SDSS observes three non-contiguous stripes in the Southern Galactic Hemisphere, at declinations of 0° , 15° and -10° , during the fall season when the northern sky is unobservable. Each stripe is scanned twice, with an offset perpendicular to the scan direction in order to interlace the photometric columns. A completed stripe slightly exceeds 2.5° in width and thus there is a small amount of overlap to allow for telescope mis-tracking and to provide multiple observations of some fraction of the sky for quality assurance purposes. The total stripe length for the 45 northern stripes will require a minimum of 650 hours of pristine photometric and seeing conditions to scan at a sidereal rate. Based upon the current experience of observing at Apache Point Observatory, it seems likely that the SDSS will only complete about 75% of the imaging after 5 years of survey operations.

2.1.2 The SDSS Spectroscopic Survey

By selecting targets from the photometric catalog produced by the imaging survey, the SDSS observes spectra of 10^6 bright galaxies to the depth of $r^* \sim 17.77$ mag with median redshift of $z \sim 0.1$ ($r^* \sim 19.5$ mag for luminous red galaxies, reaching the redshift of $z \sim 0.45$) and 10^5 brightest quasars to $i^* \sim 20.0$ mag. The spectra are observed, 640 at a time (with a total integration time of 45 minutes) using a pair of double fiber-fed spectrographs shown in Figures 2.9 and 2.10. The wavelength coverage of the spectrographs is continuous from about 3800 Å to 9200 Å, and the wavelength resolution, $\lambda/\delta\lambda$, is 1800 . The fiber diameter is 0.2 mm (3" on the sky), and adjacent fibers cannot be located more closely than 55" on the sky. The throughput of the spectrograph will be better than 25% over 4000 Å to 8000 Å excluding the loss due to the telescope and atmosphere.

Two samples of galaxies are selected from the objects classified as “extended”. The main galaxy sample consists of $\sim 900,000$ galaxies with $r^* < 17.77$. This magnitude limit was chosen to satisfy the desired target density of 90 objects per square degree. In selecting target galaxies, the SDSS uses Petrosian magnitude (Petrosian 1976), which is based on the aperture defined by the ratio of local surface brightness within an annulus to the average surface brightness inside that radius, providing redshift independent estimate of total magnitude. The SDSS also applies a surface-brightness limit at $\mu_{r*} < 24.5$ mag arcsec $^{-2}$, in order not to waste fibers on galaxies too faint to observe. This surface brightness cut eliminates just 0.1% of galaxies that would otherwise be targeted for observation. Galaxies in the main galaxy sample have a median redshift of $z \sim 0.104$. See Strauss et al. (2002) for more details of the main galaxy target selection. We show an example redshift distribution of the equatorial data of the SDSS commissioning phase in Figure 2.11.

The SDSS observes additional $\sim 100,000$ luminous red galaxies (LRG). For luminous red galaxies, redshift can be well measured with the SDSS spectrograph to $r^* \sim 19.5$ mag due to their intrinsic brightness and their strong absorption lines due to high metallicity. Galaxies located at the dynamical centers of clusters often have these properties. Reasonably accurate ($\Delta z \sim 0.03$) photometric redshifts can be determined for these galaxies, allowing the selection by magnitude and g, r, i color of an essentially distance-limited sample to a redshift of $z \sim 0.45$. See Eisenstein et al. (2001) for more details of the LRG target selection.

150,000 quasar candidates are selected from cuts in multi-color space (Richards et al. 2002) and by identifying sources from the FIRST radio catalog (Becker et al. 1995). Due to their power-law continua and the strong Ly α emission, quasars have $ugriz$ colors quite distinct from those of the vastly more numerous stars over most of their redshift range (Fan 1999). Thus, among point sources, quasar candidates are selected for spectroscopic observations as outliers from the stellar locus in color-color space. The SDSS compile

a sample of quasars brighter than $i^* \sim 19$ at $z < 3$; at redshift between 3 and 5.2, the limiting magnitude will be $i^* \sim 20$. Point sources brighter than $i^* \sim 20$ that are FIRST sources are also selected. Based on the commissioning data, it is estimated that $\sim 65\%$ of quasar candidates are genuine quasars. Comparison with samples of known quasars indicates that the completeness is $\sim 90\%$. This sample will be orders of magnitude larger than any existing quasar catalog, and will be invaluable for quasar luminosity functions, evolution and clustering studies as well as providing sources for followup absorption-line observations.

In addition to the above three classes of spectroscopic targets, which are designed to provide statistically complete samples, the SDSS also obtains spectra of many thousands of stars and for various serendipitous objects when remaining fibers are available.

In this work, we mainly use a subsample of the main galaxy sample.

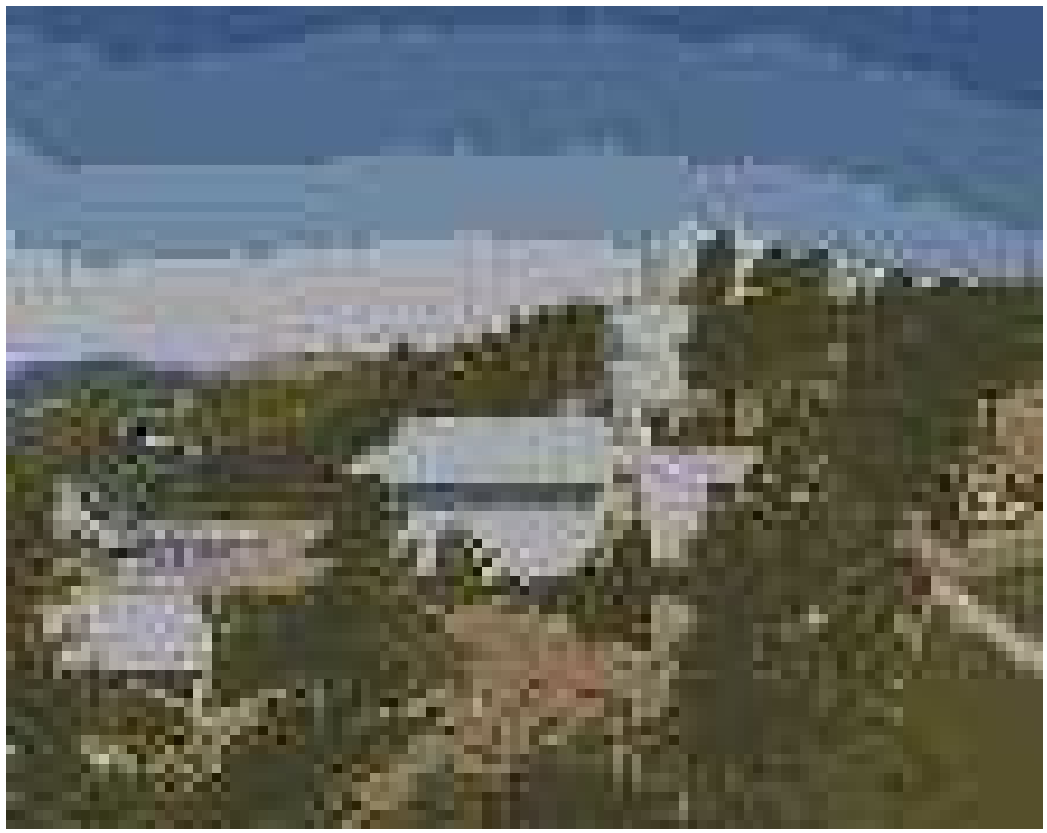


Figure 2.1: The Apache Point Observatory in New Mexico, U.S.A.



Figure 2.2: The SDSS 2.5-meter telescope located at Apache Point Observatory



Figure 2.3: The imaging camera of the SDSS. The five broadband filters are aligned in an order of *riuzg*. The narrow dark rectangles are astrometric CCDs.

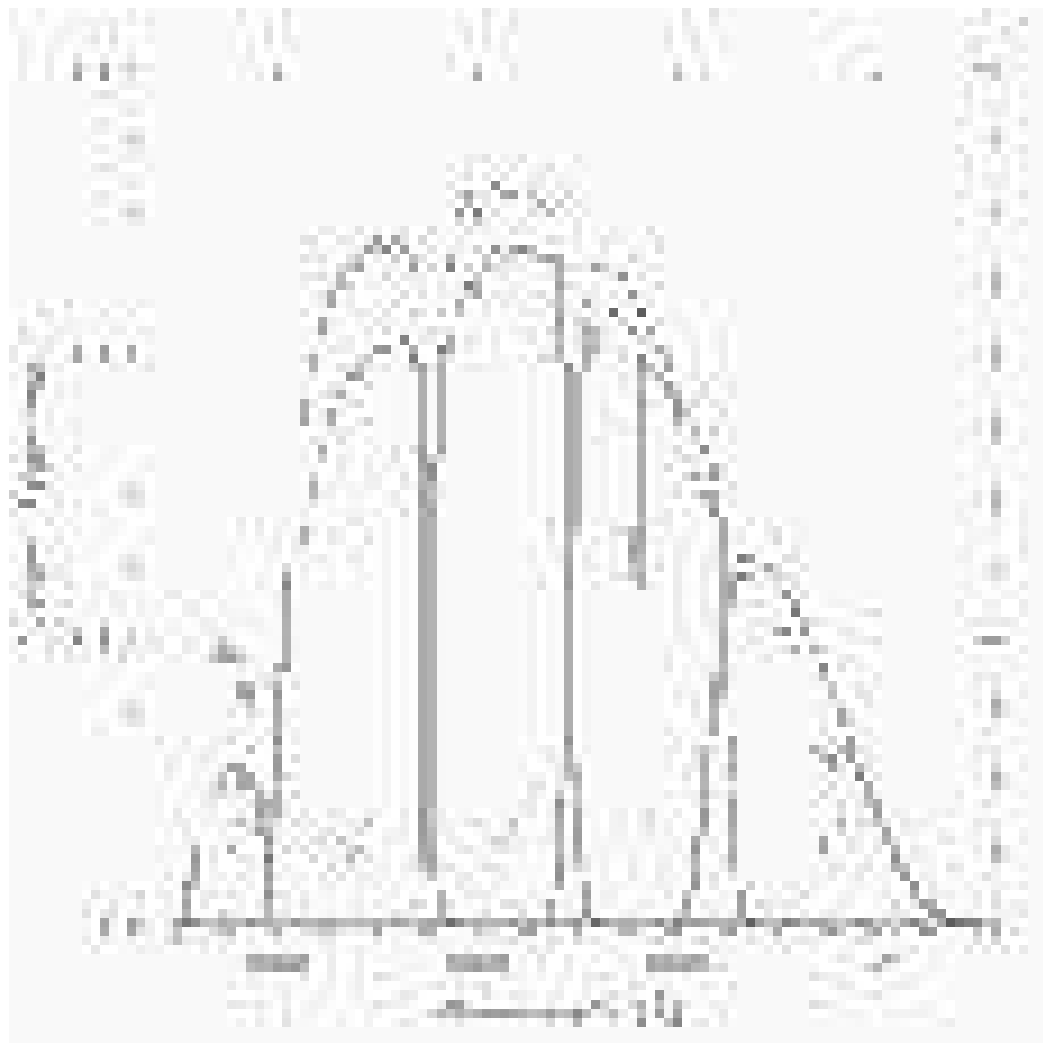


Figure 2.4: The SDSS photometric system response as a function of wavelength. The upper curves is without atmospheric extinction. The lower curve is with atmospheric extinction when observed at a typical altitude of 56° .



Figure 2.5: A galaxy cluster Abell 168, observed with the SDSS imaging camera.

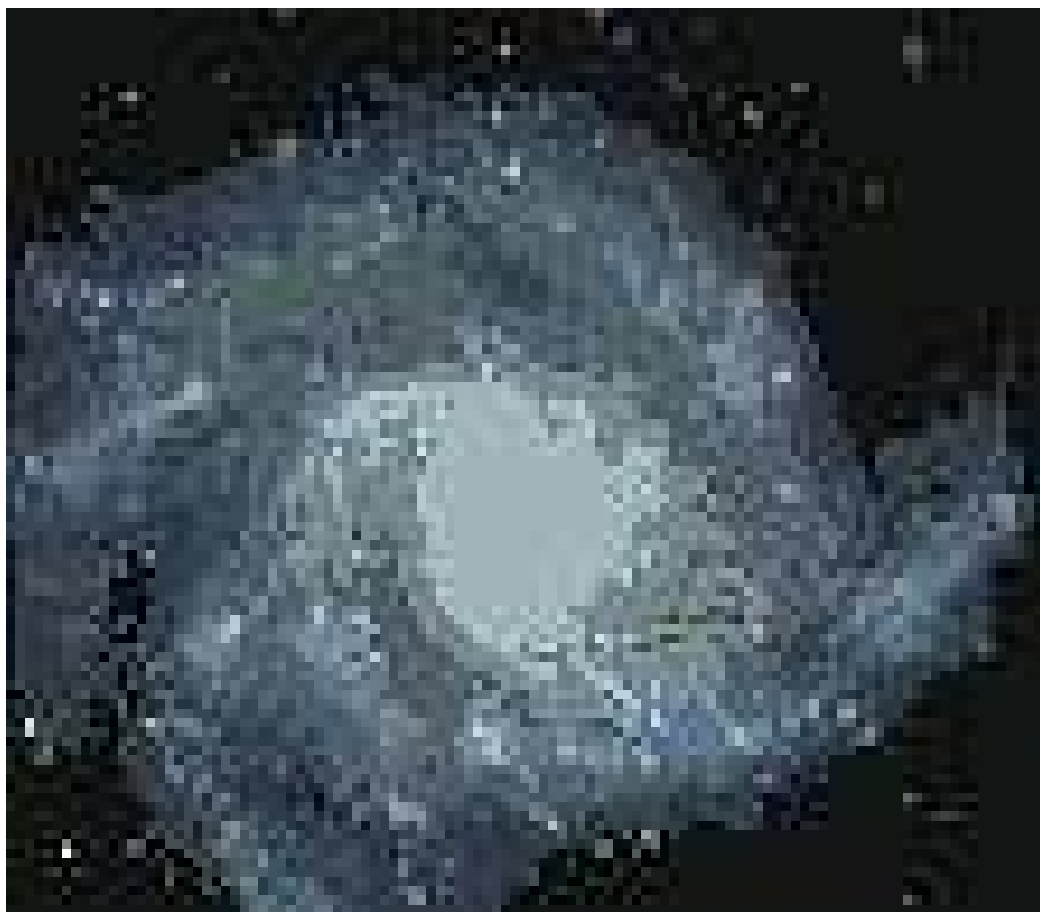


Figure 2.6: A bright spiral galaxy M101, observed with the SDSS imaging camera.



Figure 2.7: A globular cluster M2, observed with the SDSS imaging camera.

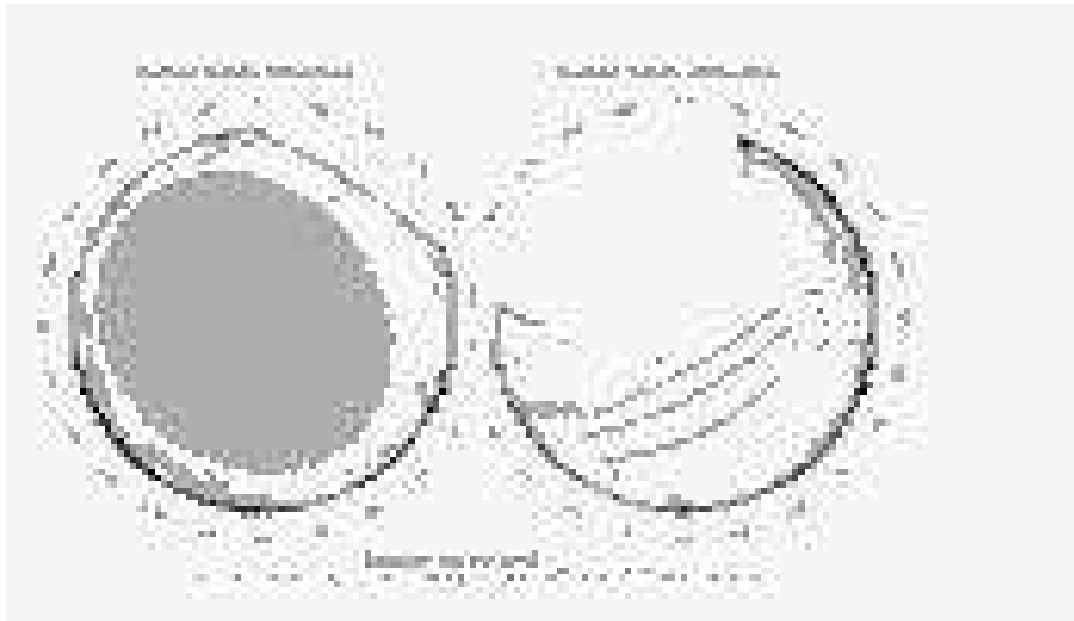


Figure 2.8: The location of the survey imaging strips plotted in a polar projection for the North (left) and South (right) Galactic hemispheres. The contours indicate the amount of reddening due to dust in our own Galaxy. Each solid line shows a 2.5 deg wide rectangular region (*stripe*) that the SDSS camera observes in two nights.

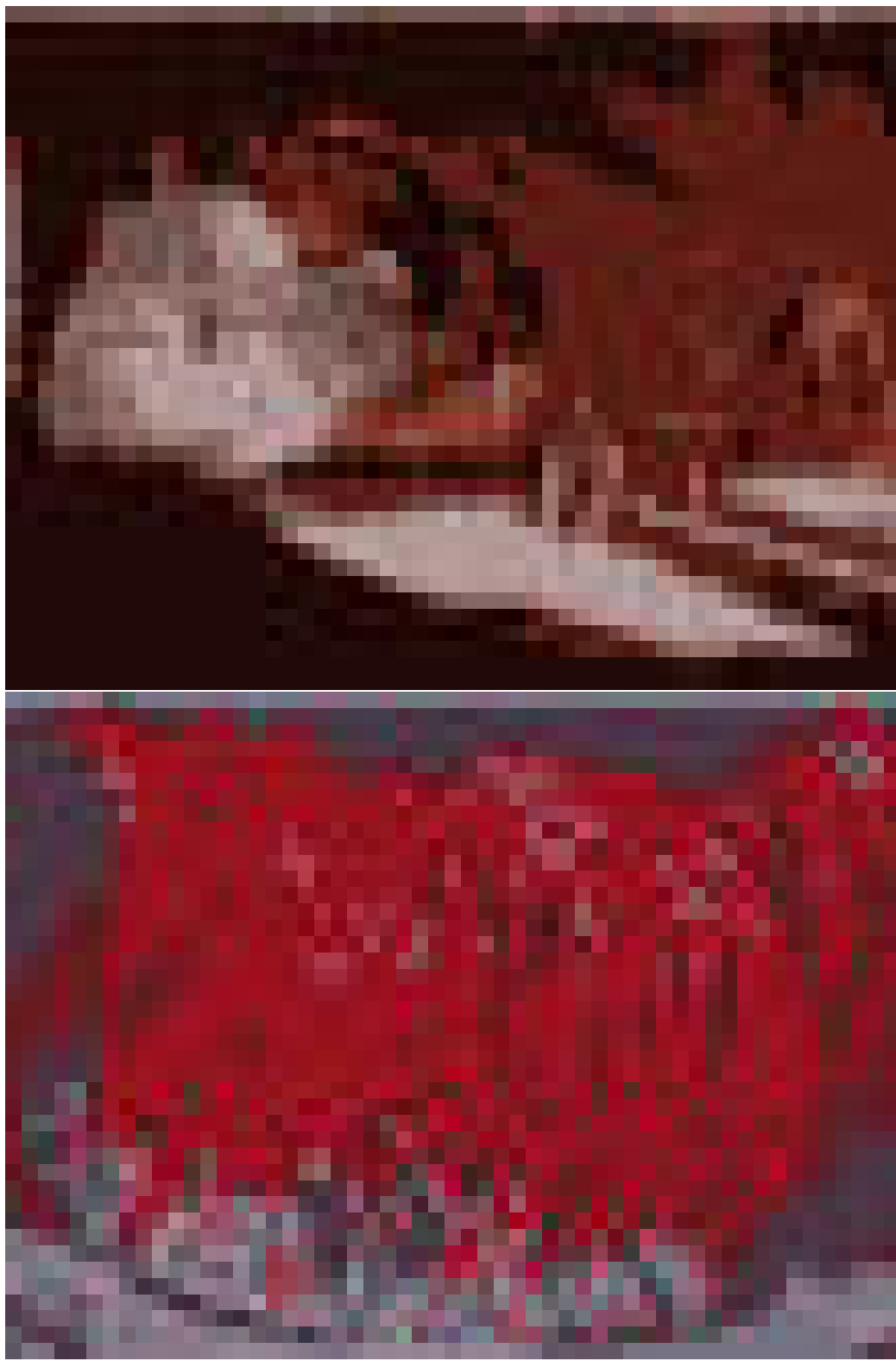


Figure 2.9: Astrophysicist Rich Kron, of the University of Chicago and Fermilab, inserts optical fibers into a pre-drilled "plug-plate," part of the Sloan Digital Sky Survey's unique spectrographic system.



Figure 2.10: The fiber-fed spectrograph is being installed to the SDSS telescope.

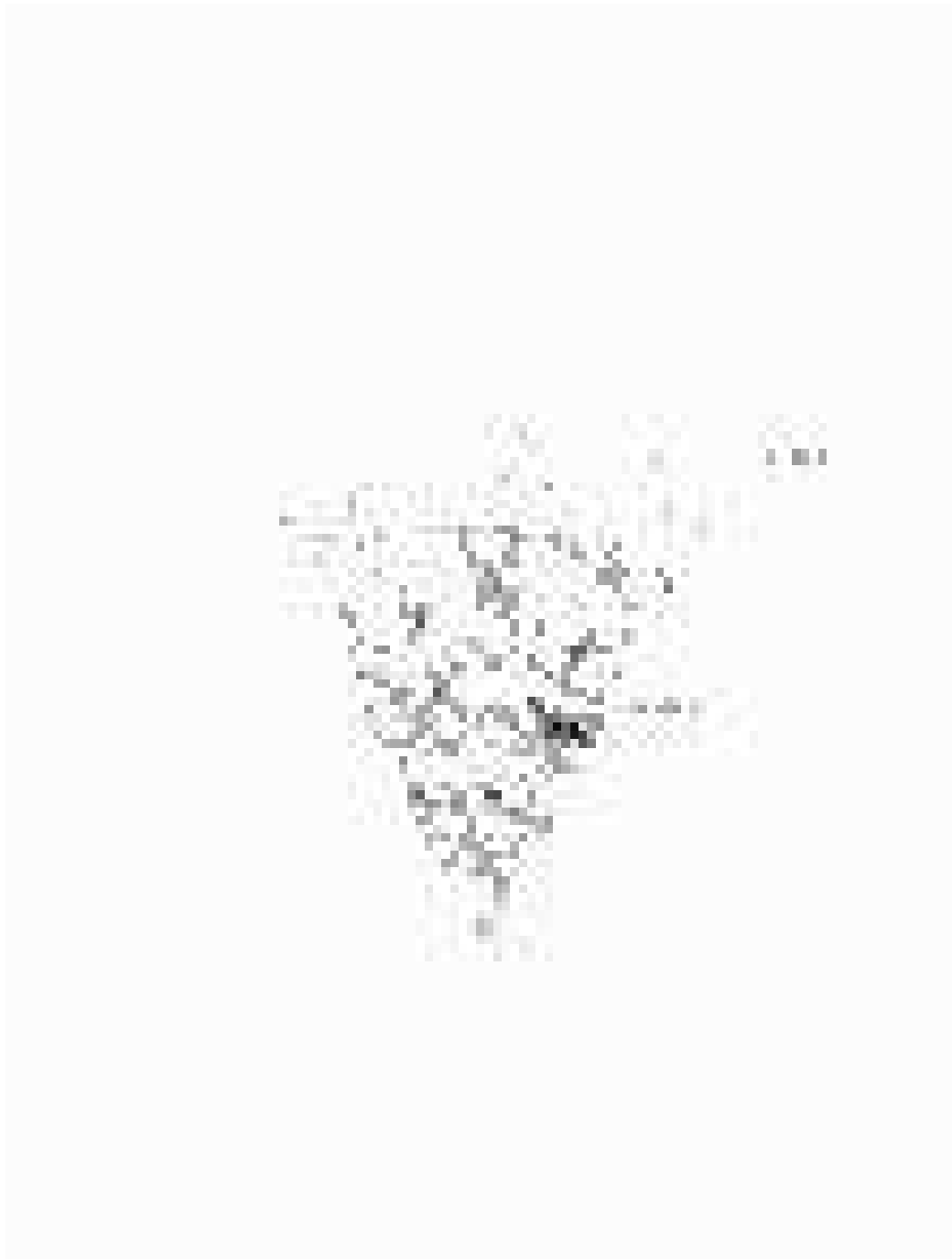


Figure 2.11: A cone diagram; redshift distribution of galaxies observed with the SDSS spectrograph. The equatorial data in the range of $145.1 < \text{R.A.} < 236.1$ are plotted.

Chapter 3

The Cut & Enhance Galaxy Cluster Catalog

3.1 Introduction

Clusters of galaxies are the most massive virialized systems known and provide powerful tools in the study of cosmology and extragalactic astronomy. For example, clusters are efficient tracers of the large-scale structure in the Universe as well as a useful tool to determine the amount of dark matter on Mpc scales (Bahcall 1998; Carlberg et al. 1996; Borgani & Guzzo 2000 and Nichol 2001 and references therein). Furthermore, clusters provide a laboratory to study a large number of galaxies at the same redshift and thus assess the effects of dense environments on galaxy evolution, for example, the morphology–density relation (Dressler et al. 1980, 1984, 1997), the Butcher–Oemler effect (Butcher & Oemler 1978, 1984) and the density dependence of the luminosity function of galaxies (Garilli et al. 1999). In recent years, surveys of clusters of galaxies have been used extensively in constraining cosmological parameters such as Ω_m , the mass density parameter of the universe, and σ_8 , the amplitude of mass fluctuations at a scale of $8 h^{-1}$ Mpc (see Oukbir & Blanchard 1992; Viana & Liddle 1996, 1999; Eke et al. 1996; Bahcall, Fan & Cen 1997; Henry 1997, 2000; Reichart et al. 1999 as examples of an extensive literature on this subject). Such constraints are achieved through the comparison of the evolution of the mass function of galaxy clusters, as predicted by the Press-Schechter formalism (see Jenkins et al. 2001 for the latest analytical predictions) or simulations (e.g., Evrard et al. 2001 and Bode et al. 2001), with the observed abundance of clusters as a function of redshift. Therefore, to obtain robust constraints on Ω_m and σ_8 , we need large samples of clusters that span a large range in redshift and mass as well as possessing a well-determined selection function (see Nichol 2001).

Despite their importance, existing catalogs of clusters are limited in both their size

and quality. For example, the Abell catalog of rich clusters (Abell 1958), and its southern extension (Abell, Corwin and Olowin 1989), are still some of the most commonly used catalogs in astronomical research even though they were constructed by visual inspection of photographic plates. Another large cluster catalog by Zwicky et al. (1961-1968) was similarly constructed by visual inspection. Although the human eye can be efficient in detecting galaxy clusters, it suffers from subjectivity and incompleteness. For cosmological studies, the major disadvantage of visually constructed catalogs is the difficulty to quantify selection bias and thus, the selection function. Furthermore, the response of photographic plates is not uniform. Plate-to-plate sensitivity variations can disturb the uniformity of the catalog. To overcome these problems, several cluster catalogs have been constructed using automated detection methods on CCD imaging data. They have been, however, restricted to small areas due to the lack of large-format CCDs. For example, the PDCS catalog (Postman et al. 1996) only covers 5.1 deg^2 with 79 galaxy clusters. The need for a uniform, large cluster catalog is strong. The Sloan Digital Sky Survey (SDSS; York et al. 2000) is the largest CCD imaging survey currently underway scanning $10,000 \text{ deg}^2$ centered approximately on the North Galactic Pole, and thus, offers the opportunity to produce the largest and most uniform galaxy cluster catalog in existence.

The quantity and quality of the SDSS data demands the use of sophisticated cluster finding algorithms to help maximize the number of true cluster detections while suppressing the number of false positives. The history of the automated cluster finding methods goes back to Shectman's count-in-cell method (1985). He counted the number of galaxies in cells on the sky to estimate the galaxy density. Although this provided important progress over the visual inspection, the results depend on the size and position of the cell. Currently the commonly used automated cluster finding method is the Matched Filter technique (MF; Postman et al. 1996; Kawasaki et al. 1998; Kepner et al. 1999; Schuecker & Bohringer 1998; Bramel et al. 2000; Lobo et al. 2000; da Costa et al. 2000 and Willick et al. 2000). The method assumes a filter for the radial profile of galaxy clusters and for the luminosity function of their members. It then selects clusters from imaging data by maximizing the likelihood of matching the data to the cluster model. Although the method has been successful, galaxy clusters that do not fit the model assumption (density profile and LF) may be missed. We present here a new cluster finding method called the *Cut-and-Enhance* (CE) method. This new algorithm is semi-parametric and is designed to be as simple as possible using the minimum number of assumptions on cluster properties. In this way, it can be sensitive to all types of galaxy overdensities even to those that may have recently undergone a merger and therefore, are highly non-spherical. One major difference between the CE and previous cluster finders is that the CE makes full use of colors of galaxies, which become available as a result of the advent of the accurate CCD photometry of the SDSS data. We apply this detection method on 350 deg^2 of the

SDSS commissioning data and construct the large cluster catalog. The catalog ranges from rich clusters to more numerous poor clusters of galaxies over this area. We also determine the selection function of the CE method.

In Section 3.2, we describe the SDSS commissioning data. In Section 3.3, we describe the detection strategy of the CE method. In Section 3.4, we present the performance test of the CE method and selection function using Monte Carlo simulations. In Section 3.5, we visually check the success rate of the CE method. In Section 3.6, we compare the CE method with the other detection methods applied to the SDSS data. In Section 3.7, we summarize the results.

3.2 The SDSS Commissioning Data

The data we use to construct the SDSS Cut & Enhance galaxy cluster catalog are equatorial scan data taken in September 1998 and March 1999 during the early part of the SDSS commissioning phase. A contiguous area of 250 deg^2 ($145.1 < \text{RA} < 236.0$, $-1.25 < \text{DEC} < +1.25$) and 150 deg^2 ($350.5 < \text{RA} < 56.51$, $-1.25 < \text{DEC} < +1.25$) were obtained during four nights, where seeing varied from $1.1''$ to $2.5''$. Since we intend to use the CE method at the faint end of imaging data, we include galaxies to $r^* = 21.5$ (Petrosian magnitude), which is the star/galaxy separation limit (Scranton et al. 2002). The details about SDSS commissioning data are described in Stoughton et al. (2002).

3.3 The Cut & Enhance Cluster Detection Method

3.3.1 Color Cut

The aim of the CE method is to construct a cluster catalog that has as little bias as possible by minimizing the assumptions on cluster properties. If a method assumes a luminosity function or radial profile, for example, the resulting clusters will be biased to the detection model used. We thus exclude all such assumptions except for a generous color cut. The assumption on colors of cluster galaxies appears to be robust, as all the galaxy clusters appear to have the same general color-magnitude relation (Gladders et al. 2000). Even a claimed “dark cluster” (Hattori et al. 1997) was found to have a normal color magnitude relation. (Benitez et al. 1999; Clowe et al. 2000; Soucail et al. 2000). A tight color-magnitude relation of cluster galaxies is known as follows; among the various galaxy populations within a cluster, (i.e., spiral, elliptical, dwarf, irregular), bright red elliptical galaxies have similar color and they populate a red ridge-line in the color-magnitude diagram. Bower, Lucey, & Ellis (1992) obtained high precision U and V photometry of spheroidal galaxies in two local clusters, Virgo and Coma, observing a

very small scatter, $\delta(U - V) < 0.035$ rms, in the color-magnitude relation. Ellis et al. (1997) studied the $U - V$ color-magnitude relation at high redshift ($z \sim 0.54$) and found a scatter of < 0.1 mag rms. Similarly, Stanford et al. (1998) studied optical-infrared colors ($R - K$) of early-type (E+S0) galaxies in 19 galaxy clusters out to $z = 0.9$ and found a very small dispersion of ~ 0.1 mag rms in the optical-infrared colors.

Figure 3.1 shows a color-magnitude diagram in ($r - i$ vs. r) using SDSS data for galaxy members in the cluster A168 ($z = 0.044$). The cluster member galaxies are identified by matching the positions of galaxies in the SDSS commissioning data with the spectroscopic observation of Katgert et al. (1998). The error bars show the standard errors of $r - i$ color estimated by the SDSS reduction software (Lupton et al. 2001). The red ridge-line of the color-magnitude relation is seen at $r^* - i^* \sim 0.4$ from $r^* = 17.5$ to $r^* = 20$. The scatter is 0.08 mag from the brightest to $r^* = 18$. Figure 3.2 shows the color-magnitude diagram (in $g - r$ vs r) for all galaxies in the SDSS fields ($\sim 8.3 \times 10^{-2}$ deg 2) that contain Abell 1577. A1577 has a redshift of $z \sim 0.14$ and Abell richness class ~ 1 . Figure 3.3 and Figure 3.4 show color-magnitude diagrams for the same field in $r - i$ and $i - z$ colors, respectively. All the galaxies in the region of the imaging data are included. Even without spectroscopic information, the red ridge-line of the color-magnitude relation is clearly visible as the horizontal distribution in the figure. The scatter in the color-magnitude relation is the largest in $g - r$ since the difference of the galaxy spectral energy distribution due to the age or metallicity difference is prominent around $3500 \sim 5000\text{\AA}$. The color distribution is much wider at faint magnitudes, partly because fainter galaxies have larger color errors, and partly because of the increase in the number of both background galaxies and cluster galaxies.

In the color-magnitude relation, fainter galaxies are known to have slightly bluer color than bright galaxies (Kodama et al. 1998). However, this tilt is relatively small in the SDSS color bands. The tilt and its scatter in the case of A1577 (Figure 3.2) is summarized in Table 3.1. The tilt is small in $g - r$ and $r - i$ (~ 0.08), and even smaller in $i - z$ (0.0018). These values are much smaller than the color cuts of the CE method. The scatters are also small: 0.081, 0.040 and 0.033 in $g - r$, $r - i$ and $i - z$, well smaller than the bin size of color cuts of the CE method as described in Section 3.3.2. The small scatter of < 0.1 mag is also often reported in previous work (Bower et al. 1992; Ellis et al. 1997; Stanford et al. 1998). Since the tilt of the color-magnitude relation is smaller than the scatter in the SDSS color bands, it is sufficient for this work to treat a color cut as essentially independent of magnitude of galaxies as described below.

Colors of the ridge-line of the color-magnitude relation become redder and redder with an increasing redshift. Figure 3.5 presents the color-color diagram, $g - r$ vs $r - i$, for all galaxies brighter than $r^* = 22$ in the SDSS fields that covers A1577, as well as the color predictions of elliptical galaxies at different redshifts (triangles; Fukugita et al. 1995). The

$g - r$ color becomes monotonously redder from $z = 0$ to $z = 0.4$. Similarly $r - i$ reddens monotonously. At $z \sim 0.4$, the 4000 \AA break of an elliptical galaxy crosses the border between g and r bands, and appears as a sharp turn in the color at this redshift (Figure 3.5). By using this color change, we can reject foreground and background galaxies, and thus can select galaxies likely to be in a certain redshift range as described below. This is a significant advantage in having multi-color data since optical cluster finders have suffered chance projections of galaxies on the sky.

To select galaxies with similar colors (and thus likely to belong to the same cluster), we divide the $g - r$ vs. r color-magnitude diagram into 11 bins. These bins are shown in Figure 3.2 as the horizontal dashed lines. The bins are not tilted because the tilt is smaller than the scatter in the SDSS color bands (see above), and because we wish to minimize the assumptions used for cluster selection. Since colors of the ridge-line of the color-magnitude relation become redder and redder with an increasing redshift, we use bluer color cuts to target low redshift clusters and redder color cuts to target high redshift clusters. We use two bins as one color cut in order to produce overlap in the color cuts; the cut is shifted by one bin each time we step to a higher redshift (redder cut). Similarly, we use ten color cuts in both $r - i$ (shown in Figure 3.3 as the dashed lines) and ten color cuts in $i - z$ (shown in Figure 3.4 as the dashed lines). The width of the bins in $g - r$, $r - i$ and $i - z$ color are 0.2 mag, 0.1 mag and 0.1 mag, respectively. The width of the $r - i$ and $i - z$ bins is smaller than the $g - r$ width since the colors of elliptical galaxies have less scatter in $r - i$ and $i - z$ than in $g - r$. When detecting cluster candidates, the above color cuts in the three colors are applied independently. To prevent faint galaxies with large color errors from weakening a signal of a cluster, we exclude galaxies with color errors larger than the size of the color bin. The standard color error estimated by the SDSS reduction software at $r^* = 21.5$ (the limiting magnitude used in the CE method) is 0.20 ± 0.09 , 0.16 ± 0.06 and 0.26 ± 0.1 in $g - r$, $r - i$ and $i - z$, respectively. In $g - r$ and $r - i$, the color error is smaller than the size of the color cut box. In $i - z$, the color error at $r^* = 21.5$ is slightly larger than the size of the color cut boxes (0.2 mag). At slightly brighter magnitude of $r^* = 20.5$, however, the errors of $i - z$ is 0.11 ± 0.05 .

In Figure 3.6 and Figure 3.7, we demonstrate the effect of the color cut. Black dots are the galaxies within $2.7'$ ($1.5h^{-1}\text{Mpc}$ at $z = 0.37$) from the center of RXJ0256.5+0006 (Romer et al. 2001). No background and foreground correction are applied. Contours represent the distribution of all the galaxies of the SDSS imaging data. The corresponding color cuts to the redshift of the cluster are drawn in each figure. In each case, the color cuts capture the red-sequence of RXJ0256.5+0006 successfully and reject foreground galaxies as designed. In fact, we show in Table 3.2, the fraction of galaxies inside of the color cut for both in cluster region and outside of cluster region. As shown in Figure 3.6, Figure 3.7 and Table 3.2, indeed the fraction in the color cut increases dramatically from 13.5%

to 36.9% in $g - r$ cut and from 42.4% to 62.1% in $r - i$ cut. The efficiency of color cut increases as we see higher redshifts since the colors of cluster galaxies are further away from the color distribution of foreground galaxies. The upper left panel in Figure 3.8 shows the galaxy distribution of the SDSS commissioning data around RXJ0256.5+0006 before applying any color cut while the upper right panel shows it after applying the $g - r$ color cut at the cluster redshift. These two panels illustrate the power of color cuts in enhancing a cluster signal.

3.3.2 Color-color Cut

When more than two colors are available, it is more effective to select galaxies in color-color space. We thus added four additional color-color-cut boxes to enhance the contrast of galaxy clusters. The cuts are low- z and high- z boxes in $g - r - i$ space and in $r - i - z$ space, as shown in Figure 3.9 and Figure 3.10. These color boxes are based on the fact that cluster galaxies concentrate in specific regions in color-color space (Dressler & Gunn 1992). In Figure 3.9, we show the $g - r$ vs. $r - i$ color-color diagram of A168 for spectroscopically confirmed member galaxies (Katgert et al. 1998) brighter than $r^*=21$. The low- z $g - r - i$ color-color-cut box is shown with the dashed lines and the high- z $g - r - i$ color-color-cut box is shown by the dotted lines. The triangles present the color prediction as a function of redshift for elliptical galaxies with a redshift step of $\Delta z = 0.1$ (Fukugita et al. 1995). The relatively wide distribution of the dots in the plots represents the fact that cluster galaxies are not all elliptical galaxies, but in reality, the mixture of different type of galaxies. Similar results are shown in Figure 3.10 for the $r - i - z$ color-color diagram of A168. Member galaxies of A168 ($z = 0.044$; Struble & Rood 1999) are well included in the low- z $g - r - i$ and $r - i - z$ boxes.

Figure 3.5 is the $g - r - i$ color-color diagram of galaxies (brighter than $r^*=22$) in the SDSS fields covering A1577 ($z = 0.14$). The low- z and high- z color-color-cut boxes are also shown. The triangle points show the color prediction for elliptical galaxies. Figure 3.11 represents similar results in the $r - i - z$ color-color space for the same field. Even though both cluster members and field galaxies are included in the plot, the concentration of cluster galaxies inside the low- z boxes is clearly seen.

The boundaries of color-color cuts are chosen based on the spectroscopic observation of Dressler & Gunn (1992) and the color prediction of elliptical galaxies (Fukugita et al. 1995). We reject galaxies that have standard color errors larger than the size of the color-color boxes. The standard color error at $r^*=21.5$ (the limiting magnitude of CE method.) is 0.20 ± 0.09 , 0.16 ± 0.06 and 0.26 ± 0.1 in $g - r$, $r - i$ and $i - z$, respectively. The smallest size of the color-color boxes is the $r - i$ side of the low- z $g - r - i$ box, which is 0.34 in $r - i$. The standard color error is smaller than the color cut boxes even at

$r^*=21.5$. In Figure 3.12 the upper left panel shows the galaxy distribution of the SDSS commissioning data in 23.75 deg^2 before applying any cut. The upper right panel shows the galaxy distribution after applying the $g - r - i$ color-color cut. Abell clusters in the region are shown their position in numbers. It illustrates the color cut enhancement of nearby clusters. We used RXJ0256.5+0006 ($z = 0.36$) to numerate the fraction of galaxies inside of the color cut for both in cluster region and outside of cluster region in Table 3.2. Indeed, the fraction of galaxies in the color cut increases from 48.8% to 58.3% in $g - r - i$ cut and from 65.7% to 76.7% in $r - i - z$ cut. Since the color cuts has overlaps at $z \sim 0.4$, $g - r - i$ high- z cut also increases the fraction of galaxies. This example shows that the signal of galaxy clusters, indeed, increases by applying the color-color cuts.

We thus use 30 color cuts and four color-color cuts independently to search for cluster signals. We then merge 34 cluster candidate lists into a final cluster catalog. Because of star/galaxy separation limit of the SDSS data, we do not use galaxies fainter than $r^*=21.5$. The only main assumption made in the CE detection method is these generous color cuts.

In Figure 3.13, we plot the color prediction of galaxies with evolving model with star formation (filled pentagons) and the same model without star formation (filled square) from $z = 0$ to $z = 0.6$ (PEGASE model, Fioc, M., & Rocca-Volmerange 1997). The model galaxies with star formation are the extreme star forming galaxies. Filled triangles show the color prediction of elliptical galaxies with a redshift step of $\Delta z = 0.1$ (Fukugita et al. 1995). Black dots are the galaxies around Abell 1577, for reference. Although the evolving model steps outside of the high- z color cut box at $z \sim 0.6$, the CE is designed to detect galaxy clusters if enough red galaxies (shown as small triangles) are in the color cut by weighting the galaxies with similar color. In fact, randomly chosen 100 spectroscopic galaxies with $0.4 < z \leq 0.5$ shown in small green triangles are well within the high- z box. As seen in the real catalog in Section 3.3.6, due to the magnitude limit of SDSS, it is difficult to find many clusters beyond $z \sim 0.4$. On the other hand, if we move the color cut bluer, we increase the contamination from $z \sim 0.3$ galaxies (which are well within the magnitude limit of SDSS). By compromising these two effects, we optimize the color cut criteria.

3.3.3 Enhancement Method

After applying the color cuts, we use a special enhancement method to galaxies within the cut in order to enhance the signal to noise ratio of clusters further. Among galaxies within a certain color cut (or color-color cut), we find all pairs of galaxies within five arcmin; this scale corresponds to the size of a galaxy cluster at $z \sim 0.3$. Selecting larger separations blurs high z clusters, while smaller separations weaken the signal of low z

clusters. We empirically investigated several separations and found $5'$ to be the best. Using the angular distance and color difference of each pair of galaxies, we distribute a Gaussian cloud representing the density of galaxies on the center position of each pair. The width of the Gaussian cloud is set to be an angular separation of the pair. The volume of a Gaussian cloud is given by its weight (W), which is calculated as follows:

$$W = \frac{1}{\Delta r + 1''} \times \frac{1}{\Delta(g - r)^2 + 2.5 \times 10^{-3}}, \quad (3.1)$$

where Δr is an angular separation between the two galaxies and $\Delta(g - r)$ is their color difference. Small softening parameters are empirically determined and added in the denominator of each term to avoid the weight becoming infinite. This enhancement method provides stronger weights to pairs which are closer both in angular space and in color space, thus are more likely to appear in real galaxy clusters. Gaussian clouds are distributed to each $30'' \times 30''$ cell on the sky. The $30''$ cells are much smaller than sizes of galaxy clusters (several arcmins even at $z \sim 0.5$).

An enhanced density map is obtained by summing up the Gaussian clouds for every pair of galaxies within $5'$. The lower panels in Figure 3.8 and 3.12 present such enhanced density maps of the region in their upper panels. RXJ0256.5+0006 is successfully enhanced in Figure 3.8. Figure 3.12 illustrates how the CE method finds galaxy clusters in a larger region. The advantage of this enhancement method in addition to the color cuts is that it makes full use of color similarity of cluster galaxies. The color cuts are used to reduce foreground and background galaxies and to enhance the signal of clusters. Since the color-magnitude relation of cluster galaxies is frequently tighter than the width of our color cuts, the use of the second term in equation (3.1) - the inverse square of the color difference - further enhances the signal of cluster, in spite of the larger width of the color cuts. Another notable feature is that the enhancement method is adaptive, that is, large separation pairs have a large Gaussian and small separation pairs have a sharp, small Gaussian. In this way, the enhancement method naturally fit to any region with any number density of galaxies in the sky. Therefore, it is also easy to apply it to data from another telescope with different depth and different galaxy density. Another benefit of the enhancement method is that it includes a smoothing scheme. And thus, conventional detection methods commonly used in astronomical community can be used to detect clusters in the enhanced density map. The enhancement method uses an angular separation in the computation of W -values. This might bias our catalog against nearby clusters ($z < 0.1$), which have a large angular extent (and thus are given less W). However, these nearby clusters are few in the SDSS commissioning data due to the small amount of the volume probed in the nearby universe. In addition, these nearby clusters will also be well sampled in the SDSS spectroscopic survey with fiber redshifts, and will thus be detected in the SDSS 3D cluster selection. (the CE cluster detection method is intended

to detect clusters using imaging data). These nearby clusters do not have a significant effect on angular or redshift-space correlations because the number of such clusters is a small fraction of any large volume-limited sample.

3.3.4 Detection

We use SourceExtractor (Bertin et al. 1996) to detect clusters from the enhanced density map discussed in Section 3.3.3. SourceExtractor identifies high density peaks above a given threshold measuring the background and its fluctuation locally. The threshold selection determines the number of clusters obtained. A high threshold selects only rich clusters. We tried several thresholds, examining the colored image, color-magnitude and color-color diagrams of the resulting cluster catalog. The effect of changing threshold is summarized in Table 3.3. The numbers of clusters detected are not very sensitive to the threshold¹. Based on the above, we have selected the threshold to be six times the background fluctuation, it is the threshold which yields a large number of clusters while the spurious detection rate is still low.

Monte Carlo simulations are sometimes used to decide the optimal threshold, where most true clusters are recovered while the spurious detection rate is still low. However, the simulations reflect an ideal situation, and they are inevitably different from true data; for example, a uniform background cannot represent the true galaxy distribution with its large scale structure. There are always clusters which do not match the radial profile or luminosity function assumed in Monte Carlo simulations and this may affect the optimization of the threshold. The optimal threshold in Monte Carlo simulation differs from the optimal threshold in the real data. Therefore, we select the threshold empirically using the actual data and later derive the selection function using Monte Carlo simulation.

At high redshifts ($z > 0.4$), the number of galaxies within the color cuts is small; therefore the rms of the enhanced density map is generally too low and the clusters detected at high redshift have unusually high signal. To avoid such spurious detections, we applied another threshold at maximum absolute flux of 1000 in the enhanced density map². Spurious detections with high signal would generally have low values of this parameter because they are not true density peaks. The threshold of maximum absolute flux of 1000 can thus reject spurious detections. The value is determined by investigating the image, color-magnitude and color-color diagrams of the detected clusters and iterating

¹The numbers of detection can increase or decrease with increasing sigma because the following two effects cancel out each other. (1) Lower threshold detects faint sources and thus increases the number of detections. (2) Higher threshold deblends the peaks and increases the number of the detections.

²FLUX_MAX+BACKGROUND=1000, where FLUX_MAX and BACKGROUND are the parameters of Source Extractor. FLUX_MAX+BACKGROUND is the highest value in the pixels within the cluster. It is an absolute value, and not affected by rms value.

the detection with different values of the maximum absolute flux threshold. The effect of changing the absolute flux threshold is summarized in Table 3.4.

To secure the detection further, at all redshifts, we demand at least two detections in the 34 cuts. Since the cluster galaxies have similar colors in all $g - r$, $r - i$ and $i - z$ colors; real clusters should thus be detected in at least two color cuts. This requirement significantly reduces spurious detections.

3.3.5 Merging

We apply the procedure of cut (Section 3.3.1, 3.3.2), enhance (Section 3.3.3) and detection (Section 3.3.4) to all of the 34 color cuts (30 color cuts + four color-color cuts) independently. After creating the 34 cluster lists, we merge them into one cluster catalog. We regard the detections within 1.2 arcmins as one cluster. To avoid two clusters with different redshifts being merged into one cluster due to the chance alignment, we do not merge clusters unless the successive two color cuts in a certain color both detect it.

An alternative way to merge clusters would be to merge only those clusters which are detected in the consistent color cut in all $g - r$, $r - i$ and $i - z$ colors, using the model of the elliptical galaxy colors. However, the catalog will be biased against clusters which have different colors than the model ellipticals. In order to minimize the assumptions on cluster properties we treat the three color space, $g - r$, $r - i$ and $i - z$, independently.

3.3.6 Redshift and Richness Estimation

One of the very important parameters for various scientific researches using a cluster catalog is redshift and richness. We estimate redshift and richness of each cluster as follows. Instead of the richness estimator introduced by Abell (1958), we count the number of galaxies inside the detected cluster radius which lie in the two magnitude range (in r) from m_3 (the third brightest galaxy) to m_3+2 (CE richness). The difference from Abell's richness is that he used a fixed $1.5 h^{-1}\text{Mpc}$ as a radius. Here we use the detection radius of the cluster detection algorithm which can be larger or smaller than Abell radius, typically slightly smaller than $1.5 h^{-1}\text{Mpc}$. Since there are a significant variety in a size of real clusters, a varying radius can measure more representative cluster richness than a fixed radius. The background galaxy count is subtracted using the average galaxy counts in the SDSS commissioning data.

For the redshift estimates, we use the strategy of the redshift estimation of the maxBCG technique (Annis et al. in prep.). We count the number of galaxies within the detected radius that are brighter than $M_{r^*}^* = -20.25$ at each redshift and are within a color range of ± 0.1 mag in $g - r$ around the color prediction for elliptical galaxies (Fukugita et al. 1995). This procedure is iterated for each redshift step of $\Delta z = 0.01$. After subtract-

ing average background number counts from each bin, the redshift of the bin that has the largest number of galaxies is taken as an estimated cluster redshift. The estimated redshifts are calibrated using the spectroscopic redshifts from the SDSS spectroscopic survey. Our redshift estimation depends on the model of Fukugita et al. (1995), but the difference from other models are not so significant, as seen in the difference between filled squares (PEGASE model) and filled triangles (Fukugita et al. 1995) of Figure 3.13. If a cluster has enough elliptical galaxies, the redshift of the cluster is expected to be well measured. If a cluster is, however, dominated only by spiral galaxies, the redshift of the cluster might be underestimated, as can be judged in the difference between the pentagons and the triangles in Figure 3.13. Figure 3.14 shows redshift accuracy of the method. The estimated redshifts are plotted against observed redshifts from the spectroscopic observation. The redshift of the SDSS spectroscopic galaxy within the detected radius and with the nearest spectroscopic redshift to the estimated redshift is adopted as a real redshift. In the fall equatorial region, 699 clusters have spectroscopic redshifts. The correlation between true and estimated redshifts is excellent: the rms scatter is $\delta z = \pm 0.0147$ for $z < 0.3$ clusters, and $\delta z = \pm 0.0209$ for $z > 0.3$ clusters. The triangles in Figure 3.14 show 15 Abell clusters whose spectroscopic redshift is available in the literature. There are three outliers at low spectroscopic redshifts. CE counterparts for these three clusters all have very small radii of several arcmin. Since these Abell clusters are at $z < 0.1$, the discrepancy is probably not in the redshift estimation but rather in the too small detection radius.

By applying this CE method including redshift and richness estimation to the SDSS commissioning data, we construct the SDSS CE galaxy cluster catalog. The SDSS CE cluster catalog contains 4638 galaxy clusters. The catalog is available at the following website: <http://astrophysics.phys.cmu.edu/~tomo>³

3.4 Monte Carlo Simulation

For statistical study using a cluster catalog, it is of extreme importance to know completeness and contamination rate of the catalog. In this section, we examine the performance of the CE method and determine the selection function using extensive Monte Carlo simulations. We also perform false positive tests.

3.4.1 Method

We perform Monte Carlo simulations both with a real background using the SDSS commissioning data and with a shuffled background. For the real background, we randomly

³Mirror sites are available at http://sdss2.icrr.u-tokyo.ac.jp/~yohnis/kokki/public_html/ce/index.html, and <http://indus.astron.s.u-tokyo.ac.jp/~yoh/ce/index.html>

choose an 1 deg^2 region of the SDSS data with seeing better than $1.7''$.⁴ For the shuffled background, we re-distribute all the galaxies in the above 1 deg^2 of SDSS data randomly in position, but keep their colors and magnitudes unchanged.

Then, we place artificial galaxy clusters on these backgrounds. We distribute cluster galaxies randomly using a King profile (King 1966; Ichikawa 1986) for the radial galaxy density, with concentration index of 1.5 and cut off radius of $2.1 h^{-1} \text{Mpc}$, which is the size of Abell 1577 (Struble & Rood 1987). For colors of the artificial cluster galaxies, we use the color and magnitude distribution of Abell 1577 (at $z \sim 0.14$, Richness ~ 1) as a model. We choose the SDSS fields which cover the entire Abell 1577 area and count the number of galaxies in each color bin. The size of the bins is 0.2 magnitude in both colors and magnitude. The color and magnitude distribution spans in four dimension space, r , $g - r$, $r - i$ and $i - z$. We count the number of field galaxies using a field of the same size near (but different from) the Abell 1577 field and subtracted the distribution of field galaxies from the distribution of galaxies in the Abell 1577 fields. The resulting color distribution is used as a model for the artificial galaxy clusters. Artificial galaxy colors are assigned randomly so that they reproduce the overall color distribution of Abell 1577. The distribution is linearly interpolated when allocating colors and magnitudes to the galaxies.

For the high redshift artificial clusters, we apply k -correction and the color prediction of elliptical galaxies from Fukugita et al. (1995). For the color prediction, only the color difference, not the absolute value, is used due to the uncertainty in zero points. Galaxies which become fainter than $r^* = 21.5$ by applying cosmological dimming and a k -correction are not used in the simulations.

3.4.2 Monte Carlo Results

First, we run a Monte Carlo simulation with only the background, without any artificial clusters, in order to measure the detection rate of the simulation itself. The bias detection rate is defined as the percentage in which any detection is found within 1.2 arcmins from the position where we later place an artificial galaxy cluster. The main reason for the false detection is that a real cluster sometimes comes into the detection position, where an artificial cluster is later placed. This is not the false detection of the CE method but rather the noise in the simulation itself. The bias detection rate with the real SDSS background is 4.3%. This is small relative to the actual cluster detection rate discussed below. The bias detection rate using the shuffled background is lower (2.4%), as expected.

⁴ Although the SDSS survey criteria for seeing is better than $1.5''$, some parts of the SDSS commissioning data have seeing worse than $2.0''$. It is expected that the seeing is better than $1.5''$ for all the data after the survey begins.

We are now ready to perform simulations with an artificial cluster. We run Monte Carlo simulations with a set of artificial clusters with redshifts ranging from $z = 0.2$ to $z = 0.6$, and with richnesses of $N_{gal} = 40, 60, 80$ and 100 , at each redshift (N_{gal} is the number of galaxies inputted into an artificial cluster). If a galaxy becomes fainter than $r^* = 21.5$, it is not counted in the CE detection method even if it is included in N_{gal}). For each set of parameters, a simulation is iterated 1000 times. In Figure 3.15, we compare N_{gal} with cluster richness where richness is defined as the number of galaxies within the two magnitude range fainter than the third brightest galaxy, located within the cluster radius that the CE method returns (Section 3.3). The error bars are 1σ standard error. $N_{gal}=50$ corresponds to Abell richness class ~ 1 .

Figure 3.16 shows the recovery rate in the Monte Carlo simulations on the real background. The recovery rate is shown in percentage as a function of redshift. Each line represents input clusters of different richness, $N_{gal}=100, 80, 60$ and 40 (top to bottom). Since the false detection rate in the simulation with real background is 4.3%, all the lines converges to 4.3% at high redshift. The detection rate drops suddenly at $z = 0.4$ because at this point, a large fraction of the cluster member galaxies are lost as a result of the magnitude limit at $r^* = 21.5$. Roughly speaking, this apparent magnitude limit determines the depth of the SDSS cluster catalog. $N_{gal}=80$ clusters are recovered $\sim 80\%$ of the time to $z < 0.3$, dropping to $\sim 40\%$ beyond $z \sim 0.4$. Clusters of the lowest richnesses, $N_{gal}=40$ clusters are more difficult to detect, as expected. The recovery rates of $N_{gal}=40$ clusters are less than 40% even at $z = 0.3$. Strangely, the recovery rate for $N_{gal}=100$ at $z = 0.2$ is not 100%. However, if we widen the detection radius from $1'.2$ to $5'.4$, the recovery rate reassuringly increases to 100%. Since the radius of $5'.4$ is fairly smaller than the size of A1577 (11' at $z = 0.2$; Struble & Rood 1987), the reason may be that a real cluster (in the real background) happens to be located close to an artificial cluster. In such a case, the detected position may be shifted away by more than the detection radius ($1'.2$) from the cluster center, resulting in the recovery rate of less than 100% within $1'.2$.

Figure 3.17 shows the positional accuracy of the detected clusters in the Monte Carlo simulation with the real SDSS background, as a function redshift and richness. The 1σ positional errors of the detected clusters is shown. Note that since the CE does not detect many clusters beyond $z = 0.4$ in the SDSS data, there is not much importance in discussing the position accuracy of beyond $z = 0.4$ with this data. The positional accuracy is better than 1' until $z = 0.4$ in all the richness ranges used. The accuracy is nearly independent of the redshift because the high redshift clusters are more compact than the low redshift ones. This partially cancels the effect of losing more galaxies at high redshift due to the flux limit of the sample. The positional accuracy roughly corresponds to the mesh size of the enhancement method, 30''. As expected, the positional accuracy is worse for high redshift poor clusters ($z = 0.4$ and $N_{gal} \leq 60$). The statistics for these objects are also

worse; the detection rate of $N_{gal}=60$ and 40 clusters are less than 20% at $z=0.4$ (Figure 3.16).

Figure 3.18 presents the recovery rate of artificial clusters in Monte Carlo simulations with the shuffled background. The recovery rates are slightly better than those with the real background since no real clusters are in the shuffled background. Again, the recovery rates drop sharply at $z=0.4$. The $N_{gal}=100$ clusters are recovered with $\sim 90\%$ probability to $z \sim 0.3$ and $\sim 40\%$ at $z \sim 0.4$. At $z \leq 0.3$, $N_{gal} > 40$ clusters are recovered at $> 40\%$. Figure 3.19 shows the positional accuracy of the detected clusters in the simulations (with shuffled background). The results are similar to those with the real background. The positional accuracy is better than $40''$ until $z=0.3$ for all the richnesses.

3.4.3 False Positive Tests

In order to test false positive rate, we prepared four sets of data: 1) Real SDSS data of 25 deg^2 . 2) Position of galaxies in the same 25 deg^2 are randomized (galaxy colors untouched.) 3) Colors of galaxies are shuffled. (galaxy position untouched.) 4) Color is shuffled and position is smeared ($5'$). Galaxy colors are randomized and positions are randomly distributed in the way that galaxies still lie within $5'$ from their original positions. This case is intended to include large scale structure without galaxy clusters. The results are shown in Figure 3.20. The solid line represents the results with the real data. The dotted line represents the results with the position shuffled data. The long-dashed line is for the color shuffled data. For color shuffled data, we subtracted the detections in the real data, because they still contain real clusters in them. It is consistent with the generous color cuts of the CE method that many clusters can still be detected in the color shuffled data. The short-dashed line is for the color shuffled smeared data. In Figure 3.21, the fraction to the real data is plotted against CE richness. The promising fact is that not so many sources are detected from the position shuffled data. The fraction to the real data is less than 20% at CE richness > 20 . More cluster candidates are detected from the color shuffled data and the smeared data but this does not mean the false positive rate of the CE is as high as those values since smeared data still contains a structure larger than $5'$, and they can be real clusters. To conclude, our simulations show that for clusters with richness > 10 , over 70% of CE clusters are likely to be real systems (as shown by the color & position shuffled simulations.)

3.5 Visual Inspection

To investigate whether the detected clusters are true clusters or spurious detection, spectroscopic observations are necessary. Although large spectrometers which can observe

the spectra of many galaxies at one time are becoming available (e.g., SDSS; 2dF), spectroscopy of large number of galaxies is still time consuming. Since the SDSS CE cluster catalog will have more than 100,000 galaxy clusters when the survey is complete, it is in fact impossible to spectroscopically confirm all the clusters in the catalog. As a preliminary check of our method, we visually inspect all the CE clusters within a given area (right ascension between 16 deg and 25.5 deg and declination between -1.25 deg and $+1.25$ deg, totaling 23.75 deg 2 . The region in Figure 3.12). A total of 278 CE galaxy clusters are located within this area (after removing clusters touching the region's borders). Out of the 278 CE galaxy clusters, we estimate that 10 are false detections. Since the strategy of the CE method is to detect every clustering of galaxies, we call every angular clustering of galaxies with the same color a successful detection here. (As we show in Section 3.4.3, 30% of clusters could be false detections, such as chance projections.)

Among the 10 false detections, three are bright big galaxies deblended into several pieces. In the other cases, a few galaxies are seen but not an apparent cluster or group. (In one case a rich cluster exists about six arcmin from the false detection). The 10 false detections are summarized in Table 3.5. σ (column[1]) is the significance of the detection; CE richness (column[2]) is its richness; z (column[3]) is the color estimated redshift; and comments are given in column[4].

As the successful examples, we show two typical examples of clusters detected only with the CE method but not with the other methods (discussed below). One is a clustering of blue galaxies. Since the CE method does not reject blue spiral galaxies, it can detect clustering of several blue spiral galaxies. Indeed, some of the detected clusters that we visually inspected are clustering of blue galaxies. The other is a clustering of numerous faint elliptical galaxies; in these regions faint elliptical galaxies spread out over a large area (~ 0.01 deg 2) but with no bright cluster galaxies. CE method detects these regions successfully with a large radius. Figure 3.22 shows the true color image of one of these clusters with numerous faint elliptical galaxies. Figure 3.23 shows a typical galaxy cluster successfully detected with the CE method.

3.6 Comparison with Other Methods

At the time of writing, the SDSS collaboration has implemented several independent cluster finding methods and have run these algorithms on the SDSS commissioning data. These methods include the Matched Filter (MF; Kim et al. 2001), the Voronoi Tessellation (VTT; Kim et al. 2001), and the maxBCG technique (Annis et al. in prep.). Therefore, we have the unique opportunity to compare the different catalogs these algorithms produce to further understand each algorithm and possible differences between them. (also see Bahcall et al. 2003 for comparisons of SDSS cluster catalogs.)

Here we provide a comparison between the CE method and the MF, VTT and maxBCG techniques using a small sub-region of the SDSS data, i.e., 23.75 deg^2 of commissioning data with RA between 16 and 25.5 degrees and Declination between -1.25 and $+1.25$ degrees (the region in Figure 3.12). We first matched the CE catalog with each of the other three catalogs using a simple positional match criterion of less than six arcmins. The number of matches between the CE and other catalogs varies significantly because each cluster-finding algorithm has a different selection function. At present, the selection functions for all these algorithms are not fully established so we have not corrected for them in this comparison. Although each algorithm measures cluster richness and redshift in its own way, the scatter between the measurement is large and it makes the comparison difficult. Therefore, we re-measured richness and redshift of the MF, VTT and maxBCG clusters using the CE method to see the richness and redshift dependence of the comparison.

In Table 3.6, we list the number of clusters each method finds in our test region (Column 2 called “N detection”). We also list in column 3 the number of clusters found in common between the CE method and each of other methods discussed above. Columns 4 and 5 of Table 3.6 give the detection rates of other methods with respect to the CE method and those of the CE method with respect to other methods, respectively. For comparison, in Table 3.7, we also compare the number and percentage of matches found between the VTT, MF and maxBCG technique. These two tables illustrate that the overlap between all four algorithms is between 20 to 60% which is simply a product of their different selection functions. Furthermore, we note we have used a simplistic matching criteria which does not account for the cluster redshift or the errors on the cluster centroids. Future SDSS papers will deal with these improvements (Bahcall et al. 2003). Tables 3.6 & 3.7 show that the CE and the maxBCG methods detect overall more clusters than the other methods, i.e., 363 and 438 clusters respectively, compared with 152 and 130 clusters for the MF and the VTT respectively. This difference in the number of clusters found is mainly due to differences in the thresholds used for each of these algorithms. As illustrated in Figure 3.24, a majority of the extra clusters in the maxBCG and CE catalogs are low richness systems. As seen in Figure 3.25, these low richness systems appear to be distributed evenly over the entire redshift range of the CE catalog, i.e., out to $z \simeq 0.4$.

3.6.1 Comparison of the Matched Filter and the CE Methods

We focus here on the comparison between the CE and the MF (see Kim et al. 2001). In Figure 3.26, we show the fraction of the MF clusters found in the CE catalog. We also split the sample as a function of CE richness. In Figure 3.27, we show the reverse relationship,

i.e., the fraction of the CE clusters found by the MF as a function of estimated redshift and CE richness. These figures show that there is almost complete overlap between the two catalogs for the highest richnesses systems at the highest redshift bin (there are, however, only 5 systems with $z > 0.3$ in the MF catalog). At low redshifts ($z < 0.3$), the overlap decreases, e.g., only 60% of the MF clusters are found in the CE catalog. To understand this comparison further, we visually inspected all the clusters found by the CE method that were missing in the MF catalog. As expected, most of these systems were compact (~ 1 arcmin) groups of galaxies.

Finally, in Figure 3.28, we plot the distribution of elongations (major to minor axis ratio) for both the whole CE clusters as well as just the CE clusters in the MF catalog. This plot shows that a majority of clusters in both samples have nearly spherical morphologies with the two distributions in good agreement up to the elongation of 3 (axes ratio of 3 to 1). However, there is a tail of 11 CE clusters which extends to higher elongations that are not seen in the CE plus the MF sub-sample. However, this is only $\sim 3\%$ of the CE clusters.

3.6.2 Comparison of the maxBCG and the CE Methods

In Figure 3.29, we show the fraction of the maxBCG clusters which are found in the CE catalog, while in Figure 3.30, we show the reverse relationship, i.e., the fraction of the CE clusters found in the maxBCG catalog. In both figures, we divide the sample by estimated redshift and observed CE richness. First, we note that the matching rate of the maxBCG clusters to the CE is $\sim 70\%$ or better for clusters with a richness of > 20 at all redshifts. For the low richness systems, the matching rate decreases at all redshifts. To further understand the comparison between these two samples of clusters, we first visually inspected all clusters detected by the CE method but were missing from the maxBCG sample and found them to be blue, nearby poor clusters. This is a reflection of the wider color cuts employed by the CE method which allows the CE algorithm to include bluer, star-forming galaxies into its color criterion. The maxBCG, however, is tuned specifically to detect the E/S0 ridge-line of elliptical galaxies in clusters. We also visually inspected all maxBCG clusters that were not found by the CE method and found these systems to be mostly faint high redshift clusters whose members mostly have fallen below the magnitude limit used for the CE method ($r^*=21.5$).

3.6.3 Comparison of the VTT and the CE Methods

In Figure 3.31, we show the fraction of the VTT clusters which were found by the CE as a function of estimated redshift and CE richness. Figure 3.32 shows the fraction of the CE clusters found in the VTT catalog as a function of estimated redshift and CE richness.

Because the CE method detects twice as many clusters as does the VTT, the matching rate is higher in Figure 3.31 than in Figure 3.32, showing that the CE catalog contains a high fraction of the VTT clusters. In Figure 3.32, the matching rate of low richness clusters improves at higher redshift because the poor clusters, which the VTT does not detect become fainter and therefore both methods can not detect these clusters at high redshift.

3.7 Summary

We have developed a new cluster finding method, the CE method. It uses 30 color cuts in the color-magnitude diagrams and four color-color cuts in the color-color diagrams to enhance the contrast of galaxy clusters over the background galaxies. After applying the color and color-color cuts, the method uses the color and angular separation weight of galaxy pairs as an enhancement method to increase the signal to noise ratio of galaxy clusters. We use the Source Extractor to detect galaxy clusters from the enhanced density maps. The enhancement and detection are performed for every color cut and every color-color cut, producing 34 cluster lists, which are then merged into a single cluster catalog.

Using the Monte Carlo simulations with a real SDSS background as well as a shuffled background, the CE method is shown to have the ability to detect rich clusters ($N_{gal}=100$) to $z \sim 0.3$ with $\sim 80\%$ completeness. The completeness drops sharply at $z=0.4$ due to the flux limit of the SDSS imaging data. The positional accuracy is better than $40''$ for clusters of all richnesses examined at $z \leq 0.3$. The false positive test shows that over 70% of clusters are likely to be real systems for CE richness > 10 . We apply the CE method to the SDSS commissioning data and produce the SDSS CE cluster catalog containing 4638 galaxy clusters in ~ 350 deg 2 . We compare the CE clusters with other cluster detection methods: the MF, the maxBCG and the VTT. The SDSS CE cluster catalog developed in this work is a useful tool to study both cosmology and property of clusters and cluster galaxies.



Figure 3.1: $r - i$ color-magnitude diagram of A168. $r - i$ color is plotted against r magnitude for confirmed member galaxies of A168. Colors and magnitude are taken from the SDSS commissioning data by matching up the positions with the spectroscopic observation of Katgert et al. (1998). The standard errors of colors estimated by the reduction software are shown as error bars. $r - i$ color cut bins are superimposed on the color-magnitude relation of Abell 168. The horizontal dotted lines are the borders of the color cuts.

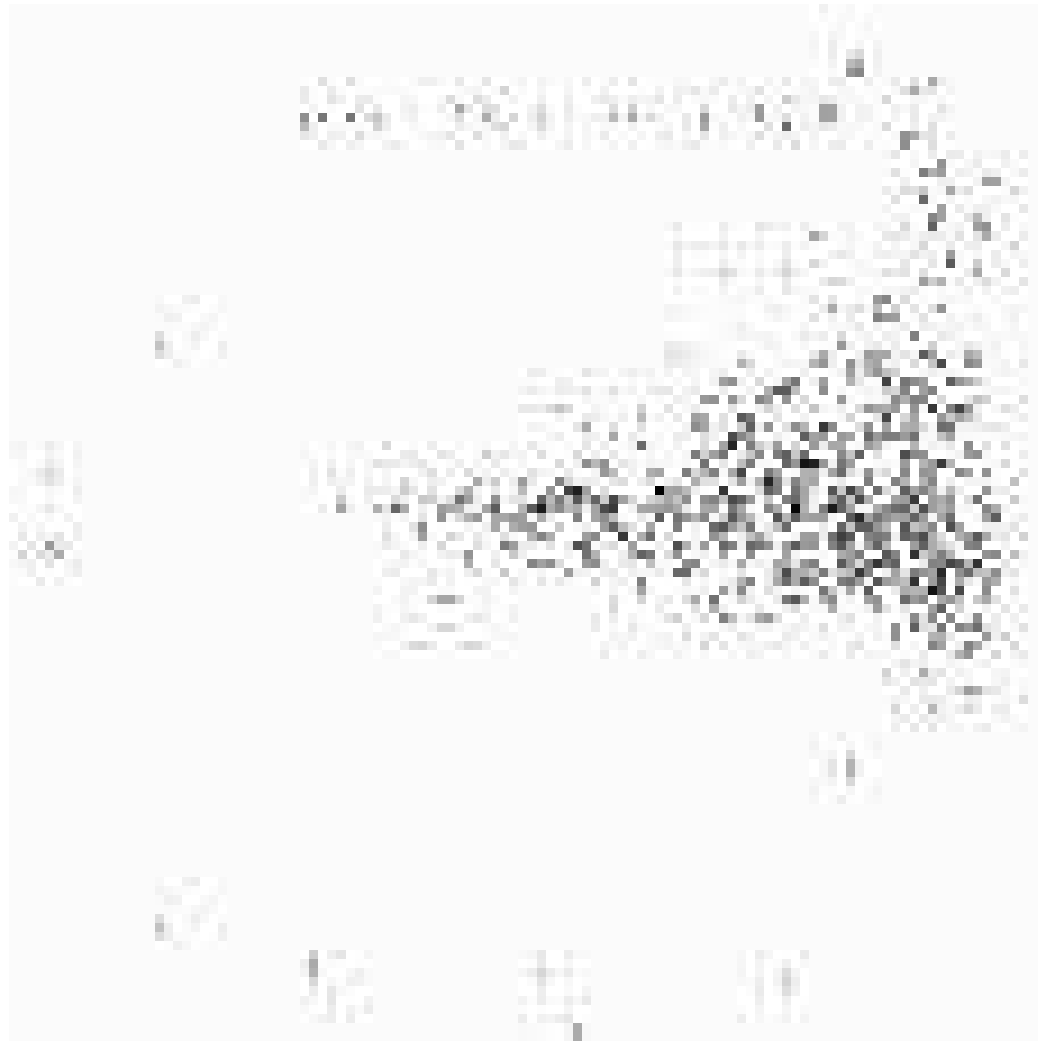


Figure 3.2: $g - r$ color-magnitude diagram. $g - r$ color cut bins are superimposed on the color-magnitude relation of Abell 1577. The abscissa is the r apparent magnitude. The ordinate is $g - r$ color. Galaxies in the SDSS fields covering A1577 ($\sim 8.3 \times 10^{-2} \text{ deg}^2$) are plotted with the dots. The horizontal dashed lines are the borders of the color cuts.

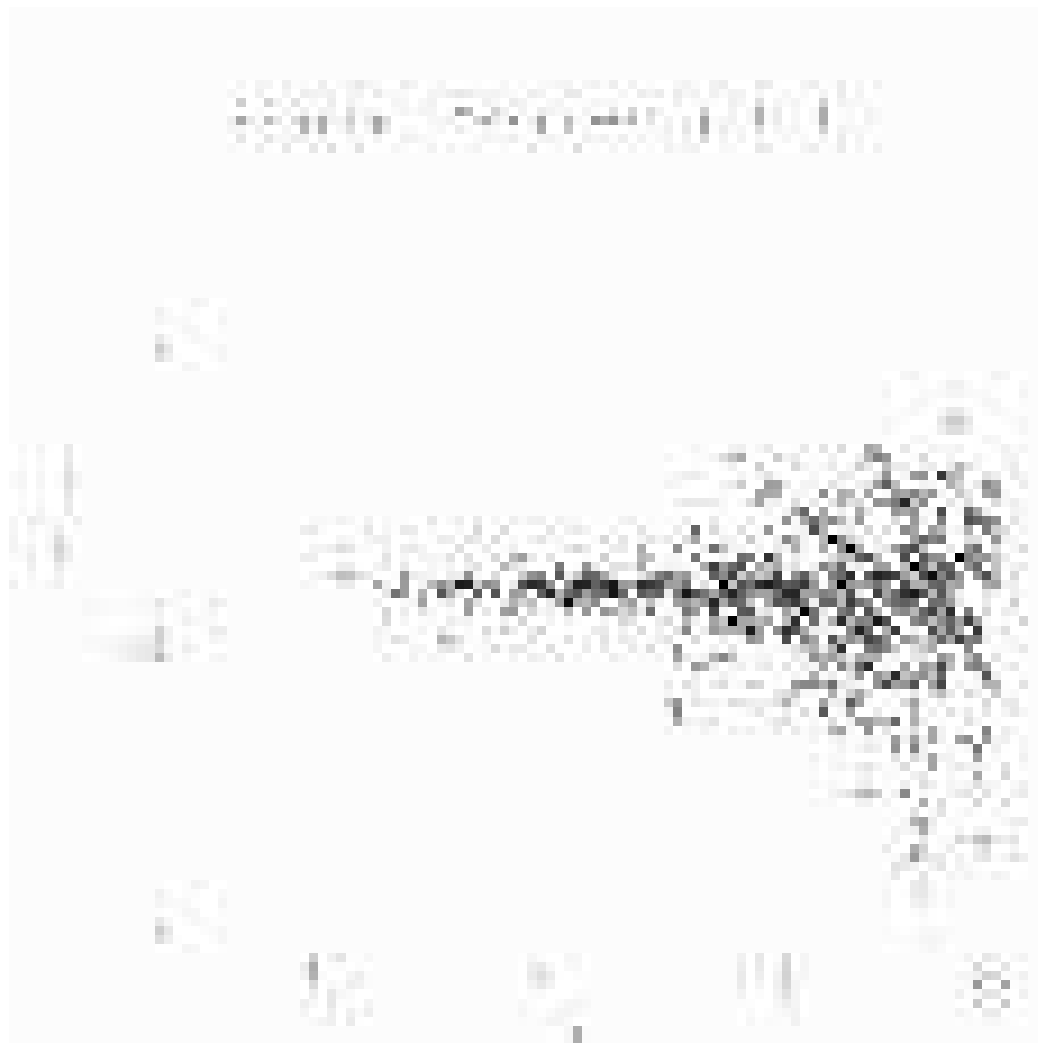


Figure 3.3: $r - i$ color-magnitude diagram. $r - i$ color cut bins are superimposed on the color-magnitude relation of Abell 1577. The abscissa is the r apparent magnitude. The ordinate is $r - i$ color. Galaxies in the SDSS fields covering A1577 ($\sim 8.3 \times 10^{-2} \text{ deg}^2$) are plotted with the dots. Colors and magnitudes are taken from the SDSS commissioning data. The horizontal dashed lines are the borders of the color cuts.

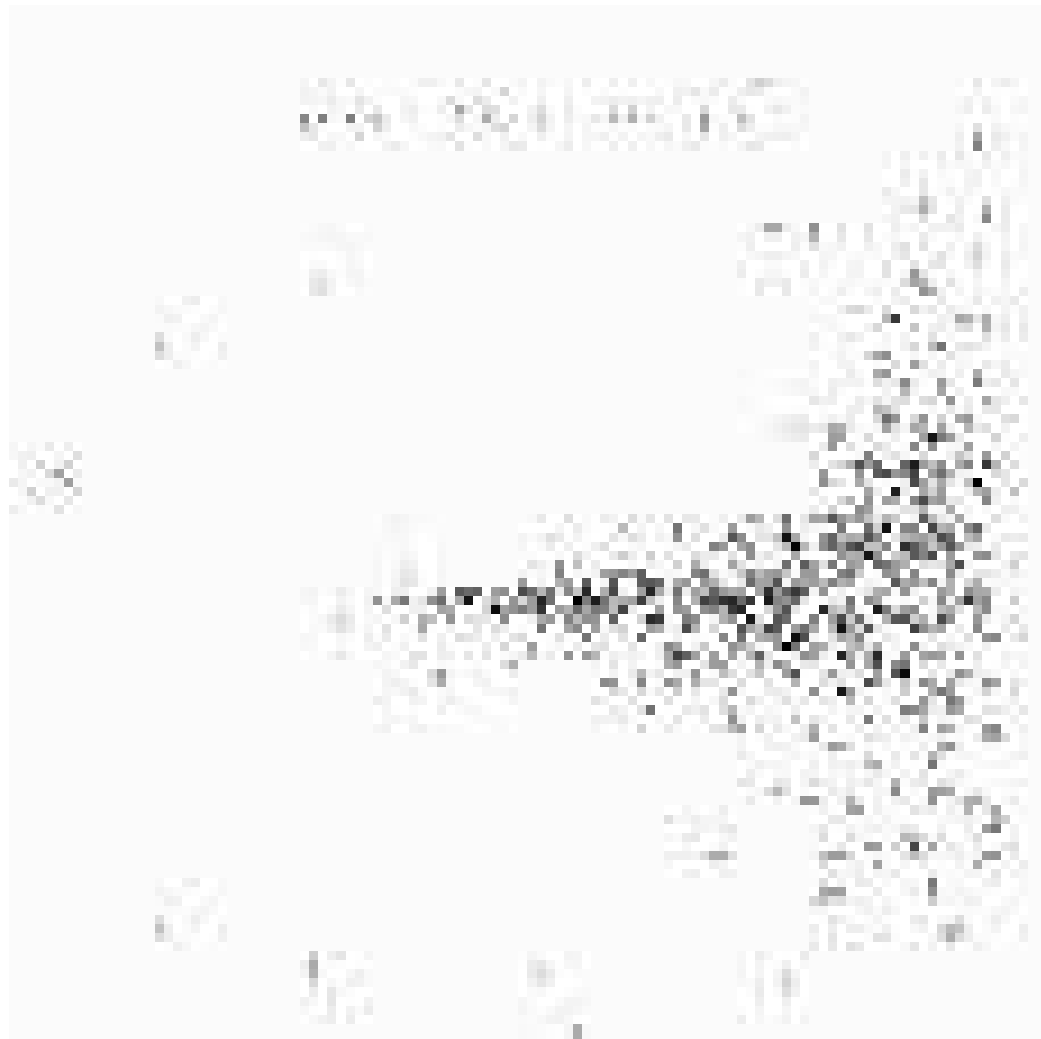


Figure 3.4: Same as Figure 3.2, but for $i - z$.

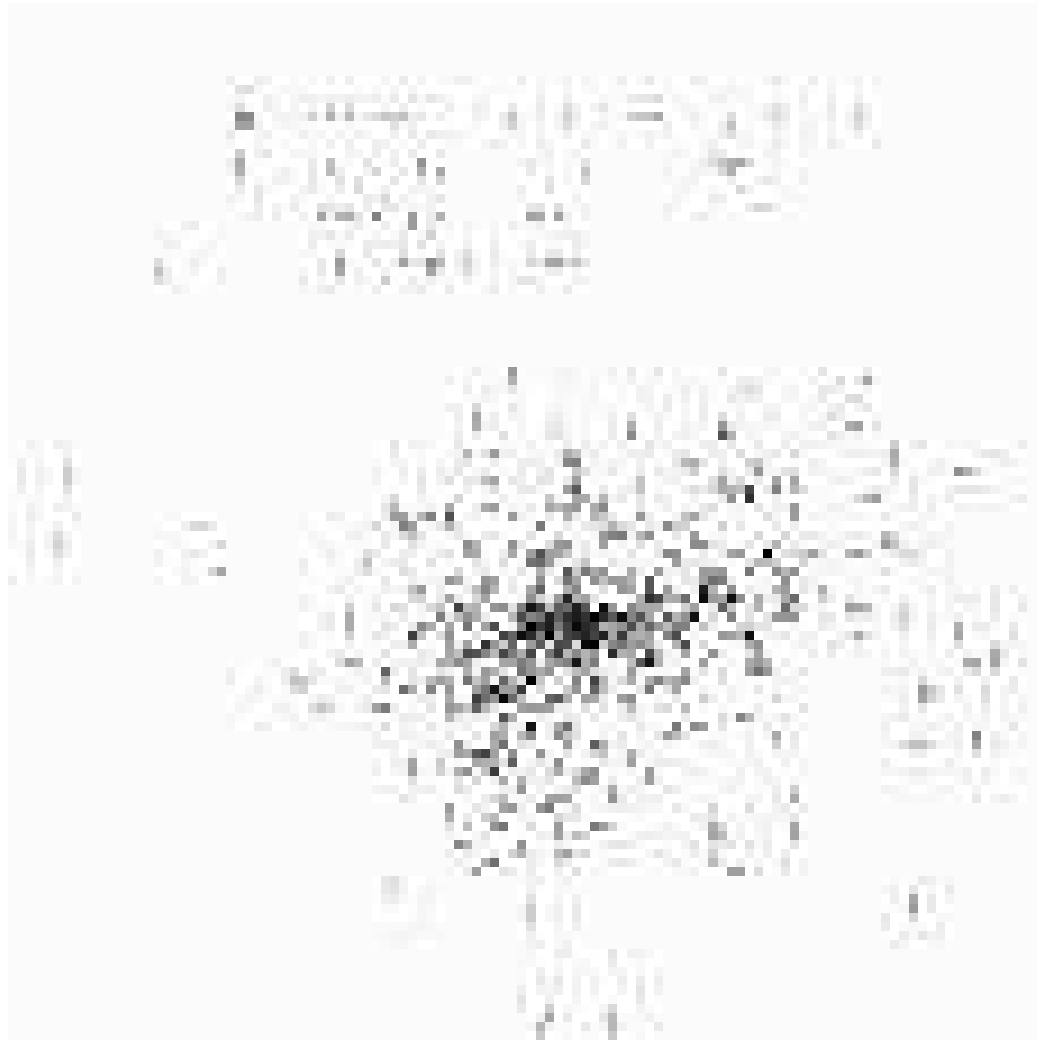


Figure 3.5: $g - r - i$ color-color boxes to find galaxy clusters. The abscissa is the $g - r$ color. The ordinate is $r - i$ color. The low- z $g - r - i$ box is drawn with the dashed lines. The high- z $g - r - i$ box is drawn with the dotted lines. Galaxies brighter than $r^* = 22$ in the SDSS fields ($\sim 8.3 \times 10^{-2} \text{deg}^2$) which covers A1577 are plotted with small dots. The triangles show the color prediction of elliptical galaxies (Fukugita et al. 1995).



Figure 3.6: An example of color-cut capturing color-magnitude relation. Galaxies within $1.5 h^{-1}\text{Mpc}$ aperture around RXJ0256.5+0006 ($z = 0.36$) are plotted as black dots. Distribution of all the galaxies in the SDSS commissioning data is drawn as contours. The $g - r$ color-cut successfully captures the red-sequence of RXJ0256.5+0006 and remove the foreground galaxies bluer than the sequence.



Figure 3.7: An example of color-cut capturing color-magnitude relation. Galaxies within $1.5 h^{-1}\text{Mpc}$ aperture around RXJ0256.5+0006 ($z = 0.36$) are plotted as black dots. Distribution of all the galaxies in the SDSS commissioning data is drawn as contours. The $r - i$ color-cut successfully captures the red-sequence of RXJ0256.5+0006 and removes the foreground galaxies bluer than the sequence.

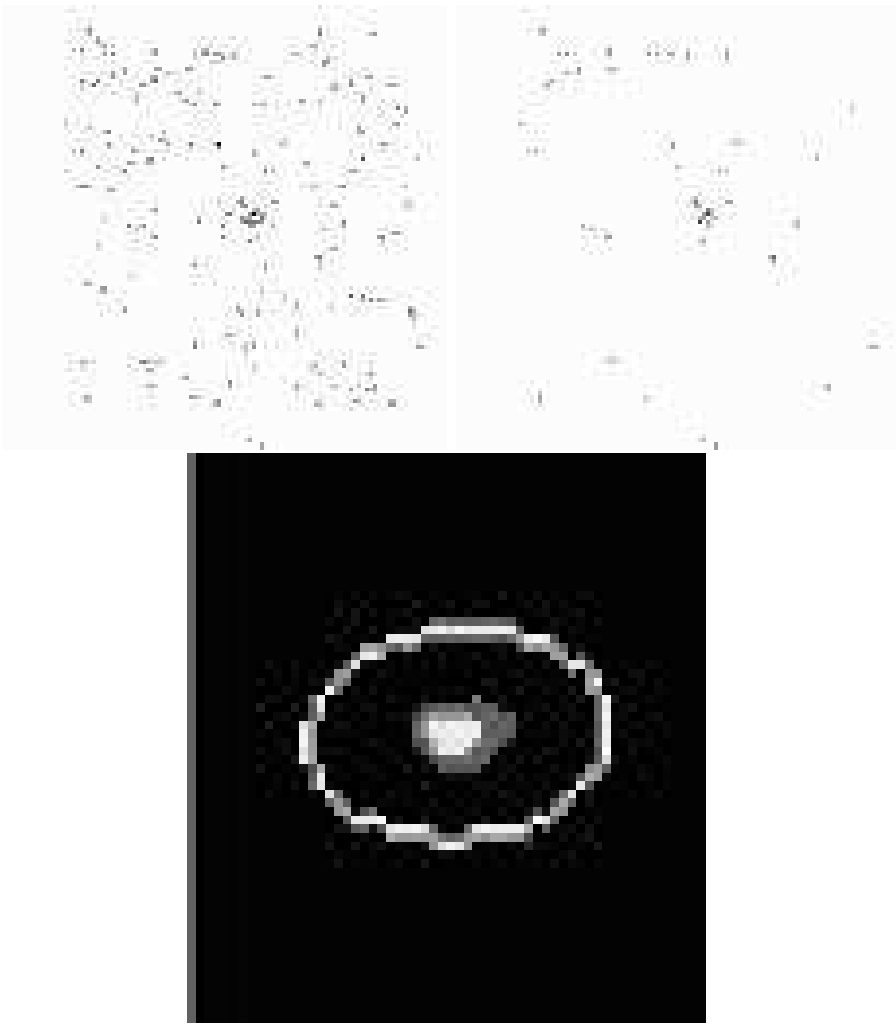


Figure 3.8: The distribution of galaxies brighter than $r^*=20.0$ around RXJ0256.5+0006. The upper left panel shows the distribution before applying any color cut. The upper right panel shows the distribution after applying $g - r$ color cut. The lower panel shows the enhanced density map. The color cut removes foreground and background galaxies as designed. RXJ0256.5+0006 is successfully detected as circled with the white line.



Figure 3.9: Color-color diagram of spectroscopically confirmed member galaxies of A168. The abscissa is $g - r$ color. The ordinate is $r - i$ color. The low- z $g - r - i$ box is drawn with the dashed lines. The high- z $g - r - i$ box is drawn with the dotted lines. Galaxies brighter than $r^* = 21$ which matched up the spectroscopically confirmed galaxies (Katgert et al. 1998) are plotted with the dots. The triangles show the color prediction of elliptical galaxies (Fukugita et al. 1995).



Figure 3.10: Color-color diagram of spectroscopically confirmed member galaxies of A168. The abscissa is $r - i$ color. The ordinate is $i - z$ color. The low- z $r - i - z$ box is drawn with the dashed lines. The high- z $r - i - z$ box is drawn with the dotted lines. Galaxies brighter than $r^* = 21$ which matched up the spectroscopically confirmed galaxies (Katgert et al. 1998) are plotted with the dots. The triangles show the color prediction of elliptical galaxies (Fukugita et al. 1995).

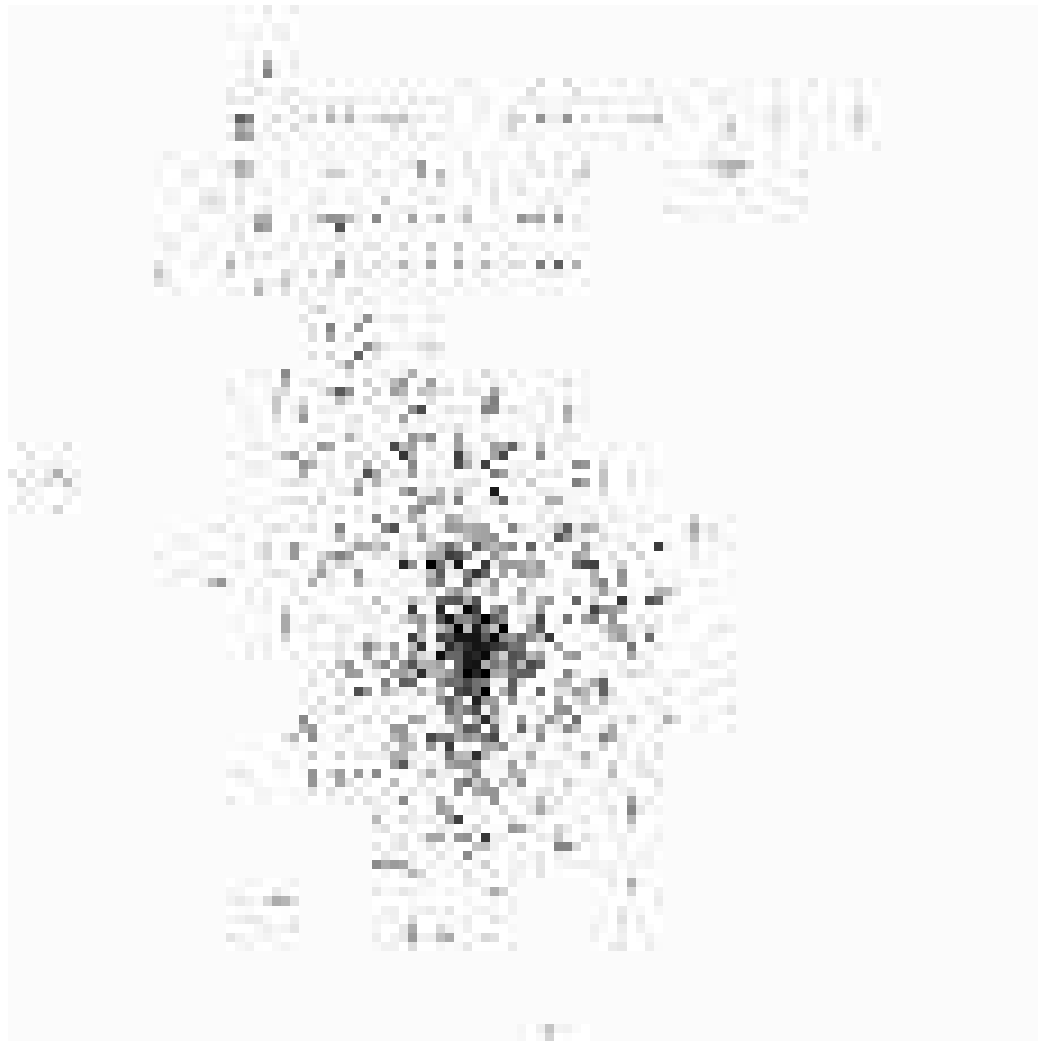


Figure 3.11: $r - i - z$ color-color boxes to find galaxy clusters. The abscissa is $r - i$ color. The ordinate is $i - z$ color. The low- z $r - i - z$ box is drawn with the dashed lines. The high- z $r - i - z$ box is drawn with the dotted lines. Galaxies brighter than $r^* = 22$ in the SDSS fields ($\sim 8.3 \times 10^{-2} \text{deg}^2$) which covers A1577 are plotted with the small dots. The triangles show the color prediction of elliptical galaxies (Fukugita et al. 1995).

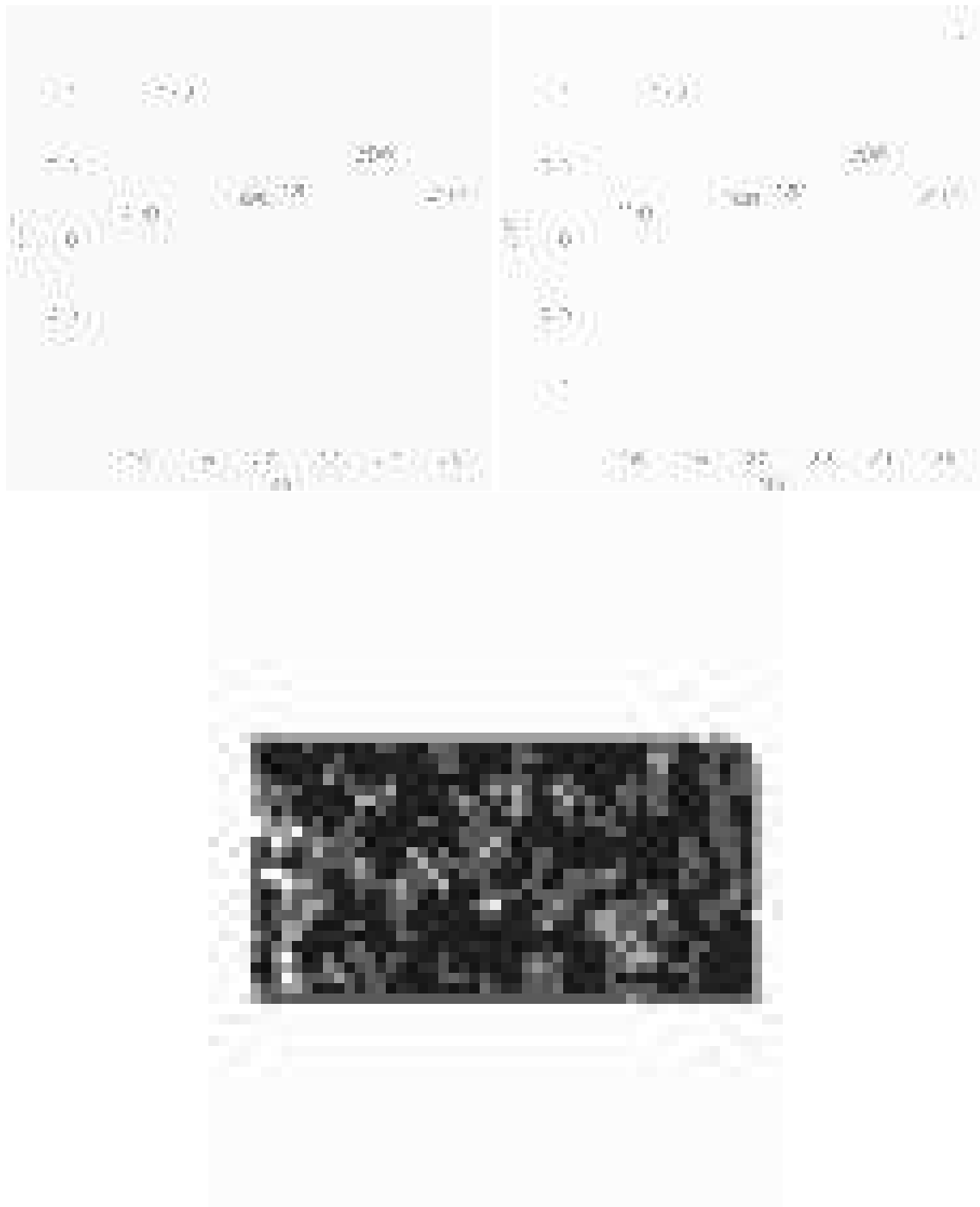


Figure 3.12: The distribution of galaxies brighter than $r^*=21.5$. The upper left panel shows the distribution before applying any cut. The upper right panel shows the distribution after applying $g - r - i$ color-color cut. The numbers show the positions of Abell clusters. The lower panel shows the enhanced density map in $g - r - i$ color-color cut. Detected clusters are circled with the white lines.



Figure 3.13: Evaluation of high- z color cut. The filled triangles show the color prediction for elliptical galaxies (Fukugita et al. 1995). The open triangles show the color prediction of non-star-forming galaxies of the PEGASE model (Fioc & Rocca-Volmerange 1997). The open squares show the color prediction of star-forming galaxies of the PEGASE model. The black dots are the galaxies around A1577. high- z color cut and low- z color cut are drawn with the dashed and the long-dashed lines.



Figure 3.14: The redshift estimation accuracy. The estimated redshifts are plotted against spectroscopic redshifts. Abell clusters are plotted with the triangles. Dots are the redshifts from SDSS spectroscopic galaxies. Extensive outliers $\delta z > 0.1$ are removed. The dispersion is 0.0147 for $z < 0.3$ and 0.0209 for $z > 0.3$.



Figure 3.15: The number of galaxies fed (N_{gal}) v.s. CE richness. The number of galaxies inputted into an artificial cluster is compared with CE richness (the number of galaxies within the detected radius whose magnitude is between the magnitude of the third brightest galaxy and the magnitude fainter than that by two mag). The error bars show 1σ standard error.

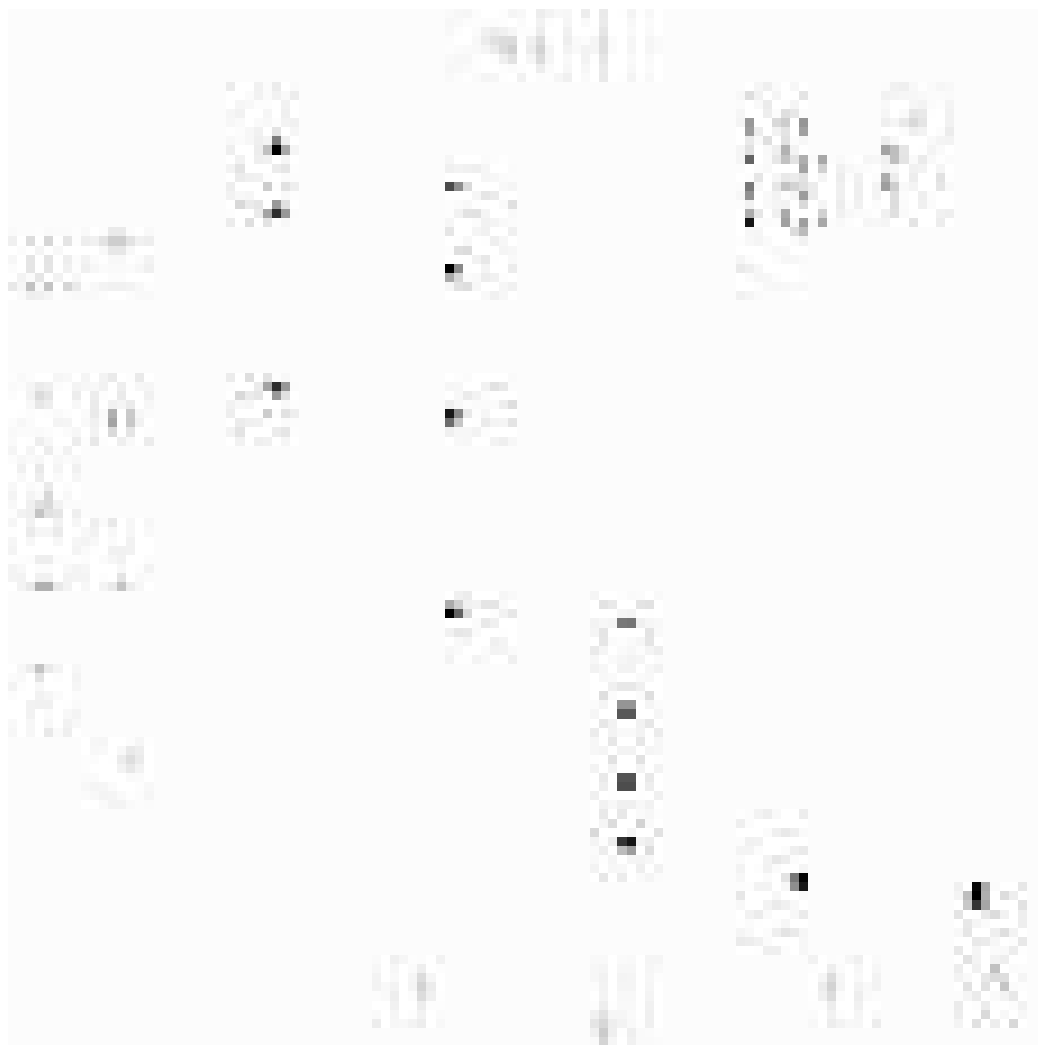


Figure 3.16: Recovery rate in Monte Carlo simulation with the real SDSS background. Recovery rate is plotted against redshift. The artificial clusters are added on the real SDSS background randomly chosen from the SDSS commissioning data. The detection is iterated 1000 times for each data point. Even at $z = 0.3$, $N_{gal} = 80$ cluster is detected with more than 75% probability.

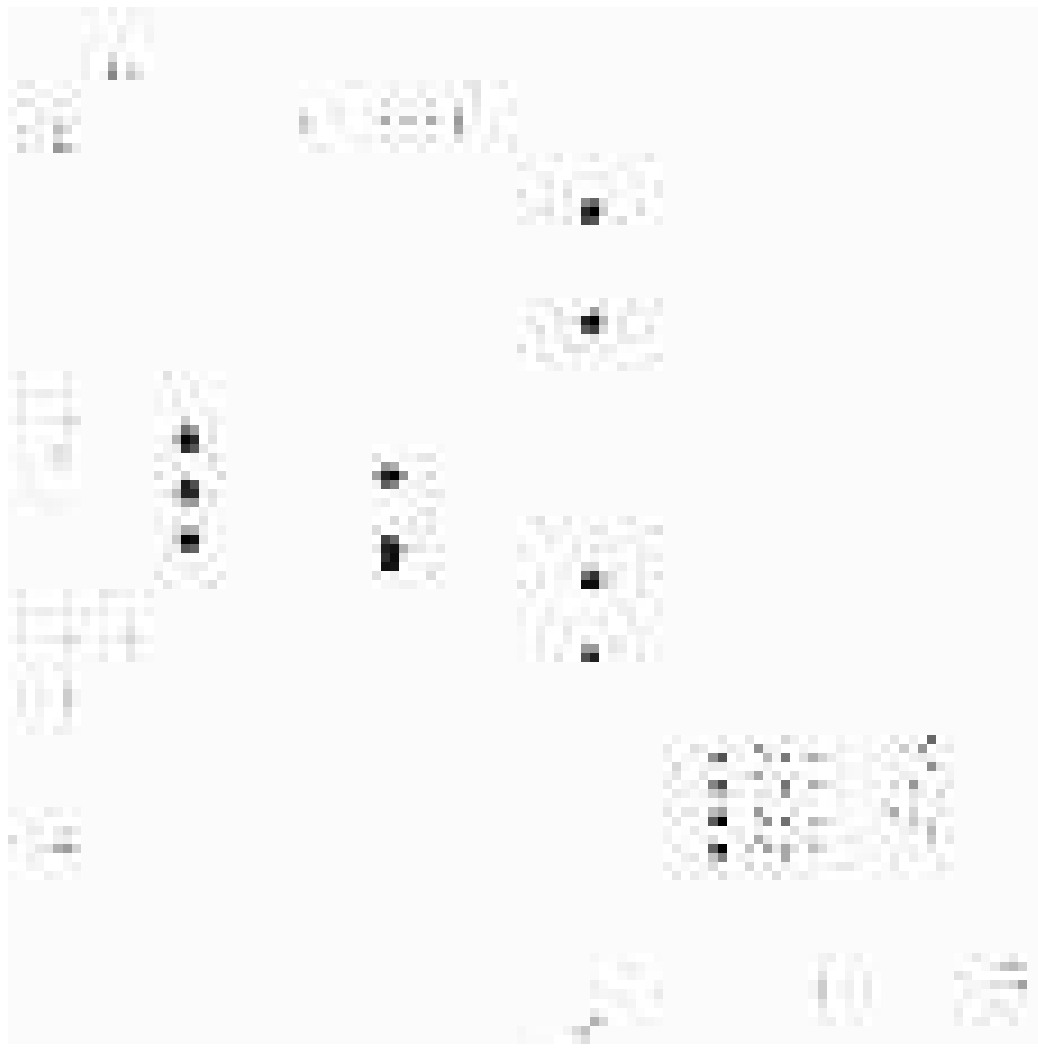


Figure 3.17: Positional accuracy with the real SDSS background. The positional accuracy is almost constant against redshift because the more distant cluster is more compact in angular space. Positional accuracy of $\sim 30''$ is reasonable considering that the mesh size of the enhancement method is $30''$.

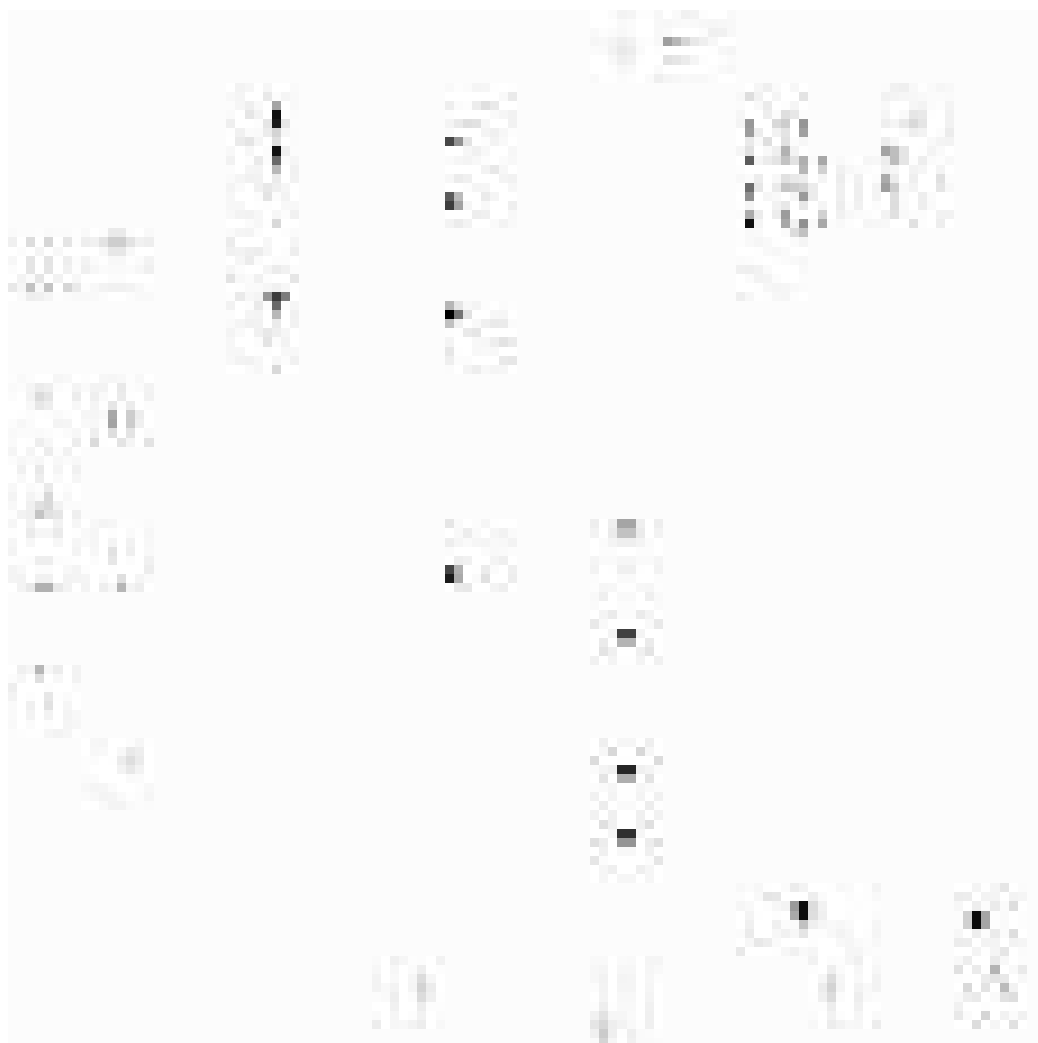


Figure 3.18: Recovery rate in Monte Carlo simulation with the shuffled background. The artificial clusters are added on the shuffled background randomly chosen from the SDSS commissioning data. The detections are iterated 1000 times.

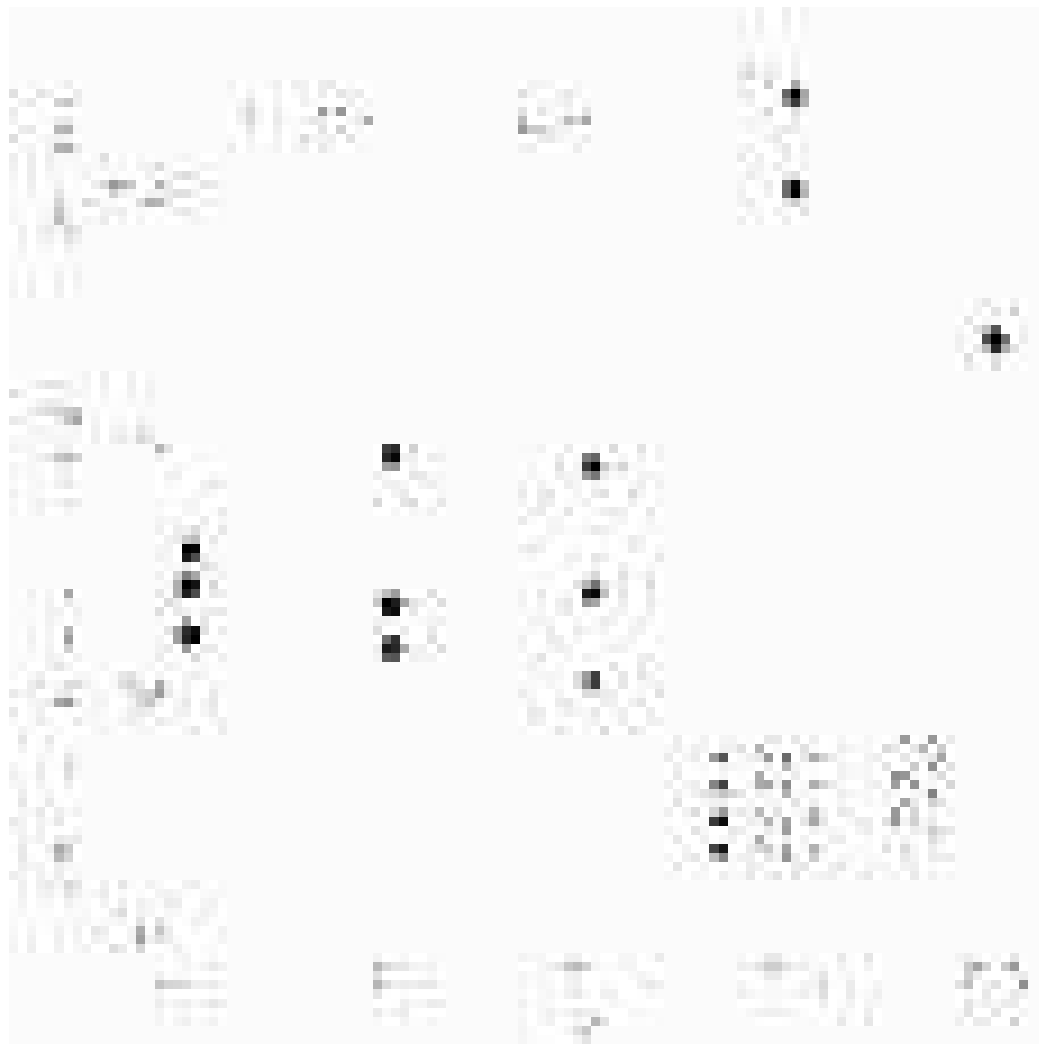


Figure 3.19: Positional accuracy with the shuffled background. The positional accuracy is almost independent of redshift because the more distant cluster is more compact in angular space. Positional accuracy of $\sim 30''$ is good considering that the mesh size of the enhancement method is $30''$.



Figure 3.20: False positive tests. Detection tests are performed using 23.75 deg^2 of the SDSS commissioning data. Number of detected clusters is plotted against the CE richness. The solid line represents the results with real data. The dotted line represents the results with position shuffled data. The long-dashed line is for color shuffled data subtracting the detection from the real data. The short-dashed line is for color shuffled smearing data.



Figure 3.21: False positive tests. Detection tests are performed using 23.75 deg^2 of the SDSS commissioning data. The fraction of false detections to the real data is plotted against the CE richness. Each line represents the ratio to the real data at the richness bin. The dotted line represents the results with position shuffled data. The long-dashed line is for color shuffled data subtracting the detection from the real data. The short-dashed line is for color shuffled smearing data.



Figure 3.22: A successful detection with the CE method. The image is $6' \times 13'$ true color image of the SDSS commissioning data. There are many faint galaxies in the region. CE method has the ability to detect the region in the sky where many faint galaxies are clustering. This cluster was found only with the CE method.



Figure 3.23: A successful detection with the CE method. The image is $6' \times 13'$ true color image of the SDSS commissioning data. The cluster position and radius is shown with the yellow circle.

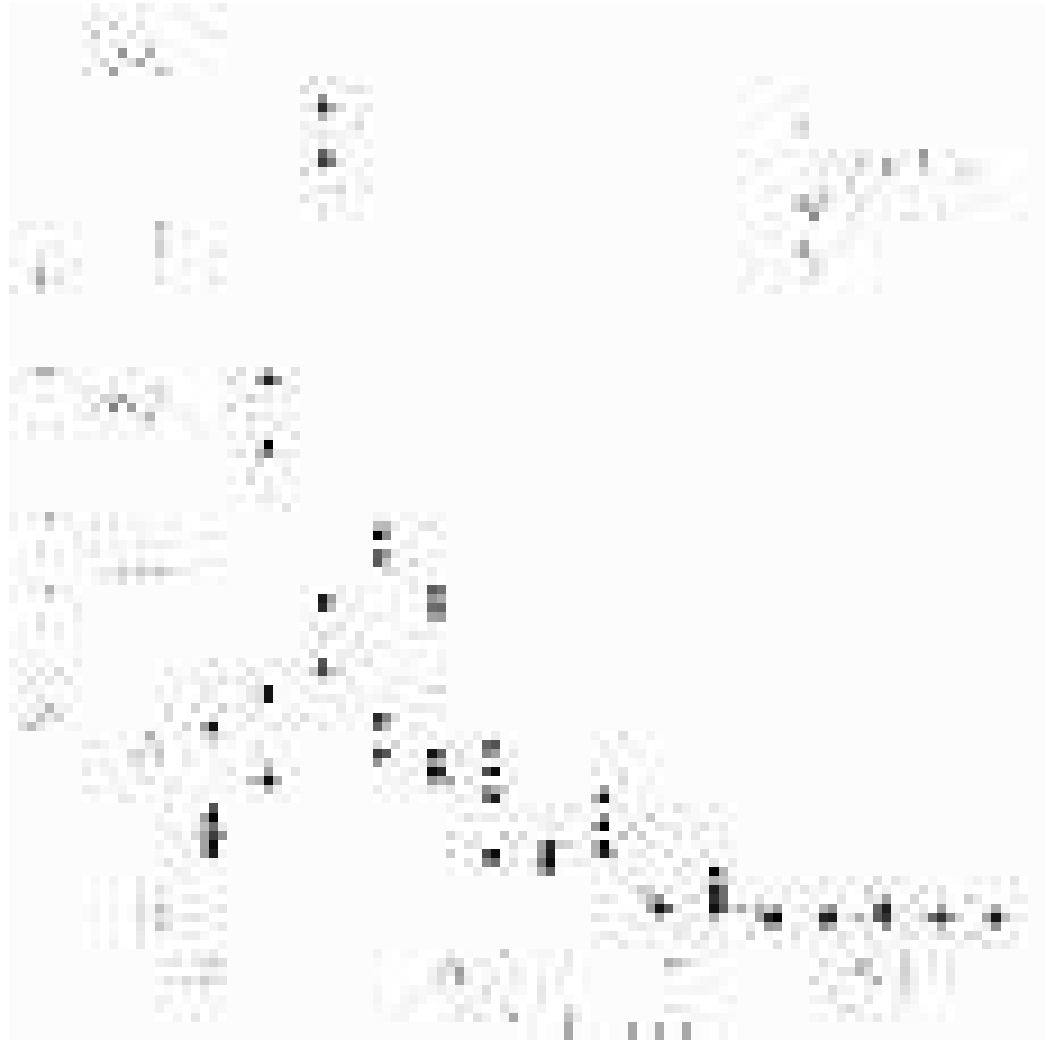


Figure 3.24: Comparison of four catalogs by richness. The abscissa is the richness of the cluster. The ordinate is the number of the detected clusters. The CE clusters are drawn with the solid lines. The maxBCG clusters are drawn with the dotted lines. Matched Filter clusters are drawn with the short-dashed lines. Voronoi tessellation clusters are drawn with the long-dashed lines. The CE and the maxBCG detect poor clusters (richness < 20) more than the MF or the VTT.



Figure 3.25: Comparison of four catalogs by redshift. The abscissa is the redshift of the clusters. The ordinate is the number of the clusters. CE clusters are drawn with the solid lines. The maxBCG clusters are drawn with the dotted lines. The Matched Filter clusters are drawn with the short-dashed lines. The Voronoi tessellation clusters are drawn with the long-dashed lines. The redshift is estimated photometrically (described in Section 3.3).



Figure 3.26: Comparison of the MF with the CE. The abscissa is the estimated redshift. The ordinate is the rate of the MF clusters which are found in the CE catalog to the number of the CE clusters. CE richness $0 \sim 20$ is plotted with the solid lines. CE richness $20 \sim 40$ is plotted with the dotted lines. CE richness $40 \sim 60$ is plotted with the dashed lines. The error bars for richness $40 \sim 60$ clusters are large and omitted for clarity (The error is 80% at $z = 0.3$). The data for richness $20 \sim 40$ and $40 \sim 60$ are shifted in redshift direction by 0.01 for clarity.



Figure 3.27: Comparison of the CE with the MF. The abscissa is the estimated redshift. The ordinate is the rate of the CE clusters which are found in the MF catalog to the number of the CE clusters. Matching rate is low for poor clusters indicating the CE detects poor clusters more. The error bars for richness 40~60 clusters are large and omitted for clarity (The error is 80% at $z = 0.3$). The data for richness 20~40 and 40~60 are shifted in redshift direction by 0.01 for clarity.



Figure 3.28: Elongation distribution of the detected clusters. The number of the clusters is plotted against elongations (ratio of the major axis to the minor axis). The solid line is for the clusters detected with the CE method. The dotted line is for the the clusters detected with both the MF and the CE method, which is shifted by 0.01 for clarity.

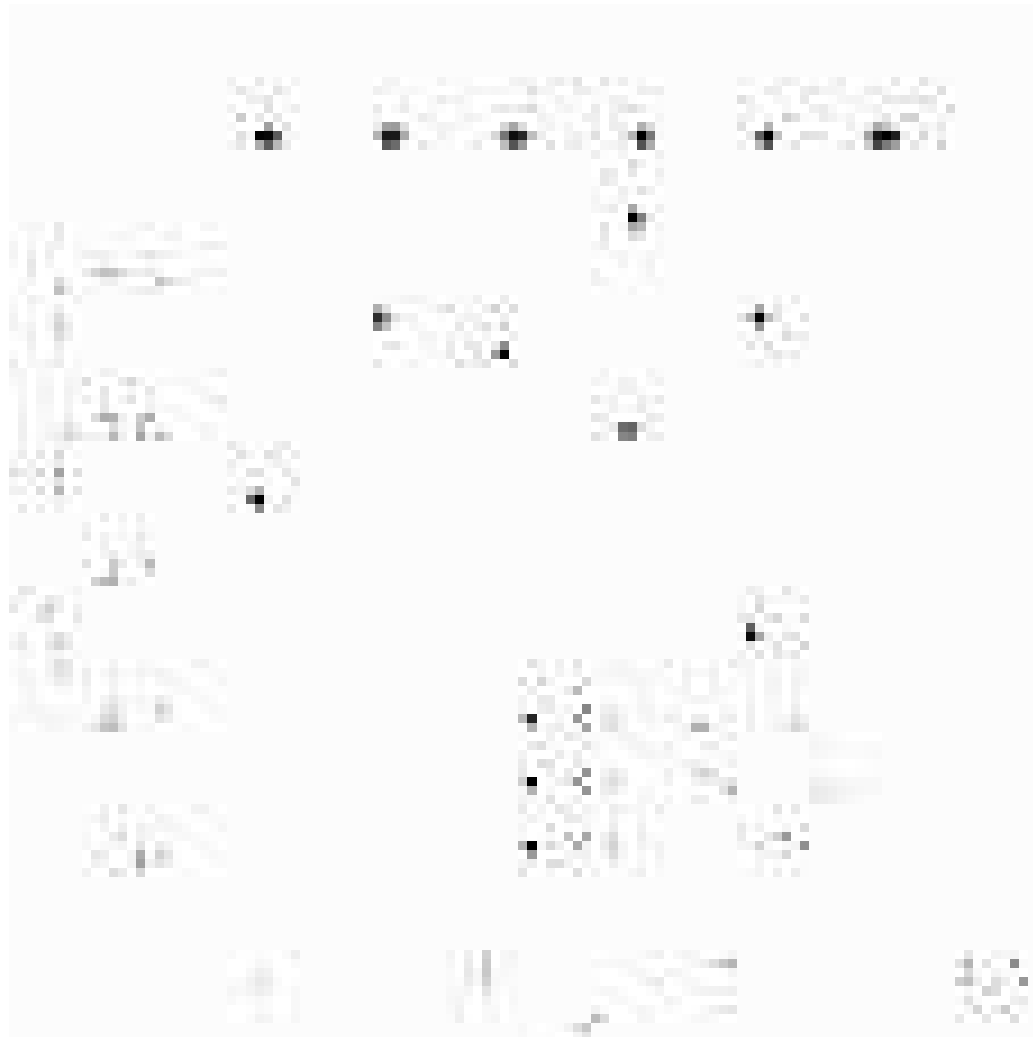


Figure 3.29: Comparison of the maxBCG clusters with the CE catalog. The abscissa is the color estimated redshift. The ordinate is the ratio of the maxBCG clusters which are found in the CE catalog to the number of the maxBCG clusters. The error bars for richness 40~60 clusters are large and omitted for clarity (The error is 80% at $z = 0.3$). The data for richness 20~40 and 40~60 are shifted in redshift direction by 0.01 for clarity.

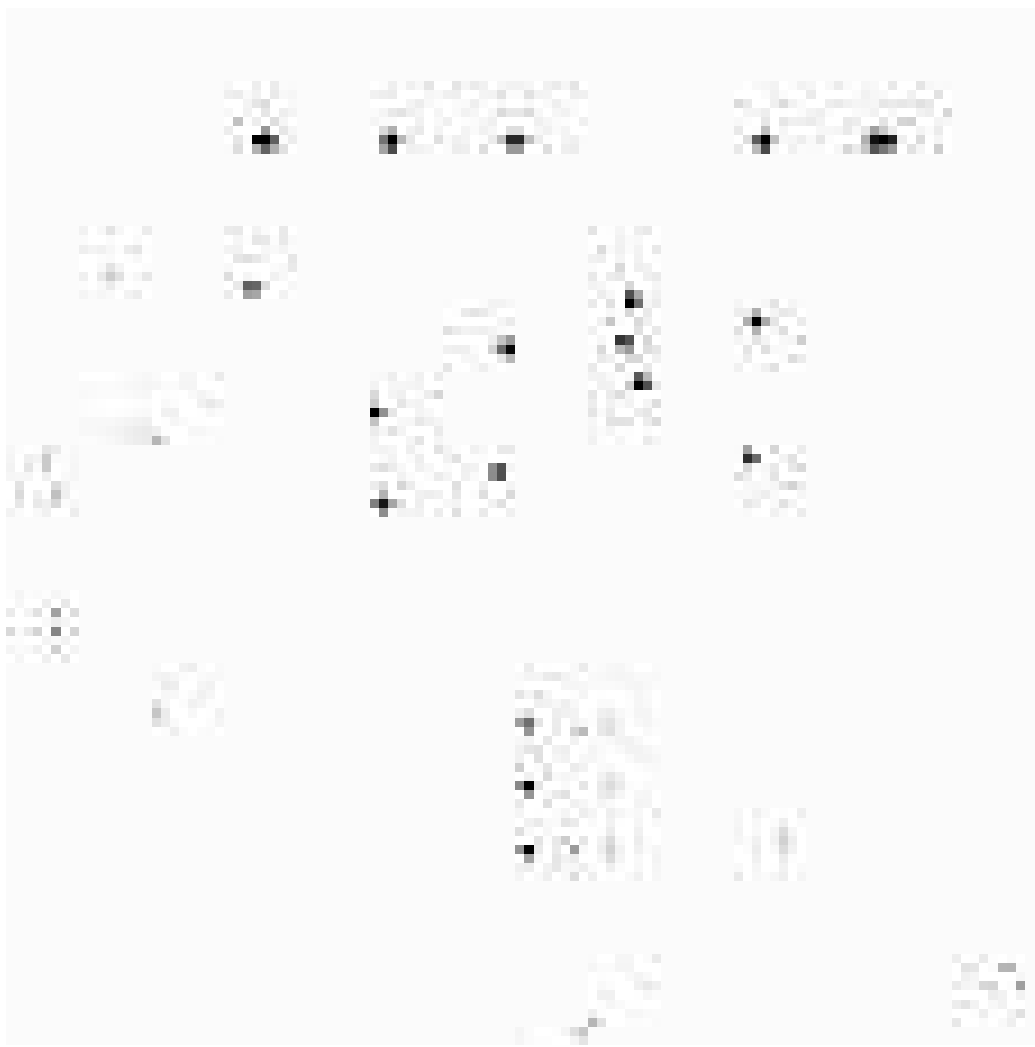


Figure 3.30: Comparison of the CE method with the maxBCG method. The abscissa is the estimated redshift. The ordinate is the rate of the CE clusters which are found in the maxBCG catalog to the number of the CE clusters. The error bars for richness 40~60 clusters are large and omitted for clarity. The data for richness 20~40 and 40~60 are shifted in redshift direction by 0.01 for clarity.

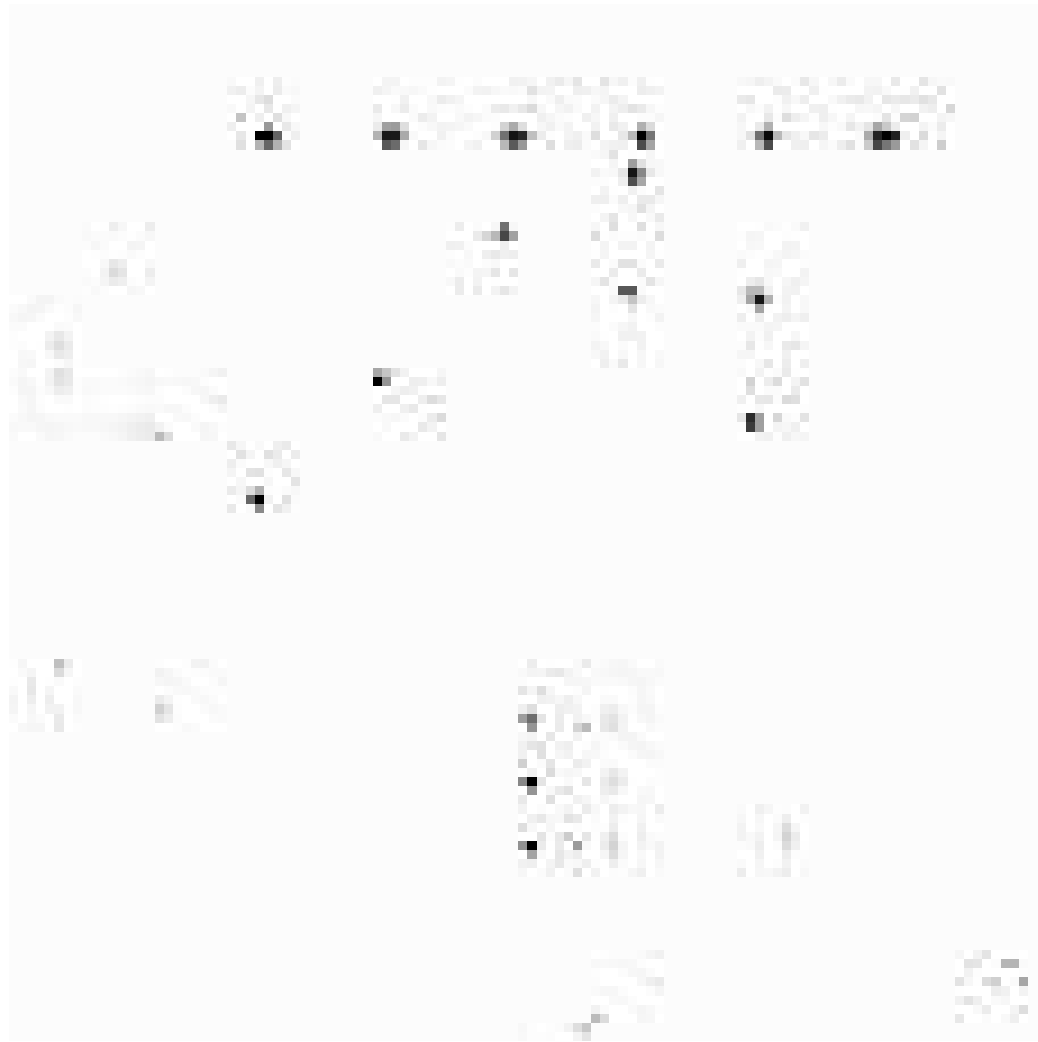


Figure 3.31: Comparison of the CE method with the VTT method. The abscissa is the estimated redshift. The ordinate is the rate of the CE clusters which are found in the VTT catalog to the number of all CE clusters. The CE detects twice as many clusters as the VTT does. The error bars for richness 40~60 clusters are large and omitted for clarity. The data for richness 20~40 and 40~60 are shifted in redshift direction by 0.01 for clarity.

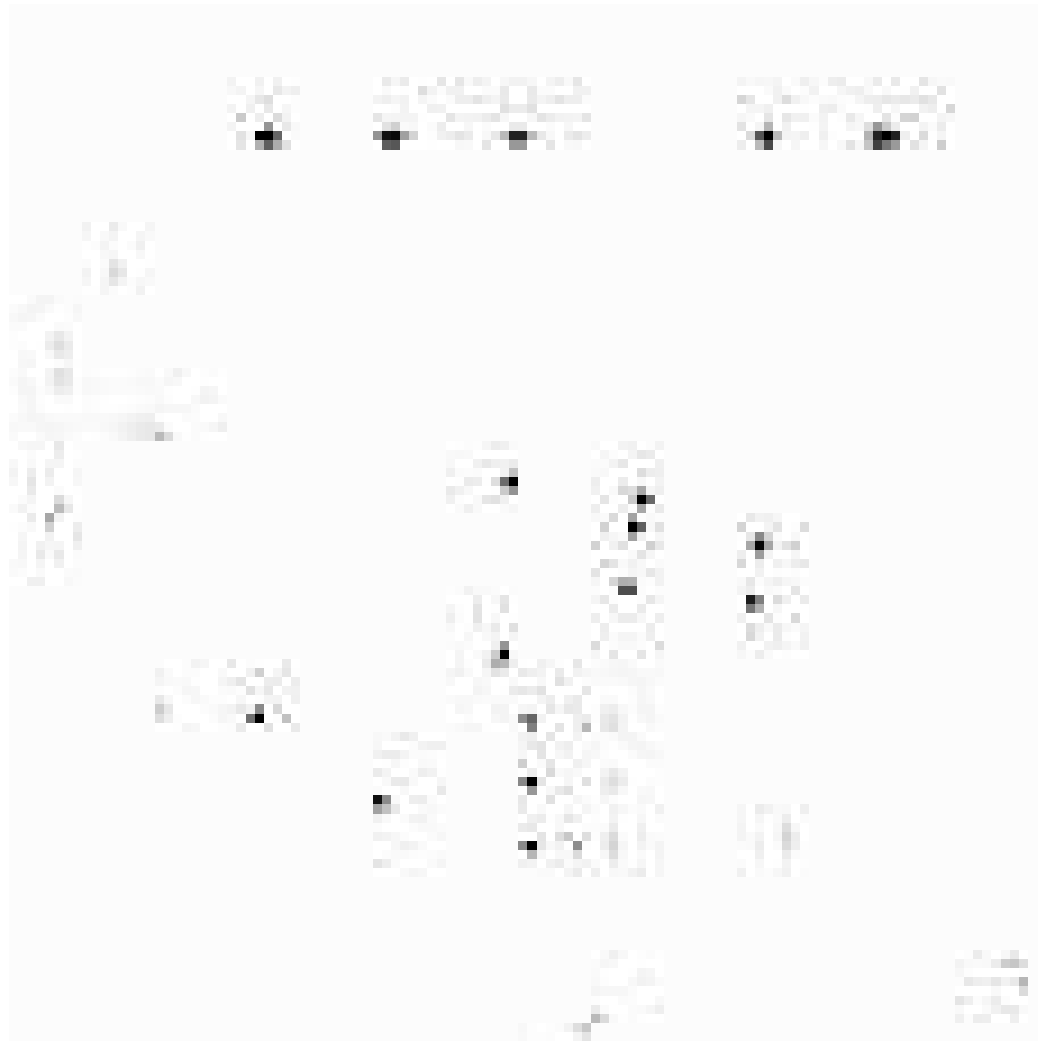


Figure 3.32: Comparison of the VTT method with the CE method. The abscissa is the estimated redshift. The ordinate is the ratio of the VTT clusters which are found in the CE catalog to the number of the VTT clusters. Note that the CE method detects twice as many as the VTT does. The error bars for richness 40~60 clusters are large and omitted for clarity. The data for richness 20~40 and 40~60 are shifted in redshift direction by 0.01 for clarity.

Table 3.1: Tilt and scatter of color-magnitude relation of A1577.

Color	Tilt (color/mag)	(magnitude range)	Scatter (mag)	(magnitude range)
$g^* - r^*$	0.0737	$r^* < 19$	0.081	$r^* < 17$
$r^* - i^*$	0.0898	$r^* < 19$	0.040	$18 < r^* < 19$
$i^* - z^*$	0.0018	$r^* < 21$	0.033	$18 < r^* < 19$

Table 3.2: The fraction of galaxies in the color-cut both for galaxies inside of the RXJ0256.5+0006 ($z = 0.36$) and outside of RXJ0256.5+0006.

Color cut	In cluster region(%)	Outside of cluster (%)
$g - r$	$36.9^{+7.0}_{-6.0}$	13.57 ± 0.03
$r - i$	$62.1^{+8.8}_{-7.7}$	42.35 ± 0.06
$i - z$	$59.2^{+8.6}_{-7.6}$	44.55 ± 0.06
$g - r - i$	$58.3^{+8.5}_{-7.6}$	48.77 ± 0.06
$r - i - z$	$76.7^{+10.7}_{-7.7}$	65.68 ± 0.07
$g - r - i$ high- z	$29.1^{+6.3}_{-5.3}$	10.86 ± 0.03
$r - i - z$ high- z	$6.8^{+3.7}_{-2.5}$	9.94 ± 0.02

Table 3.3: Sigma cut test. Sigma is a threshold when detecting clusters in the enhanced density map. The test is performed using a 23.75 deg^2 region in the data.

Sigma	2	4	6	8	10
N detection	402	437	453	434	415

Table 3.4: Test of fluxmax cut. The test is performed using a 23.75 deg^2 region in the data. A number of detections is shown as a function of fluxmax threshold.

fluxmax	500	750	1000	1500	2000
N detection	890	655	464	260	10

Table 3.5: 10 false detections of the CE method. The region examined is RA between 16 and 25.5 deg, DEC between -1.25 and $+1.25$ deg (23.75 deg^2). σ (column [1]) is the significance of the detection. CE richness (column [2]) is the richness of the detection. z (column [3]) is the color estimated redshift of the detection. Comments on the detection are in column [4].

σ	richness	z	comment
12.39	31	0.22	looks like a blank field.
7.85	21	0.18	looks like a blank field.
4.80	11	0.10	looks like a blank field.
16.74	16	0.18	looks like a blank field.
56.85	8	0.04	a big galaxy.
9.35	7	0.00	looks like a blank field.
7.06	1	0.04	eight blue galaxies.
11.0	14	0.04	looks like a blank field.
4848.39	17	0.12	a big galaxy.
25.20	7	0.00	a big galaxy.

Table 3.6: Ratio of number of clusters detected with the MF, the maxBCG and the VTT to the CE clusters. The region used is RA between 16 and 25.5 deg, DEC between -1.25 and $+1.25$ deg (23.75 deg 2). Column 1 lists the name of each method. N detection (column [2]) is the numbers of clusters detected with each method. Common detection (column [3]) is the number of clusters detected with both the method and the CE method. Rate to the CE (column [4]) is the percentage of the number of detections with each method divided by those with the CE method (CE in the table). Rate to the method (column [5]) is the percentage of the number of detections with the CE method divided by those with each method.

	N detection	Common detection	Rate to CE (%)	Rate to the method (%)
MF	152	116	32.0	76.3
maxBCG	438	183	50.4	41.8
VTT	130	96	26.4	73.8
CE	363	-	-	-

Table 3.7: The comparison of the detected clusters with the methods other than the Cut & Enhance method. Column 1 and row 1 denote the name of each method. The parentheses in row 1 are the total numbers of the clusters detected with each method in the region RA between 16 and 25.5 deg, DEC between -1.25 and $+1.25$ deg (23.75 deg 2). Rows 2~4 list the numbers of the clusters detected with both of the two methods (column 1 and row 1) and their percentage to the methods in column 1.

	MF (152)	VTT (130)	maxBCG (438)
MF	-	39.4% (60)	59.2% (90)
VTT	45.5% (60)	-	65.4% (85)
maxBCG	20.5% (90)	19.4% (85)	-

Chapter 4

Composite Luminosity Functions

4.1 Introduction

Luminosity function (LF) of galaxies within clusters of galaxies is a key tool for understanding the role of the environment on galaxy formation and evolution. The shape of the cluster LF as a function of the galaxy colors and morphologies, as well as a function of the cluster radius or local density, can provide strong observational constraints on the theories of galaxy formation. For example, Springel et al. (2001) recently showed that semi-analytical models of hierarchical structure formation could now explain both the shape of the composite cluster LF (B -band LF of Trentham 1998) and the morphology–radius relationship of Whitmore et al. (1993) using just a simple prescription for the properties of galaxies in clusters based on their merger and cooling rates (see also Okamoto, Nagashima 2001; Diaferio et al. 2001). Empirically, there is also growing evidence for a correlation between the shape of the cluster LF and the underlying cluster properties. Phillipps et al. (1998) and Driver et al. (1998) show that more evolved clusters, based on either their density profile or the presence of a cD galaxy, have flatter faint-end slopes, which they attribute to the disruption of faint galaxies in the cores of such evolved systems [see the earlier theoretical work on galaxy cannibalism by Hausman & Ostriker (1978)]. In summary, the LF of galaxies in clusters as a function of both the galaxy and cluster properties is a powerful observational test for theories of galaxy formation and evolution. The reader is referred to the seminal review by Binggeli, Sandage, and Tammann (1988), which is still relevant today.

In this Chapter, we present an analysis of the composite cluster LF based on the commissioning data of the Sloan Digital Sky Survey (SDSS; see Gunn et al. 1998; York et al. 2000; Stoughton et al. 2002). This analysis has several key advantages over previous studies of the composite cluster LF, including accurate multi-color CCD photometry for all galaxies (in optical passbands u, g, r, i and z ; Fukugita et al. 1996), large aerial cov-

erage, thus enabling us to make a local correction for the projected field LF, and finally, the availability of several objectively-measured galaxy properties like morphology. Furthermore, we selected our clusters from the SDSS Cut and Enhance (CE) cluster catalog of Goto et al. (2002a; Chapter 3), which has two major benefits over previous cluster samples used for LF studies. First, the CE catalog was objectively constructed using the latest cluster-finding algorithms, and therefore has a well-determined selection function (see Goto et al. 2002a; Chapter 3). Secondly, CE has obtained an accurate photometric redshift for each cluster based on the observed color of the E/S0 ridge-line using the maxBCG method (J. Annis et al. in preparation). The error on this cluster photometric redshift is only $\delta z = 0.015$ for $z < 0.3$ clusters (see Figure. 14 of Goto et al. 2002a; Figure 3.14 in Chapter 3) and, as we show herein, is accurate enough to allow us to determine the composite LF for a large sample of CE clusters without the need for spectroscopic redshifts. Thus, our analysis of the composite cluster LF is based on one of the largest samples of clusters to date.

We present this work now to provide a low-redshift benchmark for on-going multi-color photometric studies of high redshift clusters of galaxies. With the advent of large-area CCD imagers on large telescopes, the number of distant clusters with such data will increase rapidly over the next few years; e.g., Kodama et al. (2001) recently presented large-area multi-color CCD photometry for the distant cluster A 851 ($z = 0.41$) using Suprime-Cam on the Subaru Telescope. Gladders & Yee (2000) searched distant clusters over 100 deg² of CCD data.

This Chapter is organized as follows: In section 4.3 we describe the methods used to construct the composite LF of CE clusters and show our results as a function of passband and morphology. In section 4.4 we test the robustness of the analysis, and in section 4.5 we summarize our work. Throughout this Chapter, we use $h_0 = 0.7$, $\Omega_M = 0.3$ and $\Omega_\Lambda = 0.7$.

4.2 SDSS Data

In this section, we outline the data used in this Chapter. The photometric data used herein were taken from the SDSS commissioning data, as discussed by York et al. (2000). Our analysis focuses on the 150 deg² contiguous area made up from the overlap of SDSS photometric runs 752 & 756, i.e., $145.1 < \text{R.A.} < 236.1$ and $-1.25 < \text{Dec.} < +1.25$. This is a subset of the SDSS Early Data Release, as discussed in Stoughton et al. (2002), and similar to the data used by Scranton et al. (2002) for studying the angular clustering of SDSS galaxies. This photometric data reach 5σ detection limits for point sources of 22.3, 23.3, 23.1, 22.3 and 20.8 mag in the u, g, r, i and z passbands, respectively (for an airmass

of 1.4 and $1''$ seeing)¹. The photometric uniformity of the data across the whole area is less than 3% [see Hogg et al. (2001) and Smith et al. (2002) for photometric calibration], while the star-galaxy separation is robust to $r^* \simeq 21.0$ (Scranton et al. 2002). The SDSS is significantly better than previous photographic surveys, which suffer from larger plate-to-plate photometric fluctuations and a lower dynamic range [see Lumsden et al. 1997 for the problems associated with photographic studies of the cluster composite LF]. For each galaxy, we used the model magnitude computed by the PHOTO data analysis pipeline, which has been shown by Lupton et al. (2001) and Stoughton et al. (2002) to be the optimal magnitude for faint SDSS galaxies. It is also close to the total magnitude for the fainter SDSS galaxies. For a full discussion of the photometric data, and the galaxy parameters derived from that data, we refer the reader to Lupton et al. (2001) and Stoughton et al. (2002).

The clusters used here were drawn from the large sample of CE clusters presented in Goto et al. (2002a; Chapter 3), which were selected over the same photometric runs of 752 & 756. We only selected the richer systems which were determined by the number of galaxies brighter than -18 th magnitude, (N_{-18}). The CE clusters used here satisfy the following conditions:

- 1) Number of galaxies brighter than -18 th magnitude in the r band ($N_{-18} > 20$,
- 2) $0.02 < z < 0.25$.

Condition 1 was used to select richer systems. N_{-18} is defined as the number of galaxies brighter than -18 th magnitude in the r band after subtracting the background using the method described in section 4.3. Galaxies within 0.75 Mpc from a cluster center were used. Condition 1 is useful to avoid letting small groups with only a few very bright galaxies dominate the composite LFs in the weighting scheme (The weighting scheme is explained in detail in section 4.3). Even though we used $N_{-18} > 20$ as a criteria to select our clusters, we show in section 4.4 that our composite LFs were not affected by this richness criteria. Since the high redshift clusters ($z \sim 0.3$) are not imaged to the fainter galaxies, we restricted our clusters to be in the range $0.02 < z < 0.25$. In total, 204 clusters satisfy these criteria.

4.3 Analysis and Results

4.3.1 Construction of the Composite Cluster LF

We discuss here the construction of the composite luminosity function of galaxies within the subsample of the CE clusters discussed above. The first critical step in such an analysis

¹The photometry obtained at this early stage of SDSS is denoted u^*, g^*, r^*, i^* , and z^* to stress the preliminary nature of the calibration.

is the subtraction of the background and foreground contamination. Ideally, one would wish to do this via spectroscopic observations, but since the CE cluster catalog contains ~ 2000 clusters in the region used, it is not feasible to observe all clusters spectroscopically. Therefore, we must make a statistical correction based on the expected contamination from projected field galaxies. One of the main advantages of the SDSS data is that such a correction can be estimated locally (i.e., free from any galaxy number count variances due to the large-scale structure) for each cluster since we possess all the photometric data, to the same depth and in the same filter set, well outside of the cluster. Indeed, such local background subtraction was thought to be ideal in previous work, but was not possible due to the small coverage of the sky.

For the composite cluster LF, we only used galaxies within 0.75 Mpc of the cluster centroid. This radius was determined empirically so as not to lose statistics by using a too small radius, and not to lose the contrast of clusters against the background by using a too large radius. Foreground and background contamination were corrected for using an annulus around each cluster with an inner radius of 1.5 Mpc and an outer radius of 1.68 Mpc. These radii represent a compromise between having as large an aperture as possible to avoid removing legitimate cluster galaxies, while still providing an accurate estimate of the local projected field population. Since the background/foreground galaxies are themselves highly clustered, it is important to obtain as local an estimate as possible. The photometric redshift of each cluster was used to convert these metric apertures into angular apertures. The center of each cluster was taken from the CE catalog, and estimated from the position of the peak in the enhanced density map of Goto et al. (2002a; Chapter 3). The cluster centroids were expected to be determined with an accuracy better than ~ 40 arcsec through Monte-Carlo simulation. When an annulus touches the boundary of the SDSS data, we corrected for contamination using the number-magnitude relationship of the whole data set instead (this only affected a few of the clusters used here).

Since each sample cluster has a different redshift, each cluster reaches the SDSS apparent magnitude limit at different absolute magnitudes. Also, because they have various richnesses, the number of galaxies in each cluster is different. To take these different degrees of completeness into account, we followed the methodology of Colless (1989) to construct the composite cluster LF. The individual cluster LFs are weighted according to the cluster richness and the number of clusters which contribute to a given bin. This is written as

$$N_{cj} = \frac{m_j}{N_{c0}} \sum_i \frac{N_{ij}}{N_{i0}}, \quad (4.1)$$

where N_{cj} is the number of galaxies in the j th bin of the composite LF, N_{ij} is the number in the j th bin of the i th cluster LF, N_{i0} is the normalization of the i th cluster LF, and was measured to be the field-corrected number of galaxies brighter than $M_{r^*} = -18$, m_j

is the number of clusters contributing the j th bin and, finally, $N_{c0} = \sum_i N_{i0}$. The formal errors on the composite LF were computed using

$$\delta N_{cj} = \frac{N_{c0}}{m_j} \left[\sum_i \left(\frac{\delta N_{ij}}{N_{i0}} \right)^2 \right]^{1/2}, \quad (4.2)$$

where δN_{cj} and δN_{ij} are the errors on the j th bin for the composite and i th cluster, respectively. In this way we can take into account the different degrees of completeness.

Like other authors, we discarded the brightest cluster galaxy (BCG) within 0.75 Mpc of the cluster centroid when constructing the composite LF, since such BCGs tend not to follow the cluster LF. We only used SDSS galaxies brighter than $r^*=21.0$, since this is the limit of the SDSS star–galaxy separation (Scranton et al. 2002; Lupton et al. 2001). This magnitude limit and weighting scheme combined with our cosmology enabled us to dig LF down to $M_{r^*}=-17.5$. When converting apparent to absolute magnitudes, we assumed a k -correction for the early-type galaxy given by Fukugita et al. (1995).

In Figure 4.1, we show the composite LF of the 204 CE clusters discussed above. We present one composite LF for each of the five SDSS passbands. We also present in Table 4.1 the best-fit parameters from a fit of a Schechter function to these data. For a comparison, we also show the field values as derived by Blanton et al. (2001; corrected for $h_0 = 0.7$). In Figure 4.1, field LFs normalized to cluster LFs are shown by dotted lines. As expected, the M^* for our cluster LFs is significantly brighter (by 1 – 1.5 magnitudes depending on the bands) than those seen for the field LFs in all five bands. Furthermore, the faint end slopes (α) of the cluster composite LFs are much flatter than those seen for the field LFs. This is especially noticeable for the redder passbands (i and z) while the slope of the cluster LF systematically flattens from the u passband to the z passband.

These results are consistent with the hypothesis that the cluster LF has two distinct underlying populations, i.e., the bright end of the LF is dominated by bright early types that follow a Gaussian-like luminosity distribution, while the faint-end of the cluster LF is a steep power-law-like function dominated by star-forming (bluer) galaxies. Binggeli et al. (1988) originally suggested this hypothesis, and the recent work of Adami et al. (2000), Rakos et al. (2000) and Dressler et al. (1999) supported this idea. Particularly, Boyce et al. (2001) showed LF of Abell 868 is made up of three different populations of galaxies; luminous red and two fainter blue populations. The idea is illustrated by the fact that the cluster LFs in the redder passbands, which are presumably dominated by the old stellar populations of the early types, have much brighter M^* 's and significantly shallower slopes than those measured in the bluer passbands. Those results can also be interpreted as showing that bright elliptical galaxies are more populated in dense regions, like inside of clusters. The results are consistent with the morphology-density relation advocated by Dressler et al. (1980, 1997).

4.3.2 The Composite Cluster LF as a Function of Morphology

One of the key aspects of the SDSS photometric data is the opportunity to statistically study the distribution of galaxies as a function of their morphology. In this subsection, we discuss the composite cluster LF as a function of morphology using three complementary methods for determining the morphological type of each galaxy. These include: i) the best-fit de Vaucouleur or exponential model profile; ii) the inverse of concentration index and iii) the $u - r$ color of the galaxies. We present all three methods, since at present it is unclear which method is the most successful in separating the different morphological galaxy types. Also, each method suffers from different levels of contamination, and the differences in the methods can be used to gauge the possible systematic uncertainties in the morphological classifications. We discuss the three methods used in detail below.

The first method we consider here uses the de Vaucouleur and exponential model fits of the galaxy light profiles measured by the SDSS photometric pipeline (*PHOTO* R.H. Lupton et al., in preparation) to broadly separate galaxies into the late and early-type. If the likelihood of a de Vaucouleur model fit to the data is higher than that of an exponential model fit, the galaxy is called a late-type, and vice versa. Galaxies that have the same likelihoods for both model fits are discarded. In Figure 4.2, we present the composite cluster LF of late-type and early-type galaxies (as defined using the model fits above) for all five SDSS passbands. In Table 4.2, we present the best-fit Schechter function parameters to these data, and show the fits in Figure 4.2.

The second method uses the inverse of the concentration index, which is defined as $C = r_{50}/r_{90}$, where r_{50} is the radius that contains 50% of the Petrosian flux and r_{90} is the radius that contains 90% of the Petrosian flux (see R.H. Lupton et al., in preparation; Stoughton et al. 2002). Both of these parameters are measured by the SDSS PHOTO analysis pipeline for each galaxy. The concentration parameter used here (C) is just the inverse of the commonly used concentration parameter, and thus early-type galaxies have a lower C parameter than late-type galaxies. The correlation of C with visually-classified morphologies has been studied in detail by Shimasaku et al. (2001) and Strateva et al. (2001). They found that galaxies with $C < 0.4$ are regarded as early-type galaxies, while galaxies with $C \geq 0.4$ are regarded as late-type galaxies. Therefore, in Figure 4.3, we show the composite cluster LF of late-type and early-type galaxies as defined using this second method for all five SDSS passbands. In Table 4.3, we present the best-fit Schechter function parameters to these data.

The third method used here for morphological classification was to use the observed $u - r$ color of the galaxy which has been proposed by Strateva et al. (2001). Using the fact that k -correction for $u - r$ is almost constant until $z = 0.4$, they showed that galaxies show a clear bimodal distribution in their $u - r$ color and $u - r = 2.2$ serves as a good classifier of morphology until $z \sim 0.4$ by correlating $u - r$ classification with visual

classifications. Therefore, we have classified galaxies with $u - r < 2.2$ as early-type and galaxies with $u - r \geq 2.2$ as late-type. Figure 4.4 shows the composite cluster LF for both types of galaxies along with their best-fit Schechter functions (in all five passbands). The best-fit Schechter parameters are summarized in Table 4.4.

As expected, there are noticeable differences between early-type and late-type galaxies in these three morphological classifications, as portrayed by the differences in their composite LFs (see Figures. 4.2, 4.3, and 4.4). However, it is worth stressing here the similarities between the methods. For example, the faint end slope of the LF is always shallower for early-type galaxies than late-type, regardless of the passband and methodology. Also, the faint end slope for early-type galaxies decreases steadily toward the redder passbands, while the faint-end slope for the late-type galaxies is nearly always above -1 and consistent with (or steeper than) the field LF in most passbands. These observations are again qualitatively in agreement with the hypothesis that the bright end of the cluster LF is dominated by bright, old early-types, while the faint-end of the cluster LF represents late-type galaxies maybe in greater numbers than the average field. This model is in agreement with hierarchical models of structure formation and the model for the tidal disruption of dwarf galaxies by the dominant early types.

4.4 Discussion

In this section, we discuss various tests which we have performed on our measurement and results.

4.4.1 Monte-Carlo Simulations

To test the robustness of our methods, we performed Monte-Carlo simulations which involved adding artificial clusters to the SDSS data and computing their composite LF using the same algorithms and software as used on the real data. Our model for the artificial clusters was constructed using the SDSS data on Abell 1577 (at $z \sim 0.14$, richness ~ 1). We used the method described in Goto et al. (2002a; Chapter 3) to make artificial clusters. The radial profile for the artificial clusters was taken to be a King profile (Ichikawa 1986) with a concentration index of 1.5 and a cut-off radius of 1.4 Mpc, which is the size of Abell 1577 (Struble & Rood 1987). The color-magnitude distributions for the artificial clusters were set to be the observed, field-corrected, color-magnitude distributions of Abell 1577 binned into 0.2 magnitude bins in both color and magnitude. From this model, we then constructed artificial clusters as a function of the redshift and richness. For redshift, we created clusters at $z = 0.2, 0.3, 0.4$ and 0.5 , ensuring that we properly accounted for the cosmological effects; i.e., the clusters became smaller, redder

and dimmer with redshift. We used the k -corrections for an early type spectrum. For richness, we change the number of galaxies within each cluster randomly between 10 and 50. For each redshift, we created 100 clusters (400 clusters in total). The galaxies within these artificial clusters were distributed randomly in accordance with the radial and color-magnitude distributions discussed above. We made no attempt to simulate the density-morphology relation nor the luminosity segregation in clusters.

The artificial clusters were randomly distributed within the real SDSS imaging data and we constructed a composite LF for these clusters using exactly the same software as for the real clusters. Since the artificial clusters were all made from the same luminosity distribution, the composite LF should therefore look very similar in shape as the original input LF. Figure 4.5 shows the result of our Monte-Carlo simulations. The histogram shows the original absolute magnitude distribution of Abell 1577 after a field correction, while the symbols show the composite luminosity functions which we constructed as a function of the input redshift. The composite LFs, indeed, lie on top of the original input LF, suggesting that our code can successfully recover the input LF from the data through fore/background subtraction at any redshift.

4.4.2 Check of Photometric Redshifts

One of the most innovative parts of this analysis is the use of photometric redshifts to determine the composite luminosity function of clusters. As demonstrated in Goto et al. (2002a; Chapter 3), the accuracy of photometric redshift is excellent ($\delta z = \pm 0.015$ for $z < 0.3$) and this method will certainly be used in the near future as the number of clusters with photometric redshifts will increase rapidly, far quicker than the number of clusters with spectroscopically confirmed redshifts.

To justify our use of photometric redshifts, since all previous composite cluster LF's used spectroscopic redshifts, we constructed a composite LF using only the clusters with spectroscopically confirmed redshifts. We derived our spectroscopic redshift for CE clusters by matching the SDSS spectroscopic galaxy data with our CE clusters. This was achieved by searching the SDSS spectroscopic galaxy sample for any galaxies within the CE cluster radius and within $\delta z = \pm 0.01$ of the photometric redshift of the cluster. The radius used here was from Goto et al. (2002a; Chapter 3). If multiple galaxies satisfied this criteria, the closest spectroscopic redshift to the photometric redshift was adopted. The number of clusters with spectroscopic redshifts was 75 out of 204 at the date of this writing.

The results of this test are shown in Figure 4.1 (in the bottom right-hand panel). Also the parameters for the best-fit Schechter functions are given in Table 4.1. and referred to as $r^*(\text{spec})$. We only performed this test for the r passband. The slope and characteristic

magnitude of the best-fit Schechter function for the spectroscopically determined LF is in good agreement with that derived using photometric redshifts. As can be seen in Table 4.1, both M_r^* and the slope agree within the error. This test shows that we can truly construct composite LFs using photometric redshift of clusters.

4.4.3 Test of Cluster Centroids

One key aspect of measuring the composite cluster LF is the choice of the cluster centroid. To test the effect of different cluster centroids on the composite LF, we constructed a composite cluster LF using the position of brightest cluster galaxies (BCGs) as a centroid instead of the peak in the enhanced density map, as discussed in Goto et al. (2002a; Chapter 3). The BCGs have been determined to be the brightest galaxy among galaxies whose absolute magnitudes computed with the cluster redshift are fainter than -24 th magnitude within 0.75 Mpc from the cluster center. Galaxies brighter than -24 th magnitude are regarded as being foreground galaxies. The mean offset between the BCG position and the centroid previously used is 1.02 arcmin. Table 4.5 lists the parameters of the best-fit Schechter functions to the five SDSS passbands, which should be compared to the values obtained using the optical centroid given in Table 4.1. In all five bands, the characteristic magnitudes and slopes agree very well within the error. This test shows that our composite LFs are not dependent on the method of center determination.

4.4.4 Test of Background Subtraction

Since we constructed composite LFs from 2-dimensional projected sky image, subtraction of fore/background galaxies played an important role in this work. We test here the effect of making a global background subtraction for all clusters instead of the local background subtraction discussed above. We use the number-magnitude relation of all the galaxies in the entire 150 deg^2 region as the global background. Table 4.6 gives the best-fit Schechter parameters of composite LFs constructed using global background subtraction. Compared with Table 4.1, again, every Schechter parameter agrees very well within 1σ . Although we use annuli around clusters to subtract the background to avoid the large-scale structure disturbing the measurement of composite LFs, this test shows that our composite LFs are not dependent on background subtraction. Valotto et al. (2001) showed that a statistical background subtraction can not re-produce composite LFs using a mock galaxy catalog constructed from a large N -body simulation. Our result, however, combined with the fact that we derived the same LF as input through a Monte-Carlos simulation (in subsection 4.4.1), supports that our composite LFs are not subject to background subtraction.

4.4.5 Test of Cluster Richness

Another aspect we are concerned about is our choice of cluster richness criteria. To test this, we construct composite LFs of different subsample with $N_{-18} > 20$ and $N_{-18} > 40$, given in Table 4.7. N_{-18} here is defined as the number of galaxies brighter than -18 th magnitude after subtracting the background in the way we construct composite LFs. $N_{-18} > 20$ is used to construct composite LFs, as mentioned in section 4.3. In Table 4.7, even though M^* is slightly brighter and the slope is slightly steeper for the richer sample, they agree within 1σ . The steepening of the slopes can be interpreted as a bias in selecting richer systems using N_{-18} , i.e., clusters with steeper tails tend to have a larger value of N_{-18} . This, however, confirms that our composite LFs are not dependent on the richness criteria we chose.

4.4.6 Comparison with Other LFs

As the final test of our composite cluster LF, we compare our composite LFs with previous work. First, we must be careful to match the different cosmologies used by various authors as well as the different photometric passbands. To facilitate such a comparison, therefore, we present in Table 4.8 the best-fit Schechter function parameters for our composite LF, but calculated for each author's cosmology and passband using the color corrections of Fukugita et al. (1995) and Lumsden et al. (1992).

In the case of the three b_j photographic surveys of Colless (1989), Valotto et al. (1997), and Lumsden et al. (1997), we find a significantly brighter M^* than these studies as well as a much shallower slope. We also tried to fit a Schechter function using their α value for the slope, but M^* 's become even brighter. The fits are not good when fixed α 's are used.

Lugger (1989) found $M_R = -22.81 \pm 0.13$ and $\alpha = -1.21 \pm 0.09$ by re-analyzing nine clusters presented in Lugger (1986). The slope is steeper and M^* is slightly brighter than our results. When we fix the slope with her value at $\alpha = -1.21$, the two LFs agree well.

Garilli et al. (1999) studied 65 Abell and X-ray selected samples of galaxies in the magnitude range of $-23.0 < M_r < -17.5$ and found that $M_r^* = -22.16 \pm 0.15$ and $\alpha = -0.95 \pm 0.07$ (in isophotal magnitudes). This slope is steeper than ours. A possible difference with ours is that they used the color condition to select cluster galaxies. M^* is in agreement with our results within the error. We also tried to fit a Schechter function with a fixed value of $\alpha = 0.84$. M^* became brighter by 0.18 mag although the fit was poor.

Paolillo et al. (2001) studied composite LF of 39 Abell clusters using the digitized POSS-II plates. They obtained $M^* = -22.17 \pm 0.16$ in r . The slope is $\alpha = -1.11^{+0.07}_{-0.09}$. Although the slope differs significantly, M^* agrees well compared with our composite LF.

Yagi et al. (2002a,b) observed 10 nearby clusters with their Mosaic CCD camera

to derive composite LF. Their best-fit Schechter parameters are $M^* = -21.1 \pm 0.2$ and $\alpha = -1.49 \pm 0.05$ in R . They also studied type-specific LF using exponential and $r^{1/4}$ profile fits to classify the galaxy types. They derived $M^* = -21.1$ and $\alpha = -1.49$ for exponential galaxies and $M^* = -21.2$ and $\alpha = -1.08$ for $r^{1/4}$ galaxies. Considering that they derived composite LFs using the data taken with different instruments analyzed in a different way, it is reassuring that they reached the same conclusion as our results discussed in subsection 4.3.2, i.e., exponential galaxies have the steeper faint end tail than $r^{1/4}$ galaxies, while their M^* are almost the same.

Concerning the disagreement of our LFs with previous studies, various differences in measuring composite LFs may be the reason. The possible sources of differences are different ways of weighting, different ways of background subtraction, and different depths of the luminosity function. The sample clusters, themselves, should have, to some extent, different richness distributions. For M^* , although we tried to transform our magnitude into their magnitude, the color conversion between SDSS bands and others might not be accurate enough. Thus, the difference with the previous studies is not necessarily a mistake in the analysis, but rather it represents a different way of analysis. Throughout our analysis discussed in section 4.3 we carefully used exactly the same way to construct the various composite LFs. We thus keep our composite LFs internally consistent.

4.5 Summary

We studied the composite LF of the 204 SDSS CE galaxy clusters. The over-all composite LF is compared with other composite LFs. Comparing it to the field luminosity function, a tendency of a brighter M^* and a flatter slope is seen. This is consistent with our understanding that cluster regions are dominated by brighter galaxies than field galaxies. We divided the composite LF by galaxy morphology in three ways. In all three cases, we found that early-type galaxies have flatter slopes than late-type galaxies. These observations are in agreement with the hypothesis that the bright end of the cluster LF is dominated by bright, old early-types, while the faint-end of the cluster LF represents late-type galaxies. This is also consistent with the morphology-density relation originally advocated by Dressler (1980). We also studied these composite LFs in five SDSS color bands. The slopes become flatter and flatter toward the redder color bands. This again suggests that cluster regions are dominated by elliptical galaxies with old stellar population. These composite LFs provide a good low redshift benchmark to study higher-redshift clusters in the future. Since the data used in this work came from 2% of the SDSS data, further studies with large SDSS data will increase the statistical significance on these topics as the SDSS proceeds.

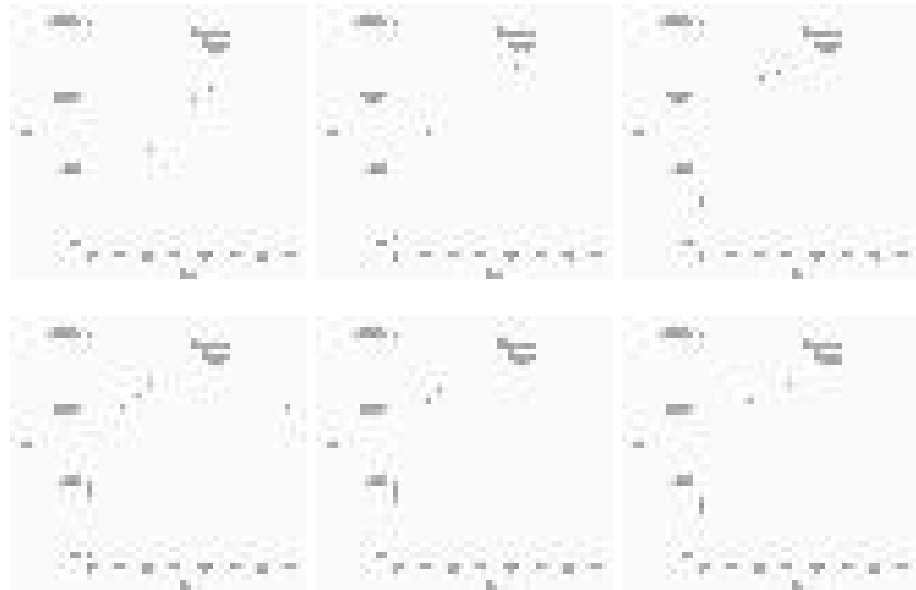


Figure 4.1: Composite LF of 204 galaxy clusters from the SDSS CE galaxy cluster catalog in five SDSS bands. The solid line is the best-fit Schechter functions. The y-axis is arbitrary. The dotted line is the field LFs from Blanton et al. (2001) re-scaled to our cosmology. The normalization of field LFs was adjusted to match the cluster best-fit Schechter functions. The lower-right panel is for 75 clusters with spectroscopic redshifts (see Section 4.4.2). The best-fit Schechter parameters are summarized in Table 4.1.

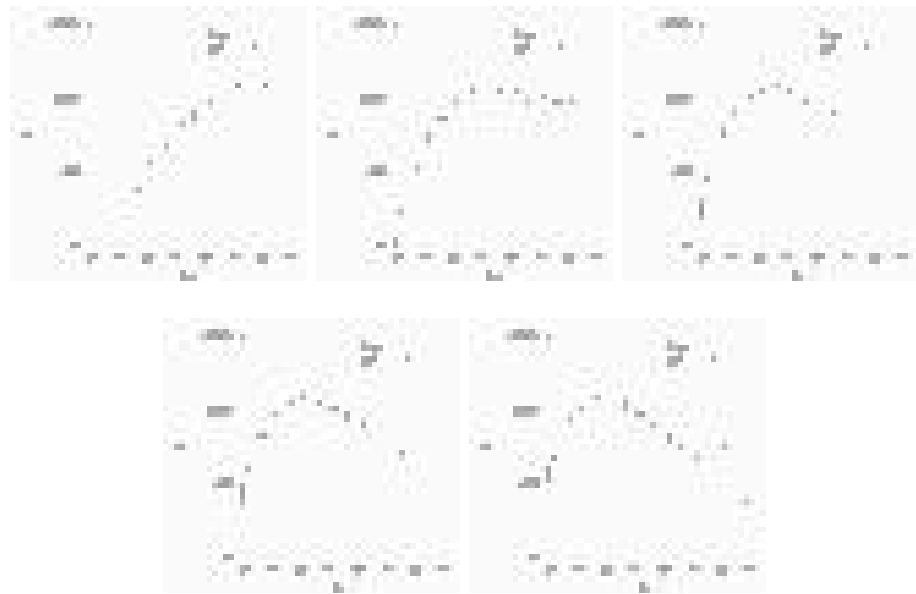


Figure 4.2: Composite luminosity functions of de Vaucouleur galaxies and exponential galaxies. The galaxies are divided into two subsamples using profile fitting. The lines show the best-fit Schechter functions (solid for de Vaucouleur galaxies, dotted for exponential galaxies). The y-axis is arbitrary. de Vaucouleur galaxies always have a brighter M^* and a flatter faint end tail. The best-fit Schechter parameters are summarized in Table 4.2.

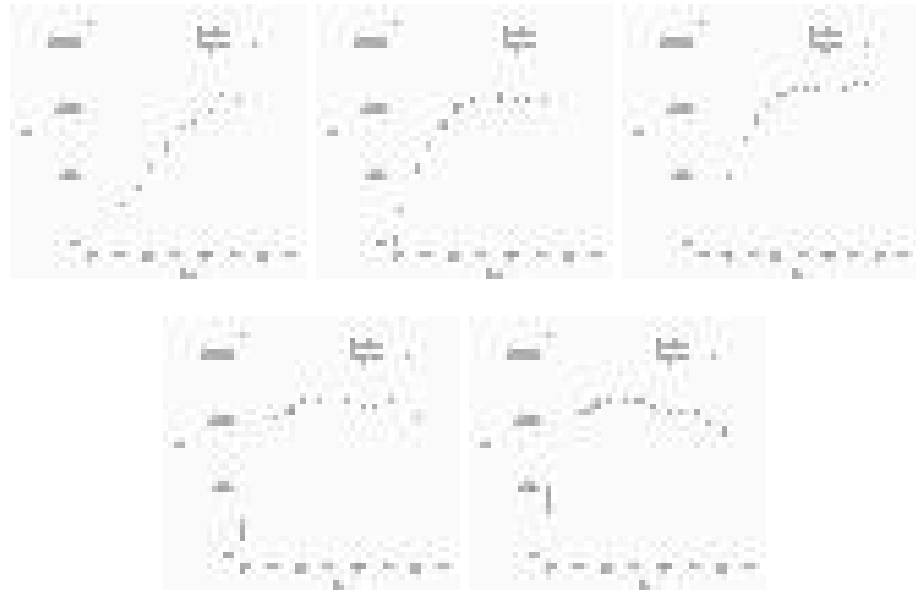


Figure 4.3: Composite luminosity functions of high-concentration and low-concentration galaxies. The concentration index (C) used here is the ratio of the 50% Petrosian flux radius to the 90% Petrosian flux radius. In this figure, early-type galaxies have $C < 0.4$, and late-type galaxies have $C \geq 0.4$. Early-type galaxies have flatter faint end tails in all five bands. Lines are the best-fit Schechter functions (solid for $C < 0.4$, dotted for $C \geq 0.4$). The y-axis is arbitrary. The best-fit Schechter parameters are summarized in Table 4.3.

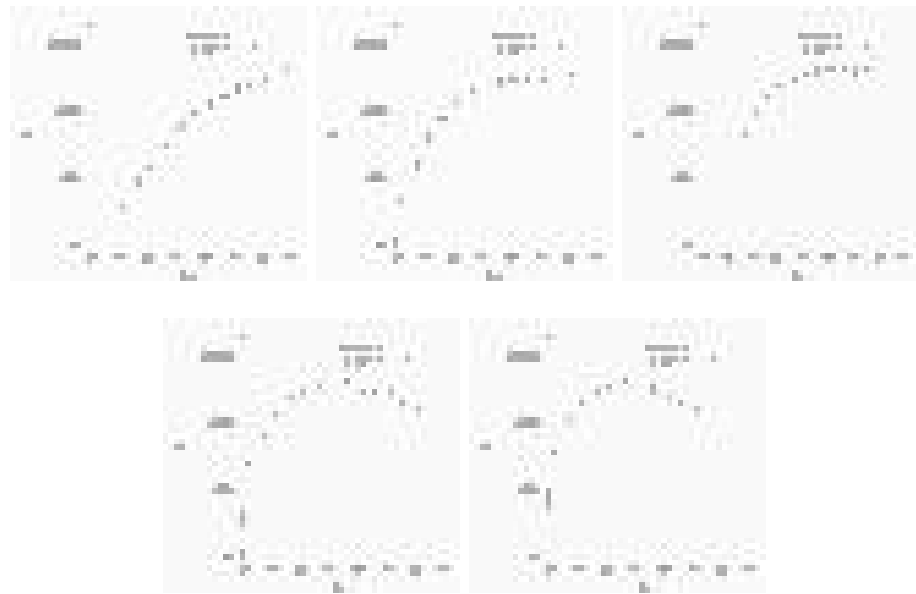


Figure 4.4: Composite luminosity functions of $u - r < 2.2$ (late-type) and $u - r \geq 2.2$ (early-type) galaxies. Early-type galaxies have flatter faint end tails in all five bands. The lines are the best-fit Schechter functions (solid for $u - r < 2.2$, dotted for $u - r \geq 2.2$). The y-axis is arbitrary. The best-fit Schechter parameters are summarized in Table 4.4.

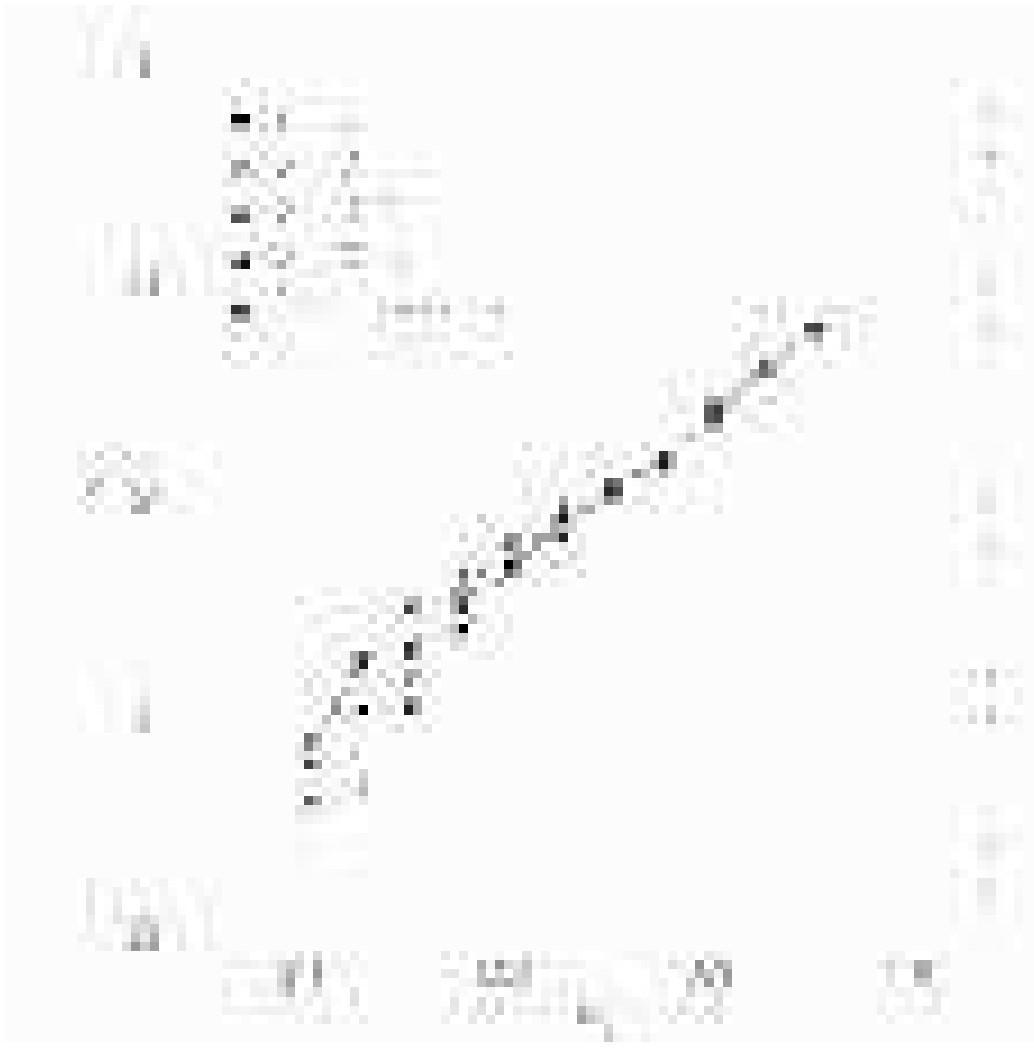


Figure 4.5: Results of a Monte-Carlo simulation to test the robustness of the weighting scheme. The histogram shows the luminosity function of model cluster A 1577. The circles, triangles, squares and pentagons represent the composite luminosity function at each redshift ($z = 0.2, 0.3, 0.4$ and 0.5 , respectively) constructed with 100 fake clusters at each redshift. The hexagonals show the composite luminosity function from all 400 fake clusters distributed on the real SDSS data.

Table 4.1: Best-fit Schechter parameters of the composite luminosity function of five SDSS bands. The field values are from Blanton et al. (2001), whose parameters were shifted to match our cosmology. Galaxies within 0.75 Mpc from the cluster center are used.

Band	M^*	α	Field M^*	Field α
u	-21.61 ± 0.26	-1.40 ± 0.11	-19.11 ± 0.08	-1.35 ± 0.09
g	-22.01 ± 0.11	-1.00 ± 0.06	-20.81 ± 0.04	-1.26 ± 0.05
r	-22.21 ± 0.05	-0.85 ± 0.03	-21.60 ± 0.03	-1.20 ± 0.03
i	-22.31 ± 0.08	-0.70 ± 0.05	-22.03 ± 0.04	-1.25 ± 0.04
z	-22.36 ± 0.06	-0.58 ± 0.04	-22.32 ± 0.05	-1.24 ± 0.05
$r(\text{spec})$	-22.31 ± 0.13	-0.88 ± 0.07

Table 4.2: Best-fit Schechter parameters for de Vaucouleur and exponential galaxies in five SDSS bands. The galaxies are divided into two subsamples using profile fitting. Galaxies within 0.75 Mpc from the cluster center are used.

Band	M^* (deV)	α (deV)	$M^*(\text{exp})$	α (exp)
u	-21.64 ± 0.30	-1.41 ± 0.12	-21.45 ± 0.13	-1.27 ± 0.07
g	-21.92 ± 0.11	-0.73 ± 0.07	-21.89 ± 0.13	-1.20 ± 0.06
r	-22.01 ± 0.07	-0.37 ± 0.06	-21.73 ± 0.12	-1.04 ± 0.06
i	-22.13 ± 0.07	-0.25 ± 0.06	-21.69 ± 0.13	-0.80 ± 0.08
z	-22.24 ± 0.06	$+0.12 \pm 0.06$	-21.76 ± 0.11	-0.65 ± 0.07

Table 4.3: Best-fit Schechter parameters for low concentration (early-type) and high concentration (late-type) galaxies in five SDSS bands. The concentration index here is the ratio of 50% Petrosian flux radius to 90% Petrosian flux radius. Early-type galaxies have a concentration of <0.4 , and late-type galaxies have a concentration of ≥ 0.4 . Galaxies within 0.75 Mpc from the cluster center are used.

Band	M^* (Early)	α (Early)	M^* (Late)	α (Late)
u	-21.42 ± 0.24	-1.28 ± 0.12	-21.82 ± 0.11	-1.42 ± 0.06
g	-22.05 ± 0.11	-0.89 ± 0.07	-22.26 ± 0.11	-1.36 ± 0.05
r	-22.31 ± 0.06	-0.92 ± 0.04	-22.24 ± 0.12	-1.32 ± 0.06
i	-21.97 ± 0.09	-0.59 ± 0.10	-22.02 ± 0.13	-1.04 ± 0.08
z	-22.08 ± 0.09	-0.47 ± 0.09	-22.09 ± 0.12	-0.87 ± 0.07

Table 4.4: Best-fit Schechter parameters for $u - r > 2.2$ (early type) and $u - r \leq 2.2$ (late type) galaxies in five SDSS bands. Galaxies within 0.75 Mpc are used.

Band	M^* (Early)	α (Early)	M^* (Late)	α (Late)
u	-21.65 ± 0.26	-1.47 ± 0.11	-21.78 ± 0.13	-1.37 ± 0.07
g	-22.04 ± 0.10	-1.03 ± 0.06	-22.30 ± 0.09	-1.38 ± 0.05
r	-22.29 ± 0.04	-0.97 ± 0.02	-22.22 ± 0.12	-1.41 ± 0.06
i	-21.91 ± 0.08	-0.58 ± 0.07	-22.17 ± 0.16	-1.23 ± 0.08
z	-21.93 ± 0.07	-0.36 ± 0.08	-22.14 ± 0.19	-1.08 ± 0.09

Table 4.5: Best-fit Schechter parameters for galaxies using positions of brightest cluster galaxies as a center in five SDSS bands. The mean deviation from the CE center is 1.02 arcmin.

Band	M^*	α
u	-21.84 ± 0.16	-1.43 ± 0.07
g	-22.16 ± 0.15	-1.05 ± 0.07
r	-22.29 ± 0.05	-0.91 ± 0.03
i	-22.31 ± 0.06	-0.73 ± 0.03
z	-22.18 ± 0.07	-0.55 ± 0.07

Table 4.6: Best-fit Schechter parameters for galaxies using global background subtraction in five SDSS bands. Instead of the annuli around the cluster, the global background was used to subtract the background galaxies to see the dependence on the background subtraction.

Band	M^*	α
u	-21.77 ± 0.17	-1.47 ± 0.07
g	-22.01 ± 0.12	-1.06 ± 0.07
r	-22.20 ± 0.05	-0.90 ± 0.03
i	-22.24 ± 0.07	-0.72 ± 0.04
z	-22.10 ± 0.06	-0.50 ± 0.06

Table 4.7: Best-fit Schechter parameters in the r band for galaxies using richer systems. The best-fit Schechter parameters for $N_{-18} > 20$ and $N_{-18} > 40$ subsamples are shown. N_{-18} is defined as the number of galaxies brighter than -18 th magnitude after subtracting the background.

Band	M^*	α	$N(\text{cluster})$
$N_{-18} > 20$	-22.21 ± 0.05	-0.85 ± 0.03	204
$N_{-18} > 40$	-22.29 ± 0.06	-0.90 ± 0.04	120

Table 4.8: Comparison with previous studies on the composite luminosity function. The CE composite LFs (this work) was re-calculated using each author's cosmology. The magnitude was transformed using data from Fukugita et al. (1995) and Lumsden et al. (1992).

Paper	M^*	α	Band	Ncluster	Cosmology
CE	-22.21 ± 0.05	-0.85 ± 0.03	r	204	$\Omega_M = 0.3 \quad \Omega_\Lambda = 0.7 \quad H_0 = 70$
Colless 89	-20.04	-1.21	bj	14 rich	$H_0 = 100 \quad q_0 = 1$
(CE)	-21.58 ± 0.12	-0.93 ± 0.06	bj	204	$H_0 = 100 \quad q_0 = 1$
(CE)	-22.20 ± 0.12	-1.21 fixed	bj	204	$H_0 = 100 \quad q_0 = 1$
Lugger 89	-22.81 ± 0.13	-1.21 ± 0.09	R (PDS)	9	$H_0 = 50$
(CE)	-22.49 ± 0.06	-0.69 ± 0.05	R (PDS)	204	$H_0 = 50 \quad q_0 = 0.5$
(CE)	-22.77 ± 0.17	-1.21 fixed	R (PDS)	204	$H_0 = 50 \quad q_0 = 0.5$
Valotto 97	-20.0 ± 0.1	-1.4 ± 0.1	bj	55 Abell APM	$H_0 = 100$
(CE)	-21.58 ± 0.12	-0.93 ± 0.06	bj	204	$H_0 = 100 \quad q_0 = 1$
(CE)	-22.69 ± 0.23	-1.4 fixed	bj	204	$H_0 = 100 \quad q_0 = 1$
Lumsden 97	-20.16 ± 0.02	-1.22 ± 0.04	bj	22 rich	$H_0 = 100 \quad q_0 = 1$
(CE)	-21.58 ± 0.12	-0.93 ± 0.06	bj	204	$H_0 = 100 \quad q_0 = 1$
(CE)	-22.22 ± 0.10	-1.22 fixed	bj	204	$H_0 = 100 \quad q_0 = 1$
Garilli 99	-22.16 ± 0.15	-0.95 ± 0.07	r (CCD)	65 Abell X-ray	$H_0 = 50 \quad q_0 = 0.5$
(CE)	-22.15 ± 0.06	-0.69 ± 0.05	r (CCD)	204	$H_0 = 50 \quad q_0 = 0.5$
(CE)	-22.28 ± 0.05	-0.84 fixed	r (CCD)	204	$H_0 = 50 \quad q_0 = 0.5$
Paolillo 00	-22.26 ± 0.16	-1.11	r (POSSII)	39 Abell	$H_0 = 50 \quad q_0 = 0.5$
(CE)	-22.15 ± 0.06	-0.69 ± 0.05	r (POSSII)	204	$H_0 = 50 \quad q_0 = 0.5$
(CE)	-22.55 ± 0.12	-1.11 fixed	r (POSSII)	204	$H_0 = 50 \quad q_0 = 0.5$
Yagi 02	-21.3 ± 0.2	-1.31 ± 0.05	R_C	10 Abell	$H_0 = 100 \quad q_0 = 0.5$
(CE)	-21.89 ± 0.10	-1.03 ± 0.05	R_C	204	$H_0 = 100 \quad q_0 = 0.5$
(CE)	-22.55 ± 0.14	-1.31 fixed	R_C	204	$H_0 = 100 \quad q_0 = 0.5$

Chapter 5

The Morphological Butcher-Oemler Effect

5.1 Introduction

The Butcher-Oemler effect was first reported by Butcher & Oemler (1978, 1984) as an increase in the fraction of blue galaxies (f_b) toward higher redshift in 33 galaxy clusters over the redshift range $0 < z < 0.54$. Butcher and Oemler's work made a strong impact since it showed direct evidence for the evolution of cluster galaxies. Much work regarding the nature of these blue galaxies followed. Rakos & Schombert (1995) found that the fraction of blue galaxies increases from 20% at $z = 0.4$ to 80% at $z = 0.9$, suggesting that the evolution in clusters is even stronger than previously thought. Margoniner & De Carvalho (2000) studied 48 clusters in the redshift range of $0.03 < z < 0.38$ and detected a strong Butcher-Oemler effect consistent with that of Rakos & Schombert (1995). Despite the trend with redshift, almost all previous work has reported a wide range of blue fraction values at a fixed redshift. In particular, in a large sample of 295 Abell clusters, Margoniner et al. (2001) not only confirmed the existence of the Butcher-Oemler effect, but also found that the blue fraction depends on cluster richness.

Although the detection of the Butcher-Oemler effect has been claimed in various studies, there have been some suggestions of strong selection biases in the cluster samples. Newberry, Kirshner & Boroson (1988) measured velocity dispersions and surface densities of galaxies in clusters and found a marked difference between local clusters and intermediate redshift clusters. More recently, Andreon & Ettori (1999) measured X-ray surface brightness profiles, sizes, and luminosities of the Butcher-Oemler sample of clusters and concluded that the sample is not uniform. The selection bias, thus, could mimic evolutionary effects. Smail et al. (1998) used 10 X-ray bright clusters in the redshift range of $0.22 \leq z \leq 0.28$ and found that the clusters have only a small fraction of blue galaxies.

The Butcher-Oemler effect was not observed with their sample. Similarly, galaxies in radio selected groups are not significantly bluer at higher redshifts (Allington-Smith et al. 1993). Garilli et al. (1996) observed 67 Abell and X-ray selected clusters and found no detectable Butcher-Oemler effect at $z < 0.2$. Fairley et al. (2002) studied eight X-ray selected galaxy clusters and found no correlation of blue fraction with redshift. Rakos & Schombert (1995)'s sample was selected from the catalog compiled by Gunn, Hoessel & Oke (1986) using photographic plates taken only in two color bands. The sample thus have a possible bias against red, high redshift clusters. In addition to the possible sample selection biases, with the exception of Margoniner et al. (2001), the number of clusters in the previous works was small, consisting of a few to dozens of clusters. Therefore the statistical uncertainty was large. Many authors also noted that cluster-to-cluster variation of the fraction of blue galaxies is considerable. The need for a larger, more uniform sample of clusters has been evident.

There have been various attempts to find another physical mechanism causing the large scatter which has been seen in almost all previous work. Wang & Ulmer (1997) claimed the existence of a correlation between the blue fraction and the ellipticity of the cluster X-ray emissions in their sample of clusters at $0.15 \leq z \leq 0.6$. Metevier, Romer & Ulmer (2000) showed that two clusters with a bimodal X-ray surface brightness profile have an unusually high blue fraction value and thus do not follow the typical Butcher-Oemler relation. They claimed that the Butcher-Oemler effect is an environmental phenomenon as well as an evolutionary phenomenon. Margoniner et al. (2001) found a richness dependence in the sense that richer clusters have smaller blue fractions. They claimed that this richness dependence causes a large scatter in the blue fraction–redshift diagram. Therefore, it is of extreme interest to explore an origin of the scatter in the blue fraction despite the redshift trend.

At the same time, various studies using morphological information have reported a similar evolutionary effect in cluster galaxies. Dressler et al. (1997) studied 10 clusters at $0.37 < z < 0.56$ and found a steep increase in the S0 fraction toward *lower* redshift, compared to nearby clusters studied earlier (Dressler 1980). Couch et al. (1994, 1998) studied three clusters at $z = 0.31$ and found their S0 fraction to be consistent with the trend observed by Dressler et al. (1997). Fasano et al. (2000) observed nine clusters at intermediate redshifts ($0.09 < z < 0.26$) and also found an increase in the S0 fraction toward lower redshift. It has been proposed that the increase in the S0 fraction is caused by the transformation of spiral galaxies into S0 galaxies through a process yet unknown. These studies, however, need to be pursued further, considering that most of the previous work was based on morphological galaxy classification by eye. Although it is an excellent tool to classify galaxies, manual classification could potentially have unknown biases. (A detailed comparison of human classifiers can be found in Lahav et al. 1995). A machine

based, automated classification would better control biases and would allow a reliable determination of the completeness and false positive rate. A further reason to investigate the evolution of cluster galaxies is the sample size. The morphological fraction studies of clusters reported so far are based on only dozens of clusters. Furthermore, the clusters themselves have intrinsic variety in the fraction of blue/spiral galaxies as reported by various Butcher-Oemler and morphological analyses listed above. Since several authors have suggested that the fraction of blue galaxies depends on cluster richness, it is important to use a uniform cluster sample, preferably selected by an automated method with a well known selection function.

Various theoretical models have been proposed to explain the Butcher-Oemler effect and the increase of the S0 fraction. These models include ram pressure stripping of gas (Spitzer & Baade 1951; Gunn & Gott 1972; Farouki & Shapiro 1980; Kent 1981; Abadi, Moore & Bower 1999; Fujita & Nagashima 1999; Quilis, Moore & Bower 2000), galaxy infall (Bothun & Dressler 1986; Abraham et al. 1996a; Ellingson et al. 2001), galaxy harassment (Moore et al. 1996, 1999), cluster tidal forces (Byrd & Valtonen 1990; Valluri 1993), enhanced star formation (Dressler & Gunn 1992), and removal and consumption of the gas (Larson, Tinsley & Caldwell 1980; Balogh et al. 2001; Bekki et al. 2002). It is, however, yet unknown exactly what processes play major roles in changing the color and morphology of cluster galaxies. To derive a clear picture explaining the evolution of cluster galaxies, it is important to clarify both the Butcher-Oemler effect and the S0 increase, using a large and uniform cluster sample in conjunction with a machine based morphological classification.

With the advent of the Sloan Digital Sky Survey (SDSS; York et al. 2000), which is an imaging and spectroscopic survey of 10,000 deg² of the sky, we now have the opportunity to overcome these limitations. The SDSS Cut & Enhance galaxy cluster catalog (Goto et al. 2002a; Chapter 3) provides a large uniform cluster catalog with a well defined selection function. The CCD-based, accurate photometry of the SDSS (Fukugita et al. 1996; Hogg et al. 2002; Smith et al. 2002) and the wide coverage of the SDSS on the sky allow accurate estimation of blue fraction with robust local background subtraction. Although the SDSS is a ground based observation, the state-of-the-art reduction software and the accuracy of CCD data make it possible to derive morphological classification in an automated way (Lupton et al. 2001, 2002). By using the SDSS data set, we are able to study one of the largest samples to date — 514 clusters — to the depth of $M_{r^*} = -19.44$ ($h=0.75$).

The purpose of this chapter is as follows. We aim to confirm or disprove the existence of the Butcher-Oemler effect using one of the largest, most uniform cluster samples. At the same time, we hope to shed light on the morphological properties of the Butcher-Oemler galaxies using morphological parameters derived from the SDSS data. Finally we

investigate the origin of the scatter in the galaxy type fraction versus redshift relation, in hope of gaining some understanding about the physical processes responsible for the scatter.

Since it is known that field galaxies also evolve both morphologically (Schade et al. 1996; Brinchmann et al. 1998; Lilly et al. 1998; Kajisawa et al. 2001; Abraham et al. 2001) and spectroscopically (Madau et al. 1996; Lilly et al. 1996; Hammer et al. 1997; Treyer et al. 1998; Cowie et al. 1999; Sullivan et al. 2000; Wilson et al. 2002), it is of extreme importance to compare the evolution of cluster galaxies with that of field galaxies to specify a responsible physical mechanism. It is possible that the Butcher-Oemler effect and morphological transition of cluster galaxies are more commonly happening including the field region of the universe, thus a cluster specific mechanism is not responsible for the evolution of galaxies. However, since the SDSS spectroscopic data are not deep enough to probe cosmologically interesting time scale, we leave it to future work.

The Chapter is organized as follows: In Section 5.2, we describe the SDSS data and the Cut & Enhance cluster catalog. In Section 5.3, we analyze the late type fraction, both spectrally and morphologically. In Section 5.4, we discuss the possible caveats and underlying physical processes in the evolution of galaxies. In Section 5.5, we summarize our work and findings. The cosmological parameters adopted throughout this chapter are $H_0=75 \text{ km s}^{-1} \text{ Mpc}^{-1}$, and $(\Omega_m, \Omega_\Lambda, \Omega_k)=(0.3, 0.7, 0.0)$.

5.2 Data

The galaxy catalog used here is taken from the Sloan Digital Sky Survey (SDSS) Early Data Release (see Fukugita et al. 1996; Gunn et al. 1998; Lupton et al. 1999, 2001, 2002; York et al. 2000; Hogg et al. 2001; Pier et al. 2002; Stoughton et al. 2002 and Smith et al. 2002 for more detail of the SDSS data). We use equatorial scan data, a contiguous area of 250 deg^2 ($145.1 < \text{RA} < 236.0$, $-1.25 < \text{DEC} < +1.25$) and 150 deg^2 ($350.5 < \text{RA} < 56.51$, $-1.25 < \text{DEC} < +1.25$). The SDSS imaging survey observed the region to depths of 22.3, 23.3, 23.1, 22.3 and 20.8 in the u, g, r, i and z filters, respectively. (See Fukugita et al. 1996 for the SDSS filter system; Hogg et al. 2002 and Smith et al. 2002 for its calibration). Since the SDSS photometric system is not yet finalized, we refer to the SDSS photometry presented here as u^*, g^*, r^*, i^* and z^* . We correct the data for galactic extinction determined from the maps given by Schlegel, Finkbeiner & Davis (1998). We include galaxies to $r^*=21.5$ (Petrosian magnitude), which is the star/galaxy separation limit (studied in detail by Scranton et al. 2002) in the SDSS data.

The galaxy cluster catalog used here is a subset of the SDSS Cut & Enhance galaxy cluster catalog (Goto et al. 2002a; Chapter 3). There are 4638 clusters in the equatorial region (See Kim et al. 2003; Bahcall et al. 2003; Annis et al. in prep. and Miller et al. in

prep. for other works on the SDSS galaxy clusters). Besides the uniformity of the catalog with its well defined selection function, the catalog has very good photometric redshifts, $\delta z=0.015$ at $z < 0.3$, which enables us to use a large sample of clusters (Goto et al. 2002a; Chapter 3; see also Gal et al. 2000 and Annis et al. 2003 for photometric redshift methods for clusters). We use clusters in the redshift range of $0.02 \leq z \leq 0.3$ and galaxies brighter than $M_{r^*} = -19.44$, which corresponds to $r^* = 21.5$ at $z = 0.3$. Since several authors in previous work claimed that biases in sample cluster selection can mimic the evolutionary effect, it is important to control cluster richness well. We use clusters with more than 25 member galaxies between $M_{r^*} = -24.0$ and -19.44 within 0.7 Mpc from the cluster center after fore/background subtraction, as explained in the next Section. The large areal coverage of the SDSS data enables us to subtract the fore/background counts reliably. We can thus control the richness of the sample clusters well. The criteria leave 514 clusters in the region.

We stress the importance of the uniformity of the cluster catalog. Although the Abell cluster catalog (Abell 1958; Abell, Corwin and Olowin 1989) has been used in many studies, it was constructed by eye, and is sensitive to projection effects. When comparing clusters at different redshifts, it is particularly important to ensure that the data quality and cluster selection techniques are uniform, to avoid the introduction of potential selection biases. The SDSS Cut & Enhance cluster catalog used here is constructed using only the data taken with the SDSS telescope. Also, clusters are detected using a single algorithm (CE) throughout the entire redshift range ($0.02 \leq z \leq 0.3$). Combined with the well controlled richness criteria, our cluster sample is not only one of the biggest but also one of the most statistically uniform cluster catalogs. To study colors of galaxies in clusters, it is also important to use a cluster catalog created without targeting the red sequence of color magnitude relation of cluster galaxies. For example, Gladders & Yee(2000) and Annis et al. (2003) use a color filter targeting the red sequence of clusters and find galaxy clusters efficiently without suffering from projection effects. These techniques, however, can potentially have biases with regards to the colors of detected galaxy clusters, since clusters with a strong red sequence is more easily detected. They may not, therefore, be ideally suited to a Butcher-Oemler type of analysis. In contrast, the SDSS Cut & Enhance cluster catalog does not pick red galaxies selectively, and is therefore more suitable for this study. (Note that the the Cut & Enhance method does use generous color cuts. Therefore it is not completely free from color originated biases although the color cut is designed to be wide enough to include blue galaxies in clusters.) In previous work, clusters have often been detected using data from only one or two color bands. This can introduce a bias, since higher redshift clusters are redder and fainter than lower redshift clusters. The SDSS Cut & Enhance cluster catalog detects clusters using four bands of the SDSS data (g, r, i and z), which minimizes the bias against redshift.

5.3 Analysis and Results

We compute the fraction of late-type galaxies in four different ways using conventional blue fraction, $u - r$ color, profile fitting, and a concentration parameter.

5.3.1 Fore/Background subtraction

Before proceeding to the computation of the late-type fractions, we describe the statistical fore/background subtraction method we use in common to all the four ways. In counting galaxies, all galaxies are assumed to be at the cluster redshift to calculate absolute magnitudes. Then galaxies whose absolute magnitudes lie between $M_{r*} = -24.0$ and -19.44 are used in the analysis. We count the number of late-type/total galaxies within 0.7 Mpc from the center of each cluster. Valotto et al. (2001) claimed that the global background correction can not correct background contamination appropriately. Following the claim, we use a local background correction. The number of late-type/total galaxies in fore/background is estimated in the same absolute magnitude range using an annular area around each cluster with an inner radius of 2.1 Mpc and an outer radius of 2.21 Mpc. The annulus-based fore/background subtraction enables us to estimate the fore/background locally, minimizing variations in galaxy number counts due to the large scale structure. When an outer annulus touches the boundary of the region, a fore/background count is globally subtracted using galaxy number counts in the entire 400 deg² region by adjusting it to the angular area each cluster subtends. This fore/background subtraction is used in the analyses described in subsections 5.3.3-5.3.7. The fraction of blue/late-type galaxies, f_{late} , and its error, δf_{late} , are computed according to the following equations.

$$f_{late} = \frac{N_{c+f}^{late} - N_f^{late}}{N_{c+f}^{all} - N_f^{all}}, \quad (5.1)$$

$$\delta f_{late} = f_{late} \times \sqrt{\frac{N_{c+f}^{late} + N_f^{late}}{(N_{c+f}^{late} - N_f^{late})^2} + \frac{N_{c+f}^{all} + N_f^{all}}{(N_{c+f}^{all} - N_f^{all})^2} - \frac{2(\sqrt{N_f^{late} \times N_f^{all}} + \sqrt{N_{c+f}^{late} \times N_{c+f}^{all}})}{(N_{c+f}^{late} - N_f^{late})(N_{c+f}^{all} - N_f^{all})}} \quad (5.2)$$

where N_{c+f}^{late} and N_f^{late} represent numbers of blue/late-type galaxies in a cluster region and a field region, respectively. N_{c+f}^{all} and N_f^{all} represent numbers of all galaxies in a cluster region and a field region, respectively. The equation (5.2) assumes that N^{late} and N^{all} are not independent. We explain the derivation of equation (5.2) in Section 5.3.2.

5.3.2 Errors on Blue/Late Type Fractions

In this section we summarize how we derived eq. (5.2) to calculate errors on blue/late type fractions. To begin with, we assume the following.

- Number of galaxies in a cluster region (N_{c+f}^{all}) follows Poisson statistics.
- Number of galaxies in a certain area of field region (N_f^{all}) follows Poisson statistics.
- N_{c+f}^* and N_f^* are independent of each other.
- Number of blue/late type galaxies in a cluster region (N_{c+f}^{late}) is strongly correlated with number of all galaxies in that region (N_{c+f}^{all}).
- Number of blue/late type galaxies in a certain field region (N_f^{late}) is strongly correlated with number of all galaxies in that region (N_f^{all}).

And we clarify the definition of our notation. In this section, δA means a deviation of a sampled value from an expectation value, $E(A)$.

$\delta A = A - E(A)$, where A is each data value.

$E(A)$ and δA satisfy the following relations.

$E(\delta A) = 0$, $E(\delta A)^2 = \sigma^2$, and if A and B are independent, $E(\delta A \delta B) = 0$. Note that the equation 5.2 is not a deviation of a single sample but the expectation value estimated from the sample, and should be written as $E(\delta f_{late}^2)$ if we write rigidly.

Under these assumptions, the error of late type fraction, δf_{late} , become

$$\delta f_{late}^2 = (X/Y)^2 \times ((\delta X^2/X^2) + (\delta Y^2/Y^2) - 2(\delta X \delta Y/XY)), \quad (5.3)$$

where $X = N_{c+f}^{late} - N_f^{late}$, $Y = N_{c+f}^{all} - N_f^{all}$, and $f_{late} = X/Y$.

Since N_{c+f}^{all} and N_f^{all} follow Poisson statistics, and they are independent.

$$E(\delta Y^2) = N_{c+f}^{all} + N_f^{all} \quad (5.4)$$

Similarly, when N_{c+f}^{all} follows Poisson statistics, N_{c+f}^{late} also follows Poisson statistics since $N_{c+f}^{late} \sim N_{c+f}^{all} \times f_{late}$. Therefore,

$$E(\delta X^2) = N_{c+f}^{late} + N_f^{late}. \quad (5.5)$$

Deriving the cross term at the end of the equation is not so straightforward. The cross term is expanded as

$$\delta X \delta Y = \delta(N_{c+f}^{late} - N_f^{late}) \delta(N_{c+f}^{all} - N_f^{all}) \quad (5.6)$$

$$= (\delta(N_{c+f}^{late}) - \delta(N_f^{late})) (\delta(N_{c+f}^{all}) - \delta(N_f^{all})) \quad (5.7)$$

$$= \delta(N_{c+f}^{late}) \delta(N_{c+f}^{all}) - \delta(N_f^{late}) \delta(N_{c+f}^{all}) - \delta(N_{c+f}^{late}) \delta(N_f^{all}) + \delta(N_f^{late}) \delta(N_f^{all}) \quad (5.8)$$

Since we assume N_f^{late} and N_{c+f}^{all} , N_{c+f}^{all} and N_f^{late} are both independent,

$$E(-\delta(N_f^{late}) \delta(N_{c+f}^{all})) = 0 \quad (5.9)$$

and

$$E(-\delta(N_{c+f}^{late})\delta(N_f^{all})) = 0. \quad (5.10)$$

Therefore,

$$E(\delta X \delta Y) = E(\delta(N_{c+f}^{late})\delta(N_{c+f}^{all}) + \delta(N_f^{late})\delta(N_f^{all})) \quad (5.11)$$

Since we assume that N_{c+f}^{late} and N_{c+f}^{all} , or N_f^{late} and N_f^{all} strongly correlate, we can approximate that

$$E(\delta(N_{c+f}^{late})\delta(N_{c+f}^{all})) = \sigma(N_{c+f}^{late})\sigma(N_{c+f}^{all}) = \sqrt{N_{c+f}^{late}}\sqrt{N_{c+f}^{all}} \quad (5.12)$$

and,

$$E(\delta(N_f^{late})\delta(N_f^{all})) = \sigma(N_f^{late})\sigma(N_f^{all}) = \sqrt{N_f^{late}}\sqrt{N_f^{all}} \quad (5.13)$$

Therefore we obtain,

$$E(\delta X \delta Y) = \sqrt{N_{c+f}^{late}}\sqrt{N_{c+f}^{all}} + \sqrt{N_f^{late}}\sqrt{N_f^{all}} \quad (5.14)$$

By substituting eq. (5.14) for $\delta X \delta Y$ in eq. (5.3), we derive eq. (5.2).

However, this is not the only way to estimate the error. Actually, the correlation between N_f^{late} and N_f^{all} is not so obvious since late type fraction in the field and that in the cluster region might be different. Although we regard the difference is so small that we can assume the eq.(5.13), if we assume that N_f^{late} , $N_f^{early}(= N_f^{all} - N_f^{late})$, N_{c+f}^{late} , and $N_{c+f}^{early}(= N_{c+f}^{all} - N_{c+f}^{late})$ are independent, we derive,

$$E(\delta(N_{c+f}^{late})\delta(N_{c+f}^{all})) = E(\delta(N_{c+f}^{late})(\delta(N_{c+f}^{late}) + \delta(N_{c+f}^{early}))) = \sigma(N_{c+f}^{late})^2 = N_{c+f}^{late} \quad (5.15)$$

and,

$$\delta(N_f^{late})\delta(N_f^{all}) = \sigma(N_f^{late})^2 = N_f^{late}. \quad (5.16)$$

Then, the expectation value of $\delta X \delta Y$ becomes,

$$E(\delta X \delta Y) = N_{c+f}^{late} + N_f^{late} \quad (5.17)$$

In this case, eq. (5.2) becomes,

$$E(\delta f_{late}) = f_{late} \times \sqrt{\frac{N_{c+f}^{late} + N_f^{late}}{(N_{c+f}^{late} - N_f^{late})^2} + \frac{N_{c+f}^{all} + N_f^{all}}{(N_{c+f}^{all} - N_f^{all})^2} - \frac{2(N_{c+f}^{late} + N_f^{late})}{(N_{c+f}^{late} - N_f^{late})(N_{c+f}^{all} - N_f^{all})}} \quad (5.18)$$

5.3.3 Blue Fraction

The blue fraction of galaxy clusters (f_b) is measured as the fraction of galaxies bluer in $g - r$ rest frame color than the color of the ridge line of the cluster by 0.2 mag. This color criterion is equivalent to Butcher & Oemler's (1984) 0.2 mag in $B - V$ and Margoniner et al.'s (2000, 2001) 0.2 mag in $g - r$. The color of the ridge line is measured from the color-magnitude diagram using the same color-magnitude box used in measuring photometric redshift (Goto et al. 2002a; Chapter 3). The colors of the ridge lines are confirmed to agree with empirical color of elliptical galaxies observed in the SDSS at the same redshift with less than 0.05 difference in $g - r$ color (Eisenstein, private communication). We also use Fukugita et al.'s (1995) model of an elliptical galaxy and a galaxy bluer than it by 0.2 mag in $g - r$. By redshifting these two galaxies, we measure $\delta(g - r)$ in the observed frame, which corresponds to the restframe $\delta(g - r) = 0.2$. In calculating f_b , we count galaxies within 0.7 Mpc from the center of each cluster, which is the same radius as Margoniner et al. (2000, 2001), and corresponds to the average radius of Butcher & Oemler (1984). (We explore possible caveats in using fixed radius in Section 5.4.8.) Galaxies between $M_{r^*} = -24.0$ and $M_{r^*} = -19.44$ are counted. The latter value corresponds to $r^* = 21.5$ at $z = 0.3$ for an average k -correction of all types of galaxies (Fukugita et al. 1995). Compared to the field luminosity function of Blanton et al. (2001), this includes galaxies as faint as $M_r^* + 1.36$. Fore/background galaxies are statistically subtracted in the way described in Section 5.3.1.

The lower left panel of Figure 5.1 shows f_b as a function of redshift. The error in f_b is estimated using equation (5.2) and the median values of the errors in f_b and z are shown in the upper left corner of the plot. Dashed line shows the weighted least-squares fit to the data. Solid lines and stars show the median values of the data. The scatter is considerable, but both of the lines show a clear increase of f_b toward higher redshift. The Spearman's correlation coefficient is 0.238 with significance of more than 99.99% as shown in Table 5.1. The correlation is weak, but of high significance. The lower left panel of Figure 5.2 further clarifies the evolution effect. A dashed and a solid line show normalized distributions of f_b for clusters with $z \leq 0.15$ and $0.15 < z \leq 0.3$, respectively. The two distributions are significantly different at the 98% level, as determined by a Kolmogorov-Smirnov test. The slope shown with the dashed line in Figure 5.1 rises up to $f_b \sim 0.2$ at $z = 0.3$ (look back time of ~ 3.5 Gyr), which is consistent with previous work such as Butcher & Oemler (1978, 1984), Rakos & Schombert (1995), and Margoniner et al. (2000, 2001), within the scatter. We conclude that the Butcher-Oemler effect is seen in the SDSS Cut & Enhance galaxy cluster catalog.

We caution readers on the systematic uncertainties in measuring f_b . Marzke et al. (1994, 1997, 1998), Lin et al. (1999) and Blanton et al. (2001) showed that luminosity functions of galaxy clusters depend significantly on galaxy type, in such a way that the

bright end of the cluster luminosity function is dominated by redder galaxies and the faint end is dominated by bluer galaxies. Boyce et al.(2001) and Goto et al. (2002b; Chapter 4) showed that a similar tendency exists for cluster luminosity functions. This difference in luminosity functions leads to a different blue fraction depending on the absolute magnitude range used. Furthermore, if the radial distributions of blue and red galaxies are different (e.g., Kodama et al. 2001), the f_b measurement depends heavily on the radius. When comparing with previous work, therefore, it is important to take account of the exact method used to calculate f_b . We discuss the uncertainty in measuring blue fractions further in Section 5.4.

5.3.4 Late Type Fraction Using $u - r < 2.2$

Recently Shimasaku et al. (2001) and Strateva et al. (2001) showed that the SDSS $u - r$ color correlates well with galaxy morphologies. In this section we use $u - r$ color to separate early ($u - r \geq 2.2$) and late ($u - r < 2.2$) type galaxies as proposed by Strateva et al. (2001). Note that although $u - r$ color is claimed to correlate well with galaxy types, it is still a color classifier and thus different from the morphological parameters we investigate in the following two sections. The methodology used to measure late type fraction is similar to the one we use to measure f_b . We regard every galaxy with $u - r < 2.2$ as a late type galaxy. We define f_{u-r} as the ratio of the number of late type galaxies to the total number of galaxies within 0.7 Mpc from the cluster center. Fore/background subtraction is performed in a way described in Section 5.3.1.

The upper left panel of Figure 5.1 shows f_{u-r} as a function of redshift. The error in f_{u-r} is calculated using equation (5.2) and the median values of the errors in f_{u-r} and z are shown in the upper left corner of the panel. The dashed line shows the least square fit to the data. The solid lines and stars show the median values of the data. As in the case of f_b , the scatter is considerable, but the weak increase of the late type galaxies is seen. The Spearman's correlation coefficient is 0.234 and is inconsistent with zero at greater than 99.99% confidence level (Table 5.1). Again, weak but significant correlation is found. The upper left panel of Figure 5.2 shows distributions of f_{u-r} for $z \leq 0.15$ clusters and $0.15 < z \leq 0.3$ clusters with a dashed and solid line, respectively. A Kolomogorov-Smirnov test shows that the distributions are different with more than a 99% significance. In addition to the increase in f_b shown in the last section, the increase in f_{u-r} provides further evidence of color evolution of cluster galaxies. Furthermore, since $u - r$ color of galaxies is sensitive to a galaxy's morphology as shown in Figure 6 of Strateva et al (2001), it suggests possible evolution of morphological types of galaxies as well. We investigate the morphological evolution of galaxies in clusters in the next subsection.

5.3.5 Late Type Fraction Using Profile fitting

One of the purposes of this chapter is to determine if there is a morphological change of galaxies in clusters as a function of redshift. The SDSS photometric pipeline (PHOTO; Lupton et al. 2002) fits a de Vaucouleur profile and an exponential profile to every object detected in the SDSS imaging data and returns the likelihood of the fit. By comparing the likelihoods of having an exponential profile against that of a de Vaucouleur profile, we can classify galaxies into late and early types. In this section, we regard every galaxy that has an exponential likelihood higher than a de Vaucouleur likelihood in r band as a late type galaxy. A galaxy with higher de Vaucouleur likelihood in r band is regarded as an early type galaxy. We define f_{exp} in the same way as in previous subsections, i.e., f_{exp} is the ratio of the number of late type galaxies to the total number of galaxies within 0.7 Mpc. Fore/background counts are corrected using the method described in Section 5.3.1.

The resulting f_{exp} is plotted in the lower right panel of Figure 5.1. The error in f_{exp} is estimated using equation (5.2) and the median values of the errors in f_{exp} and z are shown in the upper left corner of the plot. The dashed line shows the weighted least-squares fit. The solid lines and stars show the median values of the data. The scatter is considerable, but we see the increase of f_{exp} toward the higher redshift. The Spearman's correlation coefficient is 0.194, which is inconsistent with zero at more than a 99.99% confidence level (Table 5.1). The upper right panel of Figure 5.2 shows the distributions of clusters with $z \leq 0.15$ and with $0.15 < z \leq 0.3$ with a dashed and solid line, respectively. The two distributions show a difference of more than 99% significance in a Kolmogorov-Smirnov test. We emphasize that the galaxy classification used here is purely morphological — independent of colors of galaxies. The fact that we still see the increase of the late type galaxies toward higher redshift suggests that these Butcher-Oemler type blue galaxies also change their morphological appearance as well as their colors. We also point out that the slope of the change is similar to that in the lower left panel of Figure 5.1, which is $\sim 30\%$ between $z = 0.02$ and $z = 0.3$. We note that there is a potential bias associated with the use of r band profile fitting throughout the redshift range, since the r band wavelength range at $z=0.3$ is almost that of g band at restframe. We investigate this effect in Section 5.4, and conclude that it is small. Like the blue fraction, the morphological late-type fraction is also sensitive to the magnitude range considered. Binggeli et al. (1988), Loveday et al. (1992), Yagi et al. (2002a,b) and Goto et al. (2002b; Chapter 4) reported luminosity functions of elliptical galaxies have brighter characteristic magnitudes and flatter faint end tails compared to those of spiral galaxies in both field and cluster regions. Careful attention should be paid to the magnitude range used in an analysis when fractions of spiral galaxies are compared. We discuss the uncertainty further in Section 5.4.

5.3.6 Late Type Fraction Using Concentration Parameter

As another morphological galaxy classification method, we use the inverse of the concentration parameter (C_{in}) advocated by Shimasaku et al. (2001) and Strateva et al. (2001). We define C_{in} as the ratio of Petrosian 50% radius to Petrosian 90% radius in r band. They are the radii which contain 50% and 90% of Petrosian flux, respectively. (See Stoughton et al. 2002 for more details of Petrosian parameters). Since C_{in} is the inverse of a conventional concentration parameter, spiral galaxies have a higher value of C_{in} . Following Strateva et al. (2001), we use $C_{in}=0.4$ to divide galaxies into early and late type galaxies. Readers are referred to Morgan (1958,1959), Doi, Fukugita & Okamura (1993) and Abraham et al. (1994, 1996) for previous usage of concentration of light as a classification parameter. f_{Cin} is defined as the ratio of the number of galaxies with $C_{in} > 0.4$ to the total number of galaxies within 0.7 Mpc from the cluster center as in the previous subsections. Note that our early type galaxies with $C_{in} < 0.4$ include S0 galaxies in addition to elliptical galaxies since discerning elliptical and S0 galaxies is very difficult with the SDSS data, in which the seeing is typically 1.5" (See Shimasaku et al. 2001 and Strateva et al. 2001 for the correlation of C_{in} with an eye classified morphology). Fore/background number counts are corrected as described in Section 5.3.1. The absolute magnitude range used is $-24 < M_{r^*} < -19.44$.

The upper right panel of Figure 5.1 shows f_{Cin} as a function of redshift. Since the classification using $C_{in}=0.4$ leans toward late type galaxies, the overall fraction is higher than the other panels in the figure. The increase of late type fraction, however, is clearly seen. The dashed line shows the weighted least-squares fit. The solid lines and stars show the median values of the data. The error in f_{Cin} is estimated using equation (5.2) and the median values of the errors in f_{Cin} and z are shown in the upper left corner of the plot. The Spearman's correlation coefficient is 0.223 with significance of more than 99.99% as shown in Table 5.1. The upper right panel of Figure 5.2 further clarifies the evolution effect. The distribution of $z \leq 0.15$ clusters in a dashed line and the distribution of $0.15 < z \leq 0.3$ clusters in a solid line show a difference with more than a 99% significance level. We stress that the galaxy classification based on this concentration parameter is purely a morphological one. In this morphological classification, we still see the increase of the late type fraction just like the increase of f_b — as if observing the morphological equivalence of the Butcher-Oemler effect. The increase in f_{Cin} combined with the increase in f_{exp} provides rather firm evidence of morphological change in the Butcher-Oemler type galaxies. Possible caveats in the usage of C_{in} and comparisons with previous works are discussed in Section 5.4.

5.3.7 On the Origin of the Scatter

In the last four sections, we observed the increase of late type fractions toward higher redshift in all the four cases. At the same time, we see a significant amount of scatter around the late type fraction v.s. redshift relations. Although the errors on these measurements are also large, this scatter might suggest that there might be one or more physical properties which determine the amount of late-type galaxies in clusters. Table 5.3 compares median error sizes of f_b , f_{u-r} , f_{exp} and f_{Cin} with scatters around the best-fit lines (dotted lines in Figure 5.1). In fact, in all cases, real scatters are larger than the statistical errors. In the literature, several correlations are proposed such as those with X-ray shapes of clusters (Wang et al. 2001; Metevier et al. 2000), and with cluster richness (Margoniner et al. 2001). Our cluster richesses are plotted against redshift in Figure 5.3. Richesses are measured as numbers of galaxies between $M_{r*} = -24.0$ and -19.44 within 0.7 Mpc from the cluster center after fore/background subtraction, as explained in Section 5.3.1. In Figure 5.3, this richness has no apparent bias with redshift.

In Figure 5.4, the difference of the late type fraction from the best-fit line is plotted against cluster richness. The circles and solid lines show median values. In all the panels, there is a clear tendency of richer clusters having a lower fraction of late type galaxies. This tendency is in agreement with Margoniner et al. (2001) who found richer clusters had lower blue fractions. We further discuss the richness dependence of the late type fraction in Section 5.4 and Section 5.4.8. As an alternative parameter to X-ray shape, we plot the difference from the best-fit line against cluster elongation in Figure 5.5. The elongation parameter is taken from Goto et al. (2002a; Chapter 3), which is the ratio of major and minor axes in their enhanced map to find clusters. Circles and solid lines show median values. No obvious trend is seen here. Our result seems to agree with Smail et al.'s (1997) caution that a correlation between f_b and cluster ellipticity found by Wang et al. (1997) could be due to a small and diverse sample. However, since distribution of galaxy positions might not represent cluster ellipticities measured with X-ray shape well, we do not conclude that there is no dependence on cluster ellipticities. The dependence should be pursued further in the future, ideally using X-ray profile shape with a large sample of clusters.

5.4 Discussion

5.4.1 Morphological k -correction

In the upper right panel of Figure 5.1, we use C_{in} (inverse of concentration index) in the r band to classify galaxies throughout our redshift range ($0.02 \leq z \leq 0.3$). This could potentially cause redshift dependent biases in our calculation of C_{in} . Since the universe

is expanding, by analyzing the observed r band data, we are analyzing bluer restframe wavelengths in the higher redshift galaxies. In fact, the r band at $z=0.3$ is almost g band in the restframe. Various authors have pointed out that galaxy morphology significantly changes according to the wavelength used (e.g., Abraham et al. 2001). To estimate how large this bias is, we plot the normalized distributions of C_{in} in g and r bands in Figure 5.6 using the galaxies with $0.02 \leq z \leq 0.03$ in the SDSS spectroscopic data (1336 galaxies in total; See Eisenstein et al. 2001; Strauss et al. 2002 and Blanton et al. 2003 for the SDSS spectroscopic data). In this small redshift range, the color shift due to the expansion of the universe is small. We use this redshift range to study the dependence of the C_{in} parameter on the restframe wavelength. At $z=0.3$, r band corresponds to restframe g band. The solid and dashed lines show the distribution for g and r bands, respectively. The two distributions are not exactly the same, but the difference between the two distributions is small. We summarize the statistics in Table 5.4. There are 802/1336 galaxies with $C_{in} > 0.4$ in g band, and 787/1336 galaxies have $C_{in} > 0.4$ in r band. The difference is 15/1336 galaxies, which is 1.1% of the sample. In section 5.3.6, the change in f_{Cin} is $\sim 30\%$. The effect of the morphological k -correction is therefore much smaller. We also point out that this analysis assumes the largest difference in redshift ($0.02 \leq z \leq 0.3$), therefore it gives the upper limit of the bias. Since the majority of our clusters are at $z \sim 0.2$, the wavelength difference between the observed and restframe bands is typically much smaller. We conclude that the effect of the morphological k -correction is much smaller than the change in f_{Cin} we observed in Section 5.3.6.

In Section 5.3.5, we use the r band fit for all galaxies in our sample. The same redshift effect could potentially bring bias to our analysis. In Table 5.5, we limit our galaxies to $0.02 \leq z \leq 0.03$ and count the fraction of late type galaxies in the g and r bands corresponding to the observed r band at $z=0.0$ and $z=0.3$, respectively. We list the number of galaxies with exponential likelihood higher than de Vaucouleur likelihood in column 1, the total number of galaxies in column 2, and the ratio of columns 1 to 2 in column 3. As shown in the 3rd row, the difference in the fraction of late type galaxies between g band data and r band data is only 2.5%, which is much smaller than the f_{exp} change we see in the upper right panel of Figure 5.1 ($\sim 30\%$). We conclude that the change of f_{exp} and f_{Cin} is not caused by the small redshift bias in using r band data throughout the redshift range.

5.4.2 Seeing Dependence

Another possible source of bias in measuring f_{exp} and f_{Cin} is the dependence on the seeing, relative to the size of the galaxies. At higher redshift, the size of a galaxy is smaller and a seeing convolution could be more problematic. Especially for the concentration

parameter (C_{in}), galaxy light becomes less concentrated when the seeing size is comparable to the galaxy size, and thus, the effect could cause a bias towards higher C_{in} values. To check this, we plot $f_{C_{in}}$ against the point-spread function (PSF) size in the r band for two redshift limited samples in Figure 5.7. Open squares and solid lines show the distribution and medians of low z clusters ($z \leq 0.15$). Filled triangles and dashed lines show the distributions and medians of high z clusters ($0.24 < z \leq 0.3$). For the median measurements, bins are chosen so that equal numbers of galaxies are included in each bin. 1σ errors are shown as vertical bars. As expected, lower redshift clusters show almost negligible dependence on seeing size. Higher redshift clusters show about a 5% increase in $f_{C_{in}}$ between the best and worst seeing size. The evolution effect we see in the upper right panel of Figure 5.1 is more than 20%. Furthermore, as is seen from the distribution of seeing shown in Figure 5.8, 87% of our sample galaxies have seeing better than $2.0''$. Therefore we conclude that varying seeing causes a small bias which is significantly weaker than the evolution we find in Section 5.3. The effect of varying seeing is less significant for the f_{exp} parameter. In Figure 5.9, we plot f_{exp} against seeing size for two redshift samples with the same redshift ranges and symbols as in Figure 5.7. 1σ errors, shown as vertical bars, are dominant. There is no significant correlation of f_{exp} with seeing size.

5.4.3 Radius, Fore/background Subtraction and Cluster Centroids

Throughout the analyses in Section 5.3, we use a 2.1-2.21 Mpc annular region for fore/background subtraction. In return for taking cosmic variance into account, annular (local) background subtraction has larger statistical errors than global background subtraction due to its smaller angular area coverage. However, the difference is not so large. In case of blue galaxy counts (f_b) in the background, the median Poisson (1σ) uncertainty for global background is 12.2%, whereas 1σ variation of local background is 12.6%. This increases the errors, but only by 0.4 points. The actual effect to the late-type fraction is plotted in Figure 5.10. Solid lines show distributions for our default choice of 0.7 Mpc radii and 2.1-2.21 Mpc annuli. Dashed lines show distributions for global fore/background subtraction, where fore/background subtraction is performed using global number counts of galaxies for all the clusters in the sample. A Kolmogorov-Smirnov test between two samples does not show any significant difference.

For cluster radius, we use 0.7 Mpc, since we do not have information about the virial radii of each system. It is, however, ideal to use virial radii since, for example, in a standard cold dark matter cosmology, virial radii at a fixed mass scales as $\propto (1+z)^{-1}$. Another possible cause of uncertainty is the accuracy in deciding cluster centers. In this work, a center position of each cluster is taken from Goto et al. (2002a; Chapter 3),

and is estimated from the position of the peak in their enhanced density map. Although, from Monte-Carlo simulations, cluster centroids are expected to be determined with an accuracy better than ~ 40 arcsec, the offsets have a possibility to introduce a bias in our analyses. We test different choices of these parameters in Figure 5.10. Dotted lines show distributions where radii change as $0.7 \times (1+z)^{-1}$ Mpc assuming a standard cold dark matter cosmology. Long dashed lines show distributions when the position of brightest cluster galaxy (within 0.7 Mpc and $Mr < -24.0$) is used as a cluster center. Kolmogorov-Smirnov tests show no significant difference in any of the above cases. In all cases, the probability that the distributions are different is less than 26%. Our results in Section 5.3 are thus not particularly sensitive to our choice of annuli, radii or cluster centers. We further pursue the effect of radius dependence of blue/late type fractions in Section 5.4.8, and show that it does not change our main results.

5.4.4 Comparison with Late-type Fraction from Spectroscopy

To further test our late-type fraction measurement, we compare the late-type fraction obtained from the SDSS spectroscopic data with that obtained from the SDSS imaging data in Figure 5.11. Since the SDSS spectroscopic data are limited to $r^* < 17.77$ (Strauss et al. 2002), the comparison can be done only for clusters with $z < 0.06$. In the literature, three clusters are found to satisfy these criteria in the region used in this study. These clusters include ABELL 295, RXC J0114.9+0024, and ABELL 957. For these clusters, late-type fractions are measured in the same way as in section 5.3. Late-type fractions from spectroscopy are measured using all the SDSS spectroscopic galaxies within 0.7 Mpc from the cluster center and $\delta z = \pm 0.005$ from the redshift of each cluster. Note that there is no fore/background correction for spectroscopic late-type fraction. In Figure 5.11, all points agree with each other within the error. The good agreement suggests that our fore/background subtraction technique described in section 5.3.1 works properly. It would be ideal to perform the same test for high redshift clusters as well. However, the SDSS spectroscopic data are not deep enough to perform the test for higher redshift clusters.

5.4.5 The Butcher-Oemler Effect: Comparison with Previous Work

The Butcher-Oemler effect— an increase in the ratio of blue galaxies in clusters as a function of redshift— is strong evidence of direct evolution of the stellar populations in galaxies; it has been studied by numerous authors in the past. In this section, we compare our results with previous work. Since different authors use different cluster samples, color bands, cosmology, absolute magnitude ranges and methods of fore/background subtrac-

tion, which could affect the comparison, we emphasize the differences in analysis by each author. Note that one important difference is that some previous work used a sample of quite rich clusters, e.g., clusters with more than 100 members in magnitude and radius ranges comparable to those adopted in this study. Poorest systems in our sample have only 25 member galaxies after fore/background subtraction. Thus, difference in cluster samples could cause a difference in results.

Butcher & Oemler (1978, 1984) studied 33 clusters between $z = 0.003$ and $z = 0.54$. They used galaxies brighter than $M_V = -20$ ($h=0.5$ and $q_0=0.1$) within the circular area containing the inner 30% of the total cluster population. They found f_b increases with redshift for $z \geq 0.1$. Their f_b at $z = 0.3$ is ~ 0.15 , which is slightly lower than our value. Considering the large scatter in both their and our samples, we do not claim that our results are inconsistent with their value. Note that Andreon & Ettori (1999) found a trend of increasing X-ray luminosity with increasing redshift in the sample clusters of Butcher & Oemler (1984).

Rakos & Schombert (1995) studied 17 clusters using Stromgren *uvby* filters. Due to the usage of the narrow band filters redshifted to the cluster distance, their study did need to use model-dependent k -corrections. However, their high-redshift cluster sample is drawn from that of Gunn, Hoessel & Oke (1986) which is based on IIIa-J and IIIa-F photographic plates. At $z > 0.5$, these plates measure the rest-frame ultraviolet to blue region of the spectrum. Thus the cluster catalog will be biased toward clusters rich in blue galaxies at high redshift. Rakos & Schombert found $f_b \sim 0.25$ at $z = 0.3$, which is slightly higher than the estimation of Butcher & Oemler (1984) but in agreement with our results.

Margoniner et al. (2000) studied 44 Abell clusters between $z = 0.03$ and $z = 0.38$. They used galaxies between $M_r = -21.91$ and -17.91 ($h = 0.75$) within 0.7 Mpc of the cluster center. The fore/background counts are subtracted using five control fields. Their results are more consistent with the steeper relation estimated in 1995 by Rakos and Schombert than with the original one by Butcher and Oemler in 1984. The results are also consistent with ours. Margoniner et al. (2001) extended their work to 295 Abell clusters and found $f_b = (1.34 \pm 0.11) \times z - 0.03$ with a *r.m.s.* of 0.07, which is in agreement with our fitted function shown in Figure 5.1.

Ellingson et al. (2001) studied 15 CNOC1 clusters (Yee, Ellingson, & Carlberg 1996) between $z = 0.18$ and $z = 0.55$. Since they used spectroscopically observed galaxies, they do not suffer from the fore/background correction (but see Diaferio et al. 2001). They used galaxies brighter than $M_r = -19.0$ within r_{200} from the cluster center (with an average of $1.17h^{-1}$ Mpc). Their best fit shows $f_b \sim 0.15$ at $z = 0.3$. The scatter in their Figure 1 and our data are both substantial. Thus, we can not conclude that this value is inconsistent with our results.

All of these authors found considerable scatter in f_b v.s. z plot as is seen in our Figure 5.1. It is promising that our results are consistent with the previous work within the scatter, despite the differences in the radial coverage and magnitude ranges used.

5.4.6 The Morphological Butcher-Oemler effect

In Sections 5.3.4, 5.3.5, and 5.3.6, we found an increase in the fraction of late type galaxies selected by morphological parameters with increasing redshift — as if the Butcher-Oemler effect is happening morphologically. Perhaps revealing this morphological Butcher-Oemler effect is the most striking result of this study. It suggests that the Butcher-Oemler blue galaxies change their morphology from late to early type at the same time that they change their color from blue to red. Although accurately quantifying the fraction of galaxies which experience the morphological Butcher-Oemler effect is difficult due to the considerable scatter in the data, our best-fit lines suggest that $\sim 30\%$ of galaxies in clusters undergo this transition between $z = 0.3$ and $z = 0.02$.

In previous work, Dressler et al. (1997) found a deficit of S0 galaxies in 10 intermediate ($z \sim 0.5$) clusters by classifying galaxy morphology in the HST image by eye. They claimed that many S0s needed to be added to reach the fraction of S0s found in present clusters (Dressler 1980). Couch et al. (1994, 1998) also found an indication of morphological transformation in the Butcher-Oemler galaxies by studying three rich clusters at $z = 0.31$. Later, Fasano et al. (2000) showed that spiral galaxies are, in fact, turning into S0 galaxies by observing nine clusters at intermediate redshifts and analyzing them together with higher redshift clusters in the literature. Their galaxy morphology was also based on eye classification. Our SDSS data are taken using ground based telescopes with moderate seeing ($\sim 1.5''$), and thus do not allow us to separate S0 galaxies from elliptical galaxies as the *HST* does. The advantage of our classification is its automated nature, which allows accurate reproducibility and quantification of systematic biases. In particular, it is easy to compute the completeness and contamination rate for the automated classification, based on simulations; for the present sample, the completeness and contamination rate of the parameters are given in Shimasaku et al. (2001) and Strateva et al. (2001). Furthermore, an automated galaxy classification is easier to reproduce in future observational work and in detailed computer simulations. Although we can not distinguish S0s from ellipticals, the increase of blue fraction and increase of late type galaxies toward higher redshift is qualitatively consistent with the process of S0 production over the interval in cosmic time suggested by previous investigations.

Various physical mechanisms could be the cause of the morphological and spectral Butcher-Oemler effects. Possible causes include ram pressure stripping of gas (Gunn & Gott 1972; Farouki & Shapiro 1980; Kent 1981; Abadi, Moore & Bower 1999; Quilis,

Moore & Bower 2000), galaxy infall (Bothun & Dressler 1986; Abraham et al. 1996a; Ellingson et al. 2001), galaxy harassment via high speed impulsive encounters (Moore et al. 1996, 1999), cluster tidal forces (Byrd & Valtonen 1990; Valluri 1993) which distort galaxies as they come close to the center, interaction/merging of galaxies (Icke 1985; Lavery & Henry 1988; Bekki 1998), and removal & consumption of the gas due to the cluster environment (Larson, Tinsley & Caldwell 1980; Balogh et al. 2001; Bekki et al. 2002). Mamon (1992) and Makino & Hut (1997) showed that interactions/mergers can occur in a rich cluster environment despite the high relative velocities. Shioya et al. (2002) showed that the truncation of star formation can explain the decrease of S0 with increasing redshift. It has been known that preheating of intergalactic medium can effect morphologies of galaxies by strangling the gas accretion (Mo & Mao 2002; Oh & Benson 2002). In fact, Finoguenov et al. (2003) found the filamentary gas in Coma cluster and predicted quiescent star formation in galaxy disks around the filament. Although our results provide some important clues, pinpointing what processes are responsible in the morphological and spectral Butcher-Oemler effect is a more difficult challenge.

Our results suggest that the cause is a process that affects both color and morphological appearance of galaxies at the same time. Couch et al. (1998), Dressler et al. (1999) and Poggianti et al. (1999) found “passive spirals”, which are galaxies with spiral morphology but without star formation. They probably belong to the same population as “anemic spirals” found by van den Bergh (1976). The mechanism creating “passive spirals” or “anemic spirals”, however, affects only the color of galaxies and, thus, probably is not the main mechanism that accounts for the entire effect. The increase of morphologically late type galaxies toward higher redshifts at the same time as the increase of blue galaxies is consistent with mechanisms which affect the gas supply (e.g., ram-pressure stripping, galaxy infall). However, if the infalling rate of field galaxies (mostly blue/late type) is higher in the past, almost any of the mechanisms mentioned above can explain our observational results. Furthermore, although we discussed about cluster specific phenomena, it is also known that galaxies in the field region evolve as a function of redshift as well. (e.g., Hammmer et al. 1996; Lilly et al. 1996; Balogh et al. 1997, 2002). The evolution of field galaxies needs to be compared with that of cluster galaxies further in detail. Therefore, it is still an open question what mechanism causes spectral and morphological evolution of cluster galaxies.

The finding of a 30% change of the fraction during the look back time of ~ 3.5 Gyr could also give us an additional hint in finding an underlying physical process. If the gas in spiral galaxies is removed very efficiently by some physical processes (e.g., ram-pressure stripping) or consumed rapidly by star formation, the spiral arms will disappear after several disk rotation periods, ~ 1 Gyr (Sellwood & Carlberg 1984). Interaction/merger processes are quicker than gas removal processes (~ 0.5 Gyr; Mihos 1995). Moore et al.’s

(1996) simulation showed that the galaxy harassment phase lasts for several Gyr. Kodama et al. (2001) used the phenomenological simulations to show that the timescale of the morphological transformation from spiral to S0 is 1~3 Gyr. For spectral change, Shioya et al. (2002) showed that a disk needs 2-3 Gyr after the removal of gas (or truncation of star formation) to show a k spectrum. Poggianti et al. (1999) compared the spectral and morphological properties of cluster galaxies and suggested that the timescale of the morphological transition is longer than that of the spectral transition. This difference in timescale is interesting since if one process is significantly quicker than the other, we might be able to see the time difference in the decreases of the fraction of between late type galaxies and blue galaxies, which will provide a strong constraint in the evolution history of the Butcher-Oemler galaxies. In Figure 5.1, we see a \sim 30% of change in both the photometric and morphological Butcher-Oemler effect between $z = 0.02$ and $z = 0.30$ (\sim 3.5 Gyr). The scatter in our measurement, however, is considerable and our choices of criteria between late and early type galaxies do not necessarily coincide with each other. It is thus not straightforward to convert the information to the time scale of the responsible physical process. In addition, to understand change in fraction of morphological and spectral late-type galaxies, the change in infalling rate of field galaxies needs to be understood as well. Since computer simulations have recently made dramatic progress, in the near future it will become possible for state-of-the-art simulations to simulate both dynamical and spectral evolutions of cluster galaxies, plus infalling rate of field galaxies in order to compare the results with the observed trend. For example, such a simulation can be done by combining dynamical simulations (e.g., Evrard 1991; Kauffmann et al. 1995; Bekki, Shioya & Couch 2001; Vollmer et al. 2001; Bekki et al. 2002) with cluster phenomenological simulations (e.g., Abraham et al. 1996; Fujita 1998,2001; Balogh et al. 1999; Stevens, Acreman, & Ponman 1999; Balogh, Navarro, & Morris 2000; Kodama & Bower 2001). Figure 5.1 in this work provides the interesting observational data to tackle with using such a simulation of cluster galaxy formation.

5.4.7 Richness Dependence

In Section 5.3.7, we observe the tendency of richer clusters to have smaller fractions of late type galaxies, by measuring the residuals from the best-fit relations as a function of cluster richness. Our result is consistent with Margoniner et al. (2001), who used a similar optical richness to find that poorer clusters tend to have larger blue fractions than richer clusters at the same redshift. Figure 5.4, however, still shows a significant amount of scatter, which might be suggesting the existence of another factor in determining the blue fraction in addition to redshift and richness. The dependence of the late type fraction on cluster richness, however, provides another hint on the underlying physical processes. Since ram

pressure is stronger in clusters with higher temperature at the same gas density, Fujita & Nagashima(1999) theoretically predicted that if ram pressure is the only mechanism responsible for the evolution of galaxies in clusters, the fraction of blue galaxies will always be higher in lower X-ray luminosity clusters, which usually have low temperatures. Our data shown in Figure 5.4 are consistent with the prediction from their ram pressure stripping model. Although our richness is from numbers of galaxies in optical imaging data, it is reasonable to assume it correlates well with X-ray luminosity (Bahcall 1977; Bower et al. 1994). Then, the optical richness can be related to the gas temperature through the well known $L_X - T$ relation (Mitchell, Ives, and Culhane 1977; Henry & Arnaud 1991; Edge & Stewart 1991; David et al. 1993; White, Jones, and Forman 1997; Allen & Fabian 1998; Markevitch 1998; Arnaud & Evrard 1999; Jones & Forman 1999; Reichart, Castander, & Nichol 1999; Wu, Xue, and Fang 1999; Xue & Wu 2000; and see the references therein). In a simple estimation, ram pressure is proportional to ρv^2 . L_X is proportional to ρ^2 . From the virial theorem, $v^2 \propto T$. The $L_X - T$ relation studied by Xue & Wu (2000) is $L_X \propto T^{2.8}$. Therefore, ram pressure is proportional to $\sim L_X^{0.86}$. Combined with an assumption that optical richness scales with X-ray luminosity (see, e.g., Bahcall 1974; Jones & Forman 1978; Bower et al. 1994; and Miller et al. in preparation), Figure 5.4 provides another hint that ram pressure stripping induces the evolution of cluster galaxies.

In the literature, however, the dependence of blue fractions on cluster richness has been controversial. Bahcall (1977) studied 14 X-ray clusters and found that the fraction of spiral galaxies decreases with increasing X-ray luminosity. Lea & Henry(1988) observed 14 clusters in X-ray and found that the percentage of blue objects in the clusters seems to increase with the X-ray luminosity. On the other hand, Fairley et al. (2002) studied eight X-ray selected clusters and did not find any dependence of blue fractions on X-ray luminosities. Balogh et al. (2002) studied 10 clusters at $z = 0.25$ with low X-ray luminosity and found similar morphological and spectral properties of galaxies compared with clusters with high X-ray luminosity (Balogh et al. 1997). In all cases, the results were based on a small sample of clusters. We also point out that although our results are consistent with a ram-pressure stripping model, there is a possibility that other mechanisms could explain the phenomena. For example, richer clusters might have higher rate of merger/interaction due to their higher galaxy density. The same argument holds true for galaxy harassment. Thus, more study is needed to conclude about the physical mechanism causing the phenomena. In the near future, confirming the richness dependence using X-ray luminosities or velocity dispersions with a larger sample of clusters would offer us more insight on the subject.

5.4.8 Varying Radius

In Section 5.3, we used a fixed 0.7 Mpc radius to measure blue/spiral fractions among cluster galaxies since it was difficult to measure virial radius for relatively poor clusters in our sample from the SDSS imaging data. However, it is known that virial radius changes according to cluster richness; i.e., richer clusters have larger virial radius than poorer clusters. Therefore using a fixed radius could bring some bias associated with cluster richness. In this section we try to rectify this problem using cluster richness to calculate virial radius under a simple assumption. We assume that our cluster richness (number of galaxies between $M_{r^*} = -24.0$ and -19.44 within 0.7 Mpc after fore/background subtraction) is proportional to volume of a cluster, and therefore proportional to $radius^3$. Since richness is a relatively easy parameter to measure from the imaging data, we use the following equation to calculate radius for each cluster.

$$radius = 0.7 \times (Richness/32)^{1/3} \quad (5.19)$$

where median richness of our sample cluster is 32. The coefficient of the equation is adjusted so that median clusters in our sample have radius of 0.7 Mpc, which corresponds to the mean radius used in Butcher et al. (1978, 1984) and Margoniner et al. (2000, 2001). The distribution of radius calculated in this way is presented in Figure 5.12. As expected it has a peak at 0.7 Mpc. Using this varying radius, we re-calculated all figures in Section 5.3. Sample clusters are still required to have more than 25 galaxies after fore/background subtraction within the new radius. Therefore the number of sample clusters are somewhat reduced to 413 clusters. Results are presented in Figures 5.13-5.15. Reassuringly, all figures have the same trend as presented in Section 5.3. Therefore the discussion in Section 5.4 still holds. Although it is ideal to use virial radius to measure blue/spiral fractions of clusters, we regard that our analysis using fixed 0.7 Mpc radius is not hampered to the extend where our main conclusions change.

5.5 Summary

In this chapter, we have investigated the fraction of late type galaxies in four different ways using one of the largest, most uniform samples of 514 clusters between $0.02 \leq z \leq 0.3$ from the SDSS Cut & Enhance galaxy cluster catalog. All the clusters selected here have more than 25 member galaxies within 0.7 Mpc from the cluster center and between $M_{r^*} = -24.0$ and -19.44 after statistical local fore/background subtraction. The following four different ways to estimate the fractions of late type galaxies are adopted: restframe $g - r$ color (a classical Butcher-Oemler estimator), $u - r$ color, concentration index and de Vaucouleur/exponential profile fit. The last two parameters are indicators of galaxy

morphologies (Shimasaku et al. 2001; Strateva et al. 2001). In all four cases, we observe an increase of the fraction of late type galaxies toward higher redshift with a significance of more than 99.99% (Table 5.1). We draw the following conclusion from this work.

1. We confirm the presence of the Butcher-Oemler effect using $g - r$ color. The Butcher-Oemler effect is real and exists in our sample clusters as seen in the lower left panel of Figure 5.1. The slope of the increase is consistent with previous work although the scatter in the blue fraction is considerable. Previous work also noted a large scatter in the fraction of blue galaxies. The fraction of late type galaxies also shows a similar increase when we use a $u - r$ color cut.

2. We observe the morphological Butcher-Oemler effect as an increase of late type galaxies toward higher redshift, using pure morphological parameters such as a concentration parameter and de Vaucouleur/exponential profile fit. The rates of increase are consistent with previous work on the spiral to S0 transition, albeit with considerable scatter (Figure 5.1). The increase is also in agreement with the original Butcher-Oemler effect from $g - r$ color. Our results are consistent with the evolutionary scenario proposed by Dressler et al. (1997), Smail et al. (1997), Couch et al. (1998), and Kodama & Smail (2001), in which there is a progressive morphological conversion in clusters from spirals into E/S0's.

3. We find a slight tendency for richer clusters to have lower values of the late type fraction (Figure 5.4). This trend agrees with the ram pressure stripping model proposed by Bahcall (1977) and Fujita et al. (1999), in which galaxies in richer clusters are more affected by ram pressure due to their high temperature.

Although our results 1,2, and 3 are all consistent with a ram-pressure stripping model, there still remains a possibility that other physical mechanisms are responsible for the evolution of cluster galaxies. Thus, further study is needed both theoretically and observationally to reveal the underlying physical mechanism responsible for the evolution of cluster galaxies. Since this work is based on only 5% of the whole SDSS data, an increase in the data will improve the statistical accuracy as the SDSS proceeds. Extending the work to higher redshifts using 4-8 m class telescopes will offer more insight on the origin and evolution of cluster galaxies.



Figure 5.1: Photometric and morphological Butcher-Oemler effect from the 514 SDSS Cut & Enhance clusters. f_b , f_{Cin} , f_{exp} and f_{u-r} are plotted against redshift. The dashed lines show the weighted least-squares fit to the data. The stars and solid lines show the median values. The median values of errors are shown in the upper left corners of each panel. The Spearman's correlation coefficients are shown in Table 5.1.



Figure 5.2: Normalized distributions of late type fractions (f_b , f_{Cin} , f_{exp} and f_{u-r}). The dashed lines show distributions of lower redshift clusters ($z \leq 0.15$) and the solid lines show ones of higher redshift clusters ($0.15 < z \leq 0.3$). The results of Kolomogorov-Smirnov tests are shown in Table 5.2. In all cases, Kolomogorov-Smirnov tests show the two distributions are significantly different.

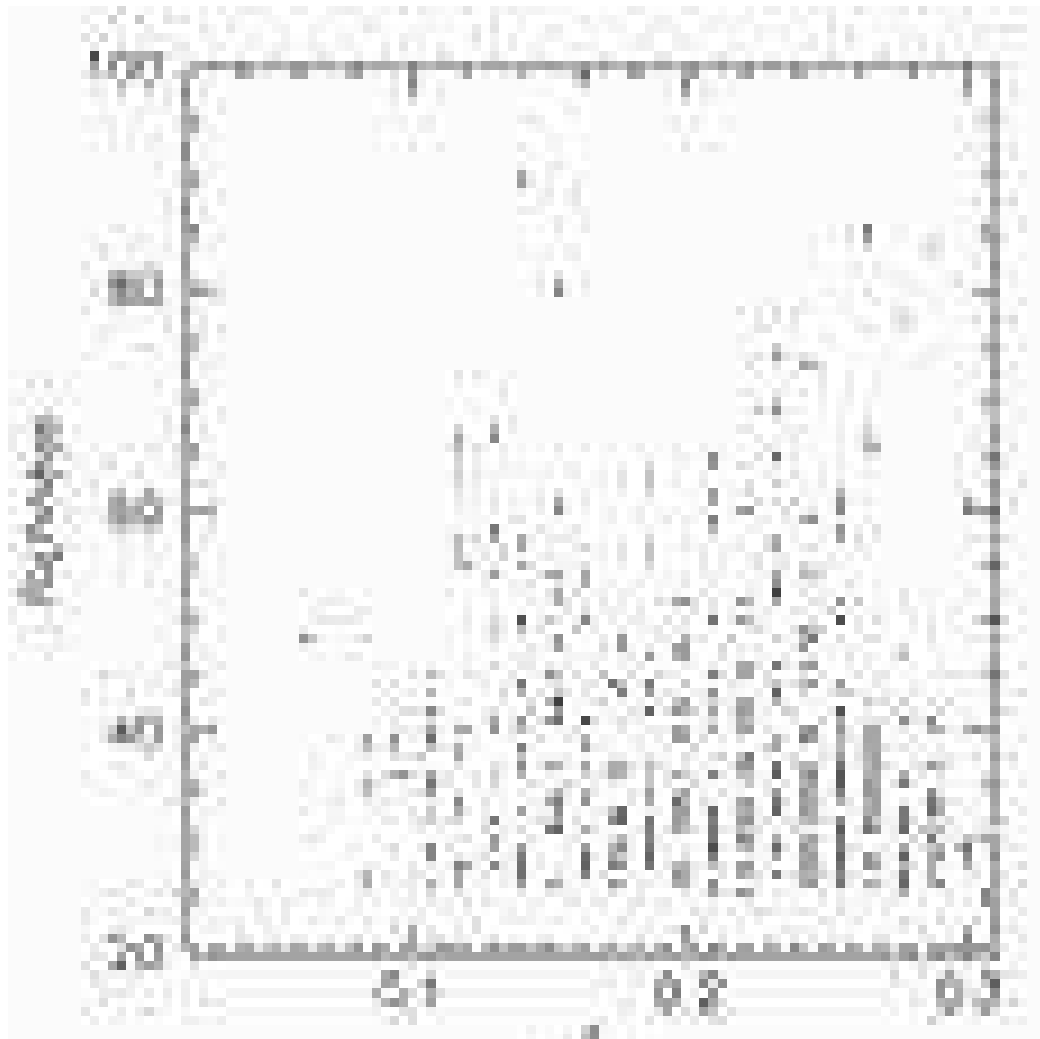


Figure 5.3: Richness distribution as a function of redshift. Richnesses are measured as the number of galaxies brighter than $M_{r^*} = -19.44$ within 0.7 Mpc from the cluster center after fore/background subtraction.

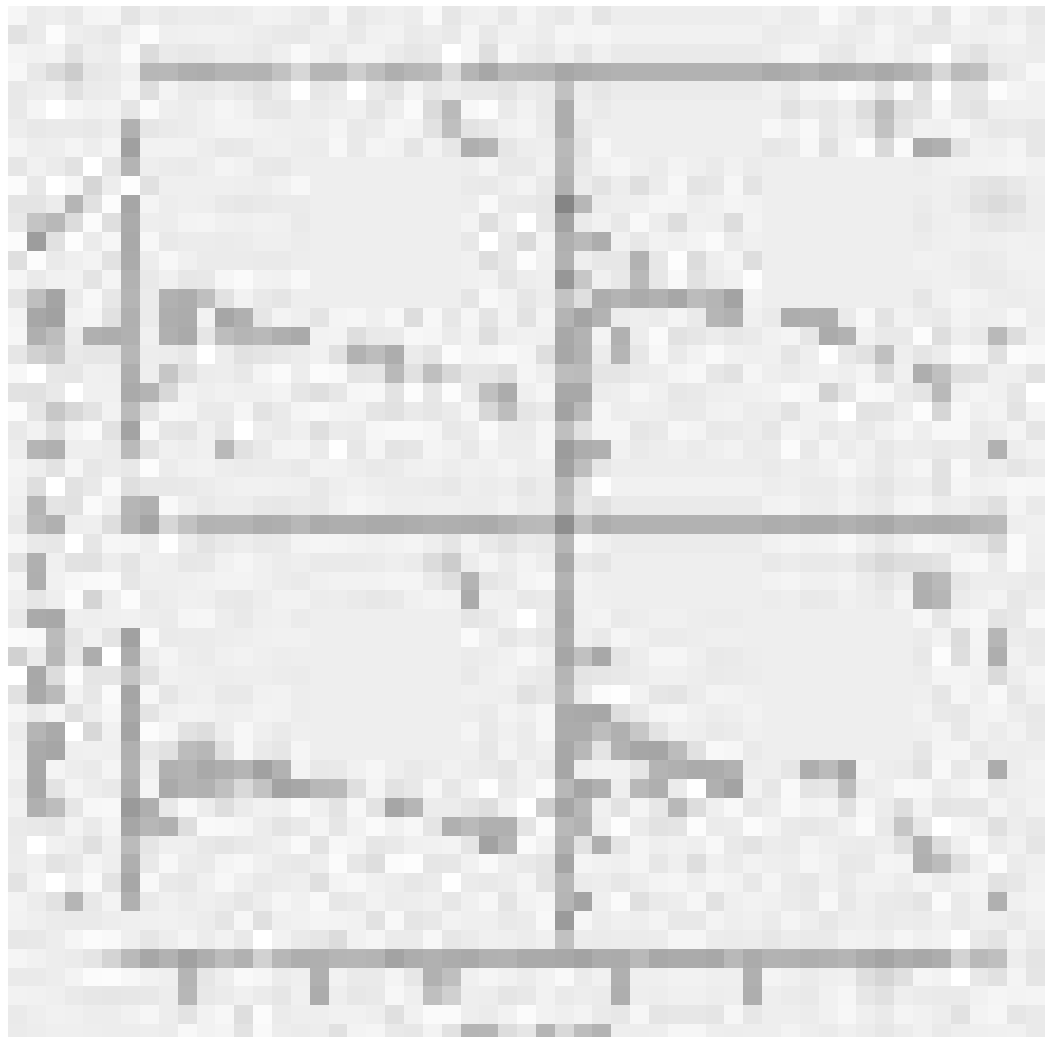


Figure 5.4: The difference of the late type fractions from the best-fit lines as a function of redshift are plotted against cluster richesses. The solid lines and circles show the median values.



Figure 5.5: The difference of late type fractions from the best-fit lines as a function of redshift are plotted against cluster elongation, which was measured as a ratio of major axis to minor axis on an enhanced density map of Goto et al. (2002a; Chapter 3). The solid lines and circles show median values.

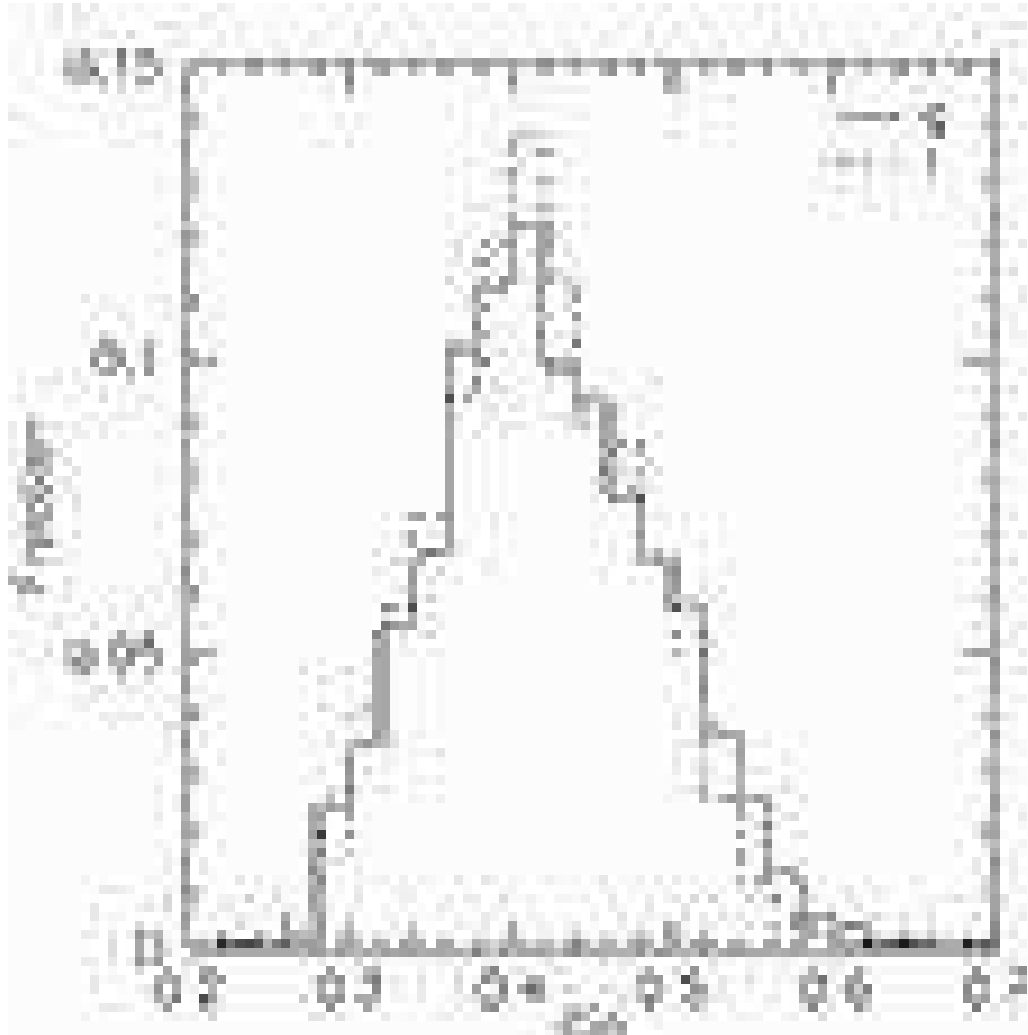


Figure 5.6: The distribution of C_{in} , the inverse of the concentration index defined as the ratio of Petrosian 50% flux radius to Petrosian 90% flux radius, for 1336 local ($0.02 \leq z \leq 0.03$) SDSS galaxies. The solid line shows the distribution of C_{in} measured in the g band image. The dashed line shows the distribution of C_{in} measured in the r band image. The difference between the g band and r band is marginal, assuring our usage of r band C_{in} in the upper right panel of Figure 5.1 from $z = 0.02$ to $z = 0.3$. The statistics are summarized in Table 5.4.

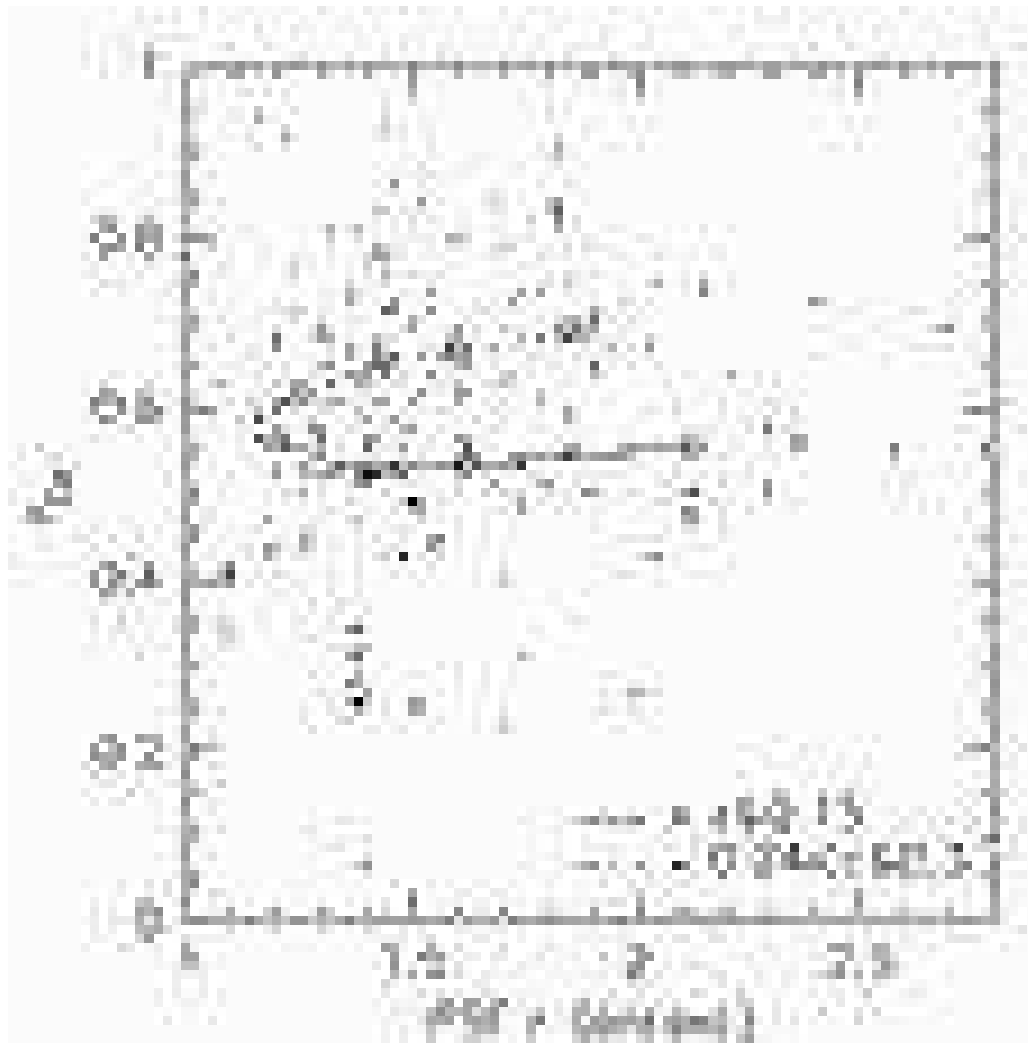


Figure 5.7: The dependence of f_{Cin} on seeing. The open squares and the solid lines show the distribution and medians of low z clusters ($z \leq 0.15$). The filled triangles and the dashed lines show the distribution and medians of high z clusters ($0.24 < z \leq 0.3$). The median bins are chosen so that equal numbers of galaxies are included in each bin.

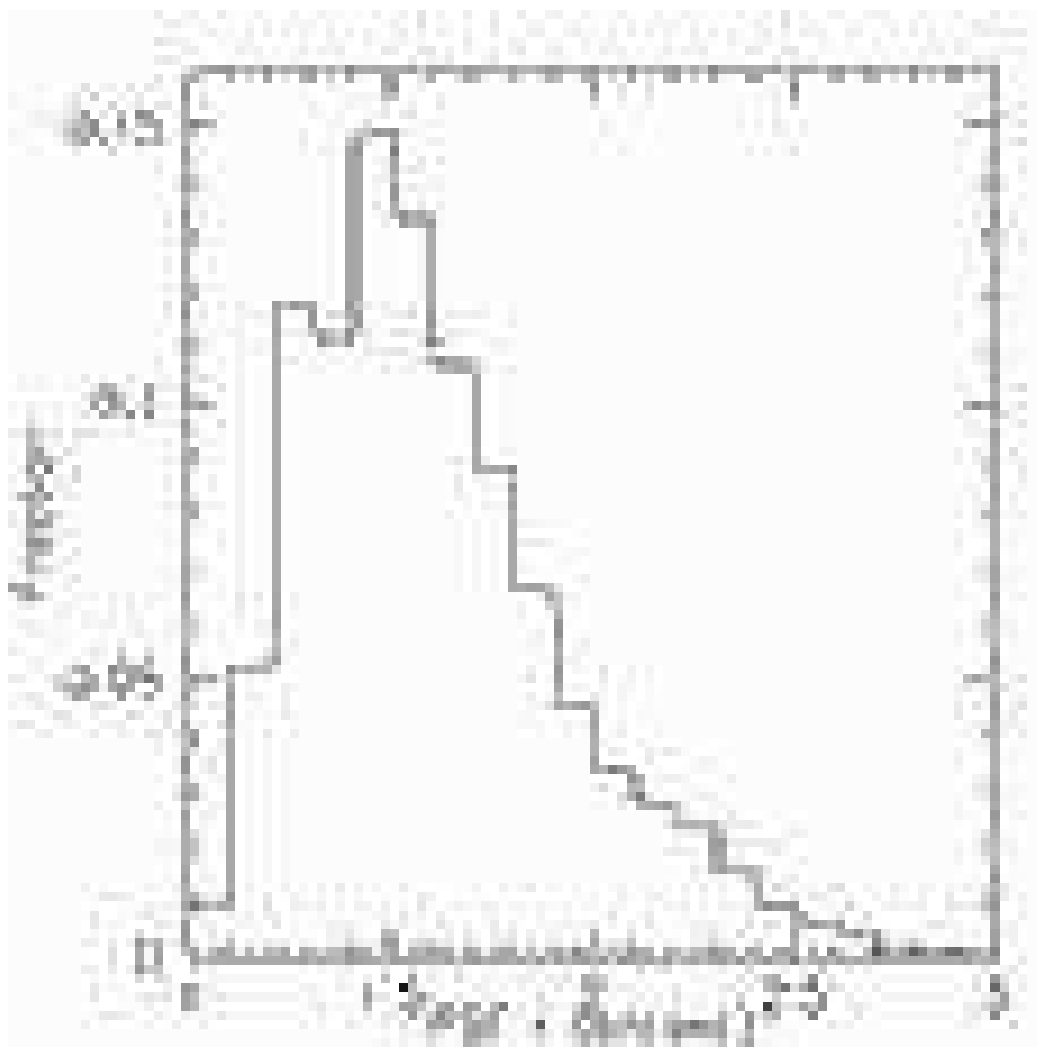


Figure 5.8: The seeing distribution of all galaxies brighter than $r=21.5$. 87% of all galaxies have seeing better than 2.0 arcsec.

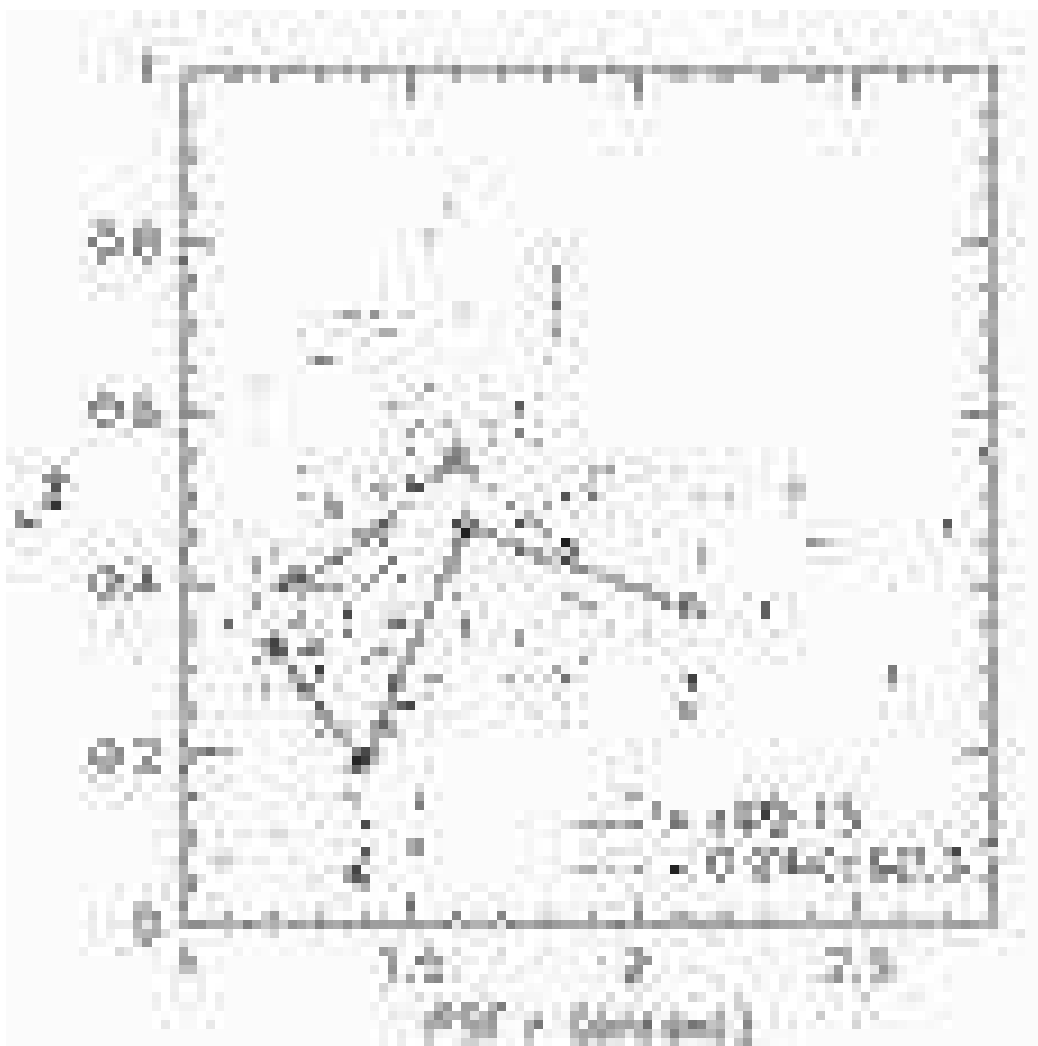


Figure 5.9: The dependence of f_{exp} on seeing. The open squares and the solid lines show the distribution and medians of low z clusters ($z \leq 0.15$). The filled triangles and the dashed lines show the distribution and medians of high z clusters ($0.24 < z \leq 0.3$). Median bins are chosen so that equal numbers of galaxies are included in each bin. 1σ errors shown as vertical bars are more dominant. There is no significant trend with seeing.



Figure 5.10: Various systematic tests. The solid lines show distributions for 2.1-2.21 Mpc annular fore/background subtraction. The dashed lines show distributions for a global background subtraction. The dotted lines show distributions using $0.7/(1+z)$ Mpc radius assuming a standard cold dark matter cosmology. The long dashed lines show distributions using the brightest galaxy position as a cluster center. In none of the cases does a Kolmogorov-Smirnov test show significant difference between the distributions (significance to be different is less than 26% in all cases).

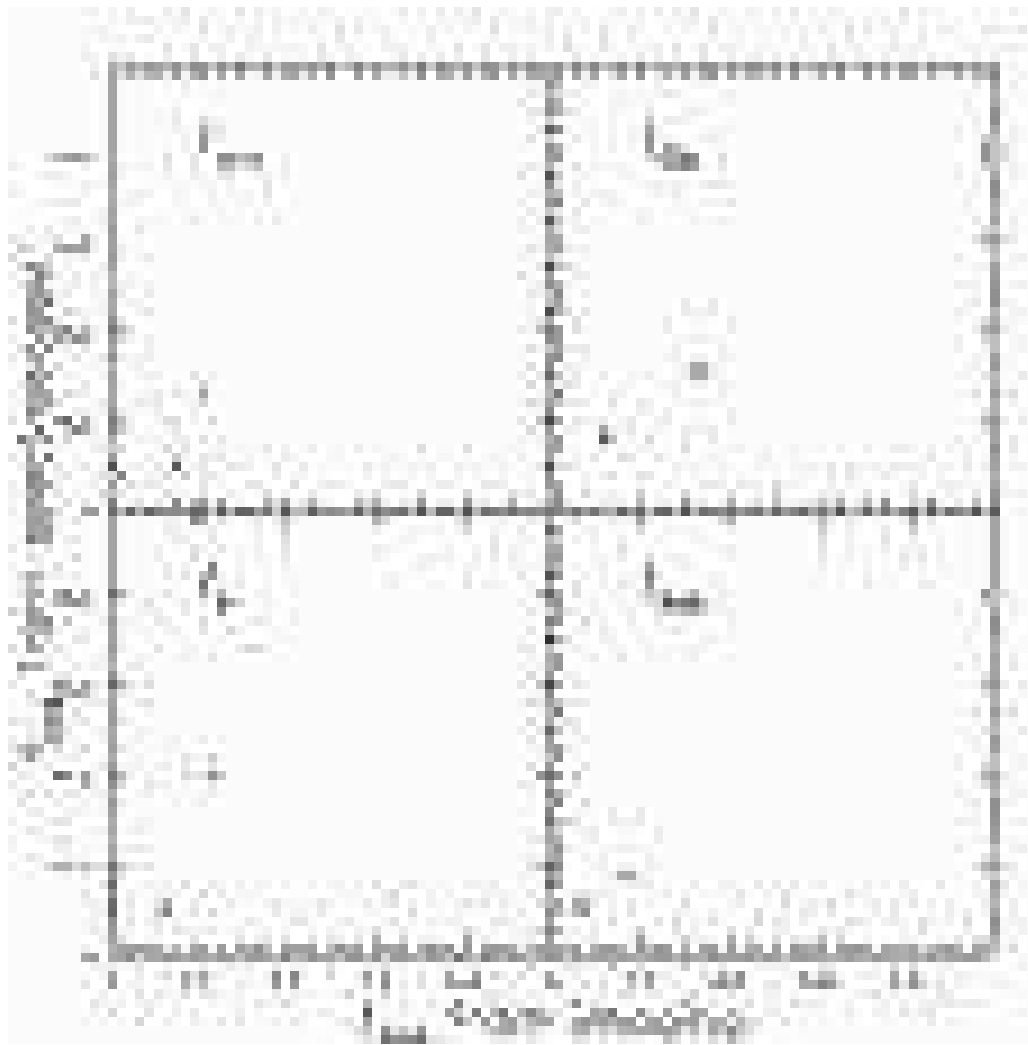


Figure 5.11: Comparison of the late-type fraction from imaging with that from spectroscopy. Late-type fractions measured using spectroscopic data are plotted against that from imaging data for three clusters with $z < 0.06$ (ABELL 295, RXC J0114.9+0024, and ABELL 957). The dashed lines are drawn to guide eyes. All points agree with each other within the error.

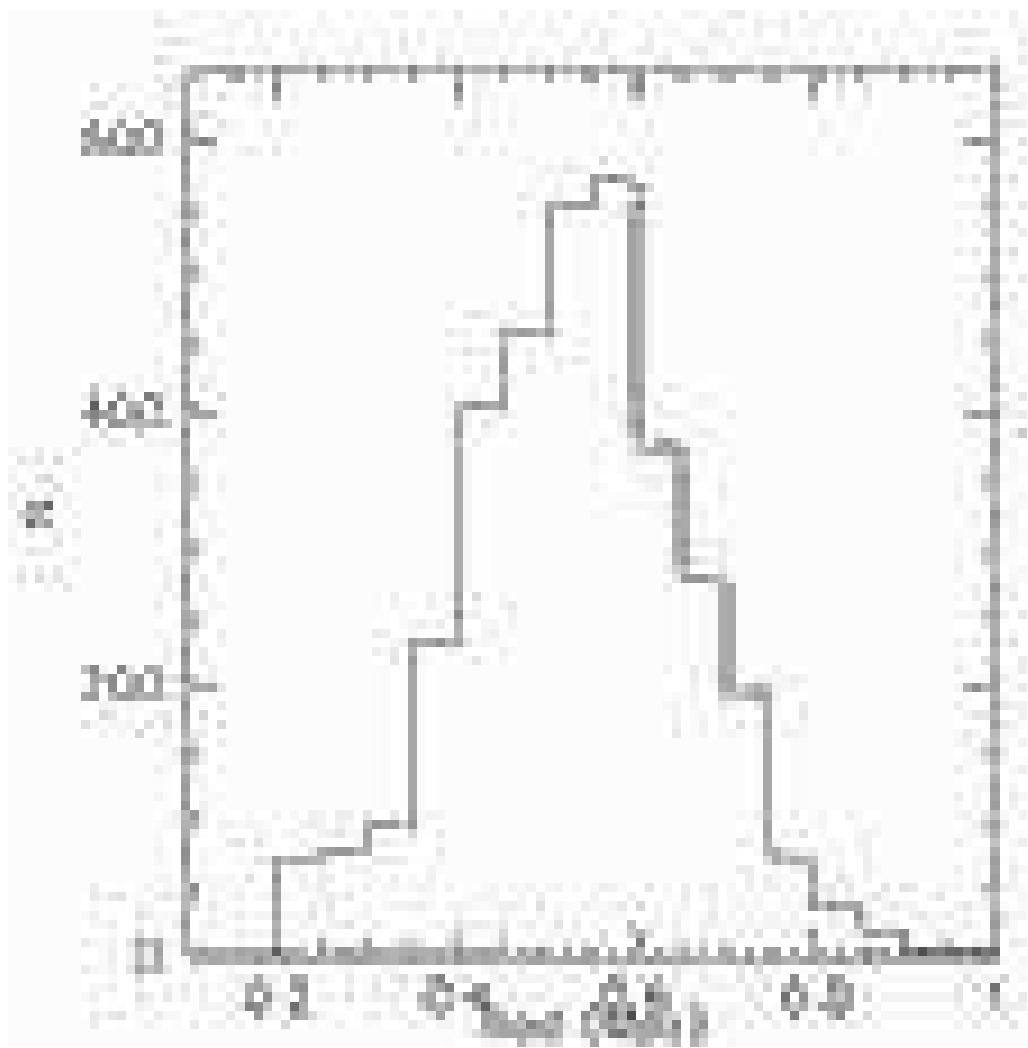


Figure 5.12: Distribution of varying radius to measure blue/spiral fractions. It has a peak at 0.7 Mpc.



Figure 5.13: The same as Figure 5.1, but measured with varying radius.

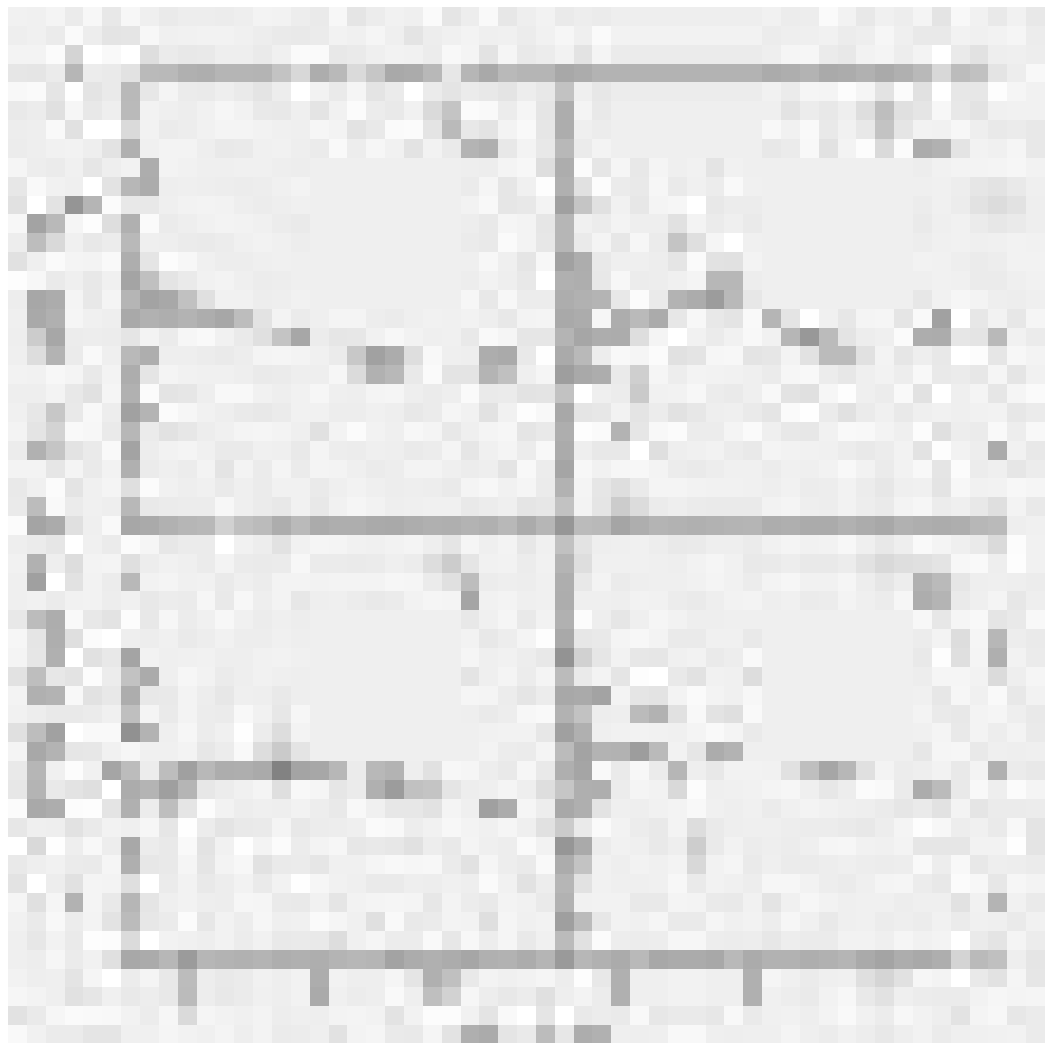


Figure 5.14: The same as Figure 5.4, but measured with varying radius.

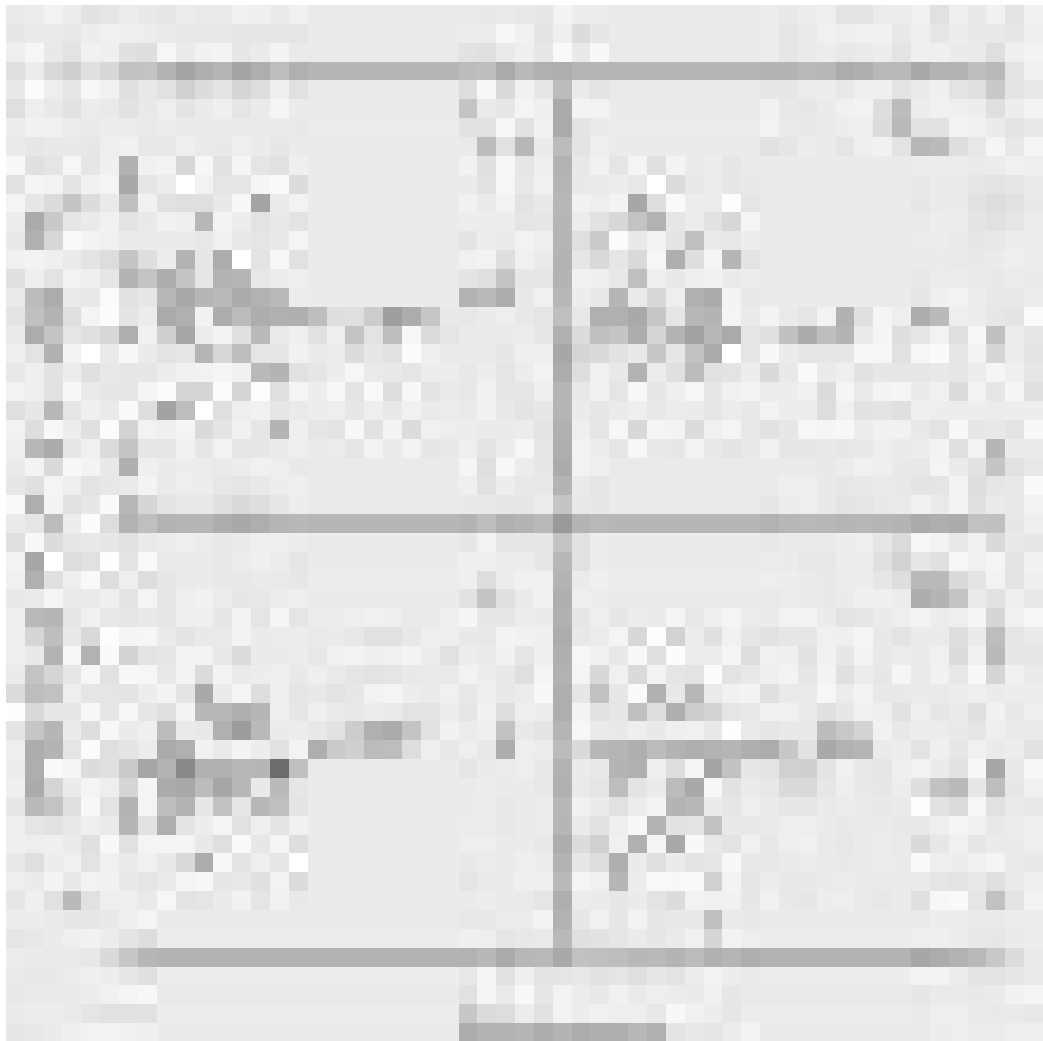


Figure 5.15: The same as Figure 5.5, but measured with varying radius.

Table 5.1: Spearman's correlation coefficients between z and fractions of late type galaxies. 514 clusters with richness >25 are chosen as a sample.

	Correlation coefficient	Significance	N clusters
f_b	0.238	4.4×10^{-8}	514
f_{u-r}	0.234	7.6×10^{-8}	514
f_{exp}	0.194	9.6×10^{-6}	514
f_{Cin}	0.223	2.9×10^{-7}	514

Table 5.2: Significances in Kolomogorov-Smirnov tests between distributions for $z \leq 0.15$ and $0.15 < z < 0.3$. In all cases, Kolomogorov-Smirnov tests show the distributions for the lower redshift sample and the higher redshift sample are significantly different.

	Significance
f_b	2.9×10^{-3}
f_{u-r}	1.0×10^{-3}
f_{exp}	3.4×10^{-4}
f_{Cin}	2.9×10^{-3}

Table 5.3: Scatters in late-type fractions around the best-fit line are compared with median errors of late-type fraction calculated with equation (5.2).

	f_b	f_{u-r}	f_{exp}	f_{Cin}
Real scatter (1σ)	0.169	0.183	0.171	0.163
Error estimate	0.078	0.069	0.050	0.089

Table 5.4: Change in the fraction of galaxies with $C_{in} > 0.4$ (late type) in two different filters(g, r).

band	N($C_{in} > 0.4$)	N(total)	Percentage(%)
g	802	1336	60.0
r	787	1336	58.9
Difference	15	1336	1.1

Table 5.5: Change in the fraction of galaxies with exponential fit likelihood greater than de Vaucouleur likelihood (late type) in two different filters(g, r). Computations are performed using the local ($0.02 \leq z \leq 0.03$) SDSS galaxies. Since we discard the galaxies with the same likelihood in this analysis, the total number of galaxies in the sample are different in g and r .

band	N(late)	N(late + early)	Percentage(%)
g	503	804	62.6
r	476	792	60.1
Difference	-	-	2.5

Chapter 6

The Morphology-Density Relation

6.1 Introduction

Morphological types of galaxies are one of the most basic properties and thus have been studied since the beginning of the extragalactic astronomy. However, it is still not very well understood where this diversity stems from. The existence of a correlation between galaxy morphology and local environment is a remarkable feature of galaxy population. Dressler (1980) studied 55 nearby galaxy clusters and found that fractions of elliptical galaxies increase and that of spiral galaxies decrease with increasing local galaxy density in all clusters. The discovery left a great impact on astronomical community since it indicates that physical mechanisms that depend on environment of each galaxy mainly affect the final configuration of stellar component. Further observational constraints on the formation and evolution of galaxies were obtained by extending the analysis of the morphology-density relation to group of galaxies in the general field. Postman & Geller (1984) extended morphology study to groups using the data from the CfA Redshift Survey (Huchra et al. 1983). The relation was completely consistent with Dressler (1980). At low densities, population fractions seemed to be independent of density below galaxy density $\sim 5 \text{ Mpc}^{-3}$. At high density, the elliptical fraction increased steeply above ~ 3000 galaxies Mpc^{-3} . Whitmore et al. (1993) re-analyzed the 55 nearby clusters (Dressler 1980) and argued that the morphology-density relation reflects a more fundamental morphology-radius relation; the correlation between morphology and cluster centric radius seems tighter than the morphology-density relation. This assertion is still controversial. The opposite results on groups came from Whitmore et al. (1995). They analyzed the morphology-density relation in groups of galaxies by carefully removing cluster galaxies from their analysis and found that the relation is very weak or non-existent in groups. Helson & Ponman (2002) also studied the morphology-density relation in groups using their X-ray bright group sample.

Later the relation between morphology and density was traced back to higher redshift. Dressler et al. (1997) studied 10 high redshift clusters at $z \sim 0.5$ and found that the morphology-density relation is strong for centrally concentrated clusters. However, the relation was nearly absent for less concentrated or irregular clusters. They also found that S0 fractions are much smaller than in nearby clusters, suggesting that S0 galaxies are created fairly recently ($z \leq 0.5$). Fasano et al. (2000) studied nine clusters at intermediate redshift ($0.1 \leq z \leq 0.25$) and compared them with local (Dressler 1980) and high redshift clusters (Dressler et al. 1997). They found that the morphology-density relation exists in high elliptical concentration clusters, but not in low elliptical concentration clusters. The finding is consistent with the results of Dressler et al. (1997). Considering that low redshift clusters have the morphology-density relation regardless of the concentration of clusters, they suggested that spiral to S0 transition happened fairly recently (last 1-2 Gyr). They also plotted morphological fraction as a function of redshift and found that S0 fraction decreases with increasing redshift, whereas spiral fraction increases with redshift.

Hashimoto et al. (1999) used data from the Las Campanas Redshift Survey (LCRS; Shectman et al. 1996) to study the concentration-density relation. They found that the ratio of high to low concentrated galaxies decreases smoothly with decreasing density. Dominguez et al. (2001) analyzed nearby clusters with X-ray and found that mechanisms of global nature (X-ray mass density) dominate in high density environments, namely the virialized regions of clusters, while local galaxy density is the relevant parameter in the outskirts where the influence of cluster as a whole is relatively small compared to local effects. Dominguez et al. (2002) studied groups in the 2dF Galaxy Group Catalog using PCA analysis of spectra as a galaxy classification and local galaxy density from redshift space as a measure of galaxy environment. They found that both morphology-density relation and morphology-group-centric radius relation is clearly seen in high mass ($M_v \geq 10^{13.5} M_\odot$) groups, but neither relation holds true for low mass ($M_v < 10^{13.5} M_\odot$) groups. These three studies made innovative step in terms of an analysis method, using automated morphological classification and three dimensional density estimation.

Various physical mechanisms have been proposed to explain the morphology-density relation. Possible causes include ram pressure stripping of gas (Gunn & Gott 1972; Farouki & Shapiro 1980; Kent 1981; Abadi, Moore & Bower 1999; Quilis, Moore & Bower 2000), galaxy infall (Bothun & Dressler 1986; Abraham et al. 1996a; Ellingson et al. 2001), galaxy harassment via high speed impulsive encounters (Moore et al. 1996, 1999), cluster tidal forces (Byrd & Valtonen 1990; Valluri 1993) which distort galaxies as they come close to the center, interaction/merging of galaxies (Icke 1985; Lavery & Henry 1988; Bekki 1998), and removal & consumption of the gas due to the cluster environment (Larson, Tinsley & Caldwell 1980; Balogh et al. 2001; Bekki et al. 2002). Mamon (1992) and Makino & Hut (1997) showed that interactions/mergers can occur in a rich

cluster environment despite the high relative velocities. Shioya et al. (2002) showed that the truncation of star formation can explain the decrease of S0 with increasing redshift. Although these processes are all plausible, the effects provided by initial condition on galaxy formation could be also important. Since field galaxies have different population ratio compared with clusters (Goto et al. 2002b; Chapter 4), a change in infalling rate of field galaxies into clusters affects population ratio of various galaxy types (Kodama et al. 2001). Unfortunately, there exists little evidence demonstrating that any one of these processes is actually responsible for driving galaxy evolution. Most of these processes act over an extended period of time, while observations at a certain redshift cannot easily provide the detailed information that is needed to elucidate subtle and complicated processes.

To extract useful information from observational data, it is necessary to have detailed theoretical predictions. In recent years, due to the progress of computer technologies, it is becoming possible to simulate the morphology-density relations by combining semi-analytic modeling with N-body simulations of cluster formation. Okamoto & Nagashima (2001) simulated the morphology-density relation using a merger-driven bulge formation model. They found that elliptical fractions are well re-produced, but there remained a discrepancy on S0 fractions. Diaferio et al. (2001) also assumed that the morphologies of cluster galaxies are determined solely by their merging histories in the simulation. They used bulge-to-disc ratio to classify galaxy types and compared the cluster-centric radial distribution with those derived from the CNOC1 sample (Yee, Ellingson, & Carlberg 1996). They found excellent agreement for bulge dominated galaxies, but simulated clusters contained too few galaxies of intermediate bulge-to-disc ratio. Springel et al. (2002) used a phenomenological simulation to predict the morphology-radius relation and compared it with Whitmore et al.(1993). Their morphological modeling is based on the merging history of galaxies. They found an excellent agreement with elliptical galaxy fractions, and some deficiency of S0 galaxies in the core of the cluster. Benson et al. (2002) combined their N-body simulation with a semi-analytic model (Cole et al. 2000) to trace the time evolution of the morphology-density relation. Interestingly, they found that a strong morphology-density relation was well established by $z=1$. The relation was qualitatively similar to that at $z = 0$. E/S0 galaxies are treated as one population in their simulation. Three of above simulations suggest that (i) elliptical fractions are consistent with the merging origin; (ii) however, the deficit of S0 galaxies shows that processes other than major-merger might be important for S0 creation. Therefore more than one mechanisms might be required to fully explain the morphology-density relation. These suggestions might be consistent with observational results from Dominguez et al. (2001), who found two different key parameters in cluster center and outskirts separately.

In the previous analysis of the morphology-density relation from observations, there

have been two major difficulties; eye-based morphological classification and the density estimate from two dimensional imaging data. Although it is an excellent tool to classify galaxies, manual classification could potentially have unknown biases (Lahav et al. 1995). A machine based, automated classification would better control biases and would allow a reliable determination of the completeness and false positive rate. Measuring local galaxy density from imaging data requires statistical background subtraction, which automatically introduces relatively large uncertainty associated with itself. Furthermore deeper imaging data require larger corrections. Therefore three dimensional density determination from redshift data is preferred. With the advent of the Sloan Digital Sky Survey (SDSS; York et al. 2000), which is an imaging and spectroscopic survey of 10,000 deg² of the sky, we now have the opportunity to overcome these limitations. The CCD imaging of the SDSS allows us to estimate morphologies of galaxies in an automated way (Yamauchi et al. 2003). Three dimensional density can be estimated from the redshift information. Due to the large area coverage of the SDSS, we are able to probe the morphology-density relation from cluster core regions to the field region without combining multiple data sets with inhomogeneous characteristics. The purpose of this chapter is as follows. We aim to confirm or disprove the morphology-density relation using the automated morphology and three dimensional density from the SDSS data. We also re-analyze the MORPHS data ($z \sim 0.5$) using an automated morphology (Smail et al. 1997). By comparing them to the SDSS, we try to observe the evolution of the morphology-density relation. Final goal of our investigation is to shed some light on the origin of the morphology-density relation.

The Chapter is organized as follows: In Section 6.2, we describe the SDSS data. In Section 6.3, we explain automated morphological classifications and density estimation. In Sections 6.4.1 and 6.4.2 we present the results from the SDSS data. In Section 6.4.4, we present the results from the MORPHS data. In Section 6.5, we discuss the possible caveats and underlying physical processes which determines galaxy morphology. In Section 6.6, we summarize our work and findings. The cosmological parameters adopted throughout this chapter are $H_0=75$ km s⁻¹ Mpc⁻¹, and $(\Omega_m, \Omega_\Lambda, \Omega_k)=(0.3, 0.7, 0.0)$.

6.2 The SDSS Data

The data we use to study the morphology-density relation are from the Sloan Digital Sky Survey Early Date Release (SDSS EDR; Stoughton et al. 2002), which covers ~ 400 deg² of the sky. The imaging part of the SDSS observes the sky in five optical bands (u, g, r, i , and z ; Fukugita et al. 1996). Since the SDSS photometric system is not yet finalized, we refer to the SDSS photometry presented here as u^*, g^*, r^*, i^* and z^* . The technical aspects of the SDSS camera are described in Gunn et al. (1998). The SDSS spectroscopic

survey observes the spectra of essentially all galaxies brighter than $r^*=17.77$. The target galaxies are selected from imaging part of the survey (Strauss et al. 2002). The spectra are observed using a pair of double fiber-fed spectrographs obtaining 640 spectra per exposure of 45 minutes. The wavelength coverage of the spectrographs is continuous from about 3800 Å to 9200 Å, and the wavelength resolution, $\lambda/\delta\lambda$, is 1800. The fiber diameter is 0.2 mm (3'' on the sky). Adjacent fibers cannot be located closer than 55'' on the sky. The throughput of the spectrograph will be better than 25% over 4000 Å to 8000 Å excluding the loss due to the telescope and atmosphere. (See Eisenstein et al. 2001; Strauss et al. 2002 and Blanton et al. 2002 for more detail of the SDSS spectroscopic data).

We use galaxies in the redshift range $0.05 < z < 0.1$ with a redshift confidence of ≥ 0.7 (See Stoughton et al. 2002 for more details of the SDSS parameters). The galaxies are limited to $Mr^* < -20.5$ and $r^* < 17.77$, which gives us a volume limited sample with 7938 galaxies. We correct magnitudes for Galactic extinction using reddening map of Schlegel, Finkbeiner & Davis (1998). We use k -correction given in Blanton et al. (2002) to calculate absolute magnitudes.

6.3 Analysis

6.3.1 Morphological classification

We use two different ways of classifying galaxy morphologies. The first one is concentration parameter C_{in} , which is defined as the ratio of Petrosian 50% light radius to Petrosian 90% light radius. Shimasaku et al. (2001) and Strateva et al. (2001) showed that this C_{in} parameter correlates well with their eye-classified morphology (See Figure 10 of Shimasaku et al. 2001 and Figure 8 of Strateva et al. 2001). We regard galaxies with $C_{in} \geq 0.4$ as late-type galaxies and ones with $C_{in} < 0.4$ as early-type galaxies. The criterion of $C_{in}=0.4$ is more conservative for late type galaxies. As shown by Shimasaku et al. (2001), $C_{in}=0.4$ provides late-type galaxy sample with little contamination and early-type galaxy sample with small contamination. The seeing dependence of C_{in} is presented in Figure 6.1 for our volume limited sample galaxies. As is shown in Figure 6.2, 87% of our sample galaxies have seeing between 1.2 and 2 arcsec where the dependence of C_{in} on seeing size is negligible.

The other classification uses morphological parameters measured by Yamauchi et al. (2003). We briefly summarize about their morphological classification. Details on the method and various systematic tests including completeness and contamination study are given in Yamauchi et al. (2003). The classification method consists of two parts. In the first part, concentration index C_i is calculated as the ratio of the Petrosian 50% light radius and Petrosian 90% radius as is for C_{in} but the parameter is corrected for

elongation of galaxies. The elongation correction prevent galaxies with low inclination (nearly edge on galaxies) from being misclassified as early-type galaxies. In the second part, coarseness of galaxies, C_n , is calculated as the ratio of *variants between a galaxy profile and the best fit to it to difference between the peak and bottom values of profile*. C_n is sensitive to arm structures of spiral galaxies, and thus larger for spiral galaxies with a clear arm structure than galaxies with a smooth radial profile such as ellipticals and S0s. This parameter, C_n , helps classifying late-type galaxies further into two types of galaxies. Finally, C_i and C_n are combined to be a final morphological parameter, T_{auto} . Both C_i and C_n are re-scaled so that their median values become 0.5, and then divided by its standard deviation to be combined to the final parameter to classify morphologies as follows.

$$T_{auto} = C_i(\text{normalized}) + C_n(\text{normalized}) \quad (6.1)$$

T_{auto} shows better correlation with eye classified morphology than C_{in} , as shown in Yamauchi et al. (2003). The correlation coefficient with eye-morphology is 0.89. Based on the T_{auto} parameter, we divide galaxies into four sub-samples in this study. We regard galaxies with $T_{auto} > 1.0$ as late-type spiral galaxies, $0.1 < T_{auto} \leq 1.0$ as early spirals, $-0.8 < T_{auto} \leq 0.1$ as S0s and $T_{auto} < -0.8$ as elliptical galaxies. Among our sample galaxies, 549 galaxies have eye-classified morphologies (Shimasaku et al. 2001; Nakamura et al. 2003). In Table 6.1, we quote completeness and contamination rate of these four types of galaxies classified by T_{auto} , using eye-classified morphology. Full discussion on contamination and completeness will be given in detail in Yamauchi et al. (2003). As shown in Figure 6.3, the parameter is robust against seeing variance in our volume limited sample galaxies. In Figure 6.4, we plot T_{auto} against redshift. Medians are shown in the solid line. In our redshift range ($0.05 < z < 0.1$), T_{auto} is essentially independent of redshift.

In Figure 6.5, C_{in} is plotted against $u-r$ color. Strateva et al. (2001) pointed out that $u-r=2.2$ serves as a good galaxy type classifier as well. The distribution shows two peaks, one for elliptical galaxies at around $(u-r, C_{in})=(2.8, 0.35)$, and one for spiral galaxies at around $(u-r, C_{in})=(2.0, 0.45)$. Our criterion at $C_{in}=0.4$ is located right between these peaks and separates these two populations well. In Figure 6.6, T_{auto} is plotted against $u-r$ color in four separate panels. Due to the inclination correction of T_{auto} , two populations degenerated in $u-r$ color (around $u-r=2.8$) are now separated into elliptical and early spiral galaxies, which is one of the major improvements of T_{auto} against C_{in} . Overplotted points are galaxies classified by eye. Upper left, upper right, lower left and lower right panels show elliptical, S0, early-spiral and late-spiral galaxies classified by eye, respectively. Compared with T_{auto} criteria to separate the galaxies ($T_{auto}=-0.8$, 0.1 and 1.0), the figure suggests that our T_{auto} criteria separate galaxies reasonably well.

The effect of inclination correction can be also seen in Figure 6.7, where T_{auto} is plotted against C_{in} . In addition to the nice correlation between the two parameters, there are galaxies with high T_{auto} and low C_{in} values in the upper left part of the figure. These are galaxies correctly classified by T_{auto} due to its inclination correction. The correlation of T_{auto} with eye morphology is studied in detail by Yamauchi et al. (2003). In Figure 6.8, we plot $H\alpha$ EW for four types of galaxies classified with T_{auto} . Later type galaxies show higher $H\alpha$ EWs, suggesting that our galaxy classification criteria work well.

6.3.2 Density Measurements

We measure local galaxy density in the following way. For each galaxy, we measure a projected distance to the 5th nearest galaxy within ± 1000 km/s in redshift space among the volume limited sample ($0.05 < z < 0.1$, $Mr^* < -20.5$). The criterion for redshift space (± 1000 km/s) is set to be generous to avoid galaxies with a large peculiar velocity slipping out of the density measurement, in other words, not to underestimate the density of cluster cores. Then, the number of galaxies (5) within the distance is divided by the circular surface area with the radius of the distance to the 5th nearest galaxy. When the projected area touches the boundary of the data, we corrected the density by correcting the area to divide. Since we have redshift information for all of the sample galaxies, our density measurement, ρ , is a pseudo-three dimensional density measurement and free from the uncertainty in background subtraction. In Figure 6.9, we present distributions of this local galaxy density for all 7938 galaxies, galaxies within 0.5 Mpc from a cluster and galaxies between 1 and 2 Mpc from a cluster. In measuring distance form a cluster, we use the C4 cluster catalog (Miller et al. in prep.). Part of the catalog is also presented in Gomez et al. (2003). For each galaxy, the distance from the nearest cluster center is measured on a projected sky for galaxies within ± 1000 km/s from a cluster redshift.

6.4 Results

6.4.1 The Morphology Density Relation for the SDSS data

In Figure 6.10, we use C_{in} to present the ratio of the number of early type galaxies to that of all galaxies as a function of the local galaxy density. The solid line shows the ratio of early type galaxies using $C_{in}=0.4$ as a separator, which separate elliptical galaxies and spiral galaxies well as shown in Figure 6.5. The fraction of early type galaxies clearly increases with increasing density. In the least dense region, only 55% are early type, whereas in the densest region, almost 85% are early type galaxies. Furthermore, it is interesting to see that around galaxy density 3 Mpc^{-2} , the slope of the morphology-density relation abruptly becomes steeper. 3 Mpc^{-2} is a characteristic density for cluster perimeter

(1-2 Mpc; see Figure 6.9) and also coincides with the density where star formation rate (SFR) of galaxies changes as studied by Lewis et al. (2002) and Gomez et al. (2003). To see the dependence of the relation to the choice of our criterion ($C_{in}=0.4$), we use slightly different criteria for dashed and dotted lines, which use $C_{in}=0.37$ and $C_{in}=0.43$ as a criterion, respectively. The former criterion is a little biased to spiral galaxies and the latter to elliptical galaxies. As is seen in the figure, both dotted and dashed lines show the morphology-density relation, but in somewhat flatter way than the solid line, indicating the effect of the contamination from spiral galaxies in case of $C_{in}=0.43$ (incompleteness in case of $C_{in}=0.37$). In the density below 3 Mpc^{-2} , the steepness of three slopes are almost identical. However, at the least dense region, only 65% is elliptical galaxies in case of $C_{in}=0.37$, whereas almost 90% is elliptical galaxies in case of $C_{in}=0.43$. Thus, the absolute amount of “elliptical” galaxies is a strong function of the C_{in} criterion. Therefore careful attention to the C_{in} criterion is needed when comparing to other work such as computer simulations and other observational data set.

In Figure 6.11, the ratio of four morphological types of galaxies are plotted against galaxy density using T_{auto} . The short-dashed, solid, dotted and long-dashed lines represent elliptical, S0, early-spiral and late-spiral galaxies, respectively. The decline of late-spiral fraction toward high density is seen. Early-spiral fractions stays almost constant. S0 fractions steadily increase toward higher density, but declines somewhat at the two highest density bins. Elliptical fractions show mild increase with increasing density and radically increase at the two highest density bins. In the figure, there exist two characteristic densities where the relation radically changes. Around galaxy density $1\text{-}2 \text{ Mpc}^{-2}$, corresponding to the cluster infalling region (Figure 6.9), the slope for late-spiral suddenly goes down and the slope for S0 goes up. At around galaxy density 6 Mpc^{-2} , corresponding to the cluster core region (Figure 6.9), S0 fractions suddenly goes down and elliptical fractions show a sudden increase. To clarify this second change in elliptical and S0 fractions, we plot S0 to elliptical number ratio against local galaxy density in Figure 6.12. As is seen in the previous figure, S0/E ratio remains almost constant from galaxy density 0.01 to 5 Mpc^{-2} , and it then suddenly declines after 6 Mpc^{-2} . We discuss the interpretation of this result in Section 6.5.

6.4.2 Morphology-Radius Relation

In Figure 6.13, we plot elliptical fractions classified with C_{in} , against a radius from the cluster center. We use the C4 galaxy cluster catalog (Miller et al. in prep.) when measuring the distance between a galaxy and the nearest cluster. For each cluster, distances are measured by converting angular separation into physical distance for galaxies within $\pm 1000 \text{ km/s}$ in redshift space. For each galaxy, the distance to the nearest cluster is

adopted as a distance to a cluster. The distance is then expressed in units of virial radii using velocity dispersion given in Miller et al. in prep. and the equation given in Girardi et al. (1998). The morphological fraction for each radius bin is measured in the same way as the last section; the solid, dashed and dotted lines represents different criteria, $C_{in} = 0.4$, 0.37 and 0.43, respectively. As seen in Figure 6.5, $C_{in} = 0.4$ best separates elliptical and spiral galaxies. In the figure, fraction of elliptical galaxies decreases toward larger distance from a cluster center. The relation becomes consistent with flat after 2 virial radius. As in the case in Figure 6.10, three criteria show similar slope. However, absolute amount of elliptical galaxies is a strong function of C_{in} criteria. In case of $C_{in}=0.4$, elliptical fractions increase from 60% to almost 90% toward a cluster center.

In Figure 6.14, we plot the morphology-cluster-centric-radius relation for four types of galaxies classified using T_{auto} . As is in Figure 6.11, the short-dashed, solid, dotted and long-dashed lines represent elliptical, S0, early-spiral and late-spiral galaxies, respectively. Fractions of late-spiral galaxies decrease toward smaller radius, whereas fractions of elliptical and S0 galaxies increase toward a cluster center. In the figure, three characteristic radii are found. Above 2 virial radii, four lines are consistent with flat, suggesting physical mechanisms responsible for the morphological change do not work beyond this radius. Between 0.3 and 1 virial radius, S0 fractions mainly increases toward a cluster center. Late and early spirals show corresponding decrease. Interestingly, S0 fractions increase more than elliptical fractions. Below 0.3 virial radius, elliptical fractions dramatically increase and S0 fractions decrease in turn. To further clarify the change between S0 and elliptical fractions, we plot S0 to elliptical number ratio in Figure 6.15. As is seen in the previous figure, the ratio slightly increase between 1 and 0.3 virial radius toward a cluster center. At 0.3 virial radius, slope changes radically and the ratio decreases toward a cluster center. We interpret these findings in Section 6.5.

6.4.3 Physical Sizes of Galaxies

It is important to understand relative galaxy sizes when we discuss transformation of galaxies. In Figure 6.16, we plot physical galaxy sizes calculated using Petrosian 90% flux radius in r band, against T_{auto} . Above $T_{auto}=0$, galaxy sizes decrease with decreasing T_{auto} . However, below $T_{auto}=0$, galaxy sizes increase with decreasing T_{auto} . We discuss the result in conjunction with Figures. 6.11 and 6.14 in Section 6.5.

6.4.4 Comparison with the MORPHS Data

In this section, we compare the morphology-density relation of the SDSS data ($z \sim 0.05$) with that of the MORPHS data ($z \sim 0.5$). The MORPHS data are used in Dressler et al. (1997) to study the morphology-density relation in high redshift clusters, and publicly

available in Smail et al. (1997). The data consist of 10 galaxy clusters at a redshift range $z = 0.37\text{--}0.55$ as summarized in Table 6.2. The sharp imaging ability of Hubble Space Telescope made it possible to measure galaxy morphology at this further away in the universe. We use concentration parameter given in Smail et al. (1997) as an automated morphology of the sample. As for the galaxy density, we count a number of galaxies brighter than $Mr^* = -19.0$ within 250 kpc and subtracted average galaxy number count of the area (Glazebrook et al. 1995). Magnitude (either F702W or F814W) are k -corrected and transformed to the SDSS r band using the relation given in Fukugita et al. (1995). To make as fair comparison as possible, we re-measured the SDSS morphology-density relation using as similar criteria as possible. We re-measure galaxy density by counting galaxies within 250 kpc and ± 1000 km/s and brighter than $Mr^* = -19.0$ in the SDSS data ($0.01 < z < 0.054$). The number of galaxies are divided by the size of the area ($250^2 \pi \text{ kpc}^2$ if it does not go outside of the boundary. If it does, the area is corrected accordingly.) We also match the criteria for both of concentration parameters. The concentration parameter of the SDSS is measured as the ratio of Petrosian 50% light radius to 90% light radius. The concentration parameter of the MORPHS data is measured using the Source Extractor. Furthermore, the seeing size compared with typical galaxy size is not exactly the same between two samples. Therefore, we have to calibrate these two concentration parameters. Fortunately, part of the SDSS galaxies are morphologically classified by eye in Dressler (1980). Since the MORPHS data are eye-classified by the same authors (Dressler et al. 1997), we regard these two eye-classified morphology essentially the same and use them to calibrate two concentration parameters. When we use the SDSS concentration criteria, $C_{in} < 0.4$, it leaves 76% of eye-classified elliptical galaxies (24% contamination). By adjusting concentration parameter for the MORPHS data to these values (76% and 24%), we found that the MORPHS concentration parameter of 0.45 leaves 75% of eye-classified elliptical galaxies. We regard this essentially the same criteria and adopt 0.45 as a criteria for the MORPHS concentration parameter which corresponds to that of the SDSS ($C_{in}=0.4$). In Figure 6.17, we plot fractions of elliptical galaxies against galaxy density for both the SDSS and MORPHS data in the solid and dashed lines, respectively. Quite interestingly, two morphology-density relations lie on top of each other. Since the MORPHS data only exist for cluster region, we are not able to probe into as low density regions as in Figure 6.11. However, it shows that the morphology-density relation was already established at $z \sim 0.5$. There is a sign of slight excess of elliptical galaxies in the SDSS data in two highest density bins.

6.5 Discussion

6.5.1 Elliptical Fractions

In previous section, we have presented fractions of elliptical galaxies in several different ways. Since our morphological classification, density measurement are different from most of previous work, it is important to know how these elliptical fractions differ due to the choice of relevant parameters. We use the result of Whitmore et al. (1993) as a benchmark for our study since they applied various systematic corrections carefully and the results are relatively widely used. Their result is elliptical:S0:spiral=18%:23%:59%. In Figure 6.10, we have 55% of ellipticals in the least dense bin and 85% of them in the densest bin. In Figure 6.13, we elliptical fractions vary from 60% to 90%. Between these two figures, our values agree each other within the errors, suggesting our values are internally consistent. However, our elliptical fractions are slightly higher than the sum of ellipticals and S0s (41%) in Whitmore et al. (1993). As noted in section 6.3, this comes from our choice of $C_{in}=0.4$ criteria slightly leaned toward spiral galaxies. Figure 6.10 showed that slight change in C_{in} criteria can change absolute amount of elliptical galaxies dramatically, and thus, careful attention is needed when comparing our work with others. In our case, $C_{in}=0.37$ criteria shown in a dotted line in Figure 6.10 is closer to the classification of Whitmore et al. (1993).

In Figure 6.11, we have 10% of ellipticals in the least dense bin and 25% in the densest bin. S0s are 25% in the least dense bin. In Figure 6.14, elliptical fractions vary from 15% to 30% and S0s vary from 25% to 40%. Again our values are consistent within the errors internally. In addition, in these cases, values are only two sigma away from Whitmore et al. (1993). If we sum up ellipticals and S0s, our values are 30% and 35%, whereas Whitmore reports 41%. Therefore in case of T_{auto} parameter, our choice of criteria is similar to that of Whitmore et al. (1993).

6.5.2 The Morphology-Density Relation with C_{in}

In section 6.4.1, two interesting results are found in the SDSS data using $C_{in}=0.4$ as a classification criterion; (i) Morphology-density relation exists in the SDSS data, however, it flattens out at low density. (ii) The characteristic galaxy density is at around 3 Mpc^{-2} . In section 6.4.2, we analyzed morphology-density relation in the view point of morphology-radius relation. The flattening at low density is seen as well and its turning point is at around $1 R_{vir}$. Since computer simulations sometimes use different magnitude range, different density measurement and different morphological classification (often bulge-to-disc ratio), it is difficult to do accurate direct comparison. However, both of morphology-density relation and morphology-radius relation are qualitatively in agree-

ment with computer simulations such as Okamoto et al. (2001), Diaferio et al. (2002), Springel et al. (2000) and Benson et al. (2002). The flattening of morphology-density relation we saw in both Figures 6.10 and 6.13 is interesting since it suggests that whatever physical mechanism is responsible for morphological change of late-spiral galaxies in dense regions, the mechanism starts working at galaxy density $\sim 3 \text{ Mpc}^{-2}$ or higher.

Various mechanism can be responsible for the morphological change. These include ram pressure stripping of gas (Spitzer & Baade 1951; Gunn & Gott 1972; Farouki & Shapiro 1980; Kent 1981; Abadi, Moore & Bower 1999; Fujita & Nagashima 1999; Quilis, Moore & Bower 2000), galaxy infall (Bothun & Dressler 1986; Abraham et al. 1996; Ellingson et al. 2001), galaxy harassment (Moore et al. 1996, 1999), cluster tidal forces (Byrd & Valtonen 1990; Valluri 1993), enhanced star formation (Dressler & Gunn 1992), and removal & consumption of the gas (Larson, Tinsley & Caldwell 1980; Balogh et al. 2001; Bekki et al. 2002). It is yet unknown exactly what processes play major roles in creating morphology-density relation. However, the mechanism must be the one that works at galaxy density 3 Mpc^{-2} or higher. It is also interesting to note that this characteristic density coincides with the density where galaxy star formation rate abruptly drops (Lewis et al. 2002; Gomez et al. 2003). The coincidence suggests that the same mechanism might be responsible for both morphology-density relation and truncation of star formation rate.

6.5.3 The Morphology-Density Relation with T_{auto}

In Figures 6.11 and 6.14, we further studied the morphology-density and the morphology-radius relation using T_{auto} parameter, which allows us to divide galaxies into four categories (elliptical, S0, early-spiral and late-spiral). In addition to the general trend found in the previous section, we found two characteristic changes in the relation at around galaxy density 2 and 6 Mpc^{-2} or in terms of radius, 0.3 and 2 virial radii. In the sparsest regions (below 2 Mpc^{-2} or outside of 2 virial radius), both relations becomes almost flat, suggesting that the responsible physical mechanisms do not work very well in these regions. In the intermediate regions (density between 2 and 6 Mpc^{-2} or virial radius between 0.3 and 2), S0 fractions dramatically increase toward denser or smaller radius regions, whereas fractions of late-spiral galaxies decrease. In the densest regions (above 6 Mpc^{-2} or inside of 0.3 virial radius), interestingly S0 fractions decrease, and in turn, elliptical fractions radically increase suddenly. The change in the densest region are further confirmed in Figures 6.12 and 6.15, where we plotted S0 to elliptical number ratio as a function of density or cluster-centric-radius. In both Figures, S0 to elliptical ratio declines suddenly at the densest region.

The existence of two characteristic change in both the morphology-density and the

morphology-radius relation suggests the existence of two different physical mechanisms responsible for each of the two morphological fraction changes. In the intermediate region (density between 2 and 6 Mpc⁻² or virial radius between 0.3 and 2), the mechanism creates S0 galaxies mostly, by reducing fractions of late-spiral galaxies. Although there is not much change in early-spiral fractions, perhaps it is natural to imagine that the mechanism turns late-spirals into early-spirals, and then early-spirals into S0s. As Figure 6.16 shows, median sizes of galaxies gradually declines from late-spirals to S0s, suggesting calm, gradual transformation of galaxies, maybe due to the truncation of star formation as observed at the same environment by Gomez et al. (2003) and Lewis et al. (2002). After the truncation of star formation, outer part of a galaxy disc fades away as massive stars die. The plausible candidates of this mechanism includes ram-pressure stripping (Gunn & Gott 1972; Farouki & Shapiro 1980; Kent 1981; Abadi, Moore & Bower 1999; Quilis, Moore & Bower 2000), unequal mass galaxy mergers (Bekki et al. 1998), galaxy harassment (Moore et al. 1999) and truncation of star formation due to the cluster environment (Larson, Tinsley & Caldwell 1980; Balogh et al. 2001; Bekki et al. 2002).

Very different consequences are found in the densest region (above 6 Mpc⁻² or inside of 0.3 virial radius), where the mechanism decrease S0 fractions and increase elliptical fractions. In Figure 6.16, there is a significant increase in median galaxy sizes from S0s to ellipticals. Both of these observational results suggest that a very different mechanism from intermediate region is working in the densest region. Since galaxy size becomes larger from S0 to ellipticals, merging scenario is one of the candidate mechanisms. Computer simulations based on the galaxy merging scenario reported the deficit of S0 galaxies (Okamoto et al. 2001; Diaferio et al. 2002; Springel et al. 2000; Benson et al. 2002), which we might have seen observationally in the densest region of our data. In previous work, Dominguez et al. (2002) also suggested that there are two mechanisms in the morphology-density relation; one with global nature and the other with local effects. Our findings of two characteristic changes in the morphology-density relation is perhaps an observational result of the same physical phenomena as Dominguez et al. (2001) noted from a different point of view.

6.5.4 Comparison with MORPHS data

In section 6.4.4, we compared the local morphology-density relation (SDSS; $z \sim 0.05$) with that seen at higher redshift (MORPHS; $0.37 < z < 0.5$). Interestingly, two morphology-density relations agreed each other. The agreement suggests that morphology-density relation was already established at $z \sim 0.5$ as it is in the present universe, i.e., the origin of morphology-density relation stays in much higher redshift universe. In the densest environments, there might be a sign of excess elliptical fractions in the SDSS than in the

MORPHS. Although two data points agrees within the error, such an excess of elliptical galaxies might suggest additional formation of elliptical galaxies between $z = 0.5$ and $z = 0.05$. Little evolution of morphology-density relation is also interesting in terms of comparison with computer simulations. Benson et al. (2002) predicted that the evolution of morphology-density relation will be seen as a shift in morphological fractions without significant change in slope. However, a caveat is that absolute value of our Figure 6.17 depends solely on the calibration of concentration parameters of the both data, which by nature is difficult to calibrate accurately due to the large scatter in both concentration parameters. Therefore the results on evolution should not be over-interpreted.

6.6 Summary

We have studied the morphology-density relation and the morphology-cluster-centric-radius relation using a volume limited SDSS data ($0.05 < z < 0.1$, $Mr^* < -20.5$). Major improvements in this work are; (i) automated galaxy morphology, (ii) three dimensional local galaxy density estimation, (iii) the extension of the morphology-density relation into the field region. Our findings are as follows.

Both the morphology-density relation and the morphology-cluster-centric-radius relation are seen in the SDSS data for both of our automated morphological classifiers, C_{in} and T_{auto} .

We found there are two characteristic changes in both the morphology-density and the morphology-radius relations, suggesting that two different mechanisms are responsible for the relations. In the sparsest regions (below 2 Mpc^{-2} or outside of 2 virial radius), both relations are not evident, suggesting the responsible physical mechanisms require denser environment. The characteristic density (2 Mpc^{-2}) or radius (2 virial radius) coincides with the sharp turn in the SFR-density relation (Gomez et al. 2003; Lewis et al. 2002), suggesting the same mechanism might be responsible for both the morphology-density relation and the SFR-density relation. In the intermediate density regions, (density between 2 and 6 Mpc^{-2} or virial radius between 0.3 and 2), S0 fractions increase toward denser regions, whereas late-spiral fractions decrease. Considering the median size of S0 galaxies are smaller than that of late-spiral galaxies (Figure 6.16) and star formation rate radically declines in these regions (Gomez et al. 2003; Lewis et al. 2002), the mechanism that gradually reduces star formation might be responsible for morphological changes in these intermediate density regions (e.g., ram-pressure stripping). The mechanism is likely to stop star formation in late-spiral galaxies, then late-spiral galaxies becomes early-spirals and eventually turns into smaller S0s after their outer discs and spiral arms become invisible as young stars die. In the densest regions (above 6 Mpc^{-2} or inside of 0.3 virial radius), S0 fractions decreases radically and elliptical fractions increase. This is a contrast-

ing results to that in intermediate regions and it suggests that yet another mechanism is responsible for morphological change in these regions. Considering that the median sizes of elliptical galaxies are larger than that of S0 galaxies, one of the candidate mechanisms is merging scenario, where merging of S0 galaxies creates larger elliptical galaxies. The deficit of S0 galaxies at the densest regions are likely to be consistent with computer simulations based on merging scenario (Okamoto et al. 2001; Diaferio et al. 2002; Springel et al. 2000), which predicted small fraction of S0 galaxies. The existence of two different mechanisms itself is consistent with the discovery of Domiguez et al. (2001), where they found two different parameters governing the morphology-density relation in cluster centers and outskirts separately.

We also compared our morphology-density relation from the SDSS ($z \sim 0.05$) with that of the MORPHS data ($z \sim 0.5$). Two relations lie on top of each other, suggesting that the morphology-density relation was already established at $z \sim 0.5$ as is in the present universe. In the densest bin, a slight sign of excess elliptical fraction was seen in the SDSS data, which might be indicating the formation of additional elliptical galaxies between $z = 0.5$ and $z = 0.05$.

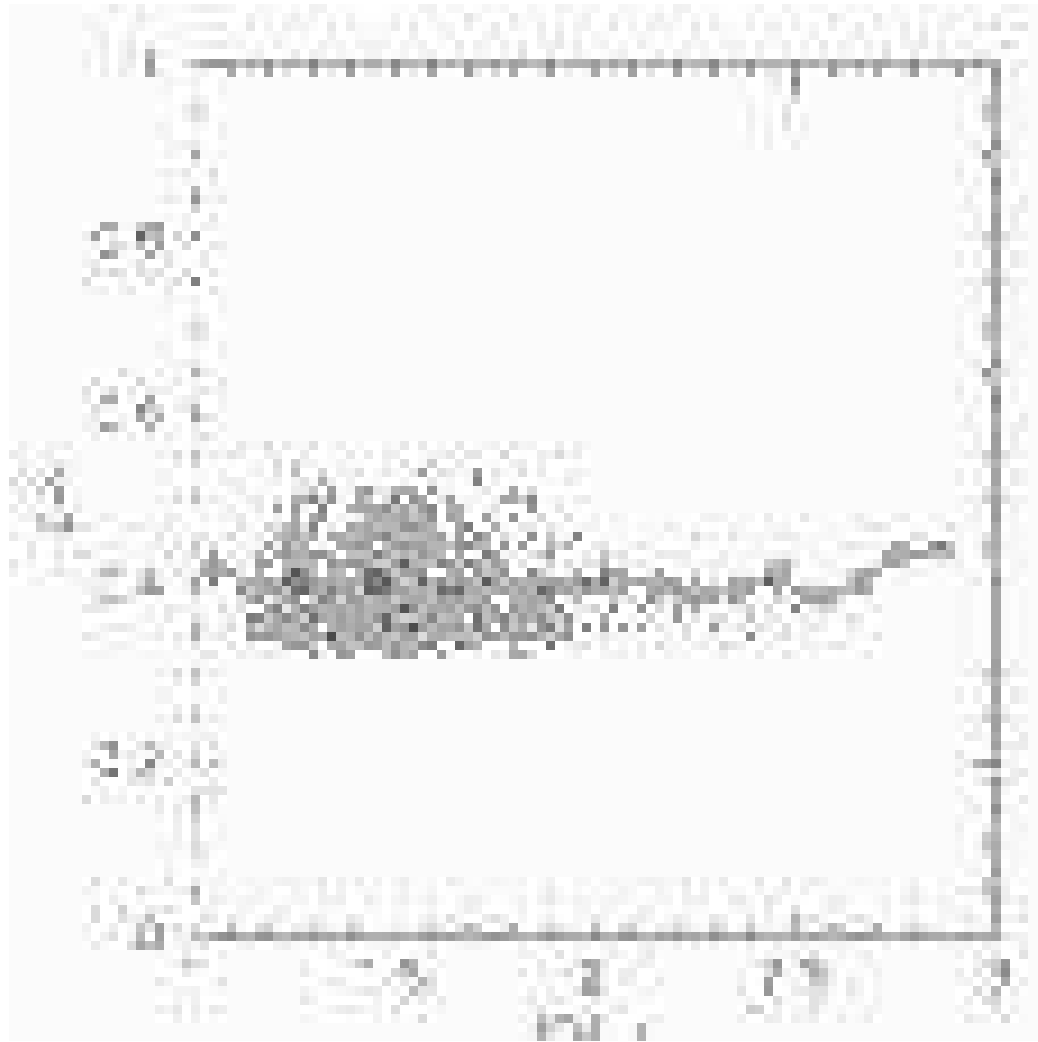


Figure 6.1: Seeing dependence of C_{in} for 7938 galaxies used in the present study. The solid lines show medians. 87% of our sample galaxies have seeing between 1.2 and 2 arcsec, where seeing dependence of C_{in} is negligible.

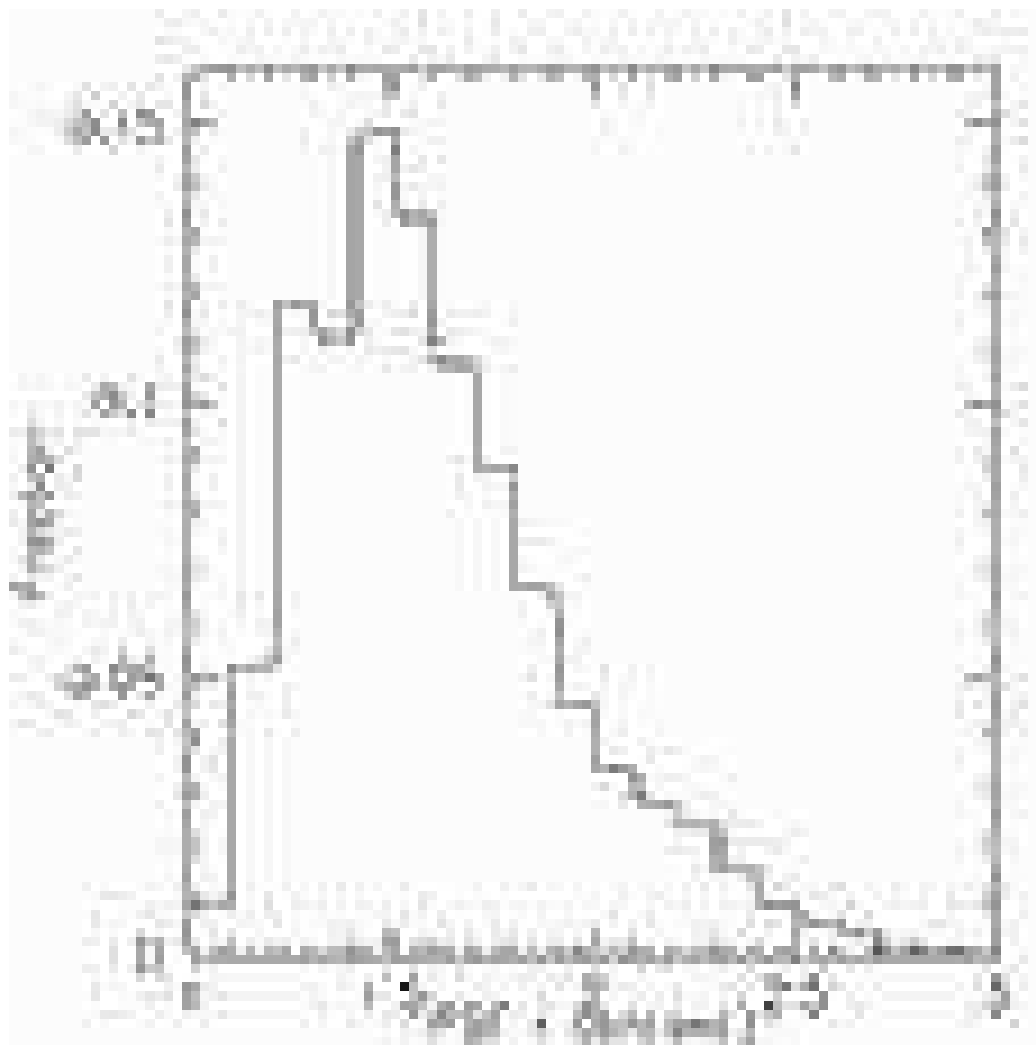


Figure 6.2: Distribution of seeing of the SDSS galaxies, measured in r band.

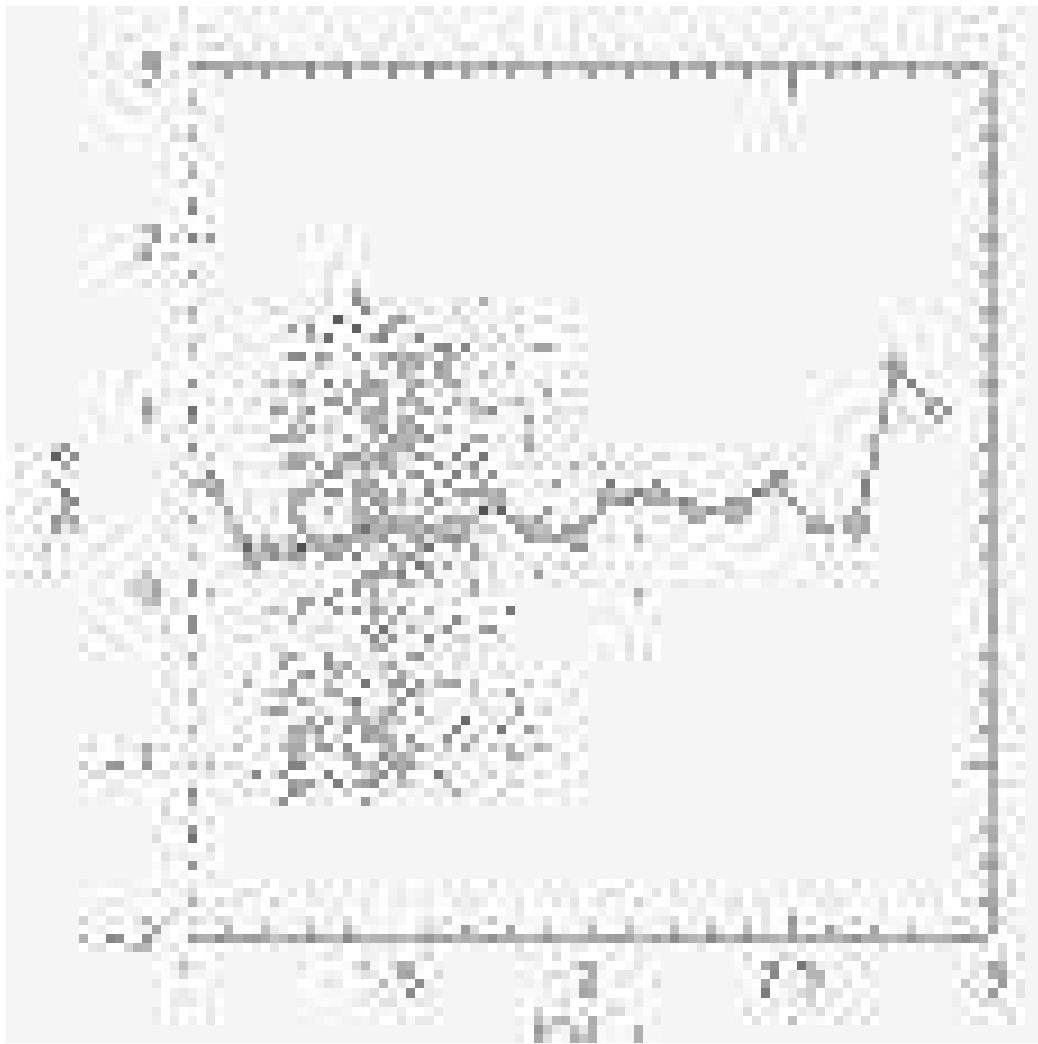


Figure 6.3: Seeing dependence of T_{auto} for 7938 galaxies used in the present study. The solid lines show medians of the distribution. T_{auto} is essentially independent of seeing size between 1.2 and 2 arcsec, where 87% of our sample galaxies lie.

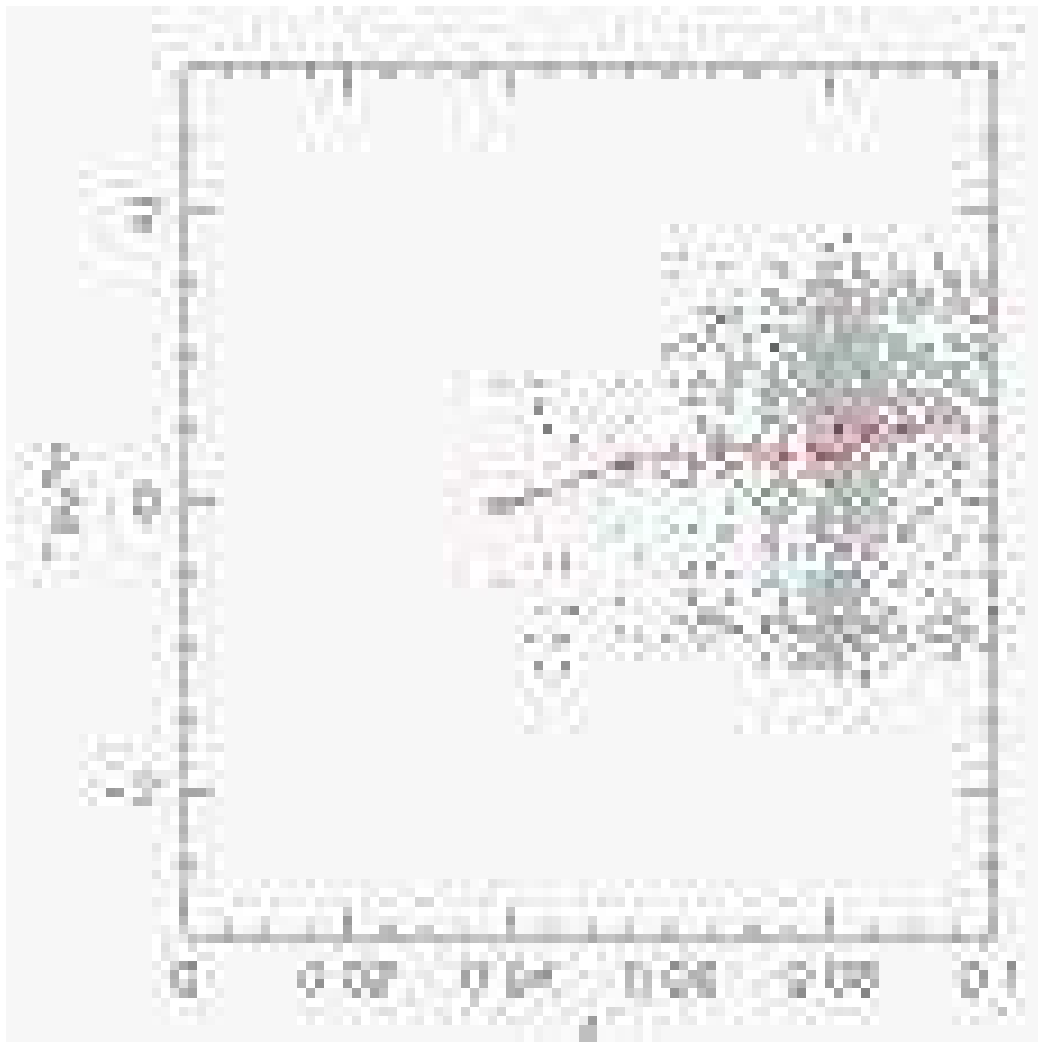


Figure 6.4: Redshift dependence of T_{auto} for 7938 galaxies used in the present study. The solid lines show medians of the distribution, which are consistent with constant throughout the redshift range we use ($0.05 < z < 0.1$). T_{auto} shows some deviation at lower redshift ($z < 0.04$) since an apparent size of a galaxy on the sky radically increases at this low redshift.

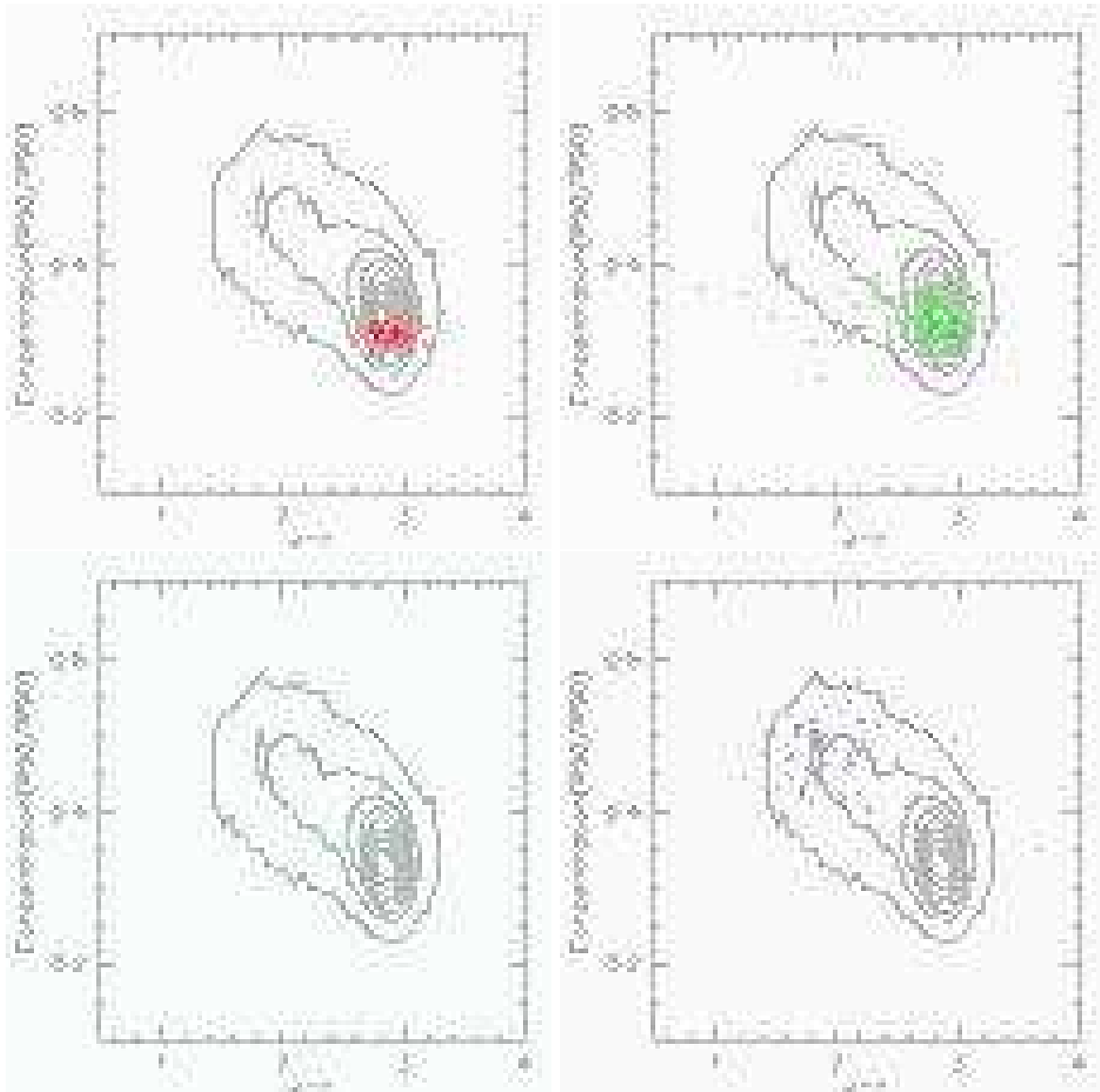


Figure 6.5: C_{in} is plotted against $u - r$. The contours show distribution of all 7938 galaxies in the volume limited sample. Points in each panel show the distribution of each morphological type of galaxies classified by eye (Shimasaku et al. 2001; Nakamura et al. 2003). Ellipticals are in the upper left panel. S0, Sa and Sc are in the upper right, lower left and lower right panels, respectively.

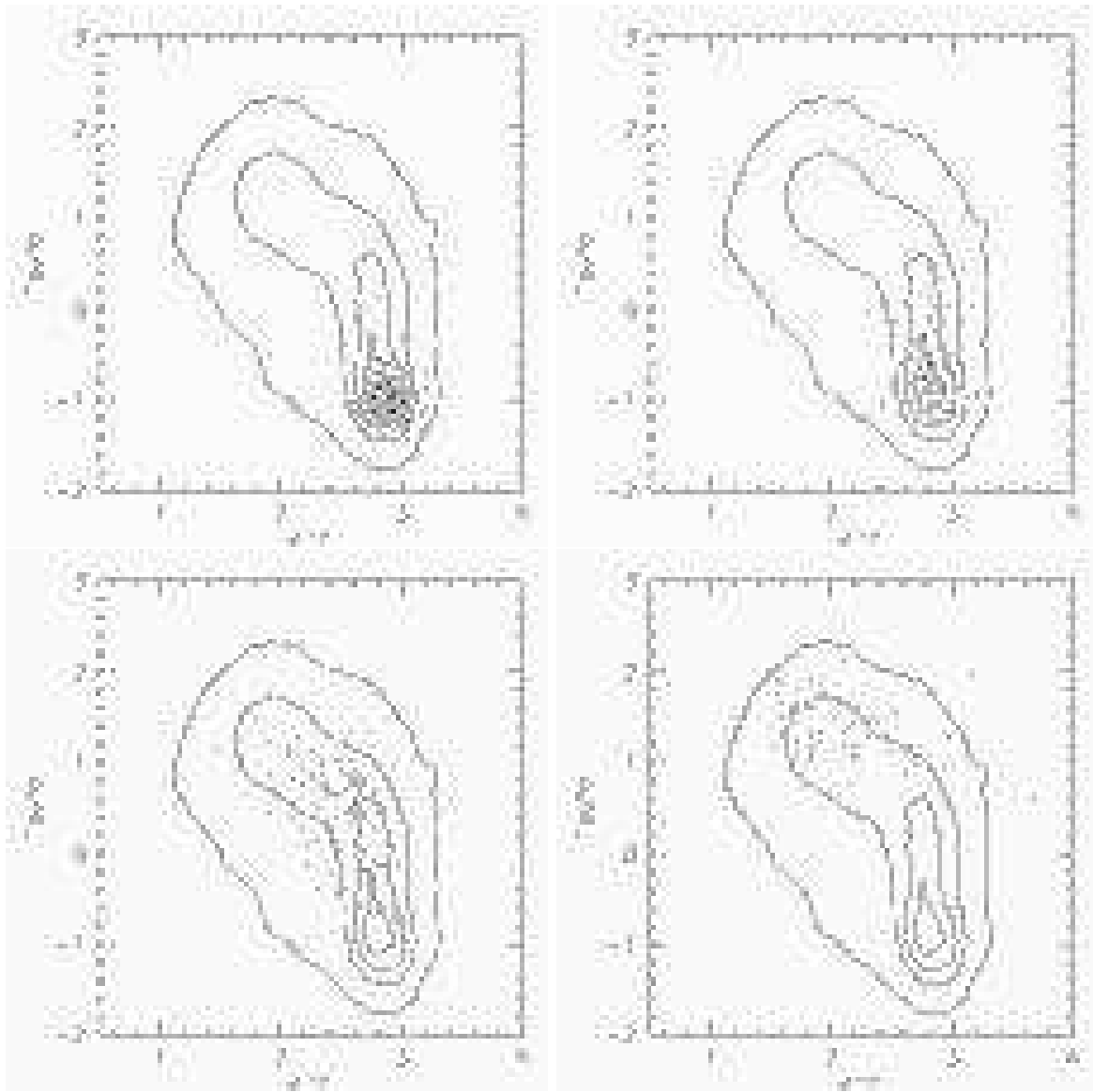


Figure 6.6: T_{auto} is plotted against $u - r$. The extension of the distribution around $u - r = 2.8$ is due to the inclination correction adopted in T_{auto} . The contours show distribution of all 7938 galaxies in the volume limited sample. Points in each panel show the distribution of each morphological type of galaxies classified by eye (Shimasaku et al. 2001; Nakamura et al. 2003). Ellipticals are in the upper left panel. S0, Sa and Sc are in the upper right, lower left and lower right panels, respectively.

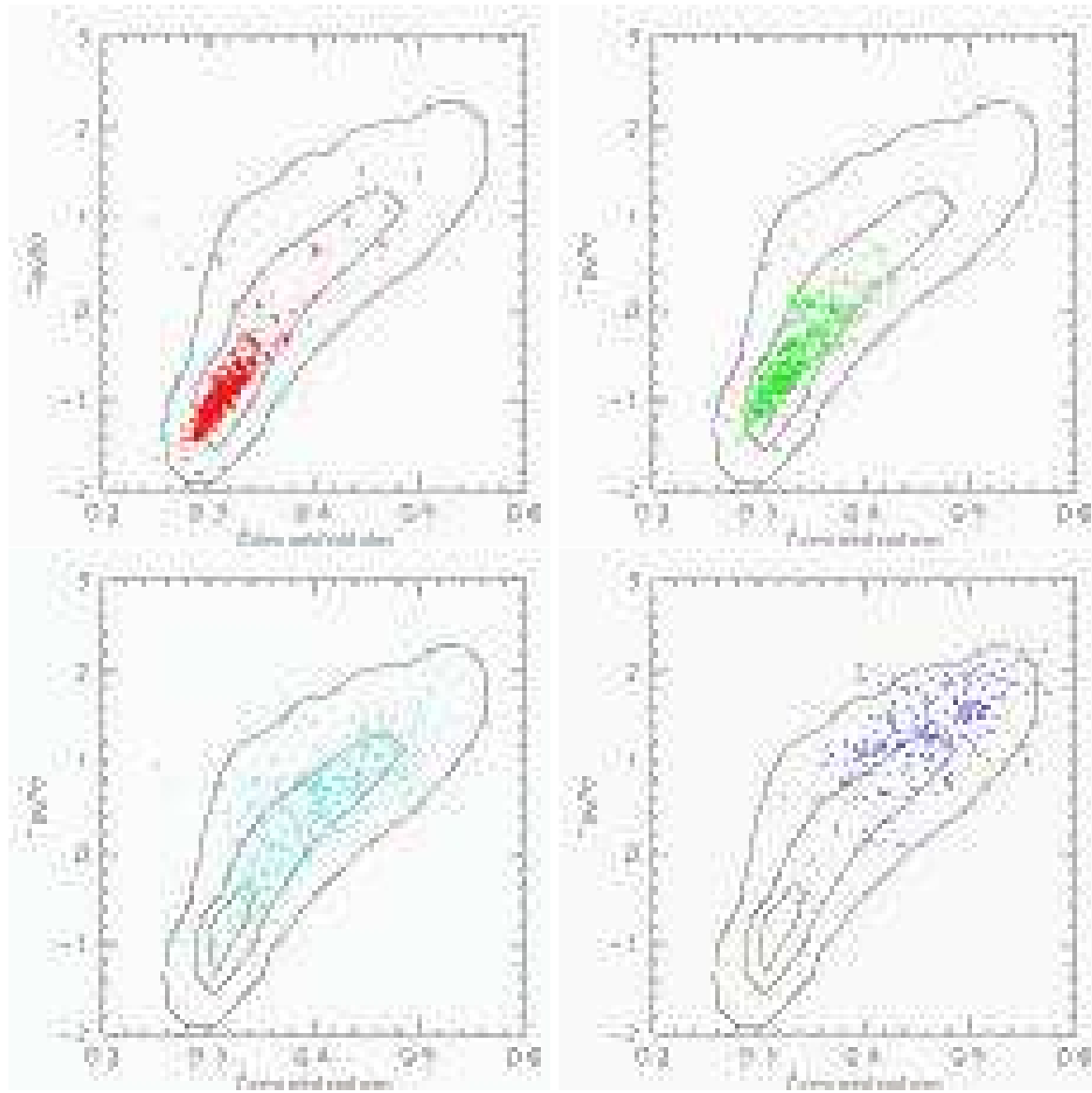


Figure 6.7: T_{auto} is plotted against C_{in} . The contours show distribution of all 7938 galaxies in the volume limited sample. A good correlation between two parameters is seen. The extension of the distribution toward the upper left corner is due to the inclination correction of T_{auto} . Points in each panel show the distribution of each morphological type of galaxies classified by eye (Shimasaku et al. 2001; Nakamura et al. 2003). Ellipticals are in the upper left panel. S0, Sa and Sc are in the upper right, lower left and lower right panels, respectively.

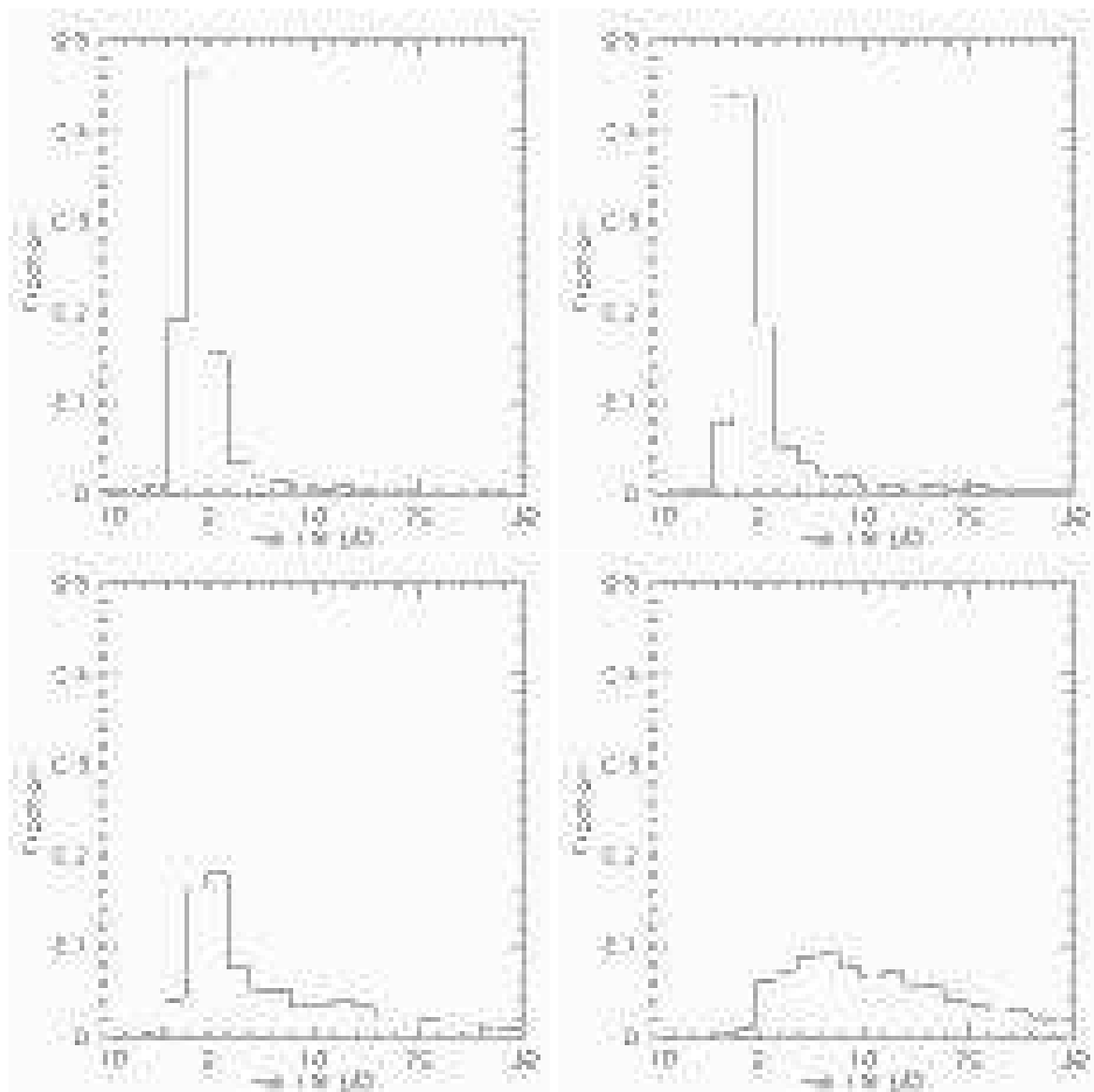


Figure 6.8: Distribution of H α EW for four types classified with *Tauto*. The histogram in each panel shows the distribution of each morphological type of galaxies classified by *Tauto*. Ellipticals are in the upper left panel. S0, Sa and Sc are in the upper right, lower left and lower right panels, respectively. An increase of H α EW toward later type galaxies suggests that our morphological classification works well.



Figure 6.9: Distribution of local galaxy density. The solid, dashed and dotted lines show distributions for all galaxies, galaxies within 0.5 Mpc from the nearest cluster and galaxies between 1 and 2 Mpc from the nearest cluster, respectively.

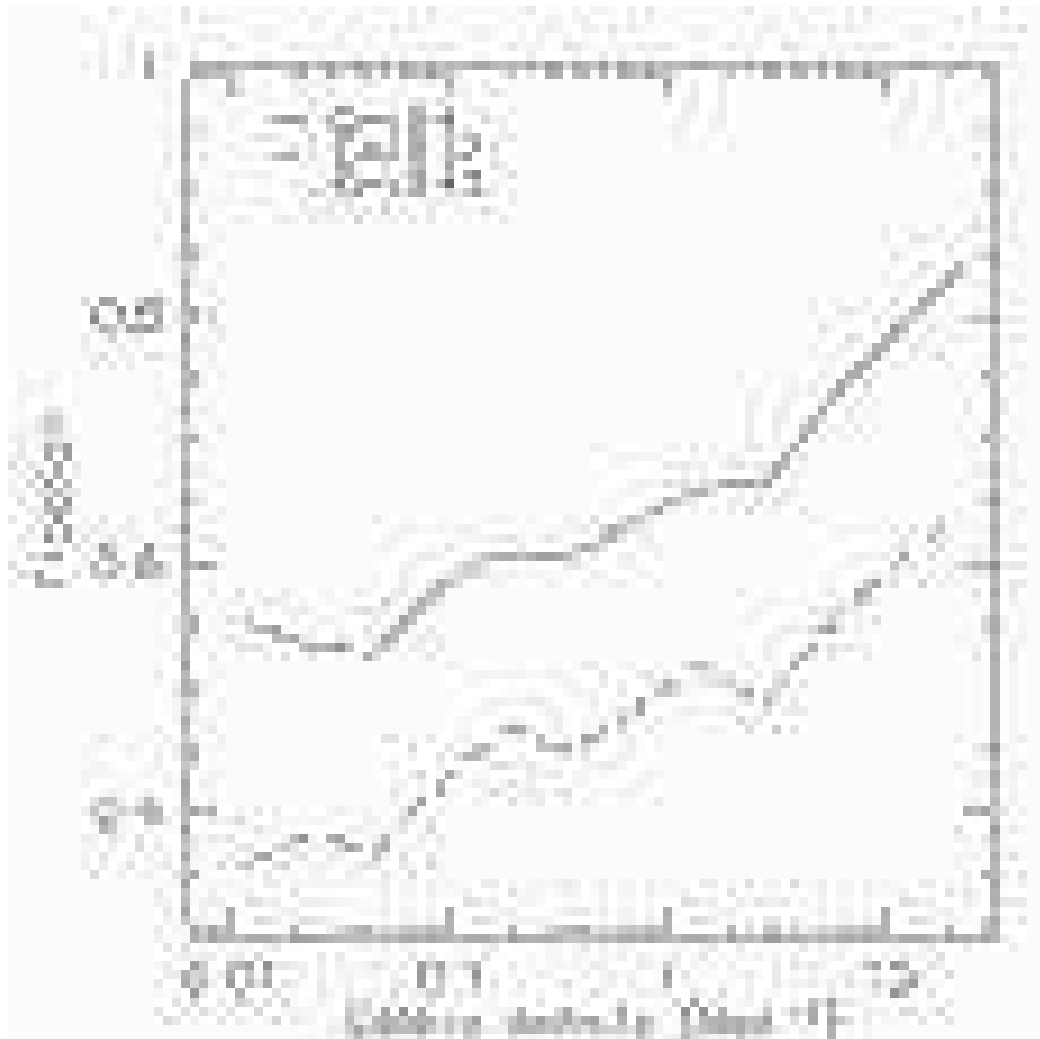


Figure 6.10: The morphology-density relation for three criteria of Cin . Fractions of elliptical galaxies are plotted against local galaxy density. Three criteria are $Cin < 0.4$, $Cin < 0.43$ and $Cin < 0.37$ in the solid, dashed and dotted lines, respectively.



Figure 6.11: The morphology-density relation for four types of galaxies classified with *Tauto*. The short-dashed, solid, dotted and long-dashed lines represent elliptical, S0, early-spiral and late-spiral galaxies, respectively.

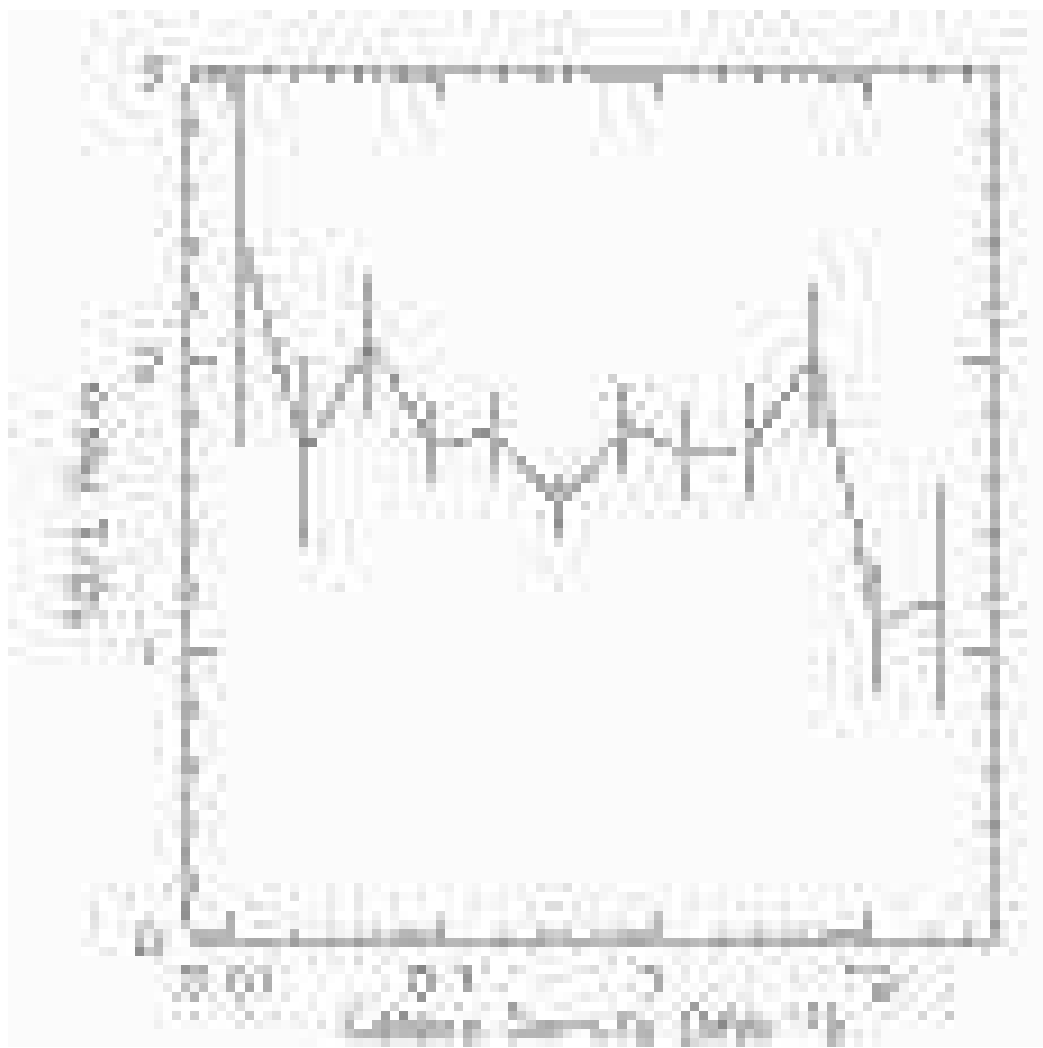


Figure 6.12: E/S0 number ratio as a function of local galaxy density.

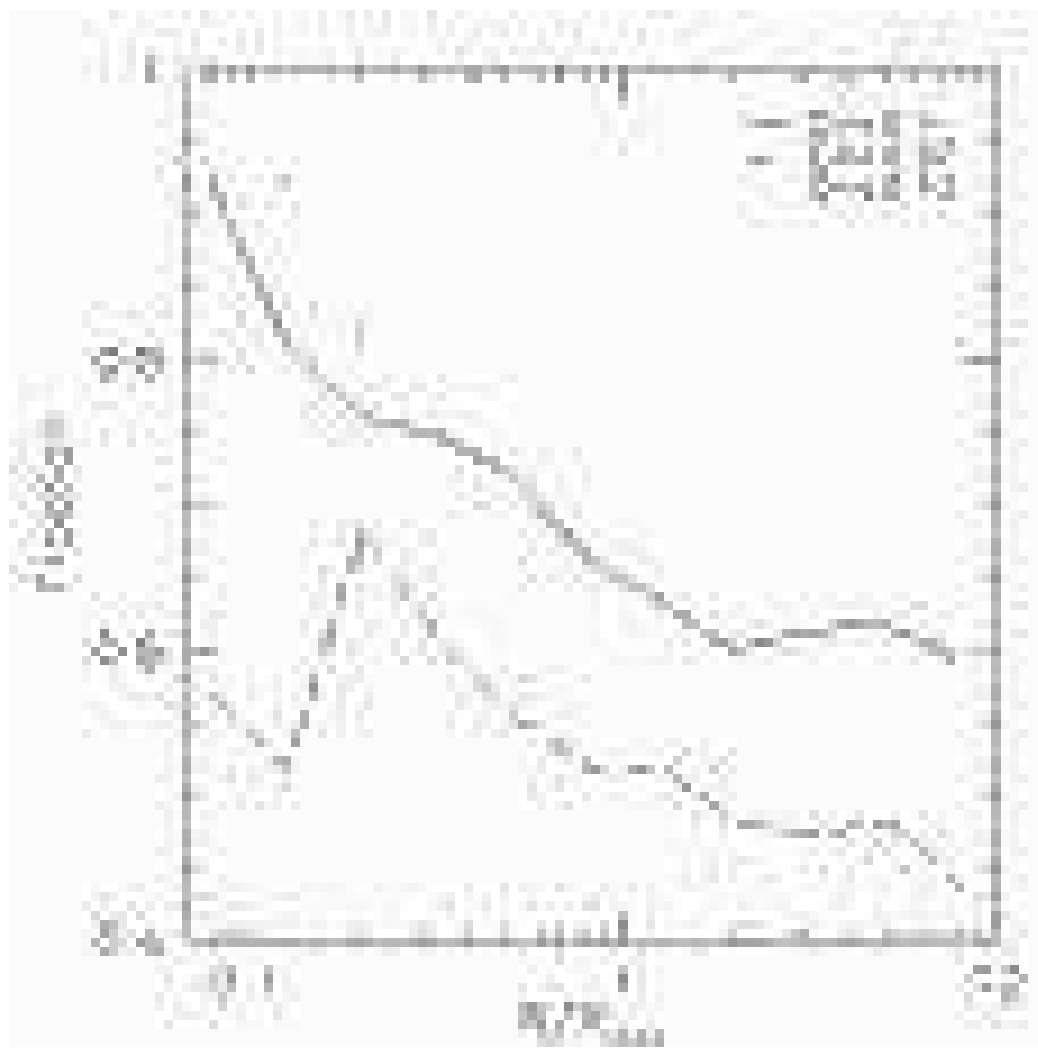


Figure 6.13: The morphology-radius relation. Fractions of elliptical galaxies are plotted against cluster centric radius to the nearest cluster. Criteria are $C_{in} < 0.4$, $C_{in} < 0.43$ and $C_{in} < 0.37$ in the solid, dashed and dotted lines, respectively.

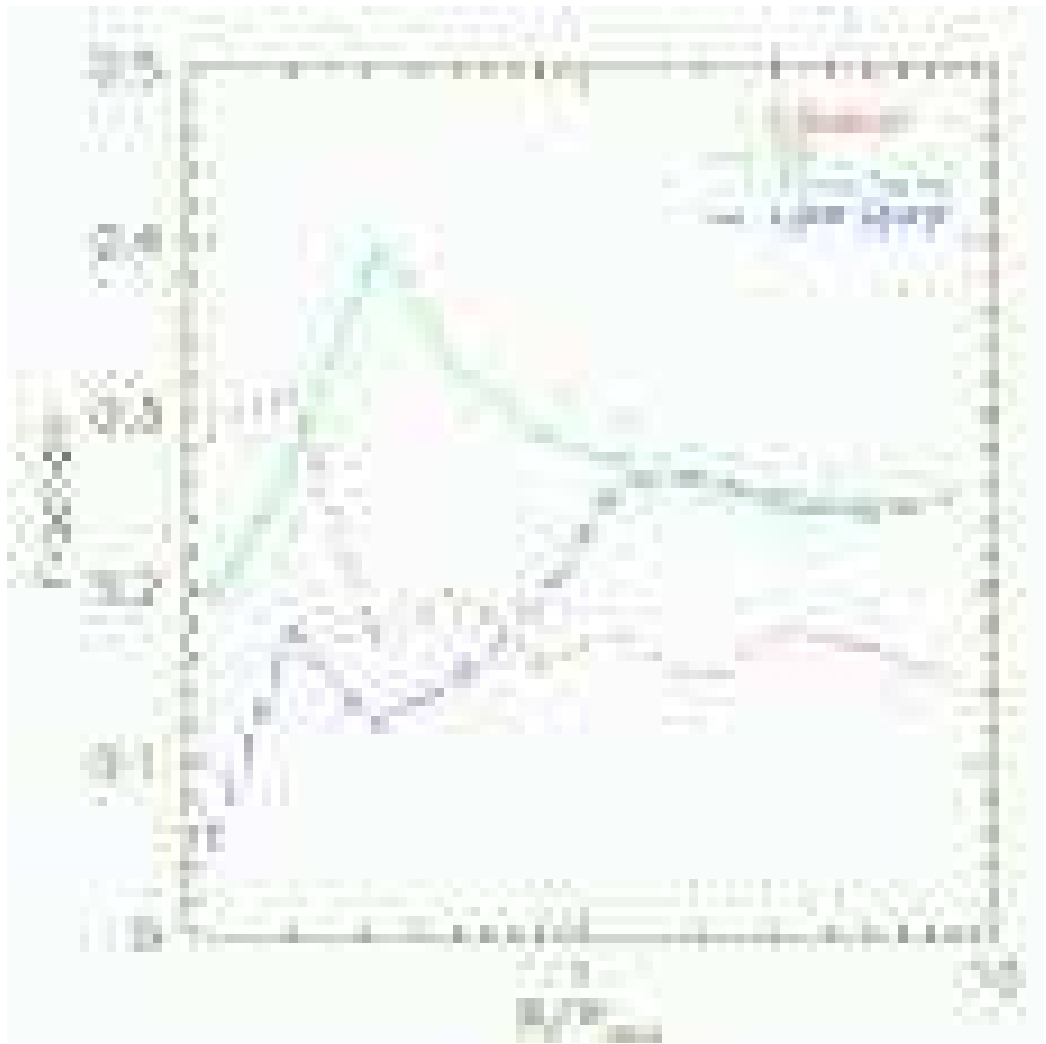


Figure 6.14: The morphology-radius relation. Fractions of each type of a galaxy is plotted against cluster centric radius to the nearest cluster. The short-dashed, solid, dotted and long-dashed lines represent elliptical, S0, early-spiral and late-spiral galaxies, respectively.

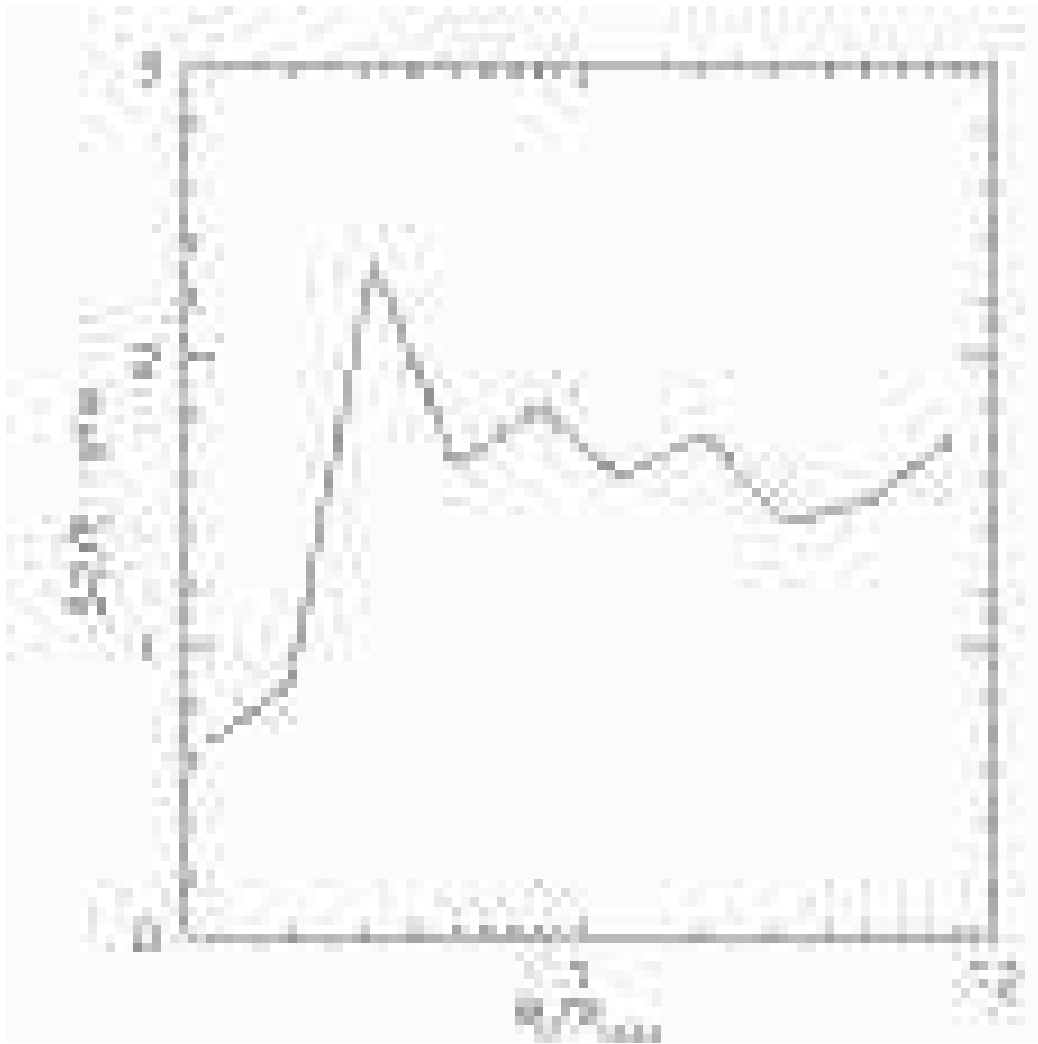


Figure 6.15: S_0 to elliptical number ratio is plotted against cluster centric radius. The ratio decreases at the cluster core region.

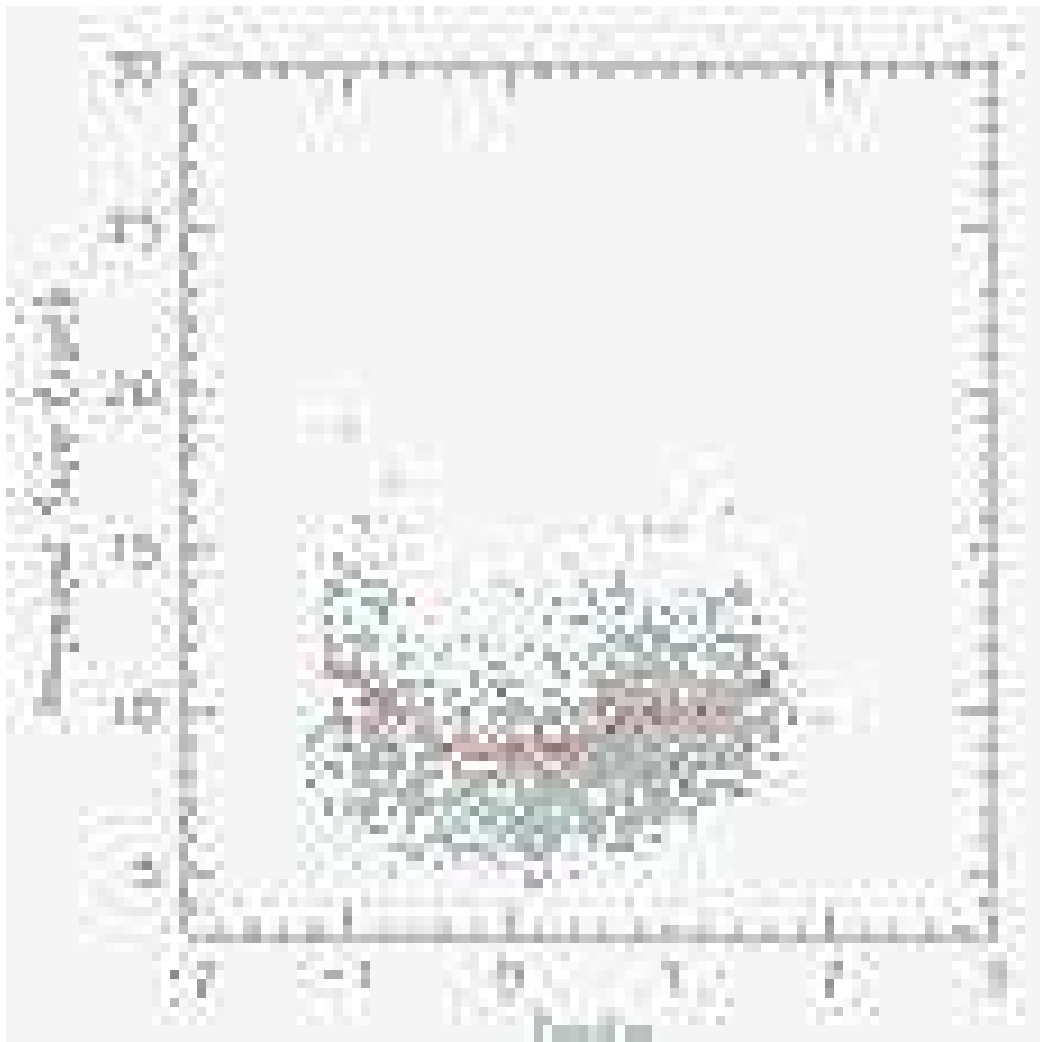


Figure 6.16: Physical sizes of all 7938 galaxies are plotted against T_{auto} . Petrosian 90% flux radius in r band is used to calculate physical sizes of galaxies. The solid line shows medians. It turns over around $T_{auto} \sim 0$, corresponding to S0 population.

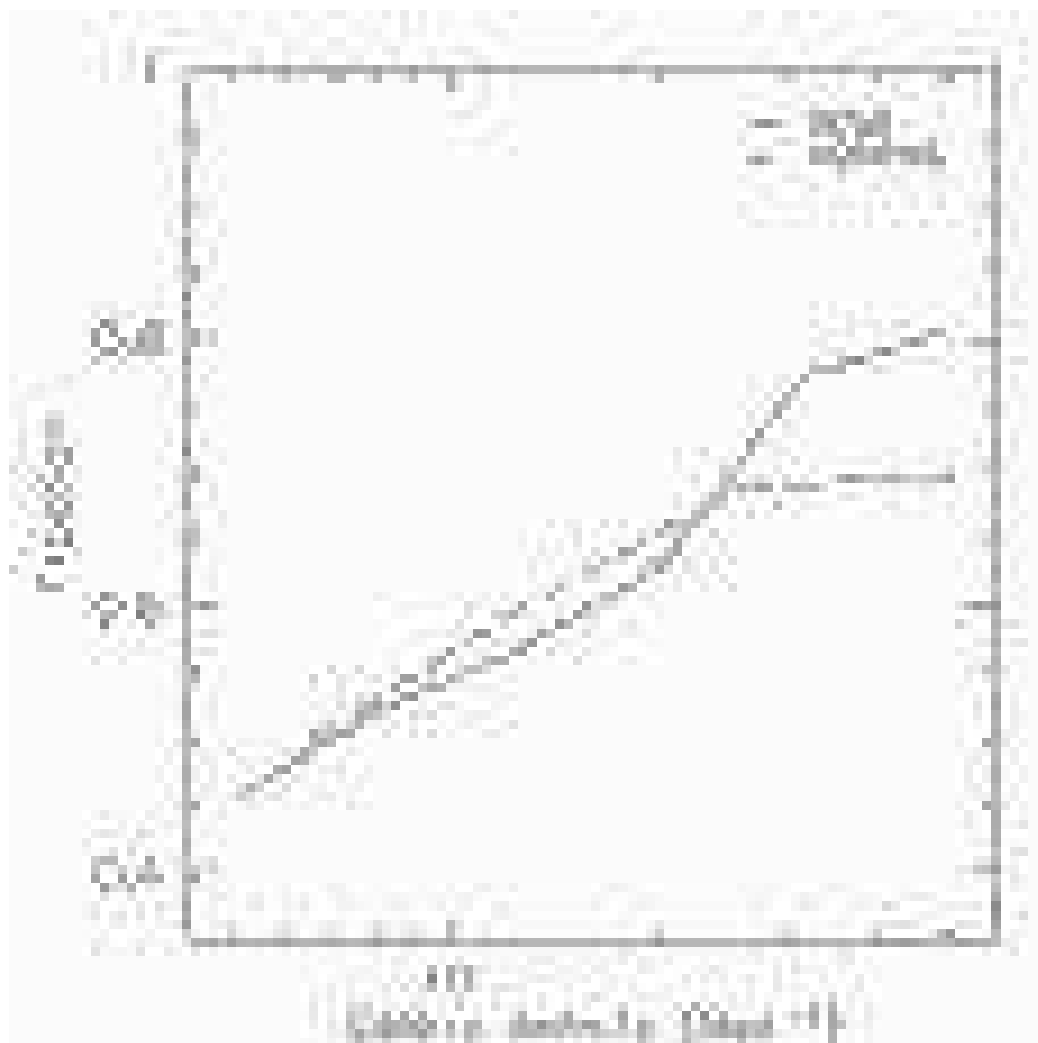


Figure 6.17: Comparison of the morphology-density relations of the SDSS(low redshift) and the MORPHS(high redshift). Fraction of elliptical galaxies are plotted against local galaxy density within 250 kpc. The MORPHS data are plotted in the solid line, and the SDSS data are plotted in the dashed line.

Table 6.1: Completeness and contamination rate of our four sample of galaxies classified by T_{auto} are calculated using eye-classified morphology.

Type	Completeness (%)	Contamination (%)
Elliptical ($T_{auto} \leq -0.8$)	70.3	28.2
S0 ($-0.8 \leq T_{auto} < 0.1$)	56.4	56.5
Early Spiral ($0.1 \leq T_{auto} < 1.0$)	53.1	24.1
Late Spiral ($1.0 \leq T_{auto}$)	75.0	45.9

Table 6.2: MORPHS cluster sample

Cluster	R.A.	Dec.	z	filter	$L_X(0.3\text{--}3.5)$	σ
A370#2	02 40 01.1	-01 36 45	0.37	F814W	2.73	1350 [34]
Cl1447+23	14 49 28.2	+26 07 57	0.37	F702W
Cl0024+16	00 26 35.6	+17 09 43	0.39	F814W	0.55	1339 [33]
Cl0939+47	09 43 02.6	+46 58 57	0.41	F814W	1.05	1081 [31]
Cl0939+47#2	09 43 02.5	+46 56 07	0.41	F814W	1.05	1081[31]
Cl0303+17	03 06 15.9	+17 19 17	0.42	F702W	1.05	1079 [21]
3C295	14 11 19.5	+52 12 21	0.46	F702W	3.20	1670 [21]
Cl0412-65	04 12 51.7	-65 50 17	0.51	F814W	0.08	...
Cl1601+42	16 03 10.6	+42 45 35	0.54	F702W	0.35	1166 [27]
Cl0016+16	00 18 33.6	+16 25 46	0.55	F814W	5.88	1703 [30]
Cl0054-27	00 56 54.6	-27 40 31	0.56	F814W	0.25	...

Chapter 7

The Environment of Passive Spiral Galaxies

7.1 Introduction

Recent morphological studies of distant cluster galaxies revealed the presence of an unusual population of galaxies with a spiral morphology and lack of star-formation activity (Couch et al. 1998; Dressler et al. 1999; Poggianti et al. 1999). The origins of these “passive spirals” have remained a mystery since it has been difficult to understand the existence of such galaxies. The phenomena suggest that star formation in these system has ended calmly, without disturbing their spiral arm structures. Many people speculated that cluster related phenomena might be responsible for creation of passive spiral galaxies since they are found during the cluster studies. However, it has not been well established if these phenomena are more relevant in clusters or they are common in the field regions as well, simply because it has been difficult to study this rare class of galaxies in the field region.

Also an existence of a similar type of galaxies has been reported. Galaxies with a low arm inter-arm contrast in their disks were classified as anemic by van den Bergh (1976). He found the excess of anemic spiral galaxies in Virgo cluster. Various HI follow-up observations revealed lower gas density in anemic spiral galaxies, which, presumably, is the cause of lower star formation rate and smoother spiral arms (Bothun & Sullivan 1980; Wilkerson 1980; Phillipps 1988; Cayatte et al. 1994; Bravo-Alfaro et al. 2001). Especially, Elmegreen et al. (2002) found the gas surface density of anemic spirals is below the threshold for star formation (Kennicutt 1989), revealing low star formation in anemic spirals in fact comes from low gas density. Although the definition of anemic spiral galaxies is somewhat different from that of passive spirals, considering similarities in properties (presence of spiral arms and lack of star formation), these two types of galaxies

could be essentially the same population of galaxies, sharing the same nature and origin.

Various possible mechanism are proposed to explain these phenomena. Poggianti et al. (1999) found passive spiral galaxies in their sample of distant clusters and speculated that these findings show that the time scale of spectral change of cluster galaxies are shorter than the time scale of morphological change of galaxies. They proposed ram-pressure stripping (Gunn & Gott 1976) as a possible physical mechanism responsible for these phenomena. Another possible cause is abrupt truncation of gas infall onto disks from the halo regions (Larson et al. 1980). Dynamical causes such as major galaxy merger or harassment, which explain other properties of cluster galaxies very well (e.g., the Butcher-Oemler effect; Butcher & Oemler 1978, 1984), cannot explain these phenomena since such processes disturb spiral arms and do not end up with passive spirals. A pioneering work to simulate passive spiral galaxies by combining numerical simulation and a phenomenological model was performed by Bekki et al. (2002). They demonstrated that halo gas stripping caused by dynamical interaction between halo gas and the hot ICM is a plausible mechanism. Although these mechanisms are all plausible, the final conclusion has not yet drawn about what mechanisms are most responsible for these phenomena.

It is also interesting to investigate a possible link between passive spirals and statistical observational features of cluster galaxies. In cluster regions, it is known that fractions of blue galaxies are larger at higher redshifts. (the Butcher-Oemler effect; Butcher & Oemler 1978, 1984; Rakos & Schombert 1995; Couch et al. 1994; 1998; Margoniner & De Carvalho 2000; Margoniner et al. 2001; Ellingson et al. 2001; Kodama & Bower 2001; Goto et al. 2003a; Chapter 5). Cluster galaxies are also known to change their morphology, e.g., spiral to S0 transition during the cosmic time scale (Couch & Sharples 1987; Dressler et al. 1997; Couch et al. 1998; Fasano et al. 2000; Diaferio et al. 2001). Goto et al. (2003a; Chapter 5) referred to this as the morphological Butcher-Oemler effect. If passive spiral galaxies are of cluster origin, they would fit well in both spectral and morphological evolution of cluster galaxies. They may be galaxies in transition between blue and red, or spiral and S0s.

Since the Sloan Digital Sky Survey (SDSS; York et al. 2000) observes spectra of one million galaxies in one quarter of the sky. It provides us with the opportunity to study this interesting population of galaxies in all environments; from cluster core regions to general field regions. In addition, wide spectral coverage of 3800-9000 Å allows us to study both [OII] and H α emission lines at the same time, which can reduce possible biases from dust extinction and stellar absorption on the emission lines. In this Chapter, we concentrate in revealing the environment of passive spiral galaxies. In Section 7.2, we explain the data used in the study. In Section 7.3, we carefully define passive spiral galaxies. In Section 7.4, we present the environment of passive spiral galaxies. In Section 7.5, we discuss the possible caveats and interpretation of the results. In Section 7.6, we summarize our

findings. The cosmological parameters adopted throughout this chapter are $H_0=75$ km s $^{-1}$ Mpc $^{-1}$, and $(\Omega_m, \Omega_\Lambda, \Omega_k) = (0.3, 0.7, 0.0)$.

7.2 Data

In this section, we outline the data used in this chapter. The galaxy catalog is taken from the Sloan Digital Sky Survey (SDSS; see Fukugita et al. 1996; Gunn et al. 1998; Lupton et al. 1999, 2001, 2002; York et al. 2000; Hogg et al. 2001; Pier et al. 2002; Stoughton et al. 2002; Strauss et al. 2002 and Smith et al. 2002 for more detail of the SDSS data). The SDSS imaging survey observes one quarter of the sky to depths of 22.3, 23.3, 23.1, 22.3 and 20.8 in the u, g, r, i and z filters, respectively (See Fukugita et al. 1996 for the SDSS filter system, Hogg et al. 2002 and Smith et al. 2002 for its calibration). Since the SDSS photometric system is not yet finalized, we refer to the SDSS photometry presented here as u^*, g^*, r^*, i^* and z^* . We correct the data for galactic extinction determined from the maps given by Schlegel, Finkbeiner & Davis (1998). We include galaxies to $r^*=17.7$ (Petrosian magnitude), which is the target selection limit of the main galaxy sample of the SDSS spectroscopic survey. The spectra are obtained using two fiber-fed spectrographs (each with 320 fibers) with each fiber subtending 3 arcseconds on the sky. (We investigate aperture bias due to the limited size of the SDSS fiber spectrograph in Section 7.5.2). The wavelength coverage of the spectrographs is 3800Å to 9200Å, with a spectral resolution of 1800. These spectra are then analyzed via the SDSS SPECTRO1D data processing pipeline to obtain various quantities for each spectrum such as redshift, spectral classification and various line parameters. (see Stoughton et al. 2002; Frieman et al., in prep, for further details). The SDSS has taken 189,763 galaxy spectra as of the date of writing. Among them we restrict our sample to galaxies with S/N in g band greater than 5 and with a redshift confidence of ≥ 0.7 . Since we use concentration parameter in selecting passive spiral galaxies, we also remove galaxies with PSF size in r band greater than 2.0" to avoid poor seeing mimicing less concentrated galaxies. Then we make a volume limited sample by restricting our sample to $0.05 < z < 0.1$ and $M_{r^*} < -20.5$. This magnitude limit corresponds to $M^*+0.3$ mag (Blanton et al. 2001). The lower redshift cut is made to avoid strong aperture effects (see Gomez et al. 2003 for detailed investigation in aperture effects in the SDSS data). When calculating absolute magnitudes, we use a k -correction code provided by Blanton et al. (2002; v1_11). In this volume limited sample, there are 25,813 galaxies remained.

7.3 Selection of Passive Spiral Galaxies

7.3.1 Line Measurements

We measure [OII], H α and H δ equivalent widths (EWs) with the flux summing method as described in Goto et al. (2003b; Appendix A). We briefly summarize the method here. To estimate continuum, we fit a line using wavelength ranges around each line as listed in Table 7.1. The continuum values are weighted according to the inverse square of the errors during the fitting procedure. We then sum the flux in the wavelength range listed in the same table to obtain the equivalent width of the lines. For H δ line, we used two different wavelength range; wider one for strong line and narrower one for weak line (details are described in Goto et al. 2003b; Appendix A). Note that for H α line, we do not deblend adjacent [NII] lines. As a result, our H α equivalent width have contamination from [NII] lines. However, the contamination is less than 5% from [NII](6648Å) and less than 30% from N[II](6583Å). These measurements show good agreement with measurements via Gaussian fitting (Goto et al. 2003b; Appendix A).

We quantified errors of these measurement using spectra observed twice in the SDSS. The procedure is exactly the same as described in Goto et al. (2003b; Appendix A). First, the difference of equivalent width are plotted against S/N of spectra . Then we fit 3rd polynomial to the 1σ of the distribution. The polynomial is later used to assign errors to every spectra according to its S/N. The exact formula are given in Goto et al. (2003b; Appendix A). Typical errors of high signal-to-noise spectra are 1.3, 1.0 and 0.4 Å for [OII], H α and H δ EWs, respectively (See Figures 9-11 of Goto et al. 2003b; Appendix A).

7.3.2 Selection Criteria

We select passive spiral galaxies using the following criteria. Galaxies with the inverse of concentration parameter, $C_{in} > 0.5$. The inverse concentration parameter (C_{in}) is defined as the ratio of Petrosian 50% light radius to Petrosian 90% light radius in r band (radius which contains 50% and 90% of Petrosian flux, respectively). Shimasaku et al. (2001) and Strateva et al. (2001) studied the completeness and contamination of this parameter in detail. See Goto et al. (2002b; Chapter 4) and Gomez et al. (2003) for more usage of this parameter. The border line between spiral galaxies and elliptical galaxies are around $C_{in}=0.33$. Therefore $C_{in} > 0.5$ picks up very less concentrated spiral galaxies. In different work, 549 galaxies in our volume limted sample were manually classified by Shimasaku et al. (2001) and Nakamura et al. (2003). In Figure 7.1, we overplot eye-classified galaxies on a C_{in} v.s. $u - r$ plane. Contours show the distribution of all galaxies in our volume limited sample. Note that our volume limited sample contains

high fraction of concentrated galaxies as shown by contours due to its bright absolute magnitude limit (Yagi et al. 2002; Goto et al. 2002b; Chapter 4). In the top left panel, eye classified ellipticals are overplotted. In the top right, bottom left, bottom right panels, eye-classified S0s, Sa-Sb, Sc or later are overplotted, respectively. As is shown in Strateva et al. (2001), $u - r = 2.2$ also separates early and late-type galaxies well. As these panels show, few of elliptical or S0 galaxies have $C_{in} > 0.5$. Therefore, we in fact are able to select spiral galaxies using C_{in} parameter, without significant contamination from E/S0 population. We caution readers that the selection of less concentrated galaxies has a known bias against edge-on galaxies, in the sense that edge-on disc galaxies are excluded from our sample. The detailed investigation and correction of this bias will be presented in Yamauchi et al. (in prep.). However, we accept this bias in our sample selection since (i) the bias is independent of local galaxy environment; (ii) edge-on galaxies might be affected by larger amount of dust extinction, and thus could cast some doubts on truly passive nature of our sample galaxies.

From spectral features, we select galaxies using the following criteria.

$$[OII] \text{ } EW - 1\sigma_{error} < 0, \quad (7.1)$$

$$H\alpha \text{ } EW - 1\sigma_{error} < 0, \quad (7.2)$$

where emission lines have positive signs. In other words, we select galaxies with [OII] and H α less than 1 σ detection (in emission). A galaxy which satisfies both of the concentration and spectral criteria is regarded as a passive spiral galaxy in this work. Figure 7.2 shows the distribution of passive spiral galaxies in the C_{in} v.s. $u - r$ plane.

Figure 7.3 shows example images ($30'' \times 30''$) of passive spiral galaxies. In Figure 7.4, corresponding spectra are shown. Unusual properties of these galaxies are already clear just by comparing these two figures, i.e., clear spiral arm structures are seen in the images, whereas there are no current star formation activity as shown by the lack of [OII] and H α emission lines in the spectra. It is interesting to study where these unique features originate from. For a comparison purpose, we also select active (normal) spiral galaxies in our sample as galaxies with $C_{in} > 0.5$ and 1 σ detections in both [OII] and H α in emission. We removed galaxies with AGN signature from the active spiral sample using a prescription given in Kewley et al. (2001) and Gomez et al. (2003). When a galaxy satisfies all three line ratio criteria to be an AGN (Figure 15, or eq. (5)(6)(7) of Kewley et al. 2001), we removed it from our sample as an AGN. Images and spectra of active (normal) spiral galaxies are shown in Figures 7.5 and 7.6. Compared with these galaxies, passive spirals have smoother profile.

Among 25813 galaxies in our volume limited sample ($0.05 < z < 0.1$ and $M_r^* < -20.5$), there are 73 ($0.28 \pm 0.03\%$) passive spiral galaxies in total. The number of active spirals

is 1059 ($4.10 \pm 0.12\%$). Relatively small percentages stem from our stringent criteria for the inverse concentration parameter, C_{in} .

7.4 Environment of Passive Spiral Galaxies

7.4.1 Local Galaxy Density

First, we aim to clarify the environment where passive spiral galaxies live. For each galaxy in our volume limited sample ($0.05 < z < 0.1$ and $Mr^* < -20.5$), we measure the projected metric distance to the 5th nearest galaxy (within ± 3000 km/s of the galaxy in redshift space) within the same volume limited sample. If the projected area (in Mpc^2), enclosed by the 5th nearest neighbor distance, touched the boundaries of the SDSS data, we corrected the area appropriately for the amount of missing area outside the survey boundaries. Then, we divide 5 (galaxies) by the area subtended by the 5th nearest galaxy to obtain local galaxy density in Mpc^{-2} . This methodology allows us to quote pseudo three-dimensional local galaxy densities for all our galaxies in the volume limited sample and without requiring any corrections for background and foreground contamination.

In Figure 7.7, we plot the local density distribution of passive spiral galaxies in the dotted line. The solid line shows distribution of all galaxies in our volume limited sample. The long-dashed line shows distribution of cluster galaxies defined as galaxies within 0.5 Mpc from the nearest C4 galaxy cluster (Miller et al. 2003; Gomez et al. 2003) in angular direction and within $\pm 3000 km s^{-1}$ from the redshift of the cluster. Kolmogorov-Smirnov tests show that all the distributions are different from each other with more than 99.9% significance level. The distribution of passive spiral galaxies (the dotted line) are right in the middle of cluster galaxies and field galaxies. It is also shown that passive spiral galaxies avoid the densest cluster core regions, and at the same time they do not show the same distribution as field galaxies. For a comparison, we plot a distribution of active (normal) spiral galaxies by the short-dashed line. Compared with that of all galaxies, the distribution slightly shifts to less dense environment, as expected from the morphology-density relation. The distribution of active spiral galaxies is different from that of passive spirals with more than 99.9% significance.

7.4.2 Cluster Centric Radius

In Figure 7.8, we plot the distribution of passive spiral galaxies as a function of cluster-centric radius. Here cluster-centric radius is measured as projected distance to the nearest cluster within ± 3000 km/s from the cluster redshift. Galaxies which do not have any cluster within ± 3000 km/s are not included in this analysis. The cluster list is taken from Miller et al. (2003), which measures a cluster center as the position of the brightest cluster

galaxy. The physical distance is normalized to virial radius using the relation given in Girardi et al. (1998). We divide distributions by that of all galaxies and then normalize them to unity for clarity. Note that comparisons of fractions among different curves are meaningless due to this normalization. The dotted, hashed line shows the distribution of passive spiral galaxies. The solid lines show that of active (normal) spiral galaxies. The dashed line is for early-type galaxies selected using C_{in} parameter ($C_{in} < 0.33$) with no constraints on emission lines. The fraction of early-type galaxies is higher at smaller cluster-centric-radii and that of spiral galaxies is higher at larger radii, which represents so-called “the morphology-density relation” (Dressler et al. 1980, 1997; Postman & Geller 1984; Fasano et al. 2000; Goto et al. 2003c; Chapter 6). Passive spiral galaxies reside preferentially in 1-10 virial radius, which, along with the results shown in Figure 7.7, suggests that they live in cluster infalling regions.

7.4.3 Photometric & Spectroscopic Properties

In Figure 7.9, we plot the distribution of passive spiral galaxies in restframe $g - r - i$ plane. Instead of Petrosian magnitude, we use model magnitude to compute colors of galaxies since signal-to-noise ratio is higher for model magnitude. In the SDSS, model magnitudes are measured using Petrosian radius measured in r band. (Thus the same radius is used to measure model magnitudes in 5 filters. See Stoughton et al. 2002 for more details on the SDSS magnitudes.) The observed color are k -corrected to the restframe using k -correction given in Blanton et al. (2002; v1_11). Contours show the distribution of all 25813 galaxies in the volume limited sample for comparison. A peak of the contour around $(g - r, r - i) = (0.75, 0.4)$ consists of elliptical galaxies. The distribution of spiral galaxies extends to the bluer direction in both $g - r$ and $r - i$. Interestingly, passive spiral galaxies are almost as red as elliptical galaxies in $g - r$, reflecting truly passive nature of these galaxies. Note that colors are photometrically measured, thus they are free from the aperture bias. In $r - i$ color, some passive spirals are almost as blue as spiral galaxies.

In Figure 7.10, we present restframe $J - K$ v.s. $r - K$ colors of passive and active galaxies in the open and solid dots, respectively. Infrared colors are obtained by matching our galaxies to the Two Micron All Sky Survey (2MASS; Jarrett et al. 2000) data. Infrared magnitudes are shifted to restframes using k -corrections given in Mannucci et al. (2001). Among our sample galaxies, 31/73 passive spirals (9317/25813 all galaxies) were measured with 2MASS. As in the previous figure, the solid lines show distribution of all galaxies in the volume limited sample. Compared with the solid lines, active spirals show slightly bluer distribution in $r - K$. Passive spirals do not show significantly bluer distribution in $r - K$ than all galaxies.

In Figure 7.11, we plot distributions of $H\delta$ EW for passive spirals (dotted lines), active

spirals (dashed lines) and all galaxies (solid lines) in the volume limited sample. $H\delta$ EWs are measured using the flux summing method discussed in Goto et al. (2003b; appendix A). The flux summing method is robust for weak absorption lines and noisy spectra. In the figure, absorption lines have positive EWs. As shown in the figure, passive spirals have very weak $H\delta$ absorption peaked around 0Å. In contrast, active spirals have much stronger $H\delta$ absorption, reflecting their strong star formation activity. Since $H\delta$ absorption becomes strong only when A stars are dominant in galaxy spectra, it is a good indicator of post-starburst phase of a galaxy. For example, E+A galaxies (Zabludoff et al. 1996; Balogh et al. 1999; Dressler et al. 1999; Poggianti et al. 1999; Chapters A and B) are thought to be a post-starburst galaxy since they do not have any current star formation (no [OII] nor $H\alpha$ in emission), but do have many A stars (strong $H\delta$ absorption). Such a phase can only appear when a starbursting galaxy truncates its starburst (a post-starburst phase). More details on $H\delta$ strong galaxies can be found in Goto et al. (2003b; appendix A). Therefore, small $H\delta$ EWs of passive spirals indicate that they are not in a post-starburst phase. The origin of passive spirals are likely to be different from that of E+A (or post-starburst) galaxies. Passive spirals seem to have stopped their star formation gradually rather than sudden truncation.

7.5 Discussion

7.5.1 A Transient in Galaxy Evolution

In Section 7.3, we have selected unusual population of galaxies with spiral morphology and without emission lines such as $H\alpha$ and [OII]. The optical color-color diagram (Figure 7.9) also revealed that these galaxies are as red as elliptical galaxies, reflecting passive nature of these galaxies. One possible explanation to these galaxies are heavy obscuration by dust. In such a case, passive spiral galaxies might have star formation activity just as normal galaxies, but the star formation activity might be hidden by dust. The scenario could be consistent with both of our observational results; lack of emission lines and red colors in optical. However, in $r - K$ color (Figure 7.10), passive spiral galaxies do not appear to be much redder than normal galaxies. This is against dust enshrouded scenario which should results in very red $r - K$ color, and thus suggesting truly passive nature of these galaxies. In addition, it is not likely that very dusty galaxies preferentially live in cluster infalling regions.

In Section 7.4, we revealed that passive spiral galaxies preferentially live in cluster infalling region, using both local galaxy density (Figure 7.7) and cluster-centric-radius (Figure 7.8). This is direct evidence to connect the origins of these galaxies to cluster environment. The characteristic environments are $1\sim2 \text{ Mpc}^{-2}$ in local galaxy density

and 1~10 virial radius in cluster-centric-radius. Quite interestingly, these environments coincide with characteristic density and radius where star formation rate declines toward cluster center or dense environment. Gomez et al. (2003) and Lewis et al. (2002) studied star formation rate in a galaxy as a function of cluster centric radius and local galaxy density and found that star formation rate declines around the same environment as we found in the present study. Furthermore, Goto et al. (2003c; Chapter 6) studied the morphology-density relation using the similar SDSS data ($0.05 < z < 0.1$ and $Mr^* < -20.5$) and an automated galaxy classification (Yamauchi et al. 2003). They found that the morphological fraction of galaxies start to change approximately at the same environment as found in our study; the fraction of S0 and elliptical galaxies start to increase (and Sc galaxies decrease) toward cluster center at ~ 1 virial radius, or toward larger galaxy density at local galaxy density $\sim 1 \text{ Mpc}^{-2}$. These coincidences in the environment suggest that the same mechanism might be responsible for all the effects happening here; creation of passive spiral galaxies, decrease of galaxy star formation rate and morphological change in relative galaxy fraction. These coincidences might be explained naturally by the following interpretation; As galaxies approach this critical environment ($1\sim 2 \text{ Mpc}^{-2}$ or $1\sim 10$ virial radius), they stop their star formation as seen in Gomez et al. (2003), by changing spiral galaxies into passive spiral galaxies as found in this study. If a spiral galaxy stops star formation calmly without its morphology disturbed, it is likely to develop to be a S0 galaxy (Bertin & Romeo 1988; Bekki et al. 2002) as is seen in the morphology-density relation of Goto et al. (2003c; Chapter 6). According to this scenario, passive spirals are likely to be a population of galaxies in transition. In addition, there have been many results from other observations and surveys, which supports this scenario. Abraham et al.(1996) reported that cluster members become progressively bluer as a function of cluster-centric distance out to 5 Mpc in A2390 ($z=0.23$). Terlevich, Caldwell & Bower (2001) reported that $U - V$ colors of early-type galaxies are systematically bluer at outside the core of Coma cluster. Pimbblet et al.(2002) studied 11 X-ray luminous clusters ($0.07 < z < 0.16$) and found that median galaxy color shifts bluewards with decreasing local galaxy density. At higher redshift, Kodama et al. (2001) reported that colors of galaxies abruptly change at sub-clump regions surrounding a cluster at $z = 0.41$. Although it is difficult to directly compare this environment with ours due to the different definitions of local galaxy density, it is highly possible that their color change happens at the same environment we found. van Dokkum et al. (1998) found S0 galaxies in the outskirt of a cluster at $z = 0.33$. These S0s show a much wider scatter in their colors and are bluer on average than those in cluster cores, providing possible evidence for recent infall of galaxies from the field. In addition, many studies reported that star formation in the cores of clusters is much lower than that in the surrounding field (e.g., Balogh et al. 1997,1998,1999; Poggianti et al. 1999; Martin, Lotz & Ferguson 2000; Couch et al. 2001; Balogh et al. 2002).

The existence of passive spiral galaxies also brings us a hint on the origin of these three phenomena. It supports a transformation of galaxies, which do not disturb arm structures of spiral galaxies. Possible preferred candidate mechanisms include ram-pressure stripping (Gunn & Gott 1972; Abadi, Moore & Bower 1999; Quilis, Moore & Bower 2000) and simple removal of gas reservoir (Larson, Tinsley & Cardwell 1980; Balogh et al. 1999). It has been known that preheating of intergalactic medium can effect morphologies of galaxies by strangling the gas accretion (strangulation; Mo & Mao 2002; Oh & Benson 2002). In fact, Finoguenov et al. (2003) found the filamentary gas in Coma cluster and predicted the existence of passive spirals around the filament. Although the characteristic environment ($1\sim 2 \text{ Mpc}^{-2}$ or $1\sim 10$ virial radius) might seem to be a little too low density environment for ram-pressure or strangulation to happen, it is possible for galaxy sub-clumps around a cluster to have local hot gas dense enough for stripping (Fujita et al. 2003). Indeed Kodama et al. (2001) found that galaxy colors change at such sub-clumps around a cluster.

Perhaps major merger/interaction origins are less preferred since such dynamical processes disturb arm structures in spiral galaxies, and thus do not result in creating passive spirals. Weak H δ absorption lines shown in Figure 7.11 also support quiescent transformation of galaxies. However, we can not exclude a minor merger origin since such a process might be able to happen without disturbing spiral arms. In their study of the morphology-density relation, Goto et al. (2003c; Chapter 6) observed decrease of S0s and increase of ellipticals at cluster cores (virial radius < 0.3 or galaxy density $> 6 \text{ Mpc}^{-2}$), and they proposed that major merger/interaction might be dominant in cluster core regions. The proposal is consistent with our results, which showed devoid of passive spiral galaxies within 0.6 virial radius or greater than $\sim 3 \text{ Mpc}^{-2}$ in local galaxy density. On the other hand, some theoretical work predicts that it is difficult to have frequent merger/interaction in cluster cores since relative velocities of galaxies are so high in such regions (Ostriker 1980; Binney & Tremaine 1987; Mamon 1992; Makino & Hut 1997). In such a case, S0s (or passive spirals) might simply fade away to be a small elliptical galaxy. In summary, implication in cluster core regions is either (i) passive spiral galaxies merged into a large elliptical galaxies in cluster cores, or (ii) the disc of passive spiral galaxies completely fade away to become small elliptical galaxies.

Also in terms of cluster galaxy evolution, passive spiral galaxies might fit well with the previous observational results. It has been known that fraction of blue galaxies are larger in higher redshift (the Butcher-Oemler effect; Butcher & Oemler 1978, 1984; Couch & Sharples 1987; Rakos & Schombert 1995; Couch et al. 1998; Margoniner & De Carvalho 2000; Margoniner et al. 2001; Ellingson et al. 2001; Kodama & Bower 2001; Goto et al. 2003a; Chapter 5) and that the fraction of cluster spiral galaxies are also larger in the past (Dressler et al. 1997; Couch et al. 1998; Fasano et al. 2000; Diaferio et al. 2001;

Goto et al. 2003a; Chapter 5). Many people speculated the morphological transformation from spiral galaxies to S0 galaxies (e.g., Dressler et al. 1997; Smail et al. 1998; Poggianti et al. 1999; Fabricant, Franx, & van Dokkum 2000; Kodama & Smail 2001). Fraction of early-type galaxies in rich clusters are smaller in the past (Andreon, Davoust, & Heim 1997; Dressler et al. 1997; Lubin et al. 1998; van Dokkum et al. 2000). In morphological point of view, since passive spiral galaxies have already stopped their star formation, in the near future, its disc structures including spiral arms will become fainter and fainter, to be seen as a disc galaxy with smoother profile, i.e., possibly S0 galaxies. Spectrally, passive spirals are already almost as red as elliptical galaxies, but their spiral arms must have had star formation activity until recently, therefore a passive spiral galaxy itself must have been much bluer in the past, just like blue population of galaxies numerous in the higher redshift clusters. Therefore, although this is not direct evidence, it is very likely that passive spiral galaxies are a population of galaxies in transition, in the course of the Butcher-Oemler effect and morphological Butcher-Oemler effect.

7.5.2 Aperture Bias

Since the SDSS spectroscopy is performed with a fiber spectrograph which captures light within 3 arcsecond aperture, aperture bias is a concern. Aperture bias could result in an increase of passive spiral galaxies with decreasing redshift since at lower redshift, 3 arcsecond fiber misses more light from a disc of a galaxy. Using the data from LCRS with a 3.5 arcsecond fiber spectrograph, Zaritsky et al. (1995) showed that at $z > 0.05$, the spectral classifications of galaxies are statistically unaffected by aperture bias. Using the similar sample of the SDSS galaxies, Gomez et al. (2003) also limited their galaxies to $z > 0.05$ and proved that aperture bias does not change their results. We followed these two authors and limited our sample with $z > 0.05$ to minimize this potential bias. In the main analysis of the chapter, there are several evidence suggesting that these passive spiral galaxies are not seriously biased by the aperture effect. In Figure 7.9, passive spiral galaxies are much redder than normal galaxies. To calculate colors, we used a model magnitude which uses Petrosian radius in r for all colors (Stoughton et al. 2002), and thus is free from 3" aperture bias. Therefore the red colors of these galaxies suggest that they are truly passive systems, and not the artifact of the aperture effect. Also in Figure 7.7, we compared density distribution of passive spirals with normal star forming spirals. The two distributions are statistically different. Again, if passive spirals are the artifact of aperture bias, the density distributions of star forming and passive spiral galaxies should be similar. Therefore this difference suggests that passive nature of these galaxies are truly unique to these galaxies. Figure 7.12 shows difference in $g - r$ color between fiber magnitude (measured with 3" aperture) and model magnitude (measured using Petrosian

radius in r , usually larger than 3'', especially in low redshift) as a function of redshift. Contours show the distribution of all galaxies in our volume limited sample. The solid, dotted and dashed lines show medians of all galaxies, passive spirals and active spirals. Since both passive and active spirals are less concentrated, their medians have somewhat higher values than all galaxies. If aperture bias is severe, $\Delta(g-r)$ should be much larger in lower redshift since the difference between 3'' aperture and Petrosian radius of galaxies are larger. However, in Figure 7.12, $\Delta(g-r)$ of passive spirals is almost constant throughout the redshift range we used ($0.05 < z < 0.1$). The figure suggests that aperture effect is not a severe effect within the redshift range. In Figure 7.13, we present the fraction of passive spiral galaxies as a function of redshift. It clearly shows strong aperture effect at $z < 0.05$. However, throughout this chapter, we limit our sample between $z = 0.05$ and 0.1, where fractions of passive spirals are consistent with constant within the error. It suggests that aperture bias is not strong within our sample. We end this section by quoting that Hopkins et al. (2003) compared star formation rate estimated from H α (SDSS data; subject to 3 arcsecond aperture bias) and that from radio flux (FIRST data; i.e., with no aperture bias), concluding that both star formation rate estimates agree with each other after correcting H α flux using the ratio of 3'' fiber magnitude to Petrosian (total) magnitude in r band.

7.6 Summary

Using a volume limited sample of the SDSS data, we have studied the environment of passive spiral galaxies as a function of local galaxy density and cluster-centric-radius. Since passive spirals are only found in cluster regions in previous work, this is the first attempt to select passive spirals uniformly, in all the environment. It is found that passive spiral galaxies live in local galaxy density $1 \sim 2 \text{ Mpc}^{-2}$ and $1 \sim 10$ virial radius. Thus the origins of passive spiral galaxies are likely to be cluster related. These characteristic environments coincide with the environment where galaxy star formation rate suddenly declines (Lewis et al. 2002; Gomez et al. 2003) and the fractions of galaxy morphology start to deviate from the field value (Goto et al. 2003c; Chapter 6). Therefore it is likely that the same physical mechanism is responsible for all of these observational results; the morphology-density relation, the decline of star formation rate and the creation of passive spiral galaxies. The existence of passive spiral galaxies suggest that a physical mechanism that works calmly is preferred to dynamical origins such as major merger/interaction since such a mechanism can destroy spiral arm structures. Passive spiral galaxies are likely to be a galaxy population in transition between red, elliptical/S0 galaxies in low redshift clusters and blue, spiral galaxies numerous in higher redshift clusters as seen in the Butcher-Oemler effect and the morphological Butcher-Oemler effect. Computationally,

simulating the evolution of passive spiral galaxies will bring more insight on the origin of cluster galaxy evolution. Such a simulation might be possible by combining a pioneering work by Bekki et al. (2002) with large cluster N-body simulation which can trace the evolution of cluster galaxies; (e.g., Diaferio et al. 2000; Benson et al. 2002).

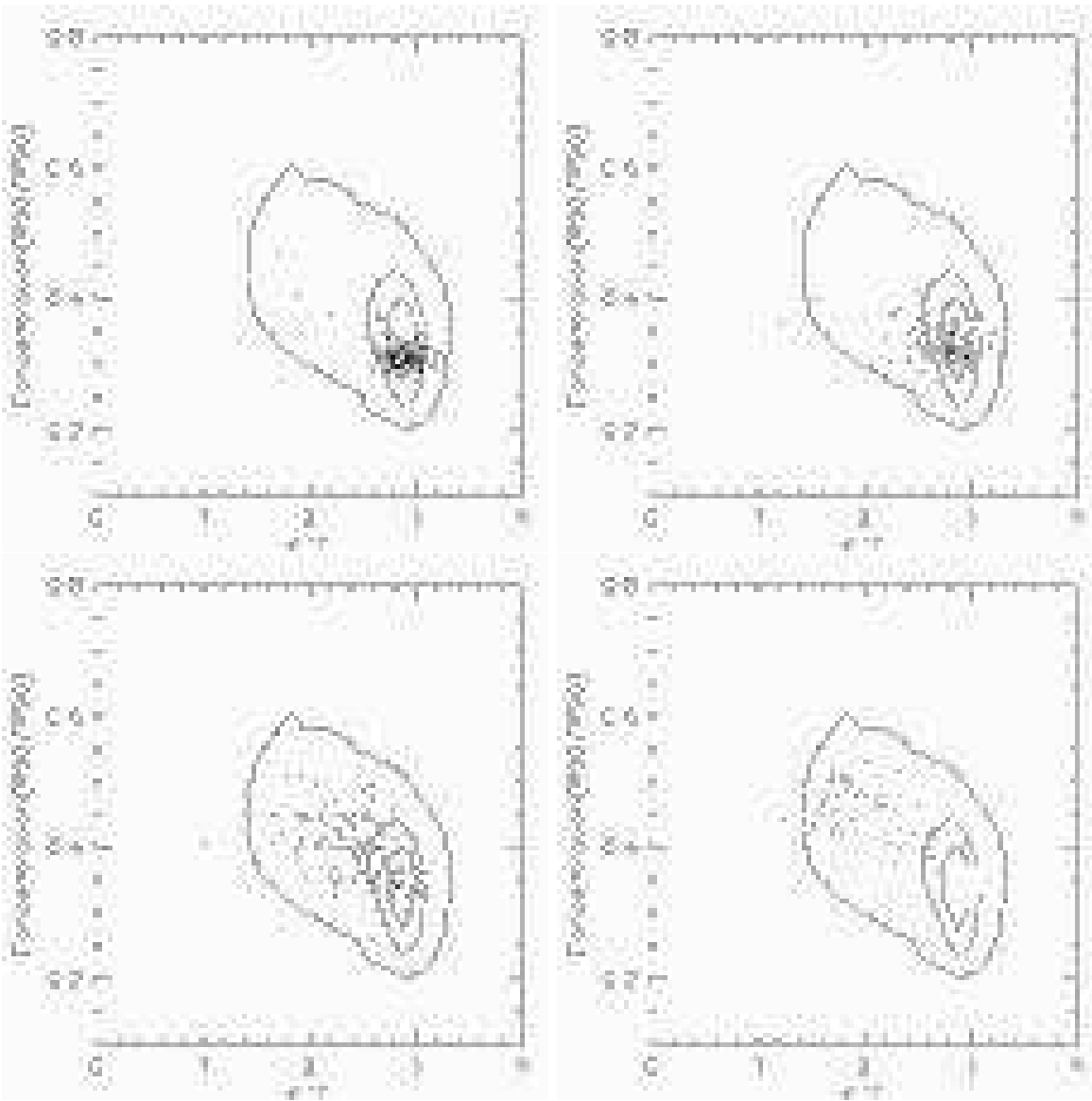


Figure 7.1: C_{in} is plotted against $u - r$. The contours show the distribution of all 25813 galaxies in the volume limited sample ($0.05 < z < 0.1$ and $M_{r^*} < -20.5$). A good correlation between two parameters is seen. Points in each panel show the distribution of each morphological type of galaxies classified by eye (Shimasaku et al. 2001; Nakamura et al. 2003); Ellipticals are in the upper left panel. S0, Sa and Sc are in the upper right, lower left and lower right panels, respectively.

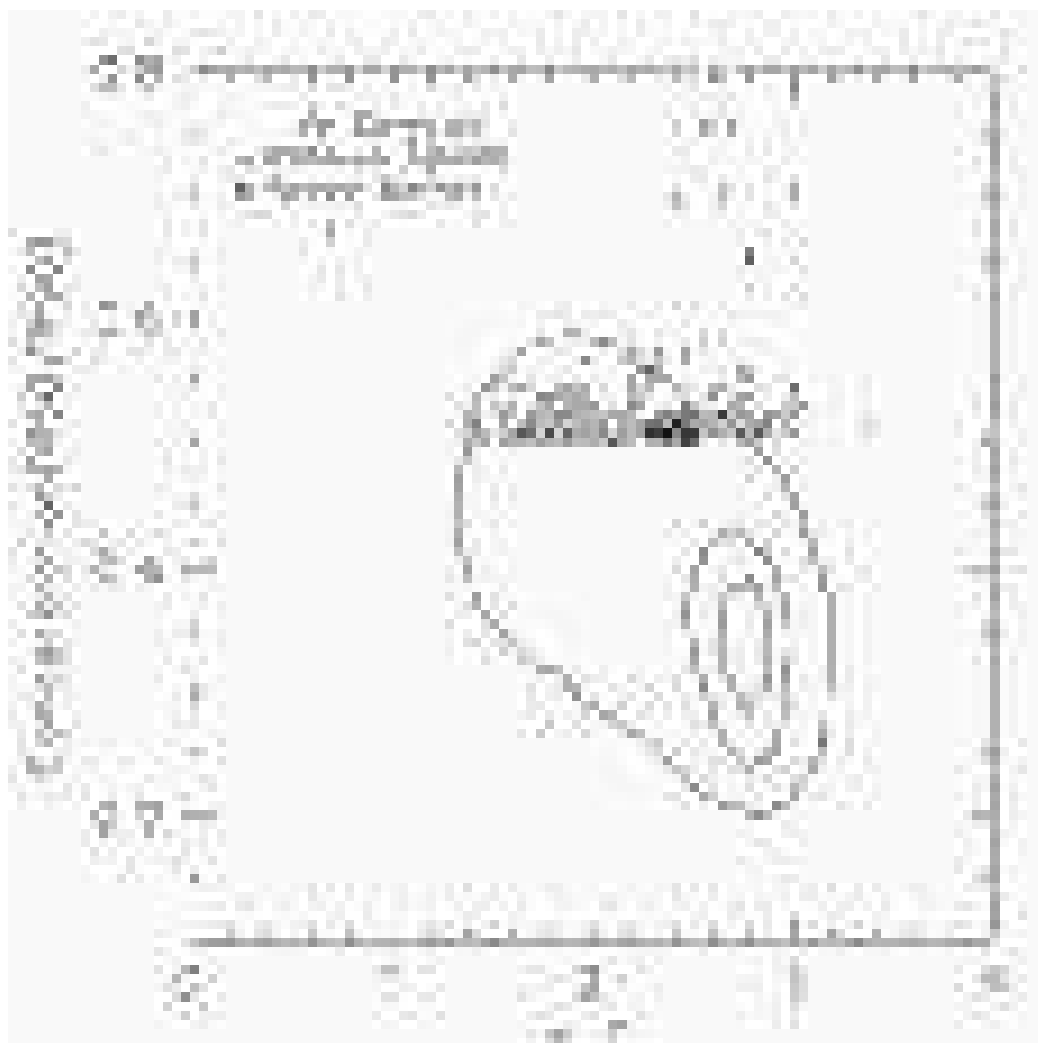


Figure 7.2: The distribution of passive spiral galaxies in C_{in} v.s. $u - r$ plane. The contours show the distribution of all 25813 galaxies in our volume limited sample. The open circle and filled dots represent passive and active spiral galaxies, respectively.

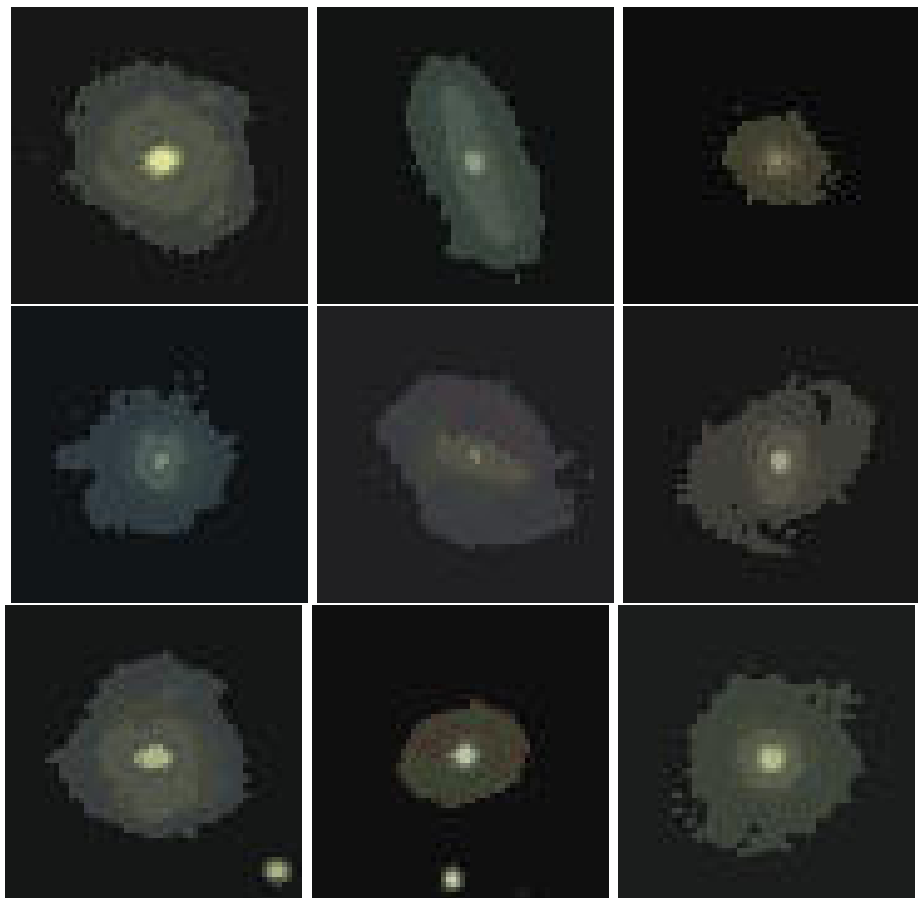


Figure 7.3: Example images of passive spiral galaxies. Each image is a composite of the SDSS *g*, *r* and *i* bands, showing $30'' \times 30''$ area of the sky with its north up. Discs and spiral arm structures are recognized.

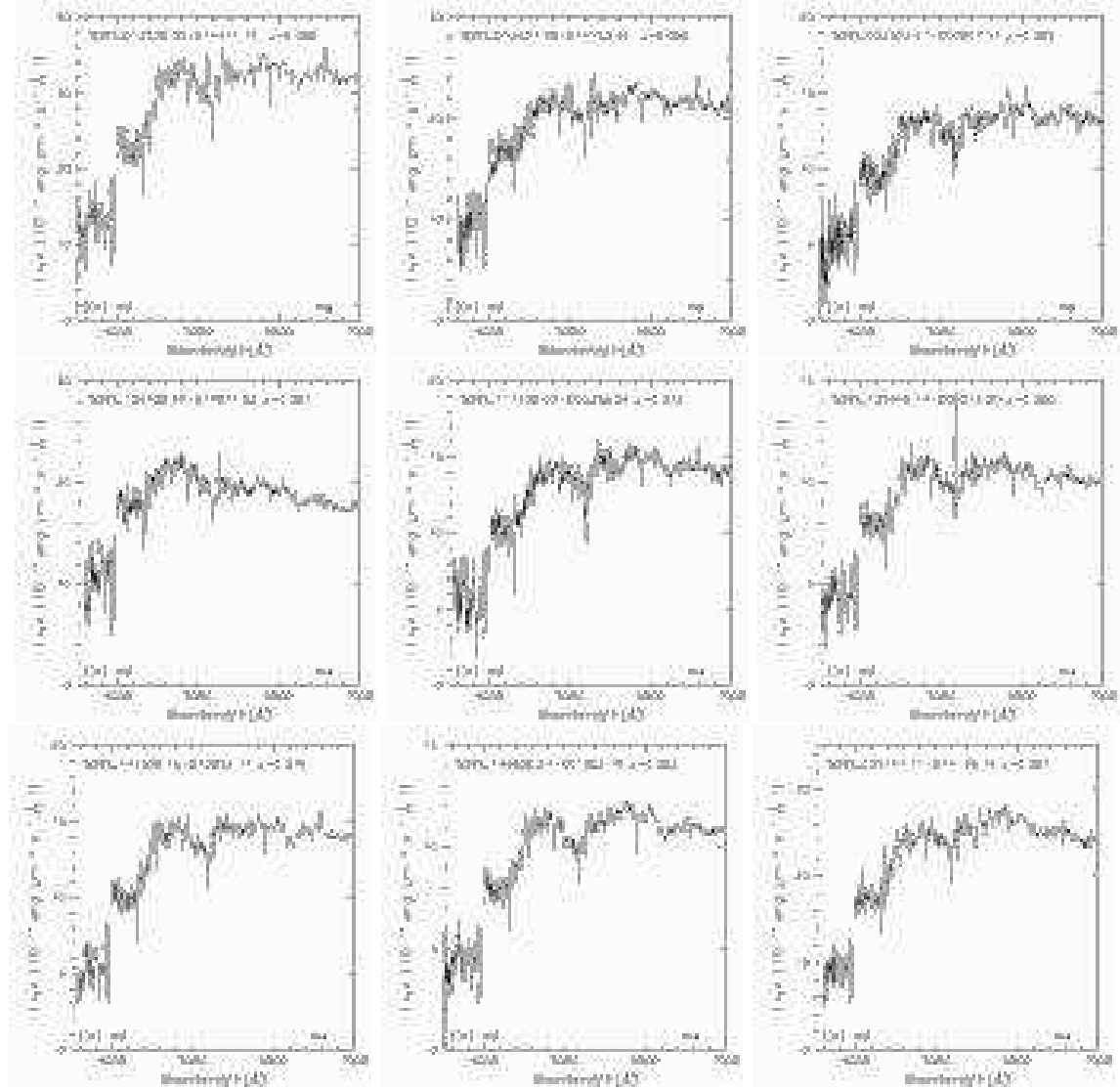


Figure 7.4: Example restframe spectra of passive spiral galaxies. Spectra are shifted to restframe and smoothed using a 10Å box. Each panel corresponds to that in Figure 7.3.

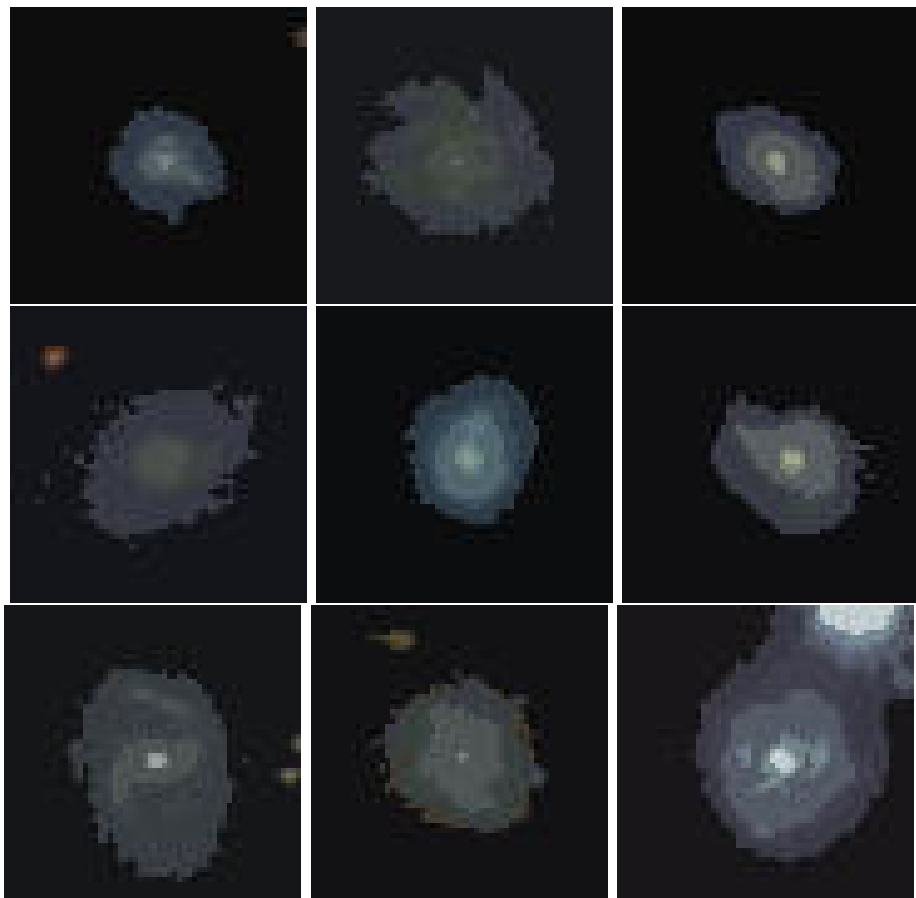


Figure 7.5: Example images of active spiral galaxies. Each image is a composite of SDSS g , r and i bands, showing $30'' \times 30''$ area of the sky with its north up. Discs and spiral arm structures are recognized.

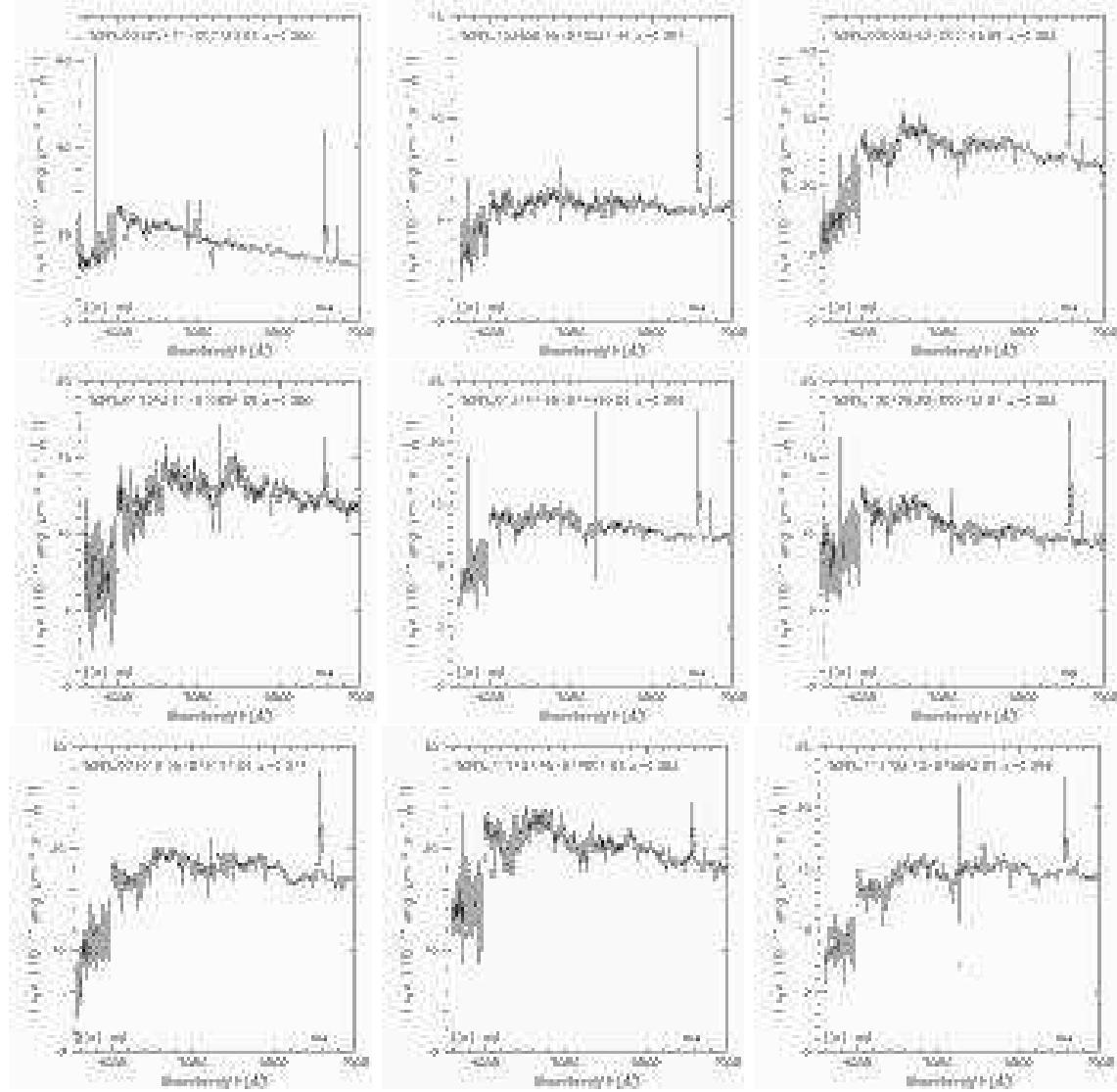


Figure 7.6: Example restframe spectra of active spiral galaxies. Spectra are shifted to restframe and smoothed using a 10 \AA box. Each panel corresponds to that in Figure 7.5.



Figure 7.7: The distribution of densities for passive spiral galaxies (hashed region) and all 25813 galaxies (solid line) in our volume limited sample. A Kolomogorov-Smirnov test shows the distribution of passive spirals and that of all galaxies are from different parent distributions. The long dashed line shows the distribution of cluster galaxies. The short dashed line shows that of active spiral galaxies.

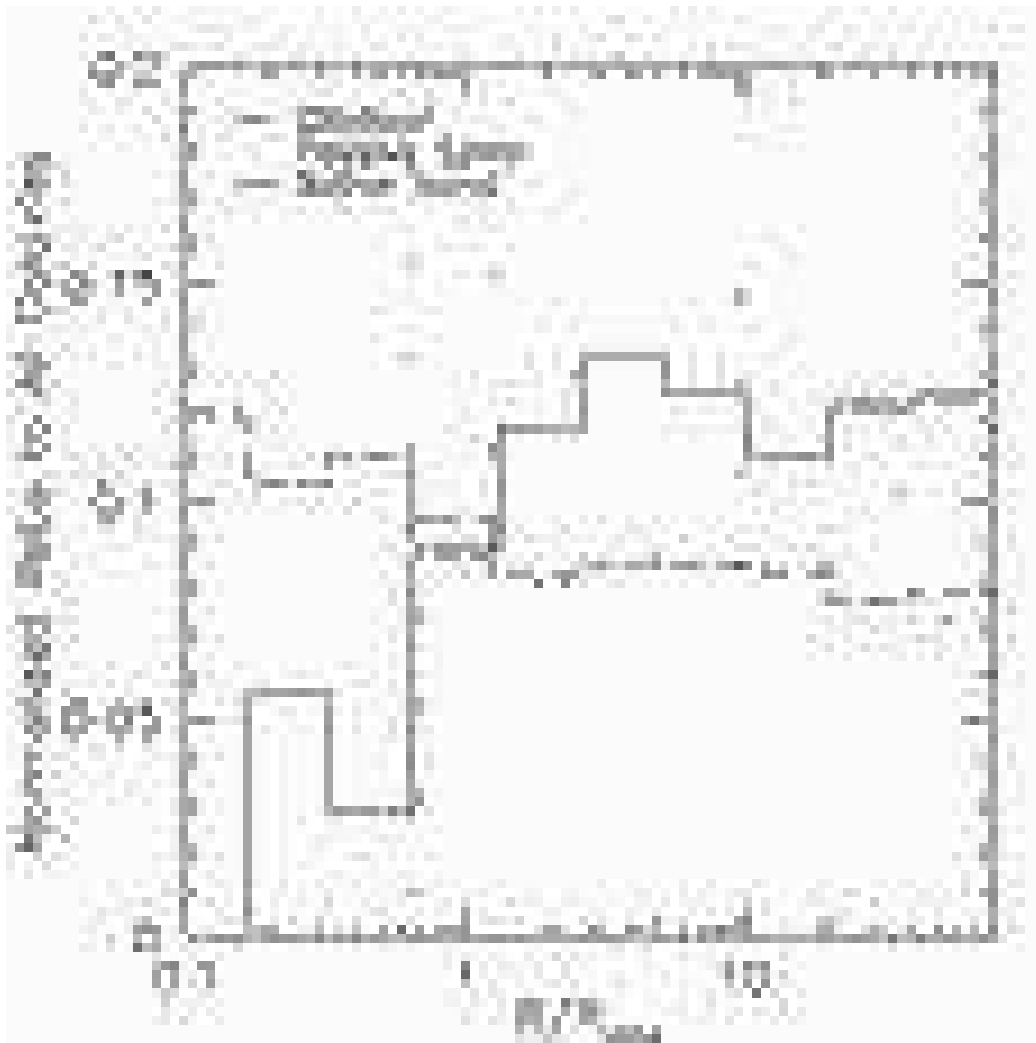


Figure 7.8: The distribution of passive spiral galaxies as a function of cluster-centric-radius. The dotted, dashed and solid lines show the distributions of passive spiral, elliptical and active spiral galaxies, respectively. The distributions are relative to that of all galaxies in the volume limited sample and normalized to be unity for clarity. The cluster-centric-radius is measured as the distance to a nearest C4 cluster (Miller et al. 2003) within $\pm 3000 \text{ km s}^{-1}$, and normalized by virial radius (Girardi et al. 1998).

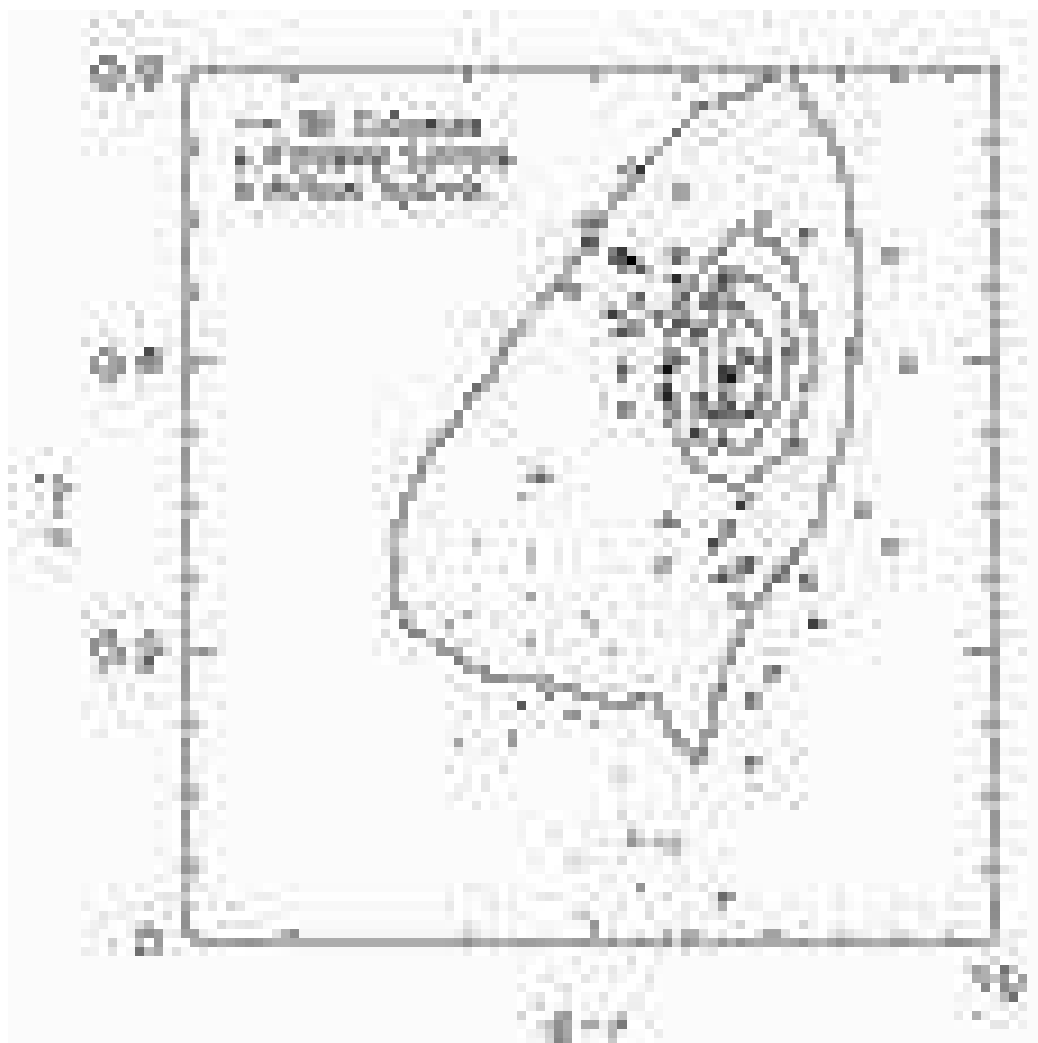


Figure 7.9: The distribution of passive spirals in restframe $g - r - i$ plane. The contours show the distribution of all galaxies in our volume limited sample. The open circle and filled dots represent passive and active spiral galaxies, respectively.

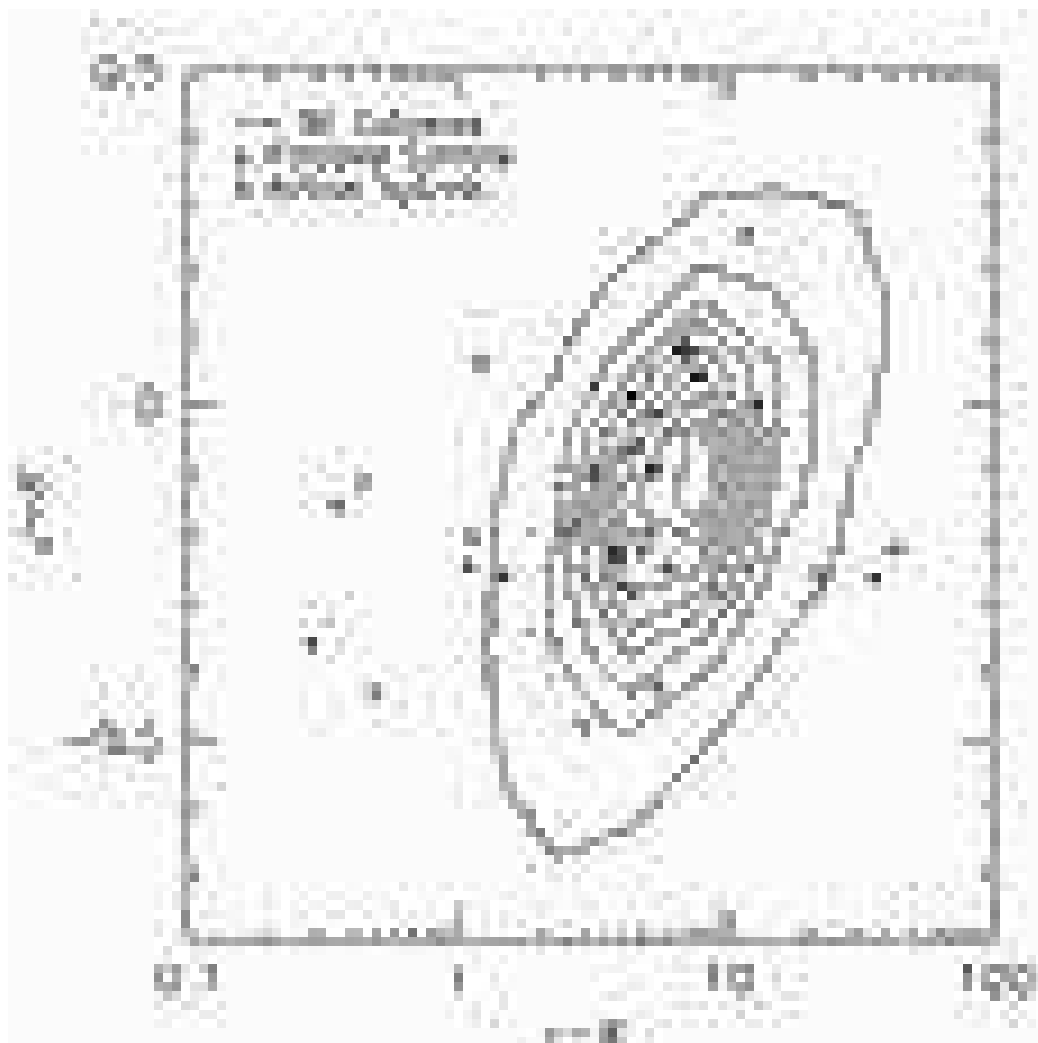


Figure 7.10: The distribution of passive spirals in restframe $J - K - r$ plane. The contours show the distribution of all galaxies in our volume limited sample. The open circle and filled dots represent passive and active (normal) spiral galaxies, respectively.

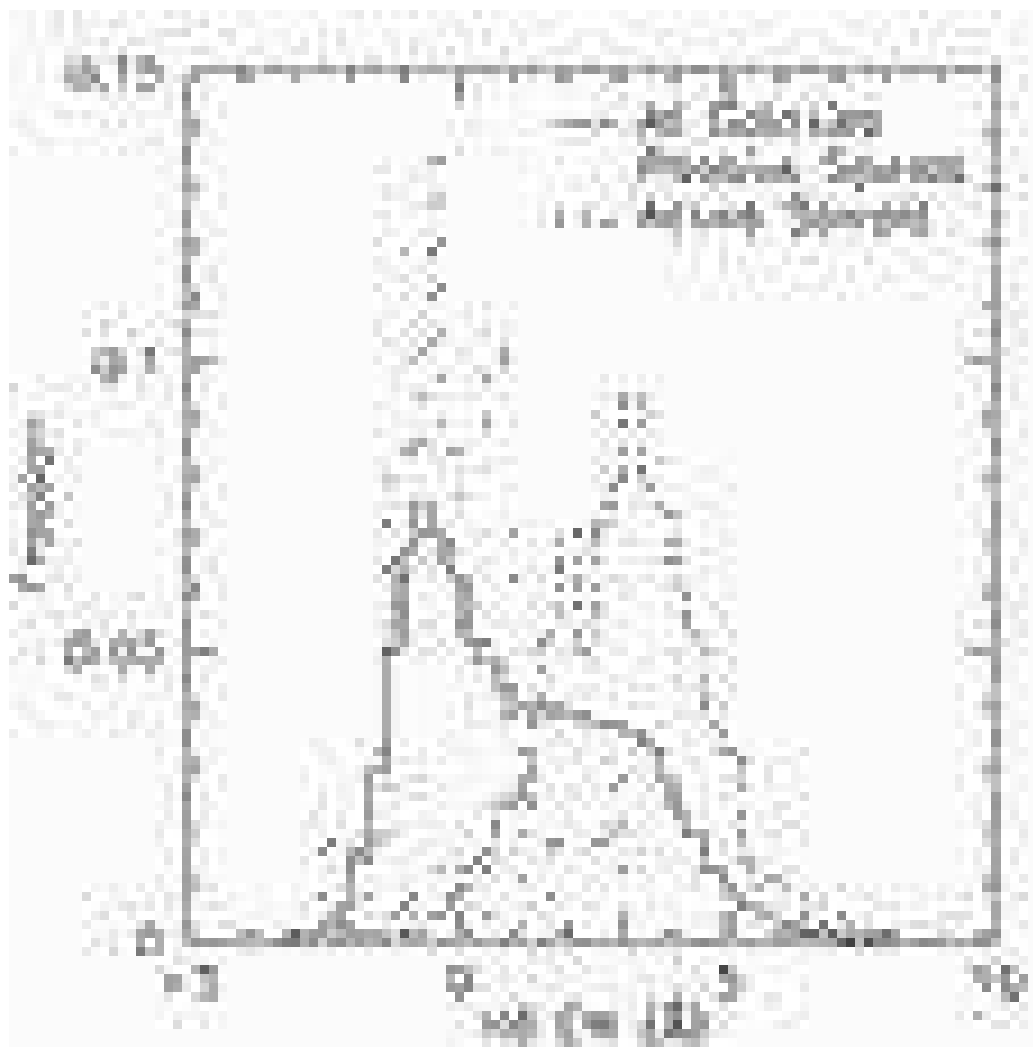


Figure 7.11: Distributions of H δ EWs of passive spiral galaxies, active spiral galaxies and all galaxies in the volume limited sample. The solid, dashed and dotted lines are for all galaxies, active spiral galaxies and passive spiral galaxies, respectively. Absorption lines are positive in this figure. Passive spiral galaxies tend to have weak H δ absorption lines.

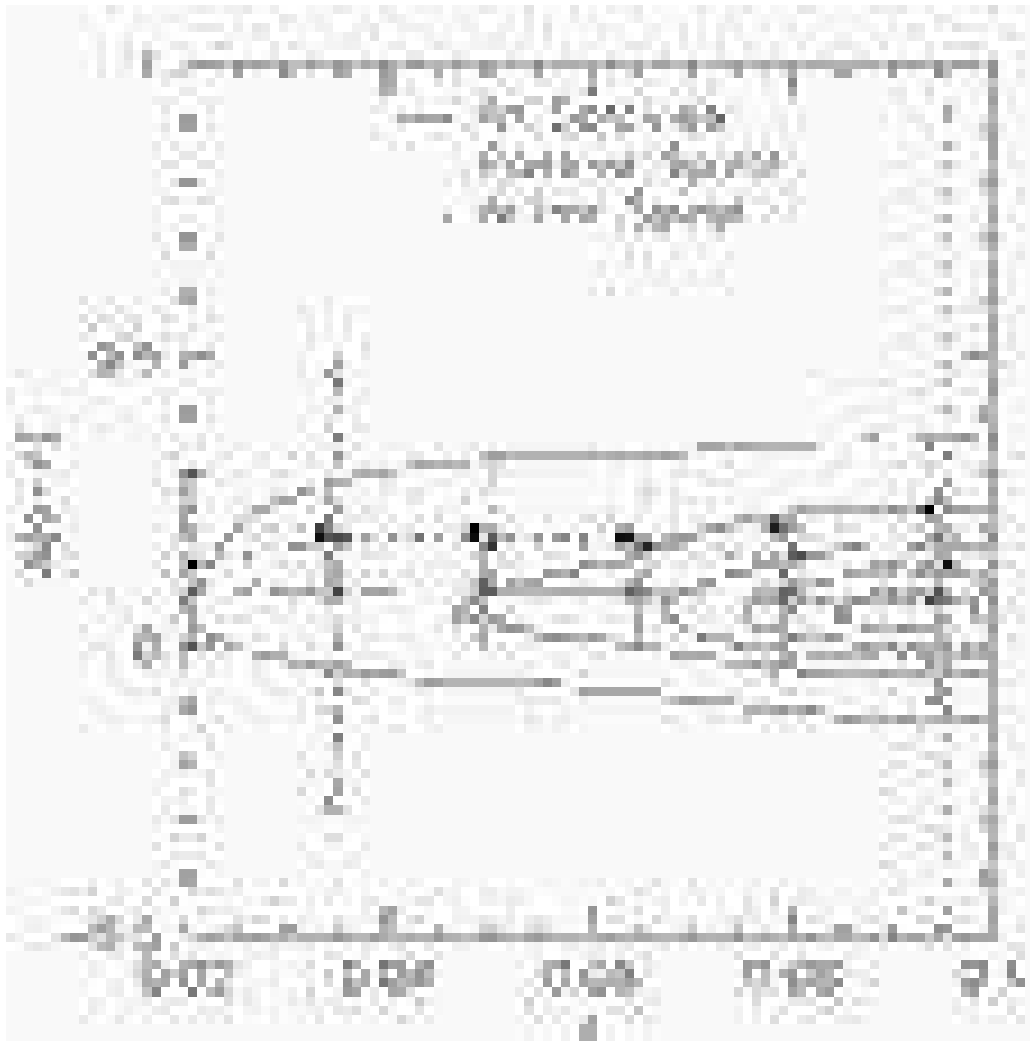


Figure 7.12: Differences between fiber color (within 3'' aperture) and model color (using Petrosian radius measured in r) are plotted against redshift. The solid, dotted and dashed lines show medians of all galaxies, passive spirals and active spirals, respectively. The difference ($\Delta(g-r)$) should be smaller at higher redshift since 3'' fiber can collect larger amount of total galaxy light at higher redshift. Both passive and active spirals have larger $\Delta(g-r)$ than all galaxies since they are less concentrated. Throughout the redshift range we used ($0.05 < z < 0.1$), $\Delta(g-r)$ of passive spirals is consistent with a constant within the error, suggesting that aperture effect is not a severe effect within the redshift range we used.

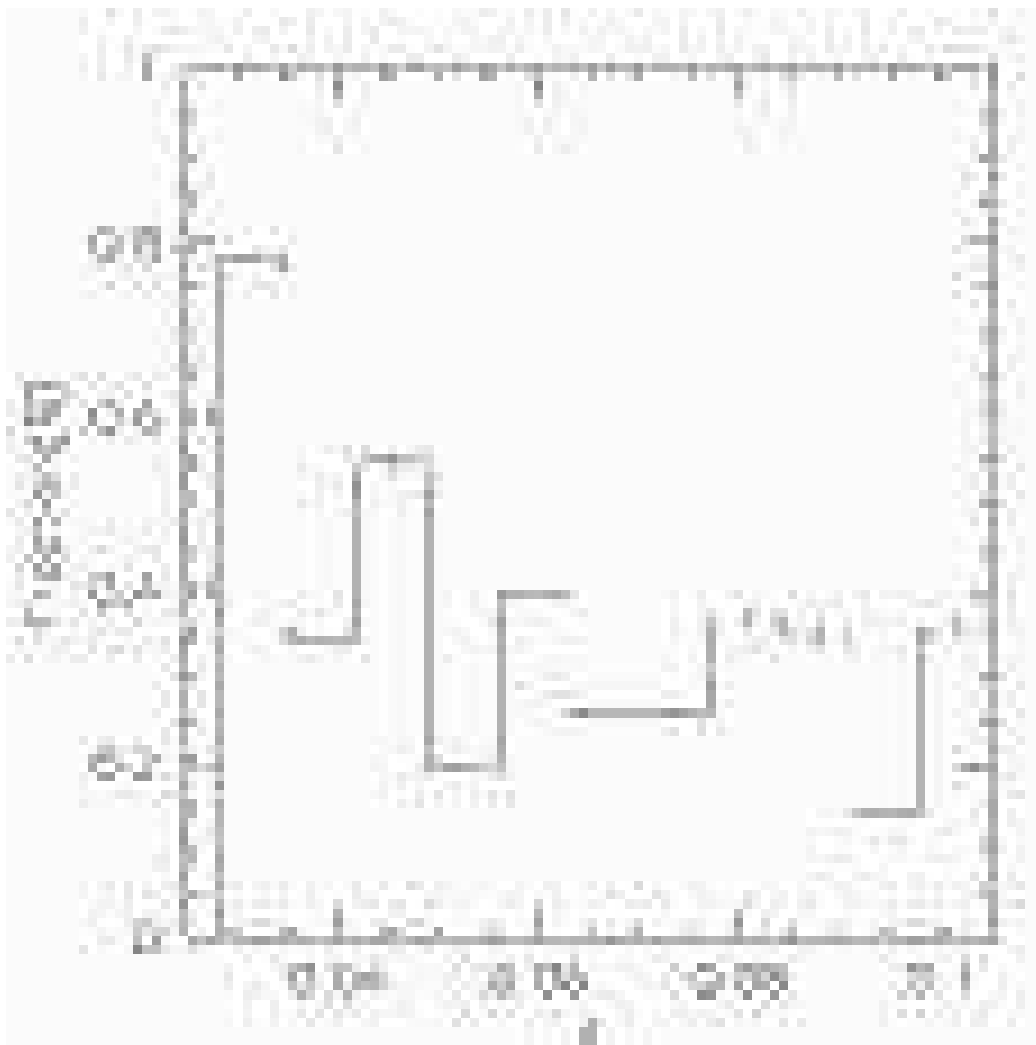


Figure 7.13: Fractions of passive spiral galaxies (in percentage) to all galaxies among the volume limited sample are shown as a function of redshift. Our sample includes passive spiral galaxies only between $z = 0.05$ and $z = 0.1$, where fractions are consistent with constant, suggesting aperture bias is not a strong effect in our sample.

Table 7.1: Wavelength ranges used to measure the equivalent widths of [OII], H α and H δ lines.

	Blue continuum	Line	Red continuum
[OII]	3653-3713Å	3713-3741Å	3741-3801Å
H α	6490-6537Å	6555-6575Å	6594-6640Å
H δ	4030-4082Å	4088-4116(4082-4122)Å	4122-4170Å

Chapter 8

Fate of Infalling Galaxies

In this chapter, we consider all of our findings in the previous chapters and summarize a possible evolutionary history of infalling cluster galaxies.

8.1 Summary of Our Findings

We have studied the environmental effects on galaxy evolution using the Sloan Digital Sky Survey (SDSS) data. Our main findings are as follows.

- We have developed a new cluster finding method, the Cut & Enhance (CE) method, which uses color and angular separation to increase the signal to noise ratio of galaxy clusters. We determine the selection function of the Cut & Enhance method via extensive Monte Carlo simulations, showing that the Cut & Enhance method can detect rich clusters ($N_{gal}=100$) to $z \sim 0.3$ with $\sim 80\%$ probability. We apply Cut & Enhance method to the SDSS commissioning data and produce an SDSS Cut & Enhance cluster catalog containing 4638 galaxy cluster candidates in ~ 350 deg 2 . The SDSS Cut & Enhance cluster catalog developed in this work is a useful tool to study cosmology as well as properties of clusters and cluster galaxies.
- We constructed composite luminosity functions (LFs) in the five SDSS bands, u, g, r, i and z , using the 204 SDSS CE clusters ranging from $z = 0.02$ to $z = 0.25$. The best-fit Schechter parameters are $(M^*, \alpha) = (-21.61 \pm 0.26, -1.40 \pm 0.11), (-22.01 \pm 0.11, -1.00 \pm 0.06), (-22.21 \pm 0.05, -0.85 \pm 0.03), (-22.31 \pm 0.08, -0.70 \pm 0.05)$ and $(-22.36 \pm 0.06, -0.58 \pm 0.04)$ in u, g, r, i and z , respectively. Compared with the field luminosity function, cluster LFs have a brighter characteristic magnitude (M^*) and a flatter slope in the g, r, i and z band, suggesting that cluster galaxies have different evolutionary histories from field galaxies. We also derived the type-specific composite LFs by dividing the cluster galaxies into early and late types using three different

criteria (concentration, galaxy profile fit and $u - r$ color). We found that early-type galaxies always have flatter slopes than late-type galaxies in all the three cases. These observations are in agreement with the hypothesis that the bright end of the cluster LF is dominated by bright, old early-types, while the faint-end of the cluster LF represents late-type galaxies.

- We investigate the evolution of the fractions of blue cluster galaxies as a function of redshift, using one of the largest, most uniform cluster samples of 514 CE clusters in the range of $0.02 \leq z \leq 0.3$. It is a significant improvement over previous work that both high and low redshift clusters are selected from the same data using the same cluster finder, excluding richness and redshift related bias prevalent in previous work. By selecting blue galaxies as those with restframe $g - r$ bluer by 0.2 than red-sequence or those with $u - r < 2.2$, we found that blue fractions of cluster galaxies increase ~ 20 points between $z = 0.02$ and $z = 0.3$ at the 99.9% significance level, confirming the presence of the Butcher-Oemler effect. The results show that cluster galaxies do evolve by changing colors redder with decreasing redshifts.
- We observed the morphological Butcher-Oemler effect as an increase of late-type galaxies toward higher redshifts, using pure morphological parameters such as a concentration parameter and de Vaucouleur/exponential profile fit. The results confirm that cluster galaxies do evolve morphologically from late- to early-type, in addition to the spectral evolution (the Butcher-Oemler effect). Previously, such a study on morphological evolution of cluster galaxies has often been performed with a heterogeneous sample of low redshift and high redshift clusters with eye-based morphology. This is the first result to show such morphological evolution with an automated morphology using a homogeneous sample of 514 clusters.
- We found a slight tendency for richer clusters to have lower values of the late-type fraction (Figure 5.4). This trend has significant implication for the underlying physical mechanism since it is expected in the ram-pressure stripping model proposed by Bahcall (1977) and Fujita et al. (1999) where galaxies in richer clusters are more affected by ram-pressure due to higher temperature of clusters.
- We studied the morphology-density relation and the morphology-cluster-centric-radius relation using a volume limited SDSS data ($0.05 < z < 0.1$, $Mr^* < -20.5$). Technical improvements compared with previous work are; (i) automated galaxy morphology classification capable to separate galaxies into four types, (ii) three dimensional local galaxy density estimation free from the fore/background correction, (iii) the extension of the morphology-density study into the field region. We found that there are two characteristic changes in both the morphology-density and the

morphology-radius relations, suggesting two different mechanisms are responsible for the relations. In the sparsest regions (below 2 galaxy Mpc⁻² or outside of 2 R_{vir}), both of the relations become flat, suggesting the responsible physical mechanisms require denser environment. In the intermediate density regions, (density between 2 and 6 galaxy Mpc⁻² or between 0.3 and 2 R_{vir}), S0 fractions increase toward denser regions, whereas late-spiral fractions decrease. Considering that the median size of S0 galaxies are smaller than that of late-spiral galaxies (Figure 6.16), we propose that the mechanism is likely to stop star formation in late-spiral galaxies, eventually turning them into S0 galaxies after their outer discs and spiral arms become invisible as young stars die. For example, ram-pressure stripping is one of the candidate mechanisms. In the densest regions (above 6 galaxy Mpc⁻² or inside of 0.3 R_{vir}), S0 fractions decreases radically and elliptical fractions increase. The behavior of S0 fractions at the cluster cores is investigated for the first time in this work. The result in the core regions is in contrast to that in intermediate regions, and it suggests that yet another mechanism might be responsible for morphological change in these regions. The deficit of S0 galaxies at the densest regions are likely to be consistent with computer simulations based on merging scenario, which predicted small fraction of S0 galaxies.

- We compared the morphology-density relation from the SDSS ($0.01 < z < 0.054$) with that of the MORPHS data ($z \sim 0.5$). Two relations lie on top of each other, suggesting that the morphology-density relation was already established at $z \sim 0.5$ as it is in the present universe. A slight sign of excess early-type fraction in the SDSS data in dense regions might be suggesting additional formation of elliptical galaxies in the cluster core region between $z = 0.5$ and $z = 0.05$. This work presented the morphology-density relation at $z \sim 0.5$ with an automated morphology instead of eye-morphology for the first time.
- Using a volume limited sample of the SDSS data ($0.05 < z < 0.1$ and $Mr^* < -20.5$), we studied the environment of passive spiral galaxies as a function of local galaxy density and cluster-centric-radius. This is the first work that revealed the environment of passive spiral galaxies. It is found that passive spiral galaxies preferentially live in local galaxy density $1 \sim 2$ galaxy Mpc⁻² and $1 \sim 10 R_{vir}$ (Figures 7.7 and 7.8). Thus the origin of passive spiral galaxies is likely to be cluster related. These characteristic environments coincide with the previously reported environment where galaxy star formation rate suddenly declines and the morphology-density relation levels off (Figure 6.14). In order to create passive spirals, a physical mechanism that works calmly is preferred to dynamical origins such as major merger/interaction since such a mechanism can destroy spiral arm structures. Compared with observed

cluster galaxy evolution such as the Butcher-Oemler effect and the morphological Butcher-Oemler effect (Figure 5.1), passive spiral galaxies are likely to be a galaxy population in transition between red, elliptical/S0 galaxies in low redshift clusters and blue, spiral galaxies more numerous in higher redshift clusters.

- Based on our observational results, we propose a new picture of the fate of cluster infalling galaxies as follows. When a star forming galaxy falls into a cluster region, the galaxy is not affected by the cluster environment until it reaches $2 R_{vir}$ or galaxy density ~ 2 galaxy Mpc $^{-2}$ (Figure 6.11 and 6.14). In the intermediate regions ($1 \sim 2$ galaxy Mpc $^{-2}$ or $1 \sim 10 R_{vir}$; Figure 6.14), the galaxy reduces its star formation rate through a gentle cluster-related process such as ram-pressure stripping, strangulation, evaporation or minor merger. Perhaps passive spiral galaxies (Figure 7.3) are in the intermediate stage of this transition, which eventually become numerous S0 galaxies (Figure 6.14) when outer discs become too faint to be visible. In the cluster core regions (above 6 galaxy Mpc $^{-2}$ or inside of $0.3 R_{vir}$), bright elliptical galaxies become dominant (Figure 6.15), perhaps originating from the merging/interaction at high redshift.

8.2 Circumstantial Evidence of Cluster Galaxy Evolution

In Chapter 4 and Chapter 5, we found circumstantial evidence of cluster galaxy evolution. We presented composite LFs of cluster galaxies using one of the largest samples consisting of 204 clusters in Chapter 4. The results showed that the bright end of the cluster LFs is dominated by bright, old early-type galaxies, while the faint-end of the cluster LF represents late-type galaxies. Compared with the field LFs (Figure 4.1), the dominance of bright elliptical galaxies in clusters suggests that these cluster galaxies might have a different evolutionary history from field galaxies. In Chapter 5, we showed that the Butcher-Oemler effect exists in the SDSS clusters, in a sense that the fraction of blue galaxies are larger in higher redshifts. According to Figure 5.1, $\sim 20\%$ of galaxies became red since $z = 0.3$. Historically, there have been some doubts on the existence of the Butcher-Oemler effect (Newberry, Kirshner & Boroson 1988; Allington-Smith et al. 1993; Garilli et al. 1996; Smail et al. 1998; Andreon & Ettori 1999; Fairley et al. 2002) although many people, on the other hand, claimed the existence of the Butcher-Oemler effect (Butcher & Oemler 1978, 1984; Rakos & Schombert 1995; Margoniner & De Carvalho 2000; Margoniner et al. 2001). The previous work used only dozens of clusters, and thus had large statistical uncertainty, which surely was part of the reason why different people ended up with different answers. In contrast, our work used by far the largest sample of

514 clusters uniformly selected from the SDSS CE galaxy cluster catalog (Chapter 3). It is also of importance that low redshift clusters and high redshift clusters are selected from the same SDSS data using the same cluster finder (Chapter 3) in this work, rectifying the inhomogeneity of the previous samples. Using the homogeneous sample, we firmly confirmed the existence of the Butcher-Oemler effect with negligible statistical uncertainty (Figure 5.1); the significance in correlation coefficient is greater than 99.99%. The result is a direct evidence that cluster galaxies evolve by changing their colors from blue to red.

In addition to the evolution in color, we showed that fractions of morphologically spiral galaxies are also larger in higher redshift (the morphological Butcher-Oemler effect). This is the first detection of this morphological transition using an automated galaxy classification and a homogeneous sample (Figure 5.1). Previous work used eye-classification and small number of clusters (a few to a few dozen) to probe morphological evolution, and thus had substantial uncertainty (Dressler et al. 1997; Fasano et al. 2000). In addition to the spectral evolution of cluster galaxies (the Butcher-Oemler effect), our result implies that cluster galaxies also change their morphology from late to early type, possibly from spiral to S0 galaxies. Figure 5.1 shows more than 20% of galaxies change their morphology from less concentrated to concentrated between $z = 0.3$ and $z = 0$.

Another important discovery in Chapter 5 is that, as a second parameter, blue/spiral fractions of cluster galaxies depend on the cluster richness, in the sense that richer clusters have smaller fractions of blue/spiral galaxies (Figure 5.4). The result has significant implication for the underlying physical mechanism since it is expected in the ram-pressure stripping model by Fujita et al. (1999), where ram-pressure stripping is stronger in clusters of higher X-ray temperatures.

8.3 Morphological Evolution of Cluster Galaxies

To investigate these cluster galaxy evolution in more detail, we studied nearby galaxies with the SDSS spectroscopic information in Chapters 6 and 7. We showed that there are two characteristic changes in the morphology-density relation using the volume limited sample ($0.05 < z < 0.1$ and $Mr^* < -20.5$) consisting of the 7938 SDSS galaxies (Figure 6.14).

In the sparsest regions where the local galaxy density is less than 2 galaxy Mpc⁻², or outside of 2 virial radius (R_{vir}), the morphology-density relation becomes less noticeable (Figure 6.11 and Figure 6.14), suggesting that physical mechanisms responsible for the morphology-density relation do not work in the sparsest regions. The characteristic density or radius where the morphology-density relation becomes flat (2 galaxy Mpc⁻² or 2 R_{vir}) coincides with the environment where the density-star formation rate (SFR) relation becomes flat. Lewis et al. (2002) and Gomez et al. (2003) studied the correla-

tion between local galaxy density and galaxy SFR to find galaxy SFR suddenly decreases at around the same galaxy density we found. This coincidence suggests that the same physical mechanism might be responsible for both the morphology-density relation and the SFR-density relation.

In the intermediate density regions (density between 2 and 6 galaxy Mpc⁻² or between 0.3 and 2 R_{vir}), we showed that S0 fractions increase toward denser regions, whereas late-spiral fractions decrease (Figures 6.11 and 6.14). In this intermediate regions, it is found that the SFR of galaxies starts to decrease toward denser environments (Lewis et al. 2002; Gomez et al. 2003). Furthermore, in Chapter 7, we found that passive spiral galaxies preferentially live in the same intermediate regions (local galaxy density 1~2 galaxy Mpc⁻² or 1~10 R_{vir} ; Figures 7.7 and 7.8). Therefore, it is likely that the same physical mechanism is responsible for all of these observational phenomena (the morphology-density relation, the SFR-density relation and the creation of passive spirals) happening around this intermediate density regions, or in other words, cluster infalling regions.

In the densest regions (above 6 galaxy Mpc⁻² or inside of 0.3 R_{vir}), S0 fractions decreases radically and elliptical fractions increase (Figure 6.15). This is a contrasting result to that in intermediate regions and it suggests that yet another mechanism might be responsible for morphological change in these regions.

Although the morphology-density relation has been studied by many authors in the past, it has been difficult to relate the correlation to underlying physical mechanisms. Benefitting from the large and high quality data from the SDSS, it has become possible, for the first time, to specify two characteristic environments where galaxy properties start to change, providing us with a great hint on the underlying physical mechanism.

8.4 Possible Hypotheses

Considering all of these observational findings, we would like to summarize a possible hypothesis which can explain all of the above results. From the results in Chapter 5, it is very likely that cluster galaxies change their morphology and colors during the course of their evolution.

In the infalling regions of clusters (below 2 galaxy Mpc⁻² or outside of 2 R_{vir}), fractions of late-type galaxies decrease and fractions of S0 galaxies increase (Figure 6.11 and Figure 6.14). Galaxies also decrease their SFR abruptly in these regions (Lewis et al. 2002; Gomez et al. 2003). It is also likely that the change in galaxy morphology and galaxy SFR in this intermediate density region is mainly responsible for the spectral and morphological evolution of cluster galaxies as shown in Figure 5.1. If a star-forming, spiral galaxy infalling to a cluster at high redshift is affected by cluster environment at this intermediate

regions as seen in Figures 6.11, 6.14, 7.7 and 7.8, then, they are likely to become a red, elliptical-like galaxy at lower redshift. If 20~30 % of cluster galaxies experience this process, the observed decrease of blue, spiral galaxies toward lower redshift (Figure 5.1) can naturally be explained.

Figure 8.1 is a schematic illustration of the cluster-related environmental effects on infalling galaxies. Possible physical mechanisms happening in the regions include ram-pressure stripping, strangulation, galaxy mergers and evaporation. However, since this is still a relatively low density regions (local galaxy density $< 2 \text{ Mpc}^{-2}$), it is difficult for major mergers to take place frequently (Kodama et al. 2001; Treu et al. 2003). In addition, since major merger destroys spiral arms, it can not explain the existence of the passive spirals in this intermediate regions. From the same reason, this cluster infalling regions are still too low gas density for ram-pressure stripping, strangulation or evaporation (interaction with intra-cluster medium) to be effective (Balogh et al. 1997; Lewis et al. 2002). However, this is the regions where overdensity of a few to a few dozen galaxies (cluster sub-clumps) can often be found. (e.g., Kodama et al. 2001). These cluster sub-clumps might be a group of galaxies infalling into a cluster. Fujita et al. (2003) showed that in these cluster sub-clump regions, stripping can take place effectively, mainly due to higher mass density of the gas in sub-clumps even though their absolute mass is much smaller than clusters. In fact, Kodama et al. (2001) found that $V - I$ colors of galaxies abruptly become redder around these cluster sub-clump regions. If ram-pressure stripping (or strangulation), is responsible for galaxy evolution in these regions, it can also explain other observational results. Since it does not disturb spiral structures of disc galaxies, it can naturally create passive spiral galaxies (Figure 7.3; Chapter 7). Since stripping is more effective in clusters with higher X-ray temperature, it can explain richness dependence of blue/late type fractions (Figure 5.1; Chapter 5). Stripped galaxies should be smaller than their progenitors, just like S0 galaxies were smaller than Sc galaxies in Figure 6.16. Therefore, we propose that stripping (including strangulation) in sub-clump regions might be the physical mechanism happening in these regions although it is also difficult to exclude other possibilities.

In the very cores of clusters (local galaxy density $\sim 6 \text{ galaxy Mpc}^{-2}$ or within $0.3 R_{vir}$), we observed that S0 fractions decrease, and in turn, elliptical fractions radically increase (Figure 6.14; Chapter 6). We also observed that passive spiral galaxies do not exist in cluster cores (Figure 7.8; Chapter 7). Possible mechanism happening in these cluster cores must be the one that reduces passive spirals and increase elliptical fractions. Major galaxy mergers seem to be able to increase elliptical fractions by merging two or more S0 galaxies into one giant elliptical galaxy. However, since the relative velocities between each galaxy is high in cluster cores, it is difficult for gravitational interactions to happen frequently (Ostriker 1980; Binney & Tremaine 1987; Mamon 1992; Makino & Hut

1997). There have been several observational results reporting that cluster ellipticals have been in the core for a long time (>5 Gyr; van Dokkum et al. 1998). Therefore, cluster ellipticals might have been created in the cluster core regions through merging when a cluster itself was much younger ($z > 1$). Since these giant ellipticals in cluster cores are numerous, the observational decrease of passive spirals and S0s at cluster cores can be also explained if S0s and passive spirals which stopped star formation in the intermediate regions become faint by the time they reach cluster cores, and drop out of the sample to increase the dominance of giant elliptical galaxies.



Figure 8.1: A schematic illustration of the evolution of galaxies due to the cluster environment.

Chapter 9

Conclusions

We have studied the environmental effects on galaxy evolution using the Sloan Digital Sky Survey (SDSS) data. Our main findings are as follows.

We have developed a new cluster finding method, the Cut & Enhance (CE) method, which uses color and angular separation to create a uniform cluster catalog with high detection sensitivity. We apply Cut & Enhance method to the SDSS commissioning data and produced an SDSS Cut & Enhance cluster catalog containing 4638 galaxy cluster candidates in $\sim 350 \text{ deg}^2$.

Using this cluster catalog, we constructed composite luminosity functions (LFs) of 204 SDSS CE clusters ranging from $z = 0.02$ to $z = 0.25$. Compared with the field luminosity function, cluster LFs have a brighter characteristic magnitude (M^*) and a flatter slope in the g, r, i and z band. We also found that early-type galaxies always have flatter slopes than late-type galaxies in the clusters.

We investigate the evolution of the fractions of blue cluster galaxies as a function of redshift, using 514 CE clusters in the range of $0.02 \leq z \leq 0.3$. This evolution has been investigated for the first time without any significant systematic bias benefitting from our large, uniform cluster catalog. By selecting blue galaxies as those with restframe $g - r$ bluer by 0.2 than red-sequence or those with $u - r < 2.2$, we found that blue fractions of cluster galaxies increase ~ 20 points between $z = 0.02$ and $z = 0.3$ at the 99.9% significance level, confirming the presence of the Butcher-Oemler effect.

We observed the morphological Butcher-Oemler effect as an increase of late-type galaxies toward higher redshifts, using pure morphological parameters such as a concentration parameter and de Vaucouleur/exponential profile fit. In addition, we found a slight tendency for richer clusters to have lower values of the late-type fraction (Figure 5.4).

We studied the morphology-density relation and the morphology-cluster-centric-radius relation using a volume limited SDSS data ($0.05 < z < 0.1$, $Mr^* < -20.5$). Our results are based on the morphological classifier, T_{auto} , which correlates with eye-classified galaxy morphology. If the galaxy classification with T_{auto} corresponds to the physical galaxy

classification, the following interpretation become possible. We found that there are two characteristic changes in both the morphology-density and the morphology-radius relations, suggesting two different mechanisms are responsible for the relations. In the sparsest regions (below 2 galaxy Mpc⁻² or outside of 2 R_{vir}), both of the relations become flat, suggesting the responsible physical mechanisms require denser environment. In the intermediate density regions, (density between 2 and 6 galaxy Mpc⁻² or between 0.3 and 2 R_{vir}), intermediate fractions ($-0.8 \leq T_{auto} < 0.1$) increase toward denser regions, whereas late-spiral fractions ($1.0 \leq T_{auto}$) decrease. In the densest regions (above 6 galaxy Mpc⁻² or inside of 0.3 R_{vir}), intermediate fractions decreases radically and early-type fractions ($T_{auto} \leq -0.8$) increase.

We compared the morphology-density relation from the SDSS ($0.01 < z < 0.054$) with that of the MORPHS data ($z \sim 0.5$). Two relations lie on top of each other, suggesting that the morphology-density relation was already established at $z \sim 0.5$ as it is in the present universe.

We studied the environment of passive spiral galaxies as a function of local galaxy density and cluster-centric-radius. It is found that passive spiral galaxies preferentially live in local galaxy density $1 \sim 2$ galaxy Mpc⁻² and $1 \sim 10 R_{vir}$ (Figures 7.7 and 7.8).

Throughout the work, we have revealed the characteristic environments where cluster galaxies evolve. These environments provide strong constraints in specifying the underlying physical mechanisms that govern cluster galaxy evolution.

Appendix A

A Catalog of H δ -strong Galaxies

A.1 Introduction

Presence of a strong H δ absorption line (equivalent width of $> 5\text{\AA}$) in the spectrum of a galaxy is an indication that the spectral energy distribution of that galaxy is dominated by A stars. Models of galaxy evolution indicate that such a strong H δ line (in the spectrum of a galaxy) can only be reproduced using models that include a recent burst of star formation, followed by passive evolution, because any on-going star-formation in the galaxy would hide the H δ absorption line due to emission-filling (of the H δ line) and the dominance of hot O and B stars, which have intrinsically weaker H δ absorption than A stars (see, for example, Balogh et al. 1999; Poggianti et al. 1999). Therefore, the existence of a strong H δ absorption line in the spectrum of a galaxy suggests that the galaxy has undergone a recent transformation in its star-formation history. In the literature, such galaxies are called “post-starburst”, “E+A”, or H δ -strong galaxies. Exact physical mechanism(s) responsible for the abrupt change in the star formation history of such galaxies remains unclear. These galaxies have received much attention as they provide an opportunity to study galaxy evolution “*in action*”.

H δ -strong galaxies were first discovered by Dressler & Gunn (1983, 1992) in their spectroscopic study of galaxies in distant, rich clusters of galaxies. They discovered cluster galaxies that contained strong Balmer absorption lines but with no detectable [OII] emission lines. They named such galaxies “E+A”, as their spectra resembled the superposition of an elliptical galaxy spectrum and A star spectrum. Therefore, E+A galaxies were originally thought to be a cluster-specific phenomenon and several physical mechanisms have been proposed to explain such galaxies. For example, ram-pressure stripping of the interstellar gas by a hot, intra-cluster medium, which eventually leads to the termination of star formation once all the gas in the galaxy has been removed, or used up for star formation (Gunn & Gott 1972; Farouki & Shapiro 1980; Kent 1981; Abadi, Moore & Bower

1999; Fujita & Nagashima 1999; Quilis, Moore & Bower 2000). Alternative mechanisms include high-speed galaxy-galaxy interactions in clusters (Moore et al. 1996, 1999) and interactions with the gravitational potential well of the cluster (Byrd & Valtonen 1990; Valluri 1993; Bekki, Shioya & Couch 2001).

To test such hypotheses, Zabludoff et al. (1996) performed a search for E+A galaxies in the Las Campanas Redshift Survey (LCRS; Shectman et al. 1996) and found that only 21 of the 11113 LCRS galaxies they studied satisfied their criteria for a E+A galaxy. This work clearly demonstrates the rarity of such galaxies at low redshift. Furthermore, Zabludoff et al. (1996) found that 75% of their selected galaxies reside in the field, rather than the cores of rich clusters. This conclusion was confirmed by Balogh et al. (1999), who also performed a search for H δ -strong galaxies in the redshift surveys of the Canadian Network for Observational Cosmology (CNOC; Yee, Ellingson, & Carlberg 1996), and found that the fraction of such galaxies in clusters was similar to that in the field. Alternatively, the study of Dressler et al. (1999) found an order-of-magnitude increase in the abundance of E+A galaxies in distant clusters compared to the field (see also Castander et al. 2001). Taken together, these studies suggest that the physical interpretation of H δ -strong galaxies is more complicated than originally envisaged, with the possibility that different physical mechanisms are important in different environment, e.g., 5 of the 21 E+A galaxies discovered by Zabludoff et al. (1996) show signs of tidal features, indicative of galaxy-galaxy interactions or mergers. Furthermore, redshift evolution might be an important factor in the differences seen between these surveys.

In addition to studying the environment of H δ -strong galaxies, several authors have focused on understanding the morphology and dust content of these galaxies. This has been driven by the fact that on-going star formation in post-starburst galaxies could be hidden by dust obscuration (See Poggianti & Barbaro 1997; Poggianti et al. 1999; Bekki et al. 2001 for more discussion). In fact, Smail et al (1999) discovered examples of such galaxies using infrared (IR) and radio observations of galaxies in distant clusters. They discovered five post-starburst galaxies (based on their optical spectra) that showed evidence for dust-lanes in their IR morphology as well as radio emission consistent with on-going star formation. However, radio observations of the Zabludoff et al. (1996) sample of nearby E+A galaxies indicates that the majority of these galaxies are not dust-enshrouded starburst galaxies. For example, Miller & Owen (2001) only detected radio emission from 2 of the 15 E+A galaxies they observed, and the derived star-formation rates (SFRs) were consistent with quiescent star formation and thus much lower than those observed for the dust-enshrouded starburst galaxies of Smail et al (1999). Chang et al. (2001) also did not detect radio emission from any of the 5 E+A galaxies they observed from the Zabludoff et al. (1996) sample and concluded that these galaxies were not dust-enshrouded starbursts. In summary, these studies demonstrate that some E+A

galaxies have dust-enshrouded star formation, but the fraction remains ill-determined. Furthermore, it is unclear how the different sub-classes discussed in the literature are related, and if there are any environmental and evolutionary processes in play.

The interpretation of H δ -strong galaxies (E+A) suffers from small number statistics and systematic differences in the selection and definition of such galaxies among the different surveys constructed to date. Therefore, many of the difficulties associated with understanding the physical nature of these galaxies could be solved through the study of a large, homogeneous sample of H δ galaxies. In this Chapter, we present such a sample derived from the Sloan Digital Sky Survey (SDSS; York et al. 2000). The advantage of this sample, over previous work, is the quality and quantity of both the photometric and spectroscopic data, as well as the homogeneous selection of SDSS galaxies which covers a wide range of local environments.

We present in this Chapter a sample of galaxies that have been selected based solely on the observed strength of their H δ absorption line. Our selection is thus inclusive, containing many of the sub-classes of galaxies discussed in the literature until now, e.g., “E+A” galaxies (Zabludoff et al. 1996; Dressler et al. 1999), post-starburst galaxies, dust-enshrouded starburst galaxies (Smail et al. 1999), H δ -strong galaxies (Couch & Sharples 1987) and the different subsamples of galaxies, i.e., e(a) and A+em, discussed by Poggianti et al. (1999) and Balogh et al. (1999). Following Couch & Sharples (1987) and Balogh et al. (1999), we call our sample of SDSS galaxies as “H δ -strong” (HDS) galaxies.

In this Chapter, we present the details of our selection and leave the investigation and interpretation of these HDS galaxies to subsequent papers. We publish our sample of HDS galaxies to help the community construct larger samples of such galaxies, which are critically needed to advance our understanding of these galaxies, as well as to promote the planning of follow-up observations and comparisons with studies of such galaxies at higher redshifts.

In Section A.2, we present a brief discussion of the SDSS and the data used in this Chapter. In Section A.3, we discuss our techniques for measuring the H δ absorption line and present comparisons between the different methodologies used to measure this line. In Section A.4, we discuss the criteria used to select of our HDS sample of galaxies and present data on 3340 such galaxies in our catalog. In Section A.5, we compare our sample of galaxies with those in the literature. A more detailed analysis of the properties of our HDS galaxies will be discussed in subsequent papers. The cosmological parameters used throughout this Chapter are $H_0 = 75 \text{ km s}^{-1} \text{ Mpc}^{-1}$, $\Omega_m = 0.3$ and $\Omega_\Lambda = 0.7$.

A.2 The SDSS Data

In this Section, we briefly describe the spectroscopic part of the SDSS. As discussed in York et al. (2000), the SDSS plans to obtain spectra for $\simeq 10^6$ galaxies to a magnitude limit of $r^* = 17.7$ (the “Main” galaxy sample; Strauss et al. 2002), $\simeq 10^5$ Luminous Red Galaxies (LRG; Eisenstein et al. 2001) and $\simeq 10^5$ quasars (Richards et al. 2002). The reader is referred to Fukugita et al. (1996), Gunn et al. (1998), Lupton et al. (1999, 2001), York et al. (2000), Hogg et al. (2001), Pier et al. (2002), Stoughton et al. (2002), Smith et al. (2002) and Blanton et al. (2002a) for more details of the SDSS and its data.

The SDSS spectra are obtained using two fiber-fed spectrographs (each with 320 fibers), with each fiber subtending 3 arcseconds on the sky. The wavelength coverage of the spectrographs is 3800Å to 9200Å, with a spectral resolution of 1800. The data from these spectrographs is automatically reduced to produce flux and wavelength-calibrated spectra (SPECTRO2D data analysis pipeline).

The SDSS spectra are then analyzed via the SDSS SPECTRO1D data processing pipeline to obtain a host of measured quantities for each spectrum (see Stoughton et al. 2002; Frieman et al., in prep, for further details). For example, SPECTRO1D determines the redshift of the spectrum both from absorption lines (via cross-correlation; Heavens 1993), and emission lines (via a wavelet-based peak-finding algorithm; see Frieman et al., in prep). Once the redshift is known, SPECTRO1D estimates the continuum emission at each pixel using the median value seen in a sliding box of 100 pixels centered on that pixel. Emission and absorption lines are then measured automatically by fitting of a Gaussian, above the best-fit continuum, at the redshifted rest-wavelength of expected lines. Multiple Gaussians are fit simultaneously for potential blends of lines, i.e., H α and [NII] lines). SPECTRO1D therefore provides an estimate of the equivalent width (EW), continuum, rest wavelength, identification, goodness-of-fit (χ^2), height and sigma (and the associated statistical errors on these quantities) for all the major emission/absorption lines in these spectra. These measurements are done regardless of whether the line has been detected or not. For this work, we have used data from rerun 15 of the SPECTRO1D analysis pipeline, which is based on version 4.9 of the SPECTRO2D analysis pipeline (see Frieman et al. in prep for details of these pipelines).

In order to construct the sample of HDS galaxies presented in this Chapter, we begin with a sample of SDSS galaxies that satisfy the following selection criteria:

1. Spectroscopically-confirmed by SPECTRO1D to be a galaxy;
2. Possess a redshift confidence of ≥ 0.7 ;
3. An average spectroscopic signal-to-noise ratio of > 5 per pixel in the SDSS photometric g passband;

4. $z \geq 0.05$, to minimize aperture effects as discussed in Zaritsky, Zabludoff & Willick (1995) and Gomez et al. (2003).

The reader is referred to Stoughton et al. (2002) for further details on all these SDSS quantities and how they are determined. After removing duplicate observations of the same galaxy (11538 galaxies in total; see Section A.3.4), 106682 galaxies satisfy these criteria, up to and including spectroscopic plate 804 (observed on a Modified Julian Date of 52266 or 12/23/01; see Stoughton et al. 2002). Of these 106682 galaxies, it was possible to measure the H δ line for only 95479 galaxies (see Section A.3.1 below) due to masked pixels at or near the H δ line. In Figure A.1, we present the distribution of signal-to-noise ratios for all 106682 spectra (the median value of this distribution is 8.3).

Throughout this analysis, we use the “smeared” SDSS spectra, which improves the overall spectrophotometric calibration of these data by accounting for light missed from the 3” fibers due to seeing and atmospheric refraction (see Gomez et al. 2003; Stoughton et al. 2002 for observational detail). Unfortunately, this smearing correction can systematically bias the observed flux of any emission and absorption lines in the spectrum, as the correction is only applied to the continuum. As shown by Hopkins et al. in prep., however, this is only a $\simeq 10\%$ effect on the flux of spectral lines, compared to using spectral data without the smearing correction applied. Furthermore, the equivalent width of our lines is almost unaffected by this smearing correction as, by definition, they are computed relative to the height of the continuum.

A.3 Spectral Line Measurements

A.3.1 H δ Equivalent Width

In this Section, we discuss the measurement of the equivalent width (EW) of the H δ absorption line in the SDSS galaxy spectra described in Section A.2. The presence of a strong H δ absorption line in a galaxy spectrum indicates that the stellar population of the galaxy contains a significant fraction of A stars, which must have formed within the last Gigayear (see Section A.1). The H δ line is preferred to other Hydrogen Balmer lines (e.g., H ϵ , H ζ , H γ , H β) because the line is isolated from other emission and absorption lines, as well as strong continuum features in the galaxy spectrum (e.g., D4000). Furthermore, the higher order Balmer lines (H γ and H β) can suffer from significant emission-filling (see Section A.3.3), while the lower order lines (H ϵ and H ζ) are low signal-to-noise in the SDSS spectra.

In previous studies, several different methods have been employed to measure the H δ line, or select post-starburst galaxies. For example, Zabludoff et al. (1996) used the average EW of the H β , H γ and H δ lines to select E+A galaxies. Alternatively, Dressler

et al. (1999) and Poggianti et al. (1999) interactively fit Gaussian profiles to the H δ line. Finally, Abraham et al. (1996b), Balogh et al. (1999) and Miller & Owen (2002) performed a non-parametric analysis of their galaxy spectra, which involved summing the flux in a narrow wavelength window centered on the H δ line to determine the EW of the line. Castander et al. (2001) used an innovative PCA and wavelet analysis of spectra to select E+A galaxies. Each of these methods have different advantages and disadvantages. For example, fitting a Gaussian to the H δ line is optimal for high signal-to-noise spectra, but can be prone to erroneous results when fit blindly to low signal-to-noise data or to weak absorption lines (such problems can be avoided if Gaussians are fit interactively; see Dressler et al. 1999; Poggianti et al. 1999). In light of the potential systematic differences among the different methods of measuring the H δ line, we have investigated the relative merits of the two main approaches in the literature – fitting a Gaussian and summing the flux in a narrow wavelength window – for determining the EW of the H δ line for the signal-to-noise ratio, resolution, and size of the SDSS spectral dataset used in this Chapter.

First, we investigate the optimal method for computing the EW of the H δ line from the SDSS spectra using the non-parametric methodology outlined in Abraham et al. (1996b) and Balogh et al. (1999), i.e., summing the flux within narrow wavelength windows centered on and off the H δ absorption line. We estimate the continuum flux via linear interpolation between two wavelength windows placed at either side of the H δ line (4030Å to 4082Å and 4122Å to 4170Å). We used the same wavelength windows as in Abraham et al. (1996b) and Balogh et al. (1999) for estimating the continuum because they are devoid of any strong emission and absorption features, and the continuum is relatively smooth within these wavelength ranges. Also, these continuum windows are close to the H δ line without being contaminated by the H δ line itself. When fitting the continuum flux level, the flux in each pixel was weighted by the inverse square of the error on the flux in that pixel. After the initial fit to the continuum, we re-iterate the fit once by rejecting 3σ outliers to the original continuum fit. This guards against noise spikes in the surrounding continuum.

The rest-frame EW of the H δ line was calculated by summing the ratio of the flux in each pixel of the spectrum, over the estimated continuum flux in that pixel based on our linear interpolation. For this summation, we investigated two different wavelength windows for the H δ line; 4088Å to 4116Å, which is the same as the wavelength range used by Balogh et al. (1999)¹ and 4082Å to 4122Å, which is the wider range used by Abraham et al. (1996b). We summarize the wavelength ranges used to measure the H δ

¹We note that Table 1 of Balogh et al. (1999) has a typographical error. The authors used the wavelength range of 4088Å to 4116Å to measure their H δ EWs instead of 4082Å to 4122Å as quoted in the paper.

EWs in Table A.1.

In Figure A.2, we compare the two non-parametric measurements of $H\delta$ using the narrow and wide wavelength windows. In this Chapter, positive EWs are absorption lines and negative EWs are emission lines. We find, as expected, a strong linear relationship between the two measurements: The scatter about the best fit linear relationship to these measurements is Gaussian with $\sigma = 0.29\text{\AA}$. However, there are systematic differences between the two measurements which are correlated to the intrinsic width of the $H\delta$ line. For example, for large EWs of $H\delta$, we find that the wide wavelength window has a larger value than the narrow window. This is because the 28\AA window is too small to capture the wings of a strong $H\delta$ line and thus a wide window is needed. The same systematic trend can be found for $H\delta$ emission lines (i.e., negative EWs), where the wide window captures more flux than the narrow window and produces smaller values of EWs.

As a compromise, we have empirically determined that the best methodology for our analysis is to always select the larger of the two $H\delta$ EW measurements (this was discovered by visually inspecting many of the spectra and their various $H\delta$ measurements). This is a crude adaptive approach of selecting the size of the window based on the intrinsic strength of the $H\delta$ line. In fact, we find that 20.2% of our HDS galaxies (see Section A.4) were selected based on the $H\delta$ measurement in the large wavelength window. Therefore, for the analysis presented in this paper, we use $H\delta_{\max}$, which is the maximum of the two non-parametric measurements discussed above.

In Figure A.3, we now compare the $H\delta_{\max}$ measurement discussed above to the automatic Gaussian fits to the $H\delta$ line from the SDSS SPECTRO1D analysis of the spectra. As expected, the two methods give similar results for the EW of the $H\delta$ line for the largest EWs. However, there are significant differences, as seen in Figure A.3, between these two methodologies. First, there are many galaxies with a negative EW (emission) as measured by SPECTRO1D, but possess a (large) positive EW (absorption) using the non-parametric method. These cases are caused by emission-filling, i.e., a small amount of $H\delta$ emission at the bottom of the $H\delta$ absorption line (see Section A.3.3). This results in SPECTRO1D fitting the Gaussian to the central emission line, thus producing a negative EW. On the other hand, the non-parametric method simply sums all the flux in the region averaging over the emission and still producing a positive EW. In Figure A.4, we present five typical examples of this phenomenon.

Another noticeable difference between the two methods seen in Figure A.3 is the deviation from the one-to-one relation for $H\delta$ EWs near zero, i.e., as the $H\delta$ line becomes weak, it is buried in the noise of the continuum making it difficult to automatically fit a Gaussian to the line. In such cases, SPECTRO1D tends to overestimate the EW of the $H\delta$ line because it preferentially fits a broad, shallow Gaussian to the noise in the spectrum. Typical examples of this problem are shown in Figure A.5. We conclude

from our study of the SDSS spectra that the non-parametric techniques of Abraham et al. (1996b) and Balogh et al. (1999) are preferred to the automatic Gaussian fits of SPECTRO1D, especially for the lower signal-to-noise SDSS spectra which are the majority in our sample (see Figure A.1). We note that many of the problems associated with the automatic Gaussian fitting of SPECTRO1D can be avoided by fitting Gaussians interactively. However, this is not practical for large datasets such as the SDSS.

A.3.2 [OII] and H α Equivalent Widths

In addition to estimating the EW of the H δ line, we have used our flux-summing technique to estimate the rest frame equivalent widths of both the [OII] and H α emission lines. We perform this analysis on all 95479 SDSS spectra. As these emission lines are the primary diagnostics of on-going star-formation in a galaxy and thus, we are interested in detecting any evidence of these lines in our HDS galaxies. As discussed in Section A.3.1, the flux-summing technique is better for the lower signal-to-noise spectra, while the Gaussian-fitting method of SPECTRO1D is optimal for higher signal-to-noise detections of these emission lines, especially in the case of H α where SPECTRO1D deblends the H α and [NII] lines.

We use the same flux-summing methodology as discussed above for the H δ line. However, we use only one wavelength window centered on the two emission lines. We list in Table A.1 the wavelength windows used in summing the flux for the [OII] and H α emission lines and the continuum regions around these lines. Once again, the continuum flux per pixel for each emission line was estimated using linear interpolation of the continuum estimated at either side of the emission lines (weighted by the inverse square of the errors on the pixel values during a line fitting procedure). We again iterate the continuum fit once rejecting 3σ outliers to the original continuum fit. We do not deblend the H α and [NII] lines and as a result, some of our H α EW measurements may be overestimated. However, the contamination is less than 5% from [NII] line at 6648Å and less than 30% from [NII] line at 6583Å. We present estimates of the external error on our measurements of [OII] and H α in Section A.3.4.

In Figure A.6, we compare our [OII] equivalent width measurements to that from SPECTRO1D for all 95479 SDSS spectra. In this Chapter, positive EWs are absorption lines and negative EWs are emission lines. There is a good agreement between the two methods for $\text{EW}(\text{[OII]}) > 10\text{\AA}$, where the scatter is $< 10\%$. However, at lower EWs, the SPECTRO1D measurement of [OII] is systematically larger than our flux-summing method which is the result of SPECTRO1D fitting a broad Gaussian to the noise in the spectrum. We are only concerned with making a robust detection of any [OII] emission, rather than trying to accurately quantify the properties of the emission line. Therefore,

we prefer our non-parametric method, especially for the low signal-to-noise cases.

In Figure A.7, we compare our $H\alpha$ equivalent width measurements against that of SPECTRO1D for all 95479 SDSS spectra regardless of their $H\delta$ EW. The two locii of points seen in this figure are caused by contamination in our estimates of $H\alpha$ due to strong emission lines in AGNs, i.e., the top locus of points have larger EWs in our flux-summing, method than measured by SPECTRO1D due to contamination by the [NII] lines. This is confirmed by the fact that the top locus of points is dominated by AGNs. At low $H\alpha$ EWs, we again see a systematic difference between our measurements and those of SPECTRO1D, with SPECTRO1D again over-estimating the $H\alpha$ line because it is jointly fitting multiple Gaussians to low signal-to-noise detections of the $H\alpha$ and [NII] emission lines. Finally, we do not make any correction for extinction and stellar absorption on our flux-summed measurements of $H\alpha$ (see Section A.3.3).

A.3.3 Emission-Filling of the $H\delta$ Line

As mentioned above, our measurements of the $H\delta$ absorption line can be affected by emission-filling, i.e., $H\delta$ emission at the bottom of the $H\delta$ absorption line. This problem could be solved by fitting two Gaussians to the $H\delta$ line; one for absorption, one for emission. We found, however, that this method is only reliable for spectra with a signal-to-noise ratio of > 20 and, as shown in Figure A.1, this is only viable for a small fraction of our spectra. Therefore, we must explore an alternative approach for correcting for this potential systematic bias; however, we stress that the sense of any systematic bias on our non-parametric summing method would be to always decrease (less absorption) the observed EW of the $H\delta$ absorption line and thus our technique gives a lower limit to the amount of $H\delta$ absorption in the spectrum.

To help rectify the problem of emission-filling, we have used the $H\alpha$ and $H\beta$ emission lines (where available) to jointly constrain the amount of emission-filling at the $H\delta$ line as well as estimate the effects of internal dust extinction in the galaxy. Furthermore, our estimates of the emission-filling are complicated by the effects of stellar absorption on the $H\alpha$ and $H\beta$ emission lines. In this analysis, we have used the SPECTRO1D measurements of $H\alpha$ and $H\beta$ lines in preference to our flux-summing technique discussed in Section A.3.2, because the emission-filling correction is only important in strongly star-forming galaxies where the $H\alpha$ and $H\beta$ emission lines are well fit by a Gaussian and, for the $H\alpha$ line, require careful deblending from the [NII] lines.

To solve the problem of emission-filling, we have adopted two different methodologies which we describe in detail below. The first method is an iterative procedure that begins with a initial estimate for the amount of stellar absorption at the $H\beta$ and $H\alpha$ emission lines, i.e., we assume $H\beta$ EW (absorption) = 1.5\AA and $H\alpha$ EW (absorption) = 1.9\AA

(see Poggianti & Barbaro 1997; Miller & Owen 2002). Then, using the observed ratio of the H α and H β emission lines (corrected for stellar absorption), in conjunction with an attenuation law of $\tau = A \lambda^{-0.7}$ (Charlot & Fall 2000) for galactic extinction and a theoretical H α to H β ratio of 2.87 (case B recombination; Osterbrock 1989), we solve for the parameter, A , in the attenuation law and thus gain extinction-corrected values for both the H β and H α emission lines. Next, using the theoretical ratio of H β emission to H δ emission, we obtain an estimate for the amount of emission-filling (extinction-corrected) in the H δ absorption line. We then correct the observed H δ absorption EW for this emission-filling. Further, assuming that the EW(H δ) absorption is equal to EW(H β) absorption and EW(H α) absorption is equal to $1.3 + 0.4 \times$ EW(H β) absorption (Keel 1983), we obtain new estimates for the stellar absorption at the H α and H β emission lines, i.e., where we began the iteration. We iterate this calculation five times, but on average, a stable solution converges after only one iteration.

Our second method uses the D4000 break to estimate the amount of stellar absorption at H β , using $\text{EW}(\text{H}\beta) = -5.5 \times \text{D4000} + 11.6$ (Poggianti & Barbaro 1997; Miller & Owen 2002). Then, assuming that $\text{EW}(\text{H}\alpha)$ absorption is equal to $1.3 + 0.4 \times \text{EW}(\text{H}\beta)$ absorption, we obtain a measurement for the amount of stellar absorption at both the H α and H β absorption lines. As in the first method above, we use the Charlot & Fall (2000) attenuation law, and the theoretical H α to H β ratio, to solve for the amount of extinction at H α and H β , and then use these extinction-corrected emission lines to estimate the amount of emission-filling at H δ . We do not iterate this method, as we have used the measured D4000 break to independently estimate the amount of stellar absorption at H β and H α .

We have applied these two methods to all our 95479 SDSS spectra, except for any galaxy that possesses a robust detection of an Active Galactic Nucleus (AGN) based on the line indices discussed in Kewley et al. (2002) and Gomez et al. (2003). For these AGN classifications, we have used the SPECTRO1D emission line measurements. We also stop our emission-filling correction if the ratio of the H β and H α line becomes unphysical, i.e., greater than 2.87. By definition, the emission-filling correction increases our observed values of the H δ absorption line, with a median correction of 15% in the flux of the H δ absorption line. In Figure A.8, we show the distributions of H δ emission EWs calculated using the two methods described above in a solid (iteration) and a dashed (D4000) line, respectively. It is reassuring that these two methods broadly give the same answer and have similar distributions.

A.3.4 External Errors on our Measured Equivalent Widths

Before we select our HDS sample of galaxies, it is important to accurately quantify the errors on our EW measurements. In our data, there are 11538 that were galaxies spectroscopically observed twice (see Section A.2). We use them to quantify the external error on our EW measurements. In Figures A.9, A.10 and A.11, we present the absolute difference in equivalent width of the two independent observations of the H δ , H α and [OII] lines, as a function of signal-to-noise ratio. In these figures, we have used the lower of the two measured signal-to-noise ratios (in SDSS g band for H δ and H β , or r band for H α) because any observed difference in the two measurements of the EW will be dominated by the error in the noisier (lower signal-to-noise) of the two spectra. From this data, we determine the 1σ error for each line as a function of signal-to-noise ratio, and assign this error to our EW measurements for each galaxy. We determine the sigma of the distribution by fitting a Gaussian (as a function of signal-to-noise ratio) as shown in Figures A.12, A.13 and A.14, and then use a 3rd order polynomial as shown in the following equation to interpolate between the four signal-to-noise bins, thus obtaining the solid lines shown in Figures A.9, A.10 and A.11.

$$\text{error} = a_0 + a_1 \times (S/N) + a_2 \times (S/N)^2 + a_3 \times (S/N)^3 \quad (\text{A.1})$$

Using these polynomial fits, we can estimate the 1σ error on our EWs for any signal-to-noise ratio. The coefficients of the fitted 3rd order polynomial for each line are given in Table A.2.

In addition to quantifying the error on [OII], H α and H δ , we have used the duplicate observations of SDSS galaxies to determine the error on our emission-filling corrections. Only 400 (564) of the 11538 duplicate observations of SDSS galaxies have strong H α and H β emission lines which are required for the iterative (D4000) method of correcting for emission-filling. The errors on the emission-filling correction are only a weak function of signal-to-noise ratio, so we have chosen to use a constant value for their error, rather than varying the error as a function of the galaxy signal-to-noise ratio as done for H δ , [OII] and H α emission lines. One sigma errors on the emission correction of H δ for the iterative method (EF1) and the D4000 method (EF2) are 0.57Å and 0.4Å in EW, respectively.

A.4 A Catalog of HDS Galaxies

We are now ready to select our sample of HDS galaxies using the non-parametric measurements of the H δ EW (i.e., $\text{EW}(\text{H}\delta_{\max})$). We begin by imposing the following threshold on $\text{EW}(\text{H}\delta_{\max})$;

$$\text{EW}(\text{H}\delta_{\max}) - \Delta\text{EW}(\text{H}\delta_{\max}) > 4\text{\AA}, \quad (\text{A.2})$$

where $\Delta\text{EW}(\text{H}\delta_{\max})$ is the error estimated from the 1σ difference in $\text{H}\delta$ EWs between two observations of the same galaxy (see Figure A.9). We have chosen this threshold (4\AA) based on visual inspections of the data and our desire to select galaxies similar to those selected by other authors (Zabludoff et al. 1996; Balogh et al. 1999; Poggianti et al. 1999), i.e., galaxies with strong recent star formation as defined by the $\text{H}\delta$ line. This threshold (Eqn. A.2) is applied without any emission-filling correction. For the signal-to-noise ratios of our spectra (Figure A.1), only galaxies with an observed $\text{H}\delta$ of $\sim 5\text{\AA}$ satisfy Eqn. A.2, which is close to the 5\AA threshold used by Balogh et al. (1999) to separate normal star-forming galaxies from post-starburst galaxies (see Figures 8 & 9 in their paper). Therefore, our HDS sample should be similar to those already in the literature, but is still conservative enough to be inclusive of the many different subsamples of $\text{H}\delta$ -strong galaxies, like k+a, a+k, A+em and e(a), as discussed in Poggianti et al. (1999) and Balogh et al. (1999). We will present a detailed comparison of our HDS sample with models of galaxy evolution in future papers.

We call the sample of galaxies that satisfy Eqn. A.2 “Sample 1”. Sample 1 contains 2760 galaxies. Among these, 2526 galaxies come from the main SDSS galaxy sample and 234 were galaxies targeted for spectroscopy for other reasons, e.g., mostly because they were LRG galaxies (see Eisenstein et al. 2002), or some were targeted as “stars” or “quasars” (see Richards et al. 2002). For comparison, if we remove the $\Delta\text{EW}(\text{H}\delta_{\max})$ term from the equation, the number of HDS galaxies increases to 10788. Instead of $\text{H}\delta_{\max}$, if we only use the narrow or wide window, the number reduces to 811 and 2273 galaxies, respectively.

We then apply the emission-filling correction to $\text{EW}(\text{H}\delta_{\max})$ for each galaxy and select an additional sample of galaxies, which were not already selected in Sample 1 via Eqn A.2, but now satisfy both the following criteria;

$$\begin{aligned} \text{EW}(\text{H}\delta_{\max}) - \Delta\text{EW}(\text{H}\delta_{\max}) - \Delta\text{EW}(\text{EF1}) &> 4\text{\AA}, \\ \text{EW}(\text{H}\delta_{\max}) - \Delta\text{EW}(\text{H}\delta_{\max}) - \Delta\text{EW}(\text{EF2}) &> 4\text{\AA}, \end{aligned} \quad (\text{A.3})$$

where $\Delta\text{EW}(\text{EF1}) = 0.57\text{\AA}$ and $\Delta\text{EW}(\text{EF2}) = 0.4\text{\AA}$ are the 1σ errors of the iterative method (EF1) and D4000 method (EF2) of the emission-filling correction discussed in Section A.3.4. Therefore, this additional sample of galaxies represents systems that would only satisfy the threshold in Eqn A.2 because of the emission-filling correction (in addition to galaxies already selected as Sample 1). We call this sample of galaxies “Sample 2” and it contains 580 galaxies. Among them, 483 galaxies come from the main SDSS galaxy sample and 97 galaxies were again targeted for spectroscopy for other reasons, e.g., LRG galaxies, “stars” or “quasars”. On average, Sample 2 galaxies have strong emission lines because, by definition, they have the largest emission-filling correction at the $\text{H}\delta$ line. We have imposed the above two criteria to control the number of extra galaxies scattered into

the sample. If we relax these criteria (i.e., remove both $\Delta\text{EW}(\text{EF1})$ and $\Delta\text{EW}(\text{EF2})$), then the sample would increase from 580 galaxies (in total) to 1171. If we only use one of the emission filling corrections, the resulting number of HDS galaxies are 1151 and 1467 for iteration method and D4000 method, respectively.

In total, 3340 SDSS galaxies satisfy these criteria (Sample 1 plus Sample 2), and we present these galaxies as our catalog of HDS galaxies. We note that only 131 of these galaxies are securely identified as AGNs using the prescription of Kewley et al. (2002) and Gomez et al. (2003). In Figure A.15, we present the fraction of HDS galaxies selected as a function of their signal-to-noise ratio in SDSS g band. It is reassuring that there is no observed correlation, which indicates that our selection technique is not biased by the signal-to-noise ratio of the original spectra.

For each galaxy in Samples 1 and 2, we present the unique SDSS Name (col. 1), heliocentric redshift (col. 2), spectroscopic signal-to-noise ratio in the SDSS photometric g band (col. 3), Right Ascension (J2000; col. 4) and Declination (J2000; col. 5) in degrees, Right Ascension (J2000; col. 6) and Declination (J2000; col. 7) in hours, minutes and seconds, the rest-frame $\text{EW}(\text{H}\delta)$ (\AA , col. 8), the rest-frame $\Delta\text{EW}(\text{H}\delta)$ (\AA , col. 9), the rest-frame $\text{EW}([\text{OII}])$ (\AA , col. 10), the rest-frame $\Delta\text{EW}([\text{OII}])$ (\AA , col. 11), the rest-frame $\text{EW}(\text{H}\alpha)$ (\AA , col. 12), the rest-frame $\Delta\text{EW}(\text{H}\alpha)$ (\AA , col. 13), the SDSS Petrosian g band magnitude (col. 14), the SDSS Petrosian r band magnitude (col. 15), the SDSS Petrosian i band magnitude (col. 16), the SDSS Petrosian z band magnitude (col. 17; all magnitudes are extinction corrected), the k-corrected absolute magnitude in the SDSS r band (col. 18), SDSS measured seeing in r band (col. 19), concentration index (col. 20, see Shimasaku et al. 2001 and Strateva et al. 2001 for definition). In Column 21, we present the AGN classification based on the line indices of Kewley et al. (2002), and in Column 22, we present our E+A classification flag, which is defined in Section A.5.1. An electronic version of our catalog can be obtained at <http://sdss2.icrr.u-tokyo.ac.jp/~yohnis/ea>.²

In addition to presenting Samples 1 and 2, we also present a volume-limited sample selected from these two samples but within the redshift range of $0.05 < z < 0.1$ and with $M(r^*) < -20.5$ (which corresponds to $r = 17.7$ at $z = 0.1$, see Gomez et al. 2003). We use Schlegel, Finkbeiner & Davis (1998) to correct for galactic extinction and Blanton et al. (2002b; v1_11) to calculate the k-corrections. In Table A.3, we present the percentage of HDS galaxies that satisfy our criteria. In this table, the number of galaxies in the whole sample (shown in the denominator) changes based on the number of galaxies that could have had their $\text{H}\delta$, $[\text{OII}]$ and $\text{H}\alpha$ lines measured because of masked pixels in the spectra.

We note here that we have not corrected our sample for possible aperture effects, except restricting the sample to $z \geq 0.05$: A 3 arcsec fiber corresponds to $2.7h_{75}^{-1}$ kpc

²Mirror sites are available at <http://kokki.phys.cmu.edu/~tomo/ea>, and <http://astrophysics.phys.cmu.edu/~tomo/ea>

at this redshift, which is comparable to the half-light radius of most our galaxies (see also Gomez et al. 2003). We see an increase of 0.33\AA ($< 10\%$) in the median observed $\text{H}\delta$ EW for the whole HDS sample over the redshift range of our volume-limited sample ($0.05 < z < 0.1$). This is probably caused by more light from the disks of galaxies coming into the fiber at higher redshifts. We see no such trend for the subsample of true E+A galaxies (see Section A.5) in our HDS sample.

A.5 Discussion

In this Section, we compare our sample of HDS galaxies against previous samples of such galaxies in the literature. Further analysis of the global properties (luminosity, environment, morphology, *etc.*) of these galaxies will be presented in future papers.

A.5.1 Comparison with Previous Work

In this Section, we present a preliminary comparison of our SDSS HDS galaxies with other samples of post-starburst galaxies in the literature. We have attempted to replicate the selection criteria of these previous studies as closely as possible, but in some cases, this is impossible. Furthermore, we have not attempted to account for systematic differences in the distribution of signal-to-noise ratios, differences in the spectral resolutions, and differences in the selection techniques used by different authors, e.g., we are unable to fully replicate the criteria of Zabludoff et al. (1996) as we do not yet possess accurate measurements of the $\text{H}\gamma$ and $\text{H}\beta$ lines. Therefore, these are only crude comparisons and any small differences seen between the samples should not be over-interpreted until a more detailed analysis can be carried out. We summarize our comparison in Table A.4 and discuss the details of these comparisons below: Table A.4 does, however, demonstrate once again the rarity of $\text{H}\delta$ -strong galaxies, especially at low redshift, as well as illustrating the sensitivity of their detection to the selection criteria used.

We first compare our sample to that of Zabludoff et al. (1996), which is the most similar to our work, especially as the magnitude limits of the LCRS (used by Zabludoff et al. 1996) and the SDSS are close, thus minimizing possible bias. Zabludoff et al. (1996) selected E+A galaxies from the LCRS using the following criteria; a redshift range of $15,000 < cz < 40,000 \text{ km s}^{-1}$, a signal-to-noise ratio of > 8 per pixel, an EW of $[\text{OII}]$ of $> -2.5\text{\AA}$, and an average EW for the three Balmer lines ($\text{H}\delta$, $\text{H}\gamma$ and $\text{H}\beta$) of $> 5.5\text{\AA}$. Using these four criteria, Zabludoff et al. (1996) selected 21 LCRS galaxies as E+A galaxies, which corresponds to 0.2% of all LCRS that satisfy the same signal-to-noise ratio and redshift limits. We find 80 SDSS galaxies (from the whole 95479 SDSS galaxies analyzed here) which lie in the same redshift range and satisfy $[\text{OII}] \text{ EW} > -2.5\text{\AA}$ as used

by Zabludoff et al. (1996) as well as having $H\delta$ EW of $>5.5\text{\AA}$, which should be close to the average of the EW of the three Balmer lines ($H\delta$, $H\gamma$ and $H\beta$) used by Zabludoff et al. (1996). Of these 80 galaxies, 71 are in our HDS sample. Given all the caveats discussed above, it is reassuring that we have found HDS galaxies at a similar frequency (see Table A.4) as Zabludoff et al. (1996) and it suggests that our criteria are consistent with theirs.

Several other authors have used similar criteria to Zabludoff et al. (1996) to search for post-starburst galaxies in higher redshift samples of galaxies. For example, Fisher et al. (1998) used an average EW of the $H\delta$, $H\gamma$ and $H\beta$ lines of $> 4\text{\AA}$ and an EW of $[\text{OII}]$ of $< 5\text{\AA}$. With these criteria, they found 4.7% of their galaxies were E+A galaxies. Similarly, Hammer et al. (1997) used an average of $H\delta$, $H\gamma$ and $H\beta$ of $> 5.5\text{\AA}$, an EW of $[\text{OII}]$ of $< 5\text{\AA}$ and $M_B < -20$ to select E+A galaxies from the CFRS field galaxy sample. They found that 5% of their galaxies satisfied these criteria.

We have also attempted to replicate the selection criteria of Dressler et al. (1999) and Balogh et al. (1999) as closely as possible, using 26863 SDSS galaxies in the volume-limited sample with measured $H\delta$, $[\text{OII}]$ and $H\alpha$. For example, the MORPHS collaboration of Dressler et al. (1999) and Poggianti et al. (1999) selected E+A galaxies using $H\delta$ EW of $> 3\text{\AA}$ and $[\text{OII}]$ EW of $< 5\text{\AA}$. Using these criteria, they found a significant excess of E+A galaxies in their 10 high redshift clusters (21%), compared with the field region (6%). On the other hand, Balogh et al. (1999) selected E+A galaxies using $H\delta$ EW of $> 5\text{\AA}$ and $[\text{OII}]$ EW of $< 5\text{\AA}$. They found instead $1.5 \pm 0.8\%$ of cluster galaxies were classified as E+A galaxies compared to $1.2 \pm 0.8\%$ for the field (brighter than $M(r) = -18.8 + 5\log h$ after correcting for several systematic effects).

In Table A.4, we present a qualitative comparison of our HDS sample with these two higher redshift studies and, within the quoted errors, the frequencies of HDS galaxies we observe are consistent with their values. However, we caution the reader not to overinterpret these numbers for several reasons. First, we are comparing a low redshift sample ($z < 0.1$) of HDS galaxies to high redshift studies ($z \simeq 0.5$) of such galaxies, and we have not accounted for possible evolutionary effects or observational biases. In particular, we are comparing our sample against the corrected numbers presented by Balogh et al. (1999), which attempt to account for scatter in the tail of the $H\delta$ distribution due to the large intrinsic errors on $H\delta$ measurements, while Dressler et al. (1999) do not make such a correction. Secondly, we are comparing a field sample of HDS galaxies to field samples of galaxies selected in the cluster field. Finally, the luminosity limit of our volume-limited sample is brighter than the high redshift studies, which may account for some of the discrepancies.

Finally, we note that the original E+A phenomenon in galaxies, as discussed by Dressler & Gunn (1983, 1992), was defined to be a galaxy that possesses strong Balmer absorption lines, but with no emission lines, i.e., a galaxy with the signature of recent

star-formation activity (A stars), but no indication of on-going star-formation (e.g., nebular emission lines). Given the quality of the SDSS spectra, we can re-visit this specific definition and select galaxies from our sample that possess less than 1σ detections of both the H α and [OII] emission lines, i.e., $\text{EW}(\text{[OII]}) + \Delta\text{EW}(\text{[OII]}) \geq 0\text{\AA}$ and $\text{EW}(\text{H}\alpha) + \Delta\text{EW}(\text{H}\alpha) \geq 0\text{\AA}$). We find that only $3.5 \pm 0.7\%$ (25/717) of galaxies in the volume limited HDS sample satisfy such a strict criteria (see Table A.3). We show example spectra of these galaxies in Figure A.16 and highlight them in the catalog using the E+A classification flag. This exercise demonstrates that true E+A galaxies – with no, or little, evidence for on-going star-formation – are extremely rare at low redshift in the field, i.e., $0.09 \pm 0.02\%$ of all SDSS galaxies in our volume-limited sample.

A.5.2 HDS Galaxies with Emission-lines

In this Section, we examine the frequency of nebular emission lines ([OII], H α) in the spectra of our HDS galaxies. This is possible because of the large spectral coverage of the SDSS spectrographs which allow us to study both the [OII] and H α emission lines for all galaxies out to a redshift of $\simeq 0.35$. We begin by looking at HDS galaxies that possess both the H α and [OII] emission lines. Using the criteria that both [OII] and H α lines must be detected at $> 1\sigma$ significance (i.e., $\text{EW}(\text{[OII]}) + \Delta\text{EW}(\text{[OII]}) < 0\text{\AA}$ and $\text{EW}(\text{H}\alpha) + \Delta\text{EW}(\text{H}\alpha) < 0\text{\AA}$), we find that $89 \pm 5\%$ (643/717) of HDS galaxies in our volume-limited sample are selected. Of these, 131 HDS galaxies possess a robust detection of an AGN, based on the line indices of Kewley et al. (2001), similar to the AGN plus post-starburst galaxy found recently in the 2dFGRS (see Sadler, Jackson & Cannon 2002). Therefore, a majority of these emission line H δ galaxies may have on-going star formation and are similar to the e(a) and A+em subsample of galaxies discussed by Poggianti et al. (1999) and Balogh et al. (1999). We show in Figure A.17 examples of these HDS galaxies that possess both the [OII] and H α emission lines. The median SFR of these galaxies (calculated from H α flux, see Kennicutt 1998) is $\simeq 0.5\text{M}_\odot/\text{yr}$, with a maximum observed SFR of $50\text{M}_\odot/\text{yr}$. We note that these SFRs have not been corrected for dust extinction or aperture effects. The true SFR for the whole galaxy could be larger than these values by a factor of 5-10 (see Hopkins et al. in prep for more detail).

We next examine the frequency of HDS galaxies with [OII] emission, but no detectable H α emission. Using the criteria of $\text{EW}(\text{H}\alpha) < 1\sigma$ detection and $\text{EW}(\text{[OII]}) > 1\sigma$ detection (i.e., $\text{EW}(\text{[OII]}) + \Delta\text{EW}(\text{[OII]}) < 0\text{\AA}$ and $\text{EW}(\text{H}\alpha) + \Delta\text{EW}(\text{H}\alpha) \geq 0\text{\AA}$), we find that $2.9 \pm 0.65\%$ (21/717) of our HDS galaxies in the volume-limited sample satisfy these criteria. The presence of [OII] demonstrates that the galaxy may possess on-going star formation activity, yet the lack of the H α emission is curious. Possible explanations for this phenomena are strong self-absorption of H α by the many A stars in the galaxy

and/or metallicity effect which could increase the [OII] emission relative to H α emission. We show several examples of these galaxies in Figure A.18, and the lack of H α emission is clearly visible. The fact that many of these galaxies possess strong [NII] lines (flanking the H α line) indicates strong self-absorption is a likely explanation for the missing H α emission line. Median [OII] EW of these galaxies is 1.3 Å. Compared with 11.5 Å of HDS galaxies with both [OII] and H α emission, these galaxies have much lower amount of [OII] in emission.

Finally, we find that $3.8 \pm 0.7\%$ (27/717) of our HDS galaxies in our volume-limited sample satisfy the criteria of $\text{EW}(\text{[OII]}) + \Delta\text{EW}(\text{[OII]}) \geq 0\text{\AA}$ and $\text{EW}(\text{H}\alpha) + \Delta\text{EW}(\text{H}\alpha) < 0\text{\AA}$; i.e., HDS with no [OII] emission but with H α emission. Only 52 of our HDS galaxies in the volume limited sample have just no [OII] emission detected (only $\text{EW}(\text{[OII]}) + \Delta\text{EW}(\text{[OII]}) \geq 0\text{\AA}$). Therefore, $52 \pm 12\%$ (27/52) of the HDS galaxies with no detected [OII] have detected H α emission. The existence of such galaxies has ramifications on high redshift studies of post-starburst galaxies, as such studies use the [OII] line to constrain the amount of on-going star-formation within the galaxies (e.g., Balogh et al. 1999, Poggianti et al. 1999). Therefore, if the H α emission comes from star-formation activity, then these previous high redshift studies of post starburst galaxies may be contaminated by such galaxies. A possible explanation for the lack of [OII] emission is dust extinction. Miller & Owen (2002) recently found dusty star-forming galaxies which do not possess [OII] in emission, but have radio fluxes consistent with on-going star formation activity. This explanation would also be consistent with the lower signal-to-noise ratio we observe in the blue-end of the SDSS spectra of these galaxies, relative to the signal-to-noise ratio seen in the red-end of their spectra. Median H α EW of these galaxies are 1.5 Å, whereas that of HDS galaxies with both [OII] and H α emission is 25.9 Å.

A.6 Conclusions

We present in this Chapter the largest, most homogeneous, search to date for H δ -strong galaxies (i.e., post-starburst galaxies, E+A's, k+a's, a+k's etc.) in the local universe. We provide the astronomical community with a new catalog of such galaxies selected from the Sloan Digital Sky Survey (SDSS) based solely on the observed strength of the H δ hydrogen Balmer absorption line within the spectrum of the galaxy. We have carefully studied different methodologies of measuring this weak absorption line and conclude that a non-parametric flux-summing technique is most suited for an automated application to large datasets like the SDSS, and that it is more robust for the observed signal-to-noise ratios available in these SDSS spectra. We have studied the effects of dust extinction, emission-filling and stellar absorption upon the measurements of our H δ lines and have determined the external error on our measurements as a function of signal-to-noise ratio,

using duplicate observations of 11358 galaxies in the SDSS. In total, our catalog of H δ -strong (HDS) galaxies contains 3340 galaxies selected from the 95479 galaxies in the Sloan Digital Sky Survey (at the time of writing). Our catalog will be a useful basis for the future studies to understand the nature of such galaxies and the comparison with studies of such systems at higher redshifts.

The measured abundance of our H δ -strong (HDS) galaxies is $2.6 \pm 0.1\%$ of all galaxies within a volume-limited sample of $0.05 < z < 0.1$ and $M(r^*) < -20.5$, which is consistent with previous studies of post-starburst galaxies in the literature. We find that only 25 galaxies ($3.5 \pm 0.7\%$) of HDS galaxies in this volume limited sample show no, or little, evidence for [OII] and H α emission lines. This indicates that true E+A galaxies (as originally defined by Dressler & Gunn) are extremely rare objects, i.e., only $0.09 \pm 0.02\%$ of all galaxies in our volume-limited sample. In contrast, $89 \pm 5\%$ of our HDS galaxies have significant detections of the [OII] and H α emission lines. Of these, 131 galaxies are robustly classified as Active Galactic Nuclei (AGNs) and therefore, the majority of these emission line HDS galaxies are star-forming galaxies, similar to the e(a) and A+em galaxies discussed by Poggianti et al. (1999) and Balogh et al. (1999). We study the global properties of our HDS galaxies in further detail in Appendix B.

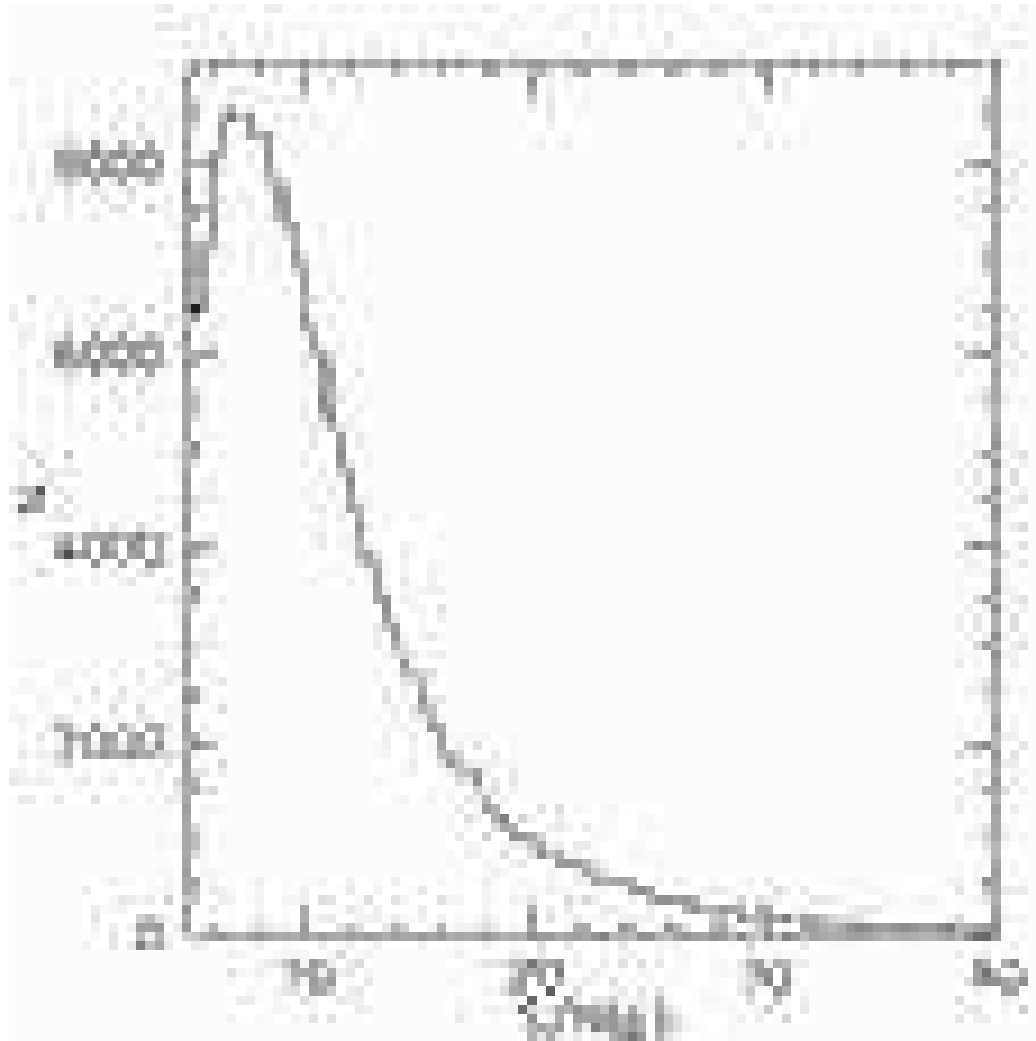


Figure A.1: The distribution of signal-to-noise ratio for 95479 spectra used in this analysis (see Section A.2). The signal-to-noise ratio presented here is the average signal-to-noise ratio per pixel over the wavelength range defined by the SDSS photometric g passband. The median signal-to-noise ratio is 8.3. Galaxies with signal-to-noise ratio less than 5 were not used in our study.

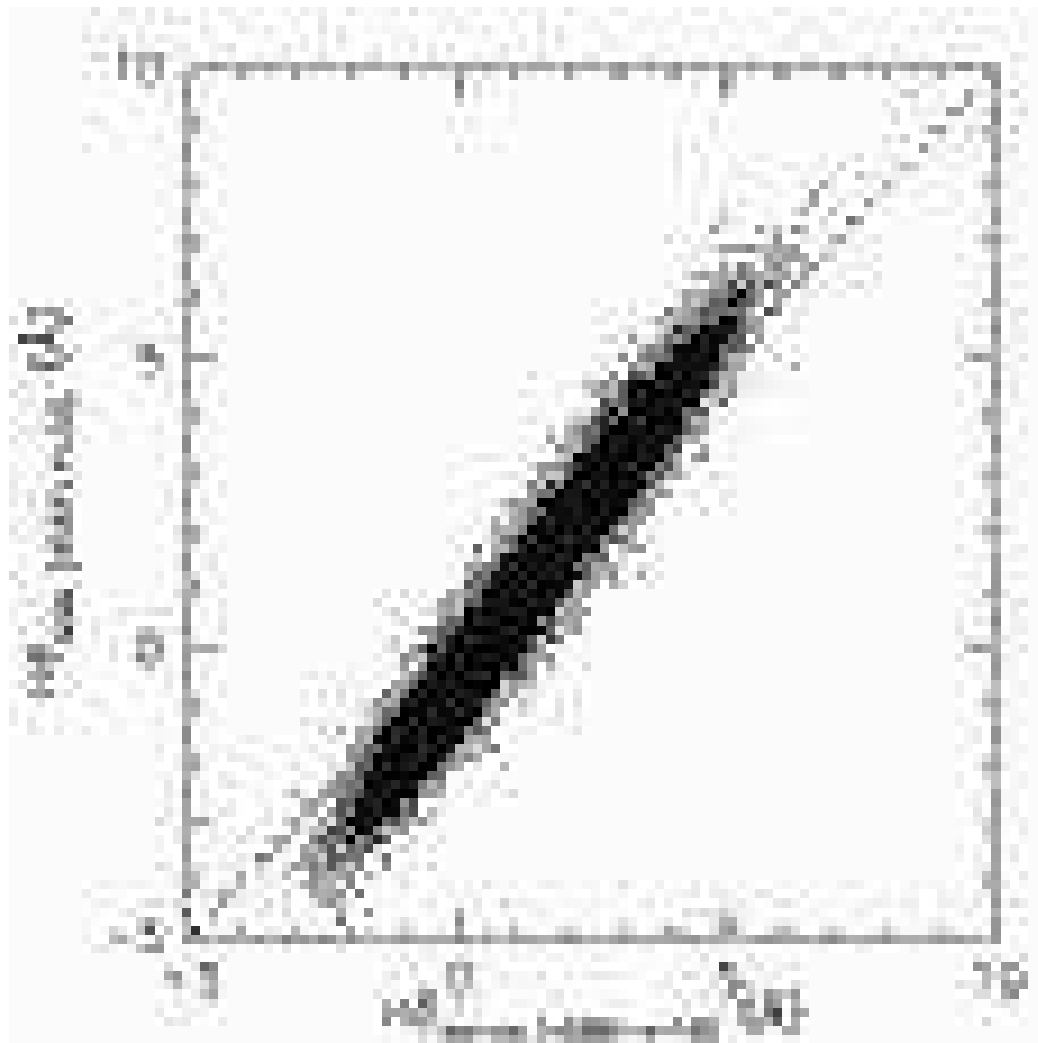


Figure A.2: The H δ EW (\AA) as measured in two different wavelength windows, i.e., the *wide* window of Abraham et al. (1996b) and the *narrow* window of Balogh et al. (1999). The expected one-to-one line is plotted to help guide the eye. For the work presented in this Chapter, absorption lines have a positive EW values and emission lines have negative EW values.



Figure A.3: A comparison of the $H\delta$ EW as measured automatically by the SDSS SPEC-TRO1D spectroscopic pipeline (a Gaussian fit to the $H\delta$ line) and the non-parametric summation technique discussed in this Chapter and presented in Figure A.2. The one-to-one line is shown to guide the eye. In our work, absorption lines have positive EW values and emission lines have negative EW values.

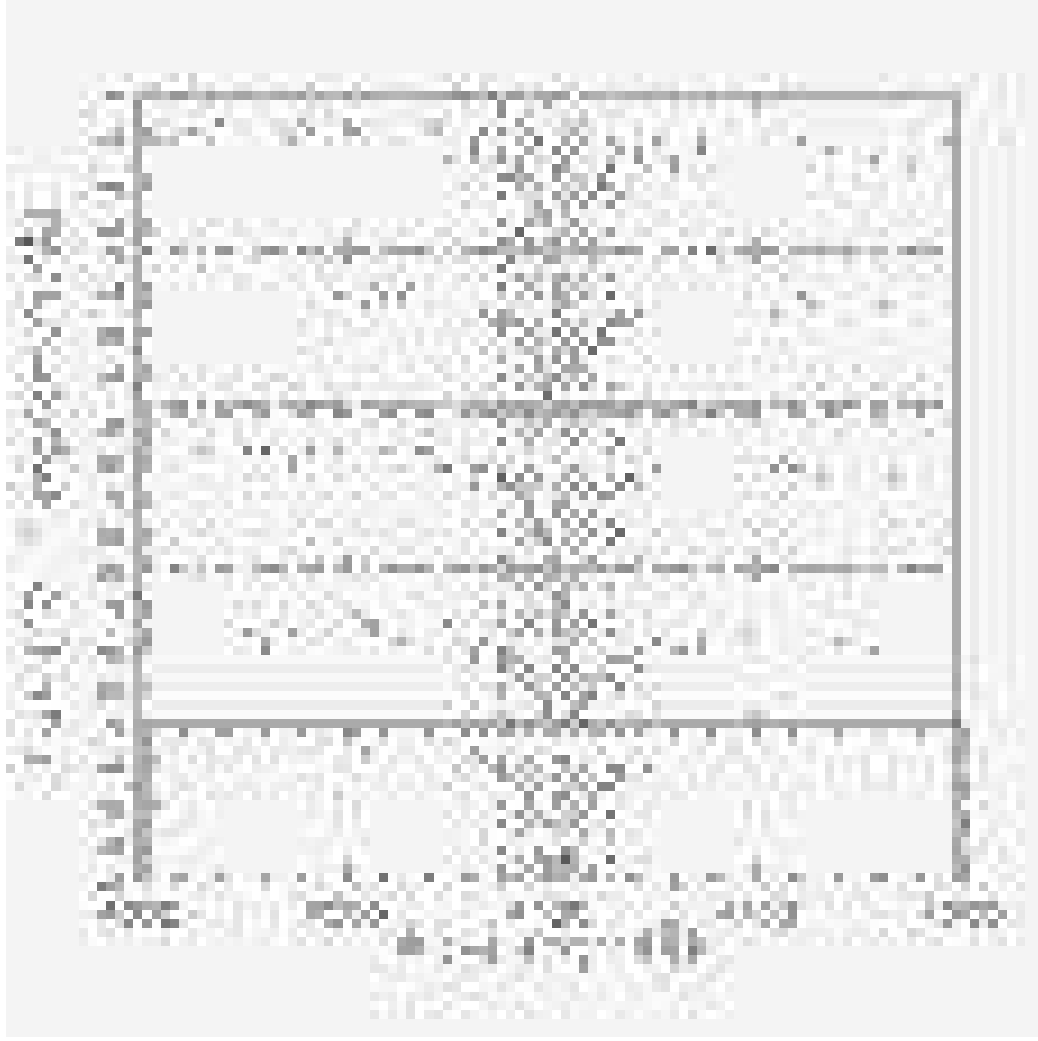


Figure A.4: Five typical examples of SDSS spectra with $H\delta$ emission filling. In such cases it is difficult to fit the $H\delta$ absorption emission with a single Gaussian due to a centrally peaked emission. The double shaded region of this figure, centered on the $H\delta$ line, represents the narrow wavelength window used to measure the EW of $H\delta$ as explained in Section A.3.1. The slightly wider shaded region, again centered on the $H\delta$ line, represents the wide wavelength window used to measure the $H\delta$ line (see Section A.3.1). Finally, the two dashed regions, at each side of the shaded regions, represent the wavelength regions used to estimate the continuum flux. See also Table A.1 for details of the wavelength windows used on measuring the $H\delta$ line.



Figure A.5: Five examples of noisy spectra where the SDSS SPECTRO1D pipeline has fit a broad absorption line, thus overestimating the H δ EW. The shaded regions are the same as presented and discussed in Figure A.4.

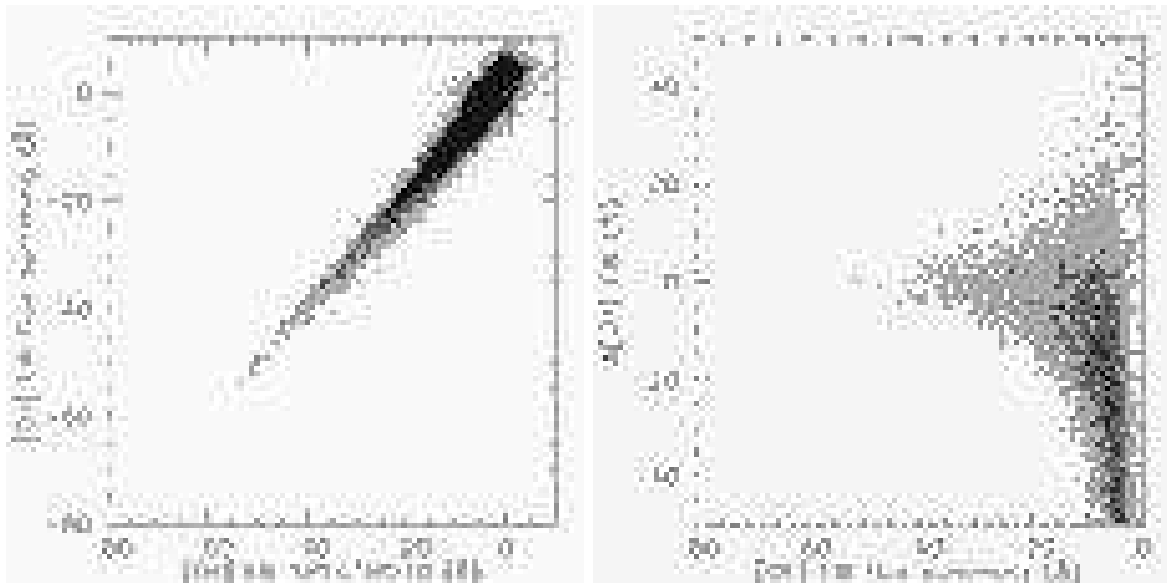


Figure A.6: In the left panel, we present the comparison of our [OII] EW measurements (flux summing) and those of SPECTRO1D (Gaussian fitting) for all 94770 SDSS spectra regardless of their H δ EWs. In the right panel, we plot the percentage difference between these two measurements. Positive percentages mean our flux summing method has a larger value.

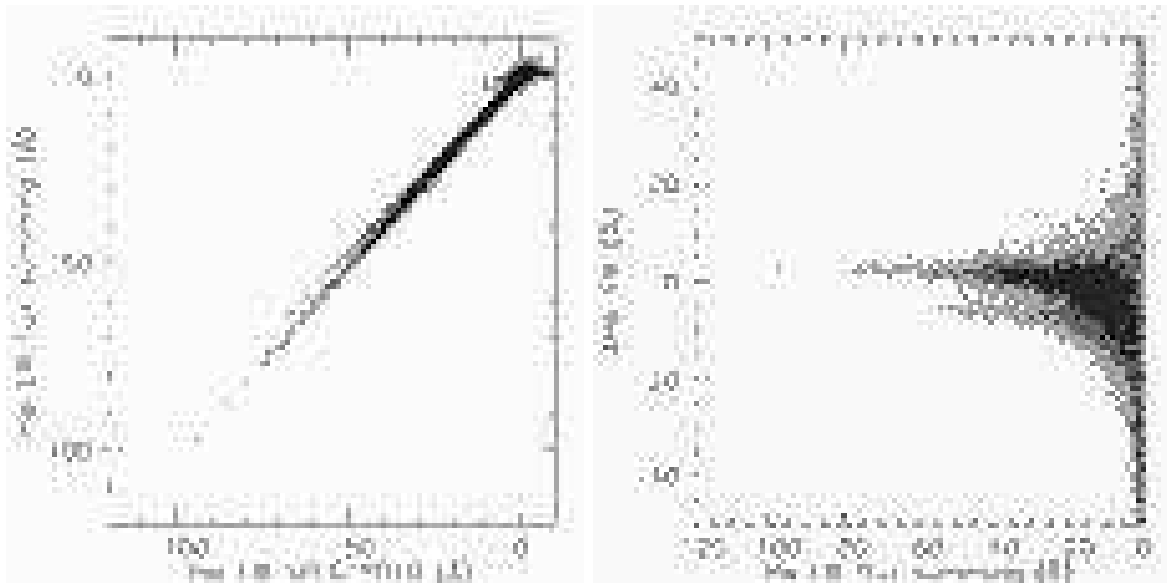


Figure A.7: In the left panel, we present the comparison of our $H\alpha$ EW measurements (flux summing) and those of SPECTRO1D (Gaussian fitting) for all SDSS 94770 spectra regardless of their $H\delta$ EWs. In the right panel, we plot the percentage difference between these two measurements. Positive percentages mean our flux summing method has a larger value.

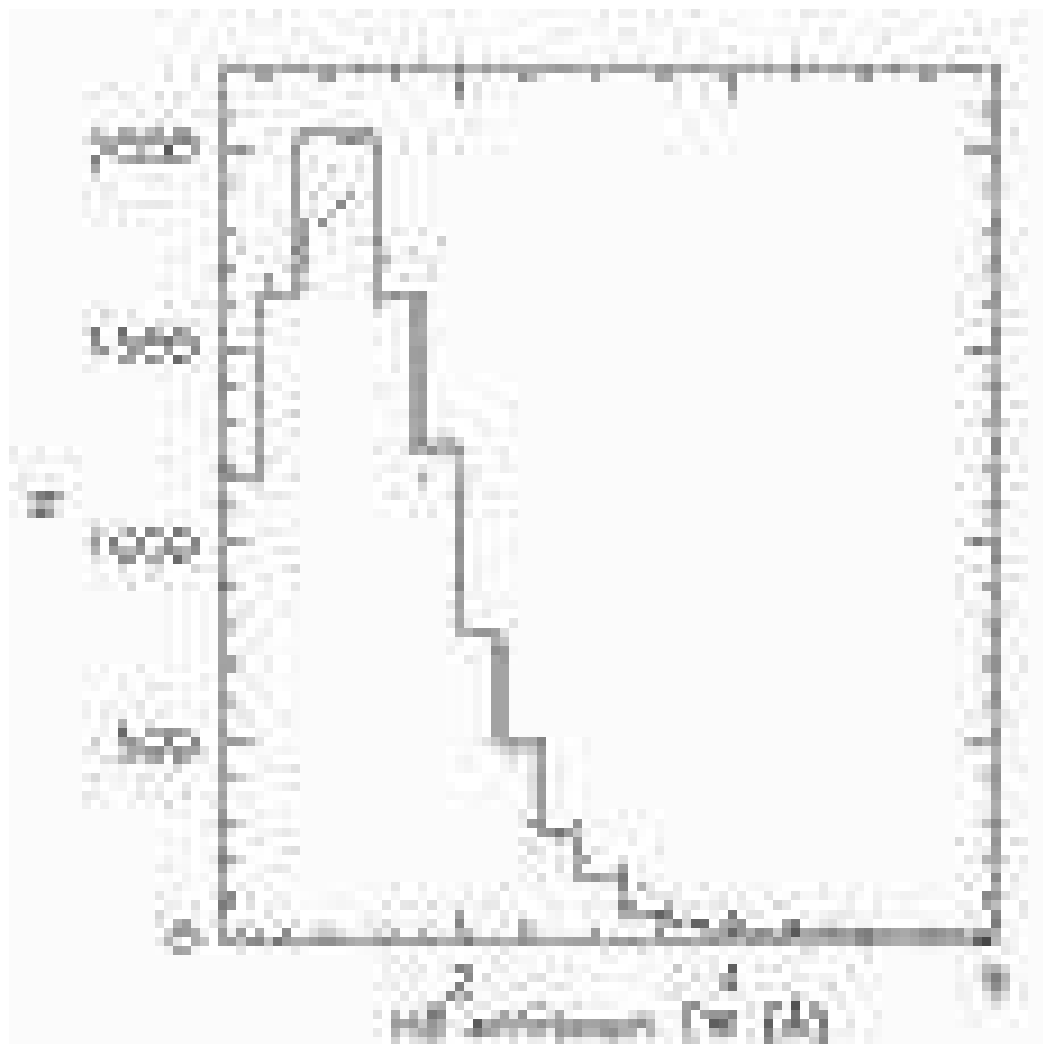


Figure A.8: The amount of emission filling correction of H δ EW. The solid line is for the iteration method (EF1) and the shaded histogram uses the D4000 method (EF2).

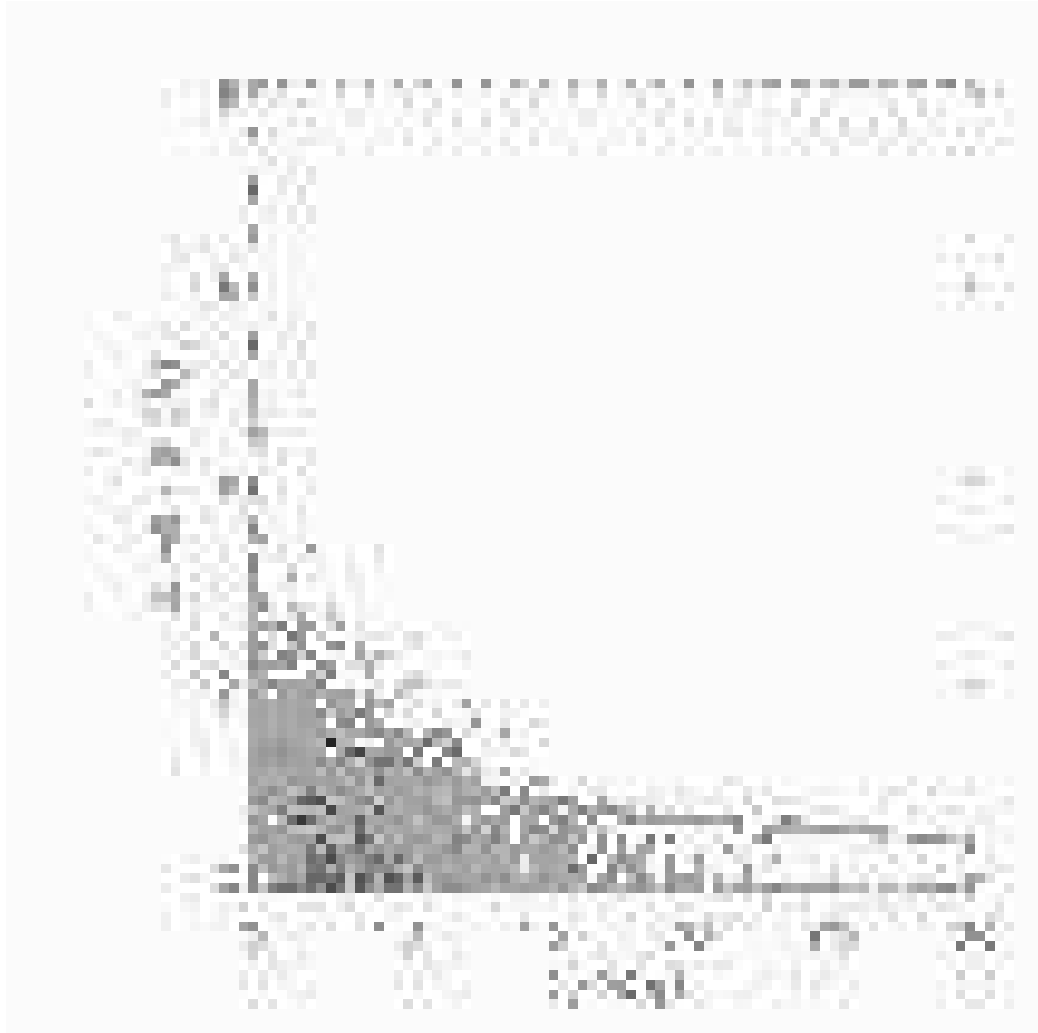


Figure A.9: The absolute difference in the measured $H\delta$ EW (\AA) for duplicate observations of 11538 SDSS galaxies as a function of signal-to-noise ratio (the lower of the two signal-to-noise ratios has been plotted here). The solid line shows the 1σ polynomial line fitted to the distribution of errors (as a function of signal-to-noise ratio).

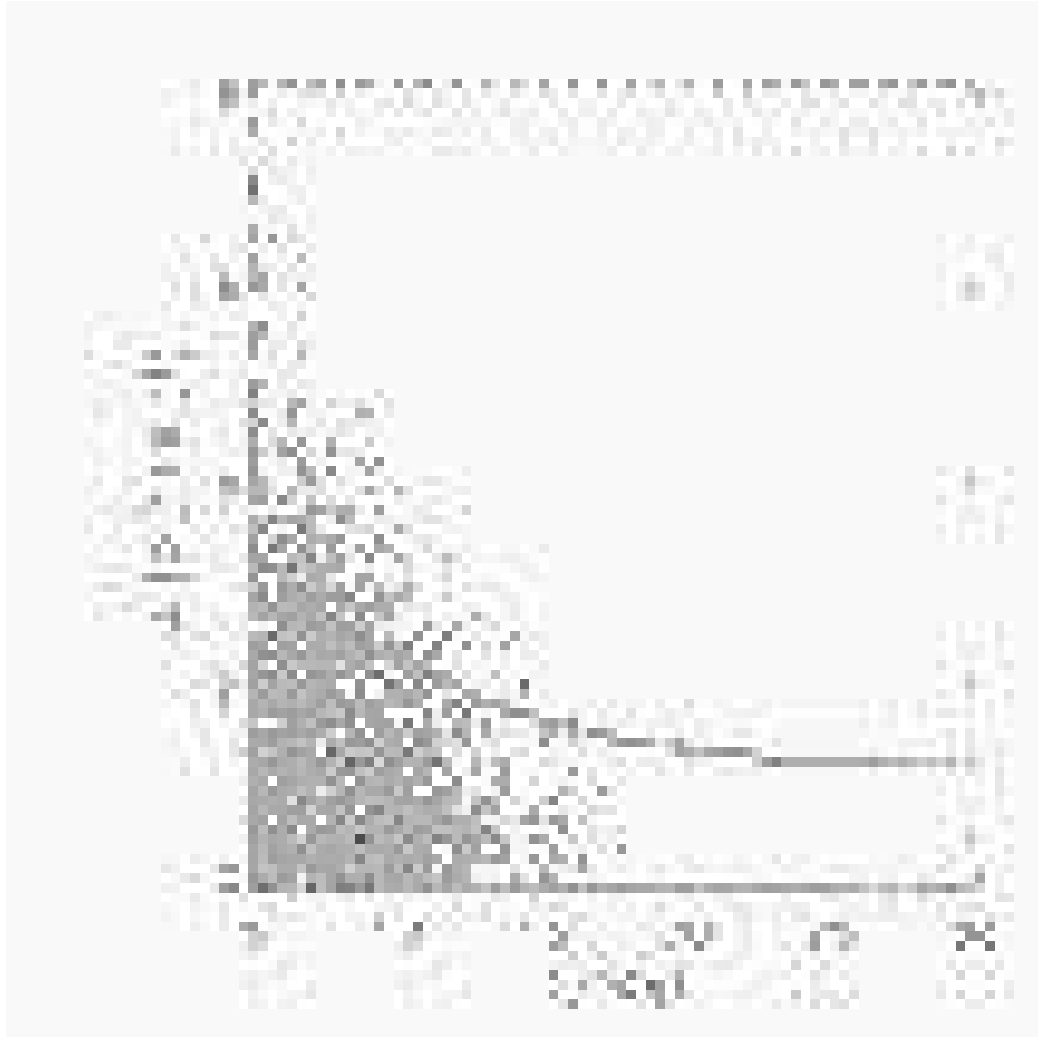


Figure A.10: The absolute difference in the [OII] EW (\AA) for duplicate observations of 11538 SDSS galaxies as a function of signal-to-noise ratio (the lower of the two signal-to-noise ratios has been plotted here). The solid line shows the 1σ polynomial line fitted to the distribution of errors (as a function of signal-to-noise ratio).

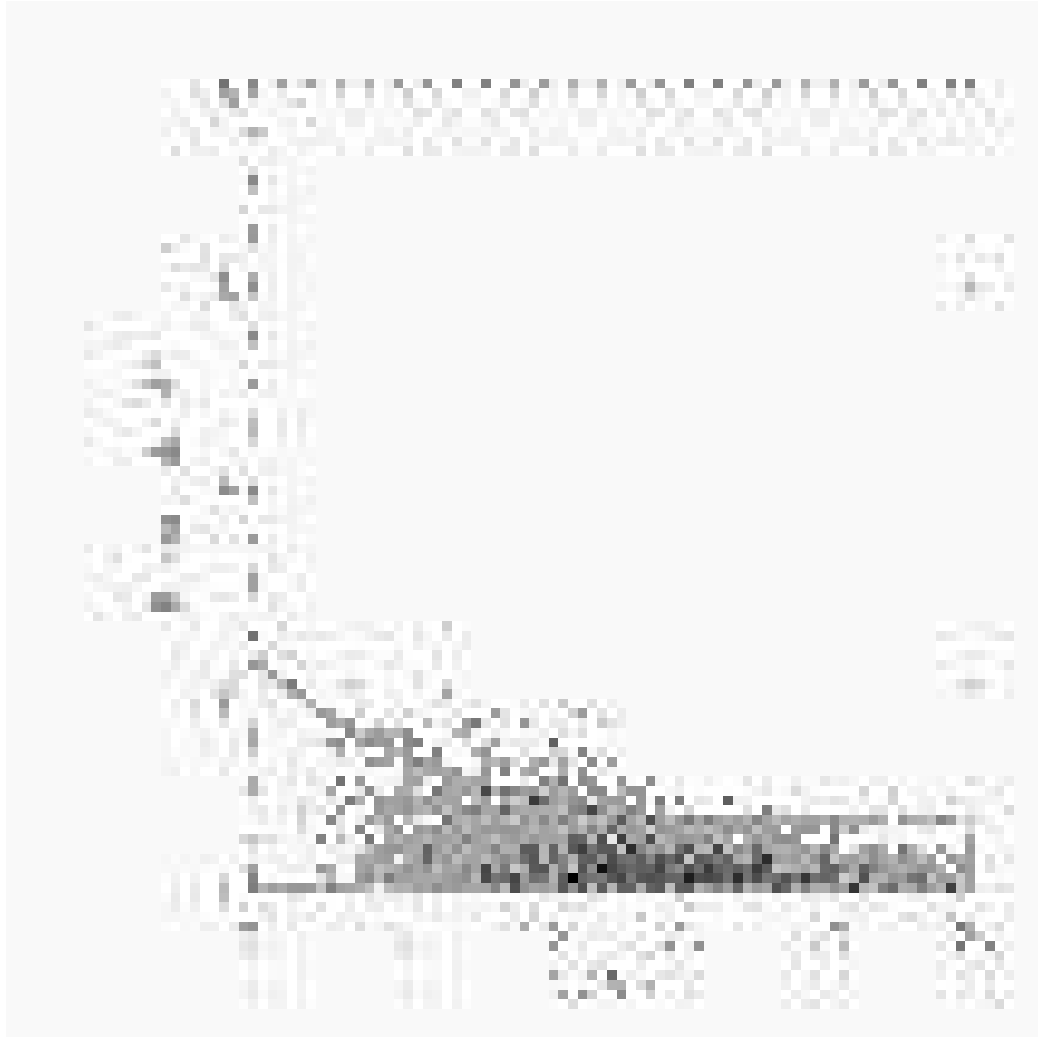


Figure A.11: The absolute difference in the H α EW (\AA) for duplicate observations of 11538 SDSS galaxies as a function of signal-to-noise ratio (the lower of the two signal-to-noise ratios has been plotted here). The solid line shows the 1σ polynomial line fitted to the distribution of errors (as a function of signal-to-noise ratio).

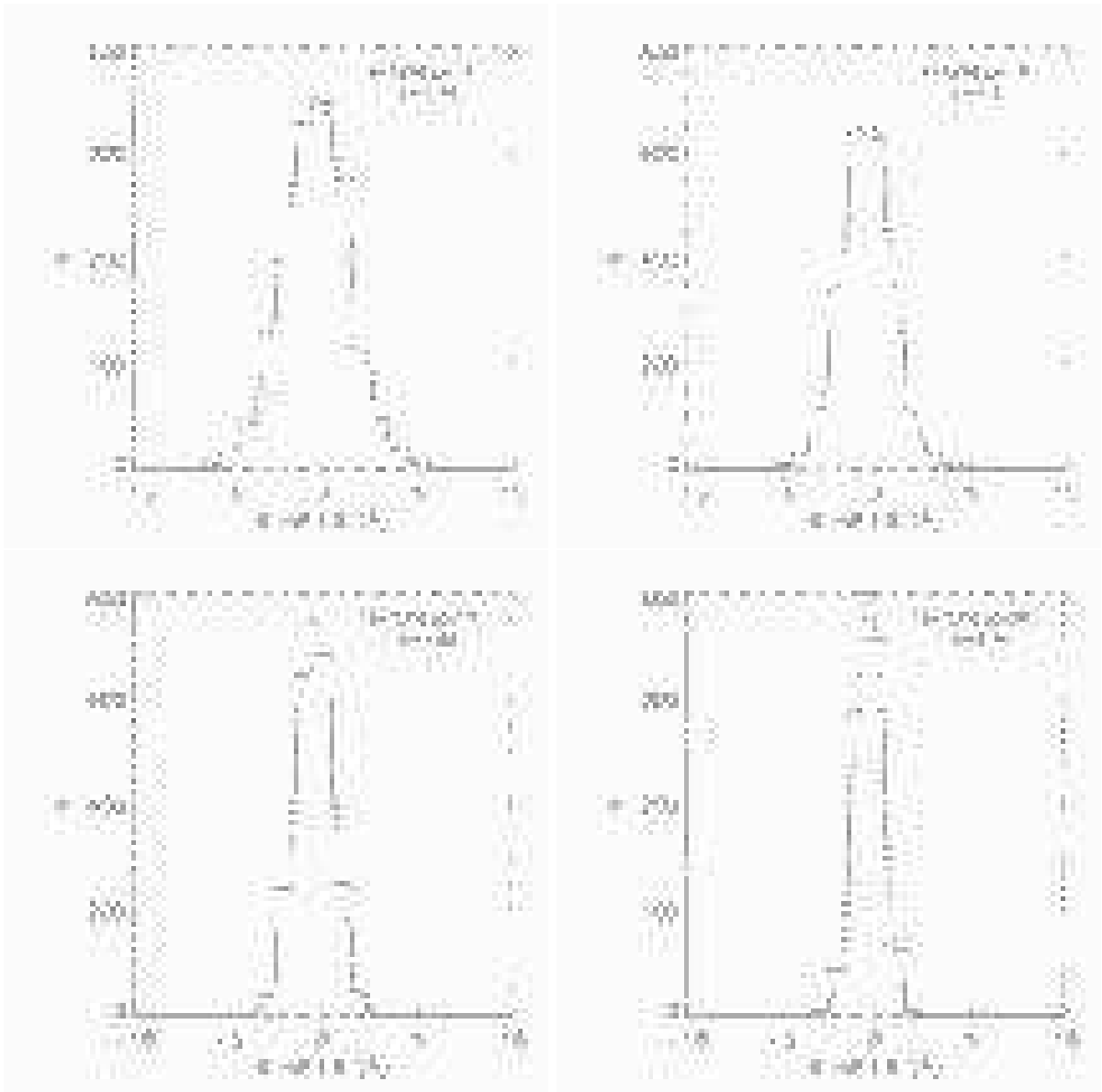


Figure A.12: We present the distribution of differences for the H δ line from our duplicate observations. The four panels denote four different bins in signal-to-noise ratio, i.e., clockwise from the top-left panel, we have $s/n < 7$, $7 < S/N < 10$, $15 < S/N < 20$ and $10 < S/N < 15$. We show in the dotted line the best fit Gaussian to these distributions, which was then used to determine the 1σ error (shown for each panel) on H δ EW as a function of signal-to-noise ratio.

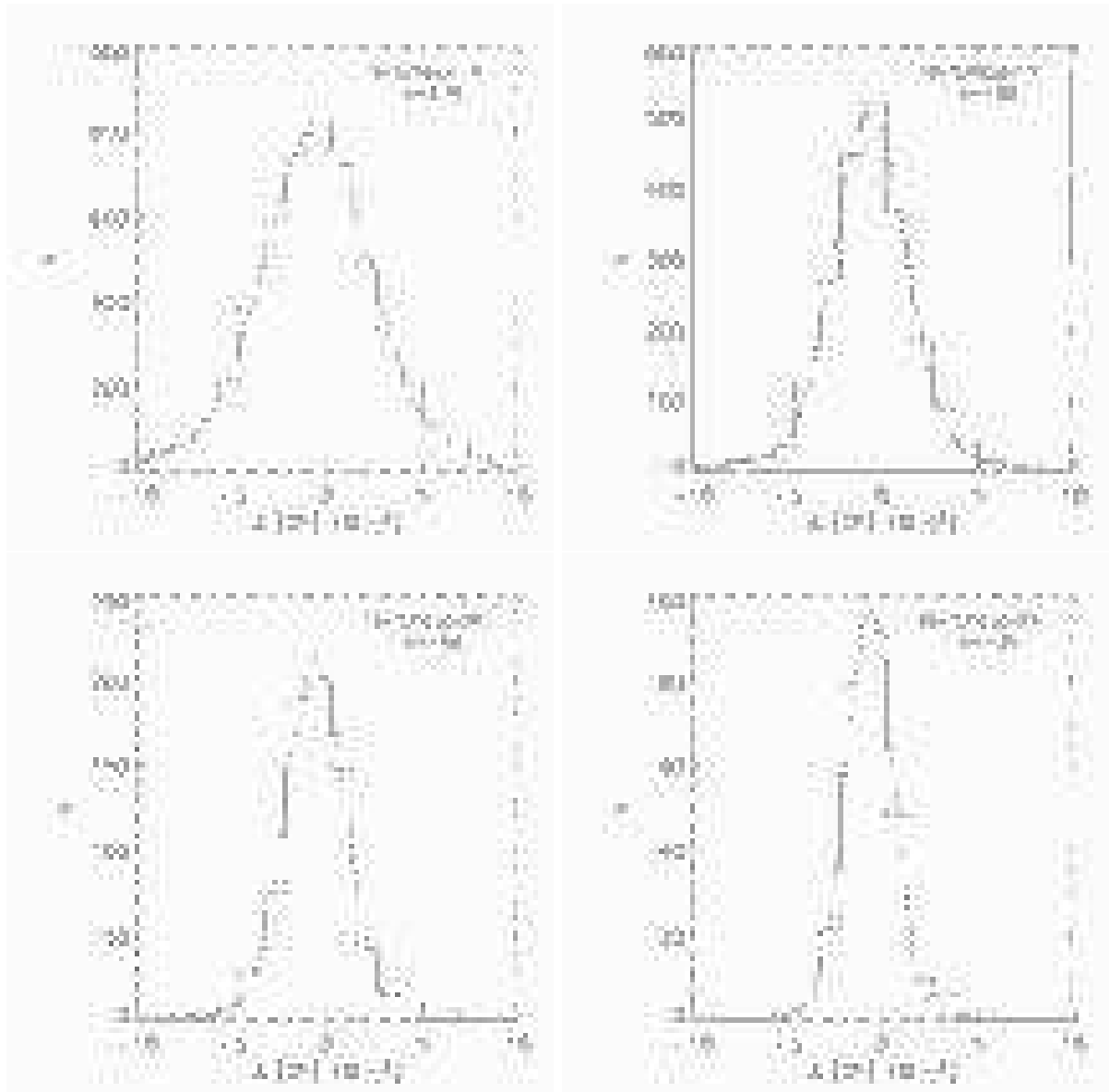


Figure A.13: The distribution of differences for the [OII] line from our duplicate observations. The four panels denote four different bins in signal-to-noise ratio, i.e., clockwise from the top-left panel, we have $5 < \text{S/N} < 10$, $10 < \text{S/N} < 15$, $20 < \text{S/N} < 25$ and $15 < \text{S/N} < 20$. We show in the dotted line the best fit Gaussian to these distributions, which was then used to determine the 1σ error on [OII] EW as a function of signal-to-noise ratio.

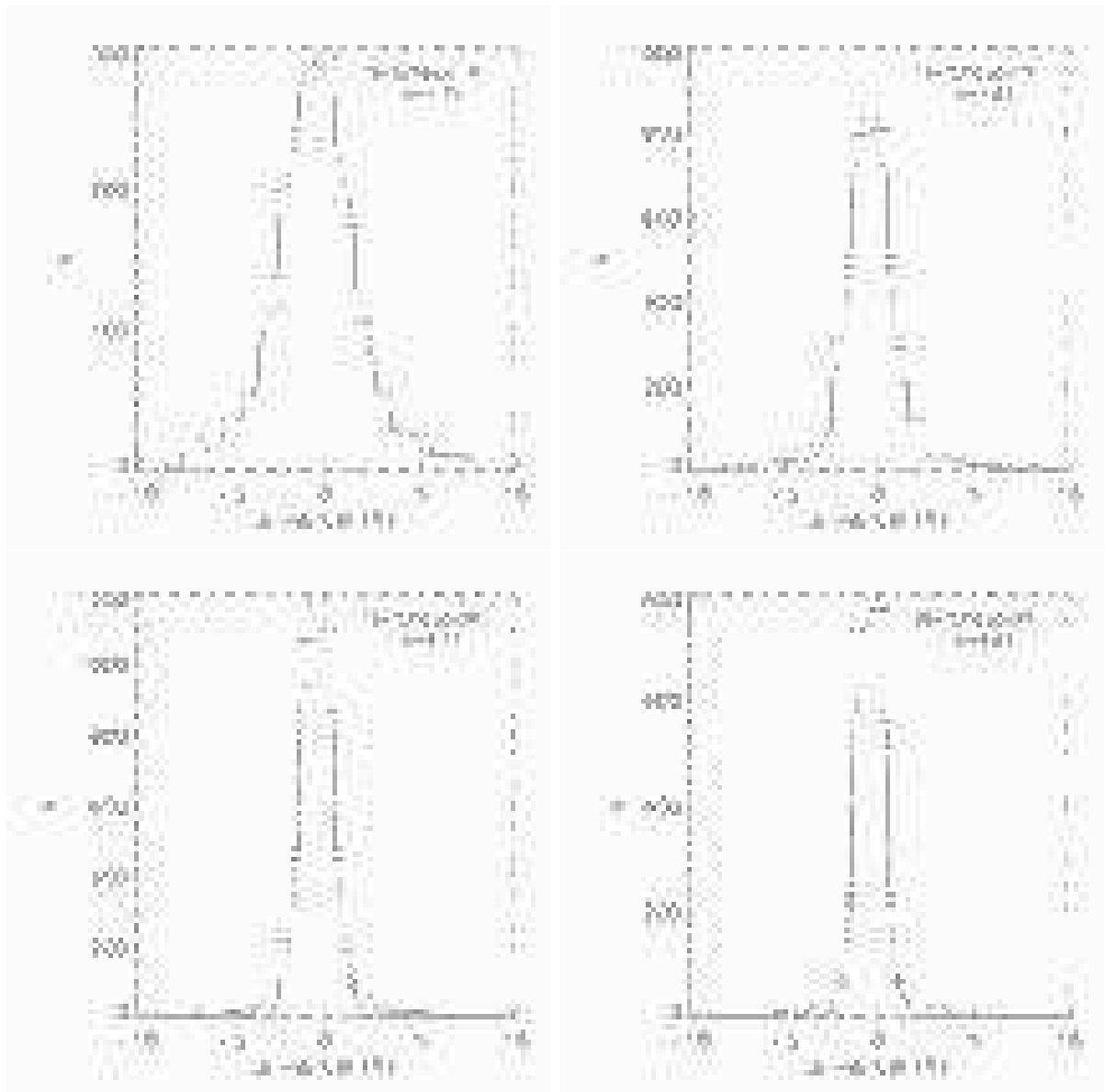


Figure A.14: The distribution of differences for the H α line from our duplicate observations. The four panels denote four different bins in signal-to-noise ratio, i.e., clockwise from the top-left panel, we have $5 < s/n < 10$, $10 < s/n < 15$, $20 < s/n < 25$ and $15 < s/n < 20$. We show in the dotted line the best fit Gaussian to these distributions, which was then used to determine the 1σ error on H α as a function of signal-to-noise ratio.

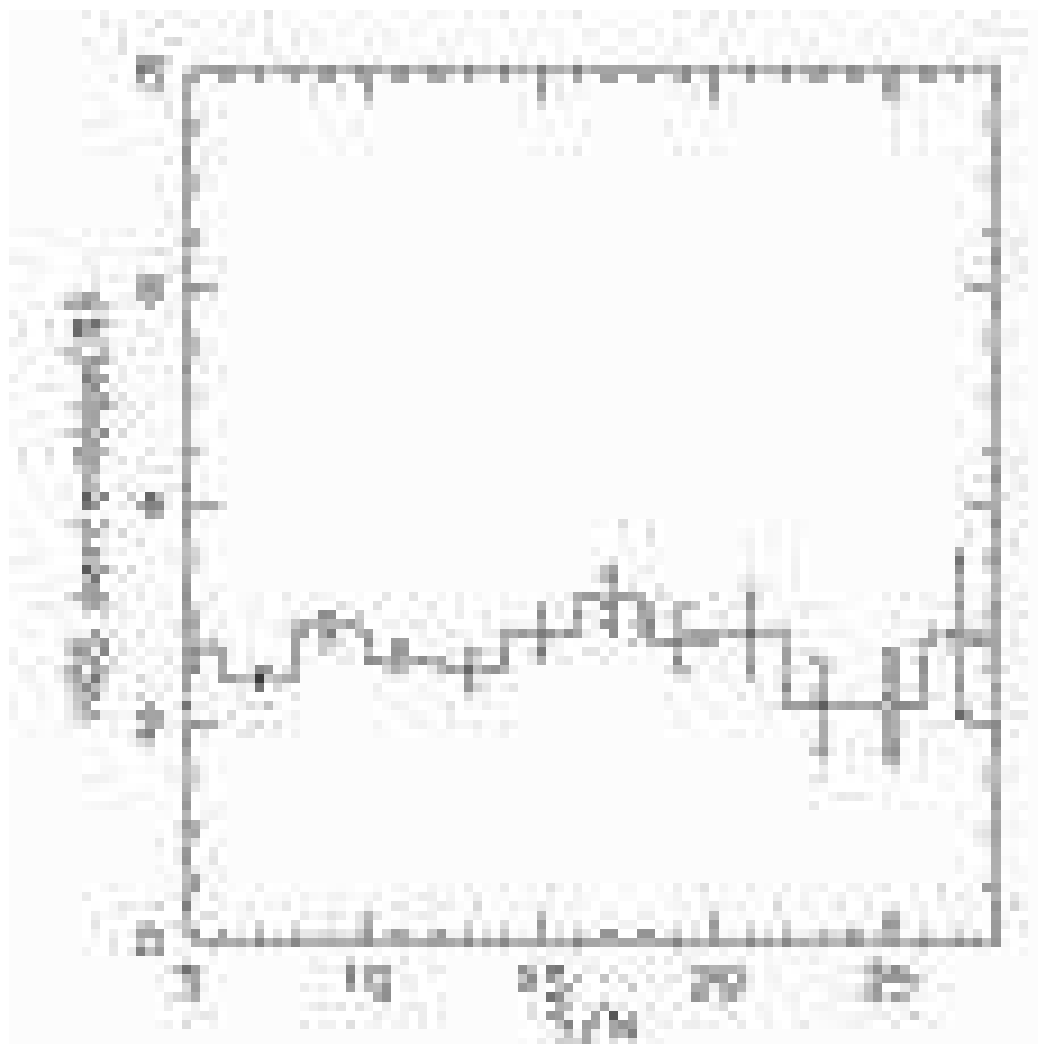


Figure A.15: The fraction of HDS galaxies as a function signal-to-noise ratio in the g band. The error bars are \sqrt{N} , where N is the number of galaxies in each bin.



Figure A.16: Five examples of spectra for the “true E+A” subsample of HDS galaxies discussed in Section A.5. These galaxies possess strong Balmer absorption lines, but have no, or little, detected [OII] or H α emission. The label shows signal-to-noise ratio, H δ EW, and measured redshift.



Figure A.17: Five example spectra of our HDS galaxies that possess detected [OII] and H α emission lines. The label shows signal-to-noise ratio, H δ EW, and measured redshift.

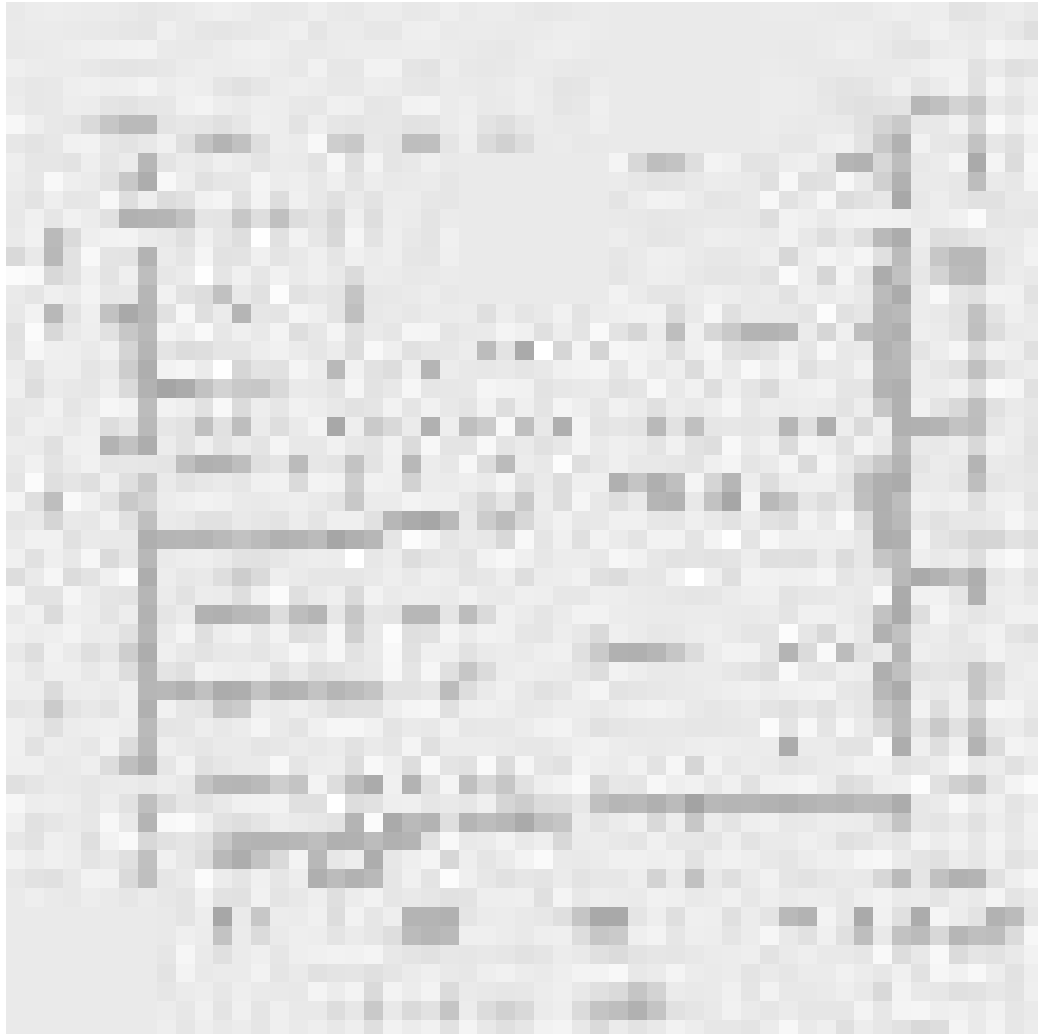


Figure A.18: Five example spectra of our HDS galaxies that possess detected [OII] emission lines, but no detected H α . The label shows signal-to-noise ratio, H δ EW, and measured redshift.

Table A.1: The wavelength ranges used to measure our H δ , [OII] and H α EWs.

	Blue continuum	Line	Red continuum
H δ (narrow)	4030-4082Å	4088-4116Å	4122-4170Å
H δ (wide)	4030-4082Å	4082-4122Å	4122-4170Å
[OII]	3653-3713Å	3713-3741Å	3741-3801Å
H α	6490-6537Å	6555-6575Å	6594-6640Å

Table A.2: Coefficients of third order polynomial fits to the error distributions shown in Figures A.9, A.10 and A.11.

Line	a ₀	a ₁	a ₂	a ₃
H δ	2.98	-0.28	0.012	-0.00018
[OII]	4.96	-0.39	0.014	-0.00016
H α	3.74	-0.36	0.014	-0.00017

Table A.3: The frequency of finding HDS galaxies.

Category	% (All galaxies)	% (Volume Limited)
Whole HDS sample	3340/95479 (3.50±0.06%)	717/27014 (2.6±0.1%)
True “E+A”	140/94770 (0.15±0.01%)	25/26863 (0.09±0.02%)

Table A.4: A comparison of our HDS sample of galaxies to previous work in the literature.

Author	Balmer lines	Emission	Their % (field)	Our %
Zabludoff et al.	$H\delta > 5.5 \text{ \AA}$	$[\text{OII}] > -2.5 \text{ \AA}$	$0.19 \pm 0.04\%$	$0.16 \pm 0.02\% \ (80/49994)$
Poggianti et al.	$H\delta > 3 \text{ \AA}$	$[\text{OII}] > -5 \text{ \AA}$	$6 \pm 3\%$	$5.79 \pm 0.15\% \ (1565/27014)$
Balogh et al.	$H\delta > 5 \text{ \AA}$	$[\text{OII}] > -5 \text{ \AA}$	$1.2 \pm 0.8\%$	$0.74 \pm 0.05\% \ (200/27014)$

Appendix B

Merger/Interaction Origin of E+A Galaxies

B.1 Introduction

Dressler & Gunn (1983; 1992) found galaxies with mysterious spectra while investigating high redshift cluster galaxies. The galaxies had strong Balmer absorption lines with no emission in either [OII] or H α . These galaxies are called “E+A” galaxies since their spectra looked like a superposition of that of elliptical galaxies (Mg_{5175} , Fe_{5270} and $Ca_{3934,3468}$ absorption lines) and that of A-type stars (strong Balmer absorption)¹. The existence of strong Balmer absorption lines shows that these galaxies have experienced starburst recently (within a Gyr). However, these galaxies do not show any sign of on-going star formation as non-detection in [OII] or H α emission lines indicates. Therefore E+A galaxies are interpreted as a post-starburst galaxy, that is, a galaxy which truncated starburst suddenly (Dressler & Gunn 1983, 1992; Couch & Sharples 1987; MacLaren, Ellis, & Couch 1988; Newberry Boroson & Kirshner 1990; Fabricant, McClintock, & Bautz 1991; Abraham et al. 1996). The reason why they started star burst, and why they abruptly stopped starburst remains one of the mysteries in galaxy evolution.

At present, there seem to be three popular explanations to the E+A phenomenon.

- Cluster-galaxy interaction
- Galaxy-galaxy interaction (in the field)
- Dust enshrouded star formation

¹Since some of E+A galaxies are found to have disk-like morphology (Franx 1993; Couch et al. 1994; Dressler et al. 1994; Caldwell et al. 1997; Dressler et al. 1999), these galaxies are sometimes called “k+A” galaxies. However, considering our findings in Section B.4, we call them “E+A” throughout this work.

(i) Cluster-Galaxy Interaction.

At first, E+A galaxies are found in cluster regions, both in low redshift clusters (Dressler 1987; Franx 1993; Caldwell et al. 1993, 1996; Caldwell & Rose 1997; Castander et al. 2001; Rose et al. 2001) and high redshift clusters (Sharples et al. 1985; Lavery & Henry 1986; Couch & Sharples 1987; Broadhurst, Ellis, & Shanks 1988; Fabricant, McClintock, & Bautz 1991; Belloni et al. 1995; Barger et al. 1996; Fisher et al. 1998; Morris et al. 1998; Couch et al. 1998; Dressler et al. 1999). Therefore a cluster specific phenomenon was thought to be responsible for the violent star formation history of E+A galaxies. A ram-pressure stripping model (Spitzer & Baade 1951, Gunn & Gott 1972, Farouki & Shapiro 1980; Kent 1981; Abadi, Moore & Bower 1999, Fujita & Nagashima 1999, Quilis, Moore & Bower 2000; Fujita 2003) can first accelerate star formation of cluster galaxies and later turn it off. Galaxy-galaxy merger/interaction in cluster regions is also a good candidate to explain E+A phenomena (Lonsdale, Persson, & Matthews 1984; Kennicutt et al. 1987; Sanders et al. 1988; Thompson 1988; Larvary & Henry 1988, 1994; Lavery et al. 1992) although several authors pointed out that merging/interaction is difficult to happen in cluster core regions since relative velocities of galaxies are too high (Ostriker 1980; Binney & Tremaine 1987; Mamon 1992; Makino & Hut 1997). Other candidate mechanisms include galaxy harassment (Moore et al. 1996, 1999), cluster tidal forces (Byrd & Valtonen 1990, Valluri 1993; Fujita 1998), removal and consumption of the gas (strangulation; Larson, Tinsley & Caldwell 1980, Balogh et al. 1997, 1998, 1999, 2000; Bekki et al. 2001; Mo & Mao 2002; Oh & Benson 2003), and evaporation of the cold gas in disk galaxies via heat conduction from the surrounding hot ICM (Cowie & Songaila 1977; Fujita 2003). Fujita et al. (1999b) discussed that a cluster-cluster merger can increase the ram-pressure, and thus, can increase the fraction of post-starburst galaxies such as E+As.

Observationally strong evolution in colors of cluster galaxies has been discovered, in a sense that there are more blue galaxies in higher redshift clusters (the so-called Butcher-Oemler effect; Butcher & Oemler 1978, 1984; Couch & Sharples 1987; Rakos & Schombert 1995; Couch et al. 1994, 1998; Margoniner & De Carvalho 2000; Margoniner et al. 2001; Ellingson et al. 2001; Kodama & Bower 2001; Goto et al. 2003a). E+A galaxies appeared to fit in the Butcher-Oemler effect naturally, as blue, star-forming galaxies at high redshifts turn off their star formation abruptly, changing their spectra to E+A type, and they become red, non-star-forming galaxies at low redshifts. In addition, if E+As are cluster related, it is of considerable interest to elucidate the connection to the spiral-to-S0 morphological evolution of cluster galaxies recently observed (Dressler et al. 1997; Fasano et al. 2000; Goto et al. 2003a). E+A galaxies might be a critical link in a galaxy evolution model in which a blue, star-forming disk galaxy evolves into a red S0 or elliptical galaxy.

(ii) Galaxy-Galaxy Interaction (in the field).

Zabludoff et al. (1996) found E+A galaxies in the field region as well. They selected 21 E+A galaxies in the Las Campanas Redshift Survey data (Shectman et al. 1996) and showed that they are not preferentially located in cluster regions. Balogh et al. (1999) also found a comparable amount of E+A galaxies in the field region as in cluster regions. Zabludoff et al. (1996) proposed that galaxy-galaxy interaction (Schweizer 1982; Lavery & Henry 1988; Liu & Kennicutt 1995a,b; Schweizer 1996) might be responsible for E+A phenomena since 5 of their 21 E+A galaxies had a tidal feature. Oegerle, Hill, & Hoessel(1991) also found a nearby E+A galaxy with a tidal feature. High resolution imaging of Hubble Space Telescope supported the galaxy-galaxy interaction scenario by identifying that some of post-starburst (E+A) galaxies in high redshift clusters show disturbed or interacting signatures (Couch et al. 1994,1998; Dressler et al 1994; Oemler, Dressler, & Butcher 1997). Liu & Kennicutt (1995a,b) observed 40 merging/interacting systems and found that some of their spectra resemble E+A galaxies. Bekki, Shioya, & Couch (2001) modeled galaxy-galaxy mergers with dust extinction, confirming that such systems can produce spectra which evolve into E+A spectra.

(iii) Dust Enshrouded Star Formation.

Another possible explanation for E+A phenomena is dust enshrouded star formation, where E+A galaxies are actually star-forming, but emission lines are invisible in optical wavelengths due to the heavy obscuration by dust. Poggianti et al. (1999) pointed out that galaxies with strong H δ and weak [OII] emissions (e(a) galaxies in their classification) might be a dust-obscured starbursting galaxy. A straightforward test for this scenario is to observe in radio wavelengths where dust obscuration is negligible (or in far-infrared, sub-millimeter to detect emission from dust). At radio wavelengths, the synchrotron radiation from electrons accelerated by supernovae can be observed. Therefore, in the absence of a radio-loud active nucleus, the radio flux of a star-forming galaxy can be used to estimate its current massive star formation rate (Condon 1992; See Hopkins et al. 2003 for comparison between radio estimated and optically estimated star formation rate). Smail et al. (1999) performed such a radio observation and found that among 8 galaxies detected in radio, 5 galaxies have strong Balmer absorption with no detection in [OII]. They concluded that massive stars are currently forming in these 5 galaxies. Owen et al. (1999) investigated the radio properties of galaxies in a rich cluster at $z \sim 0.25$ (A2125) and found that optical line luminosities (e.g., H α +[NII]) were often weaker than one would expect for the SFRs implied by the radio emission. On the other hand, Chang et al. (2001) detected none of 5 nearby E+A galaxies in radio continuum using VLA and excluded the possibility that their E+As are dust-enshrouded massive starburst galaxies. Miller & Owen (2002) observed radio continua of 15 E+A galaxies found in LCRS (Zabludoff et al. 1996) and detected moderate levels of star formation in 2 of them. The star formation rates (SFRs) of these two galaxies, however, are 5.9 and 2.2 M_{\odot} yr $^{-1}$, which are an order of magnitude

smaller than those in Smail et al. (1999), consistent with normal to low SFR instead of starburst.

These studies warn us that at least some E+A galaxies might have on-going star formation. Therefore, when we discuss E+A galaxies, it is important to acquire data in a broad wavelength range. We try to address this problem using H α emission (less affected by dust extinction than [OII] since it is at longer wavelength), infrared photometry and radio flux. As a variation of the dust enshrouded star-forming scenario, Poggianti & Wu (2000) presented the selective dust extinction hypothesis, where dust extinction is dependent on stellar age since youngest stars inhabit very dusty star-forming HII regions while older stars have had time to migrate out of such dusty regions (also see Calzetti, Kinney, & Storchi-Bergmann 1994; Poggianti et al. 2001). If O, B-type stars in E+A galaxies are embedded in dusty regions and only A-type stars have long enough lifetimes ($10^7 \sim 1.5 \times 10^9$ yr) to move out from such regions, this scenario can naturally explain E+A phenomena. However, this scenario has to explain why the selective extinction happens only in E+A galaxies since we can observe many star-forming galaxies with detectable [OII] and H α emissions.

Although these three scenarios are all plausible, the definitive conclusion has not been drawn yet. Part of the difficulty stems from the extreme rarity of E+A galaxies. Since E+A phase is very short (less than a Gyr), they are very rare. In the Las Campanas Redshift survey, there were only 21 E+A galaxies in 11113 spectra. Its rarity made it more difficult to study a statistically large number of E+A galaxies. The largest sample of E+A galaxies to date is presented by Galaz (2000), which, however, is a heterogeneous sample of only 50 E+As. The Sloan Digital Sky Survey (York et al. 2000) which is both imaging and redshift surveys of a quarter of the whole sky, provides us with the first opportunity to study E+A galaxies in a much large number (see also a parallel work by Quintero et al. 2003, which uses a sophisticated K/A ratio method to study by far a large number of ~ 1000 k+A galaxies from the same SDSS data). Furthermore, the availability of [OII] and H α lines allows us to divide strong Balmer absorption galaxies into four categories including E+As, and to study properties of galaxies in each category in detail. As shown in the following sections, we stress the importance in separating the strong Balmer absorption galaxies into these four categories. In previous work, authors might have dealt with heterogeneous samples of these four sub-samples of H δ -strong (HDS) galaxies, resulting in wide varieties in the properties of H δ -strong galaxies, partly due to the lack of H α information, and partly due to the low signal-to-noise ratio of spectra. In Chapter A, we described a robust method to select H δ -strong galaxies and presented a catalog of such galaxies. In this chapter, we study spectral and photometric properties of the whole population of H δ -strong galaxies in detail to reveal the origin of these galaxies. The cosmological parameters adopted throughout this work are $H_0 = 75$ km s $^{-1}$ Mpc $^{-1}$

and $(\Omega_m, \Omega_\Lambda, \Omega_k) = (0.3, 0.7, 0.0)$.

B.2 Data

To study H δ -strong galaxies as a whole, we created a catalog of H δ -strong galaxies in Chapter A. Chapter A presents the details of the selection methodology, which we briefly summarize here. From the Sloan Digital Sky Survey Data Release I (see Fukugita et al. 1996, Gunn et al. 1998, Lupton et al. 1999, 2001; York et al. 2000, Eisenstein et al. 2001, Hogg et al. 2001, Blanton et al. 2003a, Pier et al. 2002, Richards et al. 2002, Stoughton et al. 2002, Strauss et al. 2002, Smith et al. 2002 and Abazajian et al. 2003 for more detail of the SDSS data), we selected galaxies with $z > 0.05$ and $S/N(g) > 5$. The low redshift cut is applied to exclude the strong aperture effect. For these galaxies, we have measured H δ , [OII] and H α equivalent widths (EWs) and obtained their errors using the flux summing method as described in Section A.3 of Chapter A. This flux summing method is robust for spectra of low S/N ratio and weak lines. We selected H δ -strong galaxies as a galaxy with a H δ equivalent width (EW) greater than 4 Å with more than 1 σ significance level (Section A.4). Among 94770 galaxies which satisfy the redshift and S/N cut with measurable [OII], H δ and H α lines, 3313 galaxies are regarded as H δ -strong galaxies. Among them, we excluded 130 H δ -strong galaxies with line ratios consistent with being an AGN using the prescription given by Kewley et al. (2001). The final sample consists of 3183 H δ -strong galaxies. We classified these H δ -strong galaxies further into four sub-categories as described in the next section.

B.3 Defining Four Subsamples of H δ -strong Galaxies

Taking the full advantage of the high quality of the SDSS spectra, we divide H δ -strong galaxies into four categories. We use [OII] equivalent width and H α equivalent width to separate H δ -strong galaxies based on their current star formation activity. As seminal work by Kennicutt et al. (1992a,b) shows, H α is the best star formation indicator in optical wavelength since it is a strong line and it has fewer uncertainties (e.g., dust extinction, self absorption, metallicity dependence) than the other lines. It thus has been used in previous work frequently to study star formation of galaxies when available (e.g., Gomez et al. 2003). We use H α equivalent width measured in Chapter A. The equivalent width of [OII] (3727) line is also used in many studies as a star formation indicator (e.g., Zabludoff et al. 1996), especially when H α line is not available for high redshift galaxies (e.g., Poggianti et al. 1999). [OII] is also a suitable line to study star formation of galaxies since the line is strong and the line strength does not depend on metallicity very much. However, it is more affected by dust extinction than H α .

Based on these lines, we classify H δ -strong galaxies into four categories as follows.

$$E + A : \left(\text{EW}(\text{H}\alpha) - \Delta \text{EW}(\text{H}\alpha) < 0 \text{\AA} \right) \& \left(\text{EW}([\text{OII}]) - \Delta \text{EW}([\text{OII}]) < 0 \text{\AA} \right) \quad (\text{B.1})$$

$$HDS + [\text{OII}] : \left(\text{EW}(\text{H}\alpha) - \Delta \text{EW}(\text{H}\alpha) < 0 \text{\AA} \right) \& \left(\text{EW}([\text{OII}]) - \Delta \text{EW}([\text{OII}]) > 0 \text{\AA} \right) \quad (\text{B.2})$$

$$HDS + \text{H}\alpha : \left(\text{EW}(\text{H}\alpha) - \Delta \text{EW}(\text{H}\alpha) > 0 \text{\AA} \right) \& \left(\text{EW}([\text{OII}]) - \Delta \text{EW}([\text{OII}]) < 0 \text{\AA} \right) \quad (\text{B.3})$$

$$HDS + em : \left(\text{EW}(\text{H}\alpha) - \Delta \text{EW}(\text{H}\alpha) > 0 \text{\AA} \right) \& \left(\text{EW}([\text{OII}]) - \Delta \text{EW}([\text{OII}]) > 0 \text{\AA} \right) \quad (\text{B.4})$$

All four categories of the H δ -strong galaxies have H δ EWs greater than 4 Å with more than 1σ significance. Galaxies labeled as a possible AGN in Chapter A are not included in the sample. Table B.1 shows the number of galaxies in each category.

Figure B.1 plots [OII] EWs against H δ EWs. Contours show the distribution of all 94770 galaxies. Large open circles, triangles, squares, and small dots represent E+A, HDS+[OII], HDS+H α and HDS+em galaxies, respectively. Generally H δ -strong galaxies are a rare class of galaxies, as we see fewer points toward increasing H δ EWs. Reflecting our selection criteria, [OII] EWs are the strongest for HDS+em galaxies and become weaker for HDS+[OII], HDS+H α and E+A galaxies. Figure B.2, in turn, plots H α EWs against H δ EWs. Contours and symbols are the same as of Figure B.1. In this figure, H α EWs are the strongest for HDS+em galaxies, and become weaker and weaker toward HDS+H α , HDS+[OII] and E+A galaxies.

In Figure B.3, we show distributions of star formation rate (SFR) calculated using H α luminosity for each subsample of H δ -strong galaxies. Solid, long-dashed, dot-dashed, short-dashed and dotted lines represent all, E+A, HDS+[OII], HDS+H α and HDS+em galaxies, respectively. SFR is calculated using a conversion formula given in Kennicutt (1998), assuming constant extinction of 1 magnitude at the wavelength of H α (see Hopkins et al. in prep. for more sophisticated SFR estimation). Reflecting our selection criteria, HDS+[OII] and E+A galaxies have relatively lower SFR. HDS+em galaxies have higher SFR compared with all galaxies. HDS+H α have lower SFR than HDS+em, showing that H δ -strong galaxies without [OII] emission have in average a lower amount of H α in emission. This result might be consistent with the dusty origin of HDS+H α galaxies. In Figure B.4, we show luminosity functions for volume limited subsamples ($0.05 < z < 0.1$ and $M_r^* < -20.5$) of the H δ -strong galaxies. The solid, long-dashed, dot-dashed, short-dashed and dotted lines represent all, E+A, HDS+[OII], HDS+H α and HDS+em galaxies, respectively. According to a Kolomogorov-Smirnov test, LFs of all the four sub-samples do not show any significant difference from that of all galaxies drawn by the solid line except HDS+em galaxies. HDS+em galaxies show a slightly fainter LF, different from the others with more than 99.99% significance. The fact that we found many bright E+As

($Mr^* < -20.0$) is inconsistent with Poggianti, Bridges & Mobasher et al. (2001), where they found no luminous E+A galaxies in Coma cluster. Our finding suggests that E+A phenomena is not restricted to dwarf galaxies in the nearby universe.

Below we briefly comment on these four sub-samples of H δ -strong galaxies.

B.3.1 E+A

The selection criteria for this category are chosen to match the classical E+A galaxies which have been studied in various previous work (e.g., Dressler & Gunn 1983,1992; Zabludoff et al. 1996; Balogh et al. 1999; Poggianti et al. 1999; Dressler et al. 1999). Figure A.16 of Chapter A shows example spectra of true E+A galaxies. The strong H δ absorption line with no H α and [OII] emission lines indicates that these galaxies have had strong star burst in recent 1 Gyr, but they do not have on-going star formation at all as shown in the lack of emission lines which indicate current star formation. The reason why they had experienced starburst, and the reason why they stopped star formation is unknown.

B.3.2 HDS+[OII]

These galaxies are characterized by a strong H δ absorption line and the lack of H α emission line with the existence of detectable emission in [OII] (Figure A.18 of Chapter A). [OII] emission shows remaining star formation activity. However, the lack of H α emission remains a mystery. In Chapter A we discussed that a possible explanation is self-absorption in H α due to many A-type stars and metallicity effect that increases [OII] emission relative to H α emission. As is shown in Figure B.1, We note that [OII] emission in these systems is not so strong as in normal star-forming galaxies, which might suggest that H α emission in these systems is also weak enough to be hidden by self-absorption. Another possibility includes HI gas cloud in front of these galaxies. Such gas cloud might absorb light in H α , but not in [OII].

B.3.3 HDS+H α

These H δ -strong galaxies are characterized by the strong H δ absorption, the lack of [OII] in emission and the existence of H α in emission. The existence of this type of galaxies is scary since previous work frequently used the non-existence of [OII] in a selection of E+A galaxies due to the non-availability of H α information. If H α emission comes from star formation activity, selecting this type of galaxies as non-star-forming (E+A) galaxies is erroneous. In Chapter A we discussed that a possible explanation for the lack of [OII] emission line is a combination of strong dust extinction and metallicity effect. Relatively

small H α EWs compared with normal star-forming galaxies (Figure B.2) suggest that [OII] emissions in these galaxies might be weak enough to be hidden by dust. Another possible explanation for this type of galaxies is that H α is coming from diffuse ionized gas. In such a case, diffuse ionized gas does not emit in [OII], thus perfectly explains the spectral features. In normal galaxies, diffuse ionized gas (not associated with star-forming regions) could be responsible for 50% of the H α emission.

B.3.4 HDS+em

This type of galaxies has an indication of both recent star formation (strong H δ absorption) and currently on-going star formation (H α and [OII] in emission). Therefore these galaxies can be understood as a star-forming galaxy, possibly reducing its star formation rate currently. Also in terms of statistics, these galaxies are much more numerous than the other three types of galaxies (Table B.1), suggesting more common nature of these galaxies. Figure A.17 of Chapter A shows five typical spectra of HDS+em galaxies.

B.4 The Morphology of H δ -strong Galaxies

In this section we investigate morphologies of H δ -strong galaxies with particular attention to E+A galaxies. Since E+A galaxies have experienced the truncation of starburst fairly recently (<1 Gyr), E+As might still hold some traces of the truncation of the star-formation in their morphology (e.g., dynamically disturbed signs). Therefore we might obtain some hint on the origins of E+A galaxies by examining their morphology. In Figure B.5, we plot a concentration parameter, C_{in} , against $u - r$ color. The concentration parameter, C_{in} , is defined as the ratio of Petrosian 50% light radius to Petrosian 90% light radius in r band (radii which contain 50% and 90% of Petrosian fluxes, respectively; Shimasaku et al. 2001; Strateva et al. 2001). The border line between spiral galaxies and elliptical galaxies is around $C_{in}=0.4$. Since this concentration parameter is an inverse of a general definition of concentration parameter, concentrated (elliptical) galaxies have a smaller value of C_{in} than late-type galaxies. Strateva et al. (2001) showed that $u - r=2.2$ also separates early and late type galaxies well. In Figure B.5, contours show the distribution of all 94770 galaxies in our sample. The distribution shows two peaks, one for elliptical galaxies at around $(u - r, C_{in}) \cong (2.8, 0.35)$, and one for spiral galaxies at around $(u - r, C_{in}) \cong (1.7, 0.45)$. In the same figure, large open circles, triangles, squares, and small dots represent E+A, HDS+[OII], HDS+H α and HDS+em galaxies, respectively. This figure shows that E+A galaxies and HDS+[OII] galaxies have more elliptical-like morphology with lower C_{in} values and redder $u - r$ color. Their C_{ins} are almost as small as those of elliptical galaxies. Their $u - r$ colors, however, are not as red as those

of elliptical galaxies. HDS+em galaxies have more spiral-like morphology with higher C_{in} values and bluer $u - r$ color. HDS+H α galaxies have intermediate morphology. Some of the HDS+H α galaxies have elliptical-like morphology and others have spiral-like morphology. The center of the distribution is between the elliptical peak and the spiral peak.

It is interesting to note the following. We have selected these four subsamples of H δ -strong galaxies solely based on spectral line properties. Nevertheless, each sample shows clear morphological difference on the C_{in} vs $u - r$ plane. In particular, the difference between HDS+em and E+A is clear, suggesting the existence of a physical phenomenon governing morphological properties of these two types of H δ -strong galaxies. Our results are consistent with those by Quintero et al. (2003), who also report bulge-dominated morphologies of their E+A galaxies. Also the discovery of elliptical-like morphologies of E+A galaxies is interesting since it is against the previous observations where E+As were found to have disk-like morphologies (Couch et al. 1994, 1998; Dressler et al. 1994, 1999; Oemler et al. 1997; Smail et al. 1997; Chang et al. 2001) and it leaves an interesting question why elliptical-like galaxies experienced a starburst and truncation of the starburst.

These differences in morphologies of E+As in the literature might be understood as a result of a significant variety in definitions of E+A galaxies. Most of the previous samples did not have information on H α emission line, and thus, used only [OII] emission and Balmer absorption lines to define E+A galaxies. In addition, the previous observations did not have as high signal-to-noise spectra as the present study. In Chapter A, we showed that there are as many HDS+H α galaxies as E+A galaxies. These HDS+H α galaxies could be mis-classified as E+A galaxies if H α line is not available. In Figure B.5, HDS+H α galaxies have disk-like morphology. If previous E+A samples are contaminated by HDS+H α galaxies, the morphological difference between our E+A sample and the previous E+A samples can be naturally explained by the disk-like appearance of HDS+H α galaxies.

B.5 The Environment of H δ -strong Galaxies

The environments of H δ -strong galaxies have been actively debated over the past few years. Originally H δ -strong galaxies are found in cluster regions, and therefore, thought to be related to cluster induced phenomena (Dressler & Gunn 1983, 1992; Sharples et al. 1985; Lavery & Henry 1986; Couch & Sharples 1987; Dressler 1987; Broadhurst, Ellis, & Shanks 1988; Fabricant, McClintock, & Bautz 1991; Franx 1993; Caldwell et al. 1993, 1996, 1997; Belloni et al. 1995; Barger et al. 1996; Fisher et al. 1998; Morris et al. 1998; Couch et al. 1998; Castander et al. 2001, Rose et al. 2001). However, Zabludoff et al. (1996) showed that such galaxies were found outside clusters and groups of galaxies.

Therefore, it remains controversial if the post-starburst phenomenon is common to the whole galaxy population, or specific (or more frequent) in dense environments. Dressler et al. (1999) claims that there are an order of magnitude more post-starburst galaxies in distant clusters compared to the distant field. On the other hand, Balogh et al. (1999) find that the frequency of post-starburst galaxies is the same in distant clusters as in the field.

In this section, we investigate the environments of H δ -strong galaxies by measuring local galaxy density in the following way. For each galaxy, we measure a projected distance to the 5th nearest galaxy in angular direction using galaxies within $\pm 1000 \text{ km s}^{-1}$ in redshift space among the volume limited sample ($Mr^* < -20.5$, $0.05 < z < 0.1$). The criterion for redshift space ($\pm 1000 \text{ km s}^{-1}$) is set to be generous to avoid galaxies with a large peculiar velocity slipping out of the density measurement, in other words, not to underestimate the density in cluster cores. Then, the number of galaxies ($N=5$) within the distance is divided by the circular surface area with the radius of the distance to the 5th nearest galaxy. When the projected area touches the boundary of the data, we corrected the density by correcting the area to divide. Since we have redshift information for all of the sample galaxies, our density measurement is a pseudo-three dimensional density measurement and free from the uncertainty in background subtraction. In Figure B.6, we present distributions of this local galaxy density for cluster galaxies. Galaxies within 0.5 Mpc from the nearest cluster, galaxies between 1 and 2 Mpc from the nearest cluster, and all galaxies are plotted in the long-dashed, short-dashed and solid lines, respectively. In measuring distance from a cluster, we use the C4 cluster catalog (Miller et al. in prep.; Gomez et al. 2003). For each galaxy, the distance from the nearest cluster center is measured on the projected sky for galaxies within $\pm 1000 \text{ km s}^{-1}$ from a cluster redshift. The figure shows that the typical local galaxy density is 10, 4, 1 Mpc^{-2} for environment with a radius of 0.5 and 1-2 Mpc from the nearest cluster center.

In Figure B.7, we plot H δ EW against the local galaxy density for all galaxies in our volume limited sample ($0.05 < z < 0.1$, $Mr^* < -20.5$). For H δ line, negative EWs are absorption lines. As medians of the distribution (the solid line) show, H δ EW becomes weaker and weaker with increasing local galaxy density. In Figure B.8, we present distributions of local galaxy density for each subclass of H δ -strong galaxies. Solid, long-dashed, dot-dashed, short-dashed and dotted lines represent all, E+A, HDS+[OII], HDS+H α and HDS+em galaxies, respectively. The density distributions of all the four subclasses of H δ -strong galaxies are quite similar to that of all galaxies (solid line). In contrast, the density distributions of all the four subclasses of H δ -strong galaxies are quite different from that of cluster galaxies shown in Figure B.6. In fact, a Kolomogorov-Smirnov test shows that all the four density distributions of H δ -strong galaxies are different from that of cluster galaxies (within 0.5 Mpc from the cluster center) with more than 99.99% significance level.

These results have significant implications for the origins of H δ -strong galaxies. H δ -strong galaxies in local galaxy density $\ll 1 \text{ Mpc}^{-2}$ can not be explained with the cluster related phenomena. Therefore, these results suggest that origins of H δ -strong galaxies are not cluster related, and that they are more common phenomena in general field regions. Also, among the four subclasses of H δ -strong galaxies, there are small differences between distributions. The distributions of HDS+em and HDS+[OII] galaxies are slightly shifted to low density regions compared with that of all galaxies, while E+A and HDS+H α are not. To clarify these differences, we plot the ratio of each subclass of H δ -strong galaxies to all galaxies in Figure B.9. The left panel shows the ratio of HDS+em galaxies to all galaxies in the volume limited sample. As indicated in the previous figure, the ratio declines continuously as a function of local galaxy density. The relation is very similar to the decline of the fraction of spiral galaxies seen in the morphology-density relation (Goto et al. 2003c; Chapter 6). It is also similar to the decline of star formation rate as a function of local galaxy density (Lewis et al. 2002; Gomez et al. 2003). In the right panel of Figure B.9, we show the ratios of the rest of H δ -strong subsamples to all galaxies. The long dashed, short dashed and dotted-dashed lines represent E+A, HDS+H α and HDS+[OII] galaxies, respectively. Although the distributions are dominated by statistical errors, two characteristics are found in the panel. The HDS+[OII] fraction shows a monotonic decline as found for HDS+em galaxies. On the other hand, the HDS+H α and E+A fractions do not show much dependence on the local galaxy density.

When interpreting these results, we have to keep in mind that galaxies have the morphology-density relation and the SFR-density relation. From Figure B.5, we know that HDS+em galaxies have disk-like morphology and HDS+em are the most numerous among four sub-samples of H δ -strong galaxies. Therefore it is more likely that Figure B.7 reflects the well known morphology-density relation in terms of H δ EWs, and therefore can not be interpreted that cluster galaxies have weaker H δ EWs. In the right panel of Figure B.9, it is interesting to note that the distribution of E+A (and HDS+H α) galaxies does not depend much on the local galaxy density while the morphologies of these galaxies are more elliptical-like. Therefore it is suggested that although E+A galaxies have elliptical-like morphologies, the origin of E+As are perhaps different from that of bright cluster elliptical galaxies.

B.6 Possible Star Formation Histories

In this section, we compare SED models and observational quantities to search for possible star formation histories of H δ -strong galaxies. Using the GISSEL model by Bruzual A. & Charlot(1993), we simulated three representative star formation histories as follows; (i) *Burst* model, which has an instantaneous starburst at the beginning and no star formation

thereafter. (ii) *Constant* star formation. (iii) *Exponentially* decaying star formation. In all the three models, we use the Salpeter initial mass function (Salpeter 1955) with a single stellar population. Figure B.10 plots H δ EWs against time (or galaxy age) for the three models. Dashed, solid and dotted lines show the models with instantaneous burst, constant star formation and exponentially decaying star formation rate. The burst model has a strong H δ EW right after its burst at 1 Gyr. However, its H δ EW declines rapidly, and becomes less than 3Å at 1 Gyr after the burst. The exponentially decaying model maintains strong H δ for a longer time. Its H δ EW becomes 3Å in 5 Gyrs. The constantly star-forming model maintains a large H δ EW (>6Å) beyond 14 Gyr.

In Figure B.11, we plot restframe $g - r$ color against $r - i$ color. We first plot the models in this figure to compare later with the observational data. The dashed, solid and dotted lines are for the models with an instantaneous burst, constant star formation and exponentially decaying star formation rate. We show the models for two different metallicity in this figure ($Z=0.02$ and $Z = 0.1$). While a galaxy is star-forming, its colors stay around $(g - r, r - i) \cong (0.4, 0.2)$, where the constant star formation model stays. As soon as the galaxy stops star formation, its colors become redder and redder, approaching to the peak colors of elliptical galaxies at around $(g - r, r - i) \cong (0.8, 0.4)$. An increase in metallicity results in redder $r - i$ color.

We now add the observational data to compare with these models. Observed colors are shifted to the restframe using the k -correction code by Blanton et al. (2003; v1_11). Compared with contours showing distribution of all galaxies in our sample, the SED models reproduce observed colors of galaxies reasonably well. Open circles, small dots, triangles and squares represent E+A, HDS+em, HDS+H α and HDS+[OII], respectively. HDS+em galaxies (small dots) have bluer colors in both $g - r$ and $r - i$, which are consistent with the colors of normal star-forming galaxies. All the three models also show blue colors consistent with HDS+em galaxies, when the models have star formation in their early stage. E+A galaxies (open circles) have somewhat redder color in $g - r$, but not as red as elliptical galaxies ($g - r \sim 0.8$) with some exceptions, suggesting that they are a still evolving population of galaxies. The $r - i$ colors of E+As are widely spread. Some of them are as blue as star-forming galaxies in $r - i$. These bluer colors of E+As are consistent with the continuum dominated by many A-type stars. Compared with the models, colors of E+As are consistent with the exponentially decaying model and the burst models at the stage where the models start stopping their star formation. HDS+H α galaxies have a wide spread color distribution in both $g - r$ and $r - i$, with its center between elliptical galaxies and star-forming galaxies. In the exponentially decaying and the burst model, these colors are at the stage where star formation is declining. The distribution of HDS+[OII] galaxies is similar to that of E+A galaxies except that there are no HDS+[OII] galaxies as blue in $r - i$ as E+A galaxies, perhaps representing a

somewhat flatter continuum shape than E+As (see Figure A.18 of Chapter A).

In Figure B.12, we plot $J - K$ vs $r - K$, where infrared magnitudes are derived from the Two Micron All Sky Survey (2MASS; Jarrett et al. 2000) and k -corrected to restframe using Mannucci et al. (2001). Note that infrared colors are in AB system in this figure. Optical-infrared color is sensitive to the amount of dust since infrared color is less obscured by dust than optical. Dusty galaxies should be redder by ~ 1 mag in optical-infrared color (e.g., see Figure 2 of Smail et al. 1999). In Figure B.12, contours show the distribution of all galaxies in our sample. Open circles, small dots, triangles and squares represent E+A, HDS+em, HDS+H α and HDS+[OII], respectively. E+A galaxies (open circles), which are often suspected to be dust enshrouded star forming galaxies, do not show any redder colors than the normal galaxies (contours). Therefore our data suggest that E+A galaxies are not likely to be a dust enshrouded star-forming galaxy. Some of the HDS+em galaxies are about 0.5 mag redder in $r - K$ than the normal galaxies. These galaxies might have a significant amount of dust. In the figure, the models are plotted in dashed, solid and dotted lines for the instantaneous burst, constant star formation and exponentially decaying models. Three sets of models are plotted for different metallicities. All three models with solar metallicity ($Z=0.02$) show a good agreement with the behavior of the observational data.

We provide further evidence suggesting that E+As are not dusty star-forming galaxies in Figure B.13, where radio derived SFR is plotted against redshift. Under the assumption that the radio emission is due to star formation, we calculated radio estimated SFR using the following conversion (Yun, Reddy & Condon 2001).

$$SFR(M_{\odot} \text{ yr}^{-1}) = 5.9 \times 10^{-22} L_{1.4Ghz}(WHz^{-1}) \quad (\text{B.5})$$

This conversion assumes a Salpeter initial mass function integrated over all stars ranging from 0.1 to 100 M_{\odot} and hence represents the total SFR of a galaxy. We also have applied k -correction in the shape of $(1.0+z)^{-0.8}$. The radio data are taken from the Faint Images of the Radio Sky at Twenty-cm Survey (FIRST; Becker et al. 1995), whose detection limit is regarded to be 1 mJy. In Figure B.13, contours show the distribution of all galaxies in our sample. Open circles, small dots, triangles and squares represent E+A, HDS+em, HDS+H α and HDS+[OII], respectively. We have excluded galaxies with a possible AGN sign (section B.3). When a galaxy is within the FIRST survey area, and is not detected, we assigned 1mJy to the galaxy as an upper limit of the radio flux. In Figure B.13, points along with the line around $10 M_{\odot} \text{ yr}^{-1}$ are thus those with no detection, showing an upper limit of the radio SFR. Only one E+A has a moderate SFR of $\sim 10 M_{\odot} \text{ yr}^{-1}$. The other E+As are not detected in the FIRST and thus only shown as an upper limit. In this redshift range, none of the E+As has radio SFR greater than $100 M_{\odot} \text{ yr}^{-1}$. Although it is difficult to exclude the possibility that E+As have a moderate rate of dust hidden SFR,

we can safely conclude that E+As do not hold dust hidden starburst. The same is true for HDS+H α and HDS+[OII] galaxies except one HDS+H α galaxy with SFR of ~ 40 M $_{\odot}$ yr $^{-1}$. On the other hand, some of the HDS+em galaxies have strong star formation of ~ 100 M $_{\odot}$ yr $^{-1}$, consistent with their emission lines in optical.

Next we compare the models and the data on the H δ EW vs D4000 plane (strength of the 4000Å break) in Figure B.14. Since D4000 is sensitive to old stellar populations and H δ EW traces the amount of young A-type stars, the H δ EW vs D4000 plane is a suitable space to study the star formation history of H δ -strong galaxies. A caveat, however, is that models become less accurate on the plane since both H δ EWs and D4000 is more difficult quantities to reproduce than broad band colors. For models, we use H δ EWs given in the GISSEL model, which were measured using the flux between 4083.50 and 4122.25 Å. This is essentially the same window as used to measure H δ EWs from the observational data (4082-4122Å; Chapter A). For D4000, the SED model uses the flux ratio of the 3750-3950Å window to the 4050-4250 Å window (Bruzual 1983). Observationally D4000 is measured using the ratio of the flux in the 3751-3951Å window to that in the 4051-4251 Å (Stoughton et al. 2002). We regard these two D4000 measurements as essentially the same.

In all the panels in Figure B.14, we plot the three models. The dashed, solid and dotted lines are for the models with an instantaneous burst, constant star formation and exponentially decaying star formation rate. We subtracted 1Å from the model H δ EWs to compensate for possible stellar absorption. Different panels are for three different metallicities ($Z=0.0001, 0.02$ and 0.1). Compared with the distribution of all the observed galaxies represented by the solid contours, the models might have a slight shift toward larger D4000 and H δ directions. However, the behavior of the models on this plane well reproduce expected behavior of galaxies, in a sense that star-forming galaxies evolve into large D4000 and small H δ EWs. Therefore, we regard that qualitative interpretation based on the models as valid. The latest version of the GISSEL model will solve these problems (Kauffmann et al. 2003a,b; Charlot et al. in prep.). Observational data are plotted using open circles, small dots, triangles and squares for E+A, HDS+em, HDS+H α and HDS+[OII], respectively. In the plane, E+A galaxies occupy an upper right part of the panel, having high H δ EWs (>5 Å) and large D4000 (~ 1.5) at the same time. This part of the plane can be reached only with the burst models, which is consistent with the previous interpretation of E+A galaxies as a post-starburst galaxy. According to the instantaneous burst model with the solar metallicity ($Z=0.02$), E+A phase is found to be 130-800 Myrs after the burst. On the other hand, HDS+em galaxies are at the tip of the contours, and can be reached using both the exponentially decaying model and the constant star formation model, which reflects that these galaxies are more common galaxies. These star formation histories are also consistent with HDS+em galaxies having

both [OII] and H α in emission. Note that in the lowest metallicity model ($Z=0.0001$), the exponentially decaying model can reach the region occupied by E+A galaxies. Therefore, some of E+As might be extremely metal poor galaxies with an exponentially decaying star formation history. HDS+[OII] galaxies occupy the similar place on the plane to E+A galaxies. HDS+H α galaxies show a somewhat wider distribution. However, their distribution is closer to that of E+As than HDS+em. (See Kauffmann et al. 2003a,b for a more detailed discussion of the behavior of various types of galaxies on the D4000 vs H δ plane and its dependence on stellar mass).

Finally, we compare the models and the data on the $u - g$ vs H δ EW plane. We aim to study the relation between the on-going and previous (recent) star formation activities, using $u - g$ and H δ EWs as indicators of on-going and previous star formation activities, respectively. Although the emission lines such as [OII] and H α are more direct indicators of on-going star formation, we found it more difficult to reproduce them with the current version of the model, and therefore, more difficult to perform quantitative comparisons with the observational data (However, see Charlot et al. 2001; Shioya et al. 2001,2002; Bekki et al. 2001 for such an attempt). Instead of H α and [OII], we use $u - g$ color as an indicator of on-going star formation since it shows better agreement between the SED models and the observational data. In Figure B.15, we plot $u - g$ against H δ EW for the three models and the observational data. Three panels represent different metallicities. Symbols are the same as previous figures. The model $u - g$ color depends on metallicity to some extent, showing bluer $u - g$ color with decreasing metallicity. The solar metallicity model in the upper right panel shows a good agreement with the observational data. In the panel, the exponentially decaying model and the constant star formation model well explain the HDS+em galaxies. The instantaneous burst model, on the other hand, explains E+A galaxies well. The agreement again indicates that E+A galaxies are in a post-starburst phase, and cannot be explained by more normal star formation histories. If the burst model with solar metallicity is assumed, somewhat tighter constraints on the time scale can be obtained from this figure than that obtained by Figure B.14. E+A galaxies are found to be in 270-800 Myrs after the burst.

More interestingly, E+A galaxies are beautifully aligned on the time sequence of the instantaneous burst model from 270 Myr to 800 Myr. Therefore, according to this model, E+A galaxies with larger H δ EWs are younger than E+A galaxies with smaller H δ EWs. In the next section, we investigate those E+A galaxies with large H δ EWs in more detail, as young E+A galaxies.

B.7 Properties of young E+A Galaxies

In the last section, we found that E+A galaxies with larger H δ EWs are younger E+A galaxies, assuming the instantaneous burst model. We select possible young E+A galaxies from our E+A sample using the following criteria.

$$E + A \text{ and } H\delta \text{ EW} > 7\text{\AA} \quad (\text{B.6})$$

Among our 133 E+A galaxies, 28 galaxies satisfy these criteria. In Figure B.16, we show example spectra of these young E+A galaxies. All the spectra show very strong H δ absorption with the lack of [OII] and H α emission lines. According to the instantaneous burst model, these young E+As are found to be around 270-430 Myrs after the burst. The entire E+A phase continues until \sim 800 Myrs after the burst (Figures B.10 and B.15). Table B.2 shows median properties of these young E+As and all the E+As in our sample. Errors are quoted using 75 and 25 percentiles. Both samples show quite similar properties except strong H δ EWs and absolute magnitude. The brighter absolute magnitude for the young E+As is consistent with the hypothesis that these are younger galaxies which evolve into normal E+A galaxies as their stellar populations become older and fainter.

If these galaxies are truly in younger phase of E+As, they are also closer to the initial burst, and therefore closer to the epoch of physical change (only 270-430 Myr after the burst and truncation of star formation). Therefore, by examining the images of the young E+As, we might obtain some hints on the physical mechanisms causing the burst and truncation. Figure B.17 shows randomly sampled example images of these young E+A galaxies. Each panel in the figure corresponds to that in Figure B.16. Interestingly, more than half of these galaxies have their companions/tidal features within 60" of the image, suggesting recent merger/interaction with accompanying galaxies. These results indicate that the origin of E+A galaxies might be merger/interaction, which can dynamically disturb galaxies and cause starburst and sudden truncation of it (Lonsdale, Persson, & Matthews 1984; Kennicutt et al. 1987; Sanders et al. 1988). Elliptical-like morphology of E+As (Figures B.5, B.17) might stem from the merger/interaction already in progress. Indeed, numerical simulations have shown that merger/interaction is able to produce elliptical morphology of galaxies (Ostriker & Hausman 1977; Hausman & Ostriker 1978; Miller 1983; Merritt 1984; Malumuth & Richstone 1984; Bode et al. 1994; Athanassoula, Gario, & García Gómez 2001).

We calculated the number of accompanying galaxies within 50 or 75 kpc from the young E+As using galaxies from the SDSS imaging data, and compared it with that of 1000 randomly selected SDSS galaxies with a similar redshift distribution. We calculated M_r^* assuming that all galaxies within 50 or 75 kpc in the imaging data are at the same redshift as the central galaxy, and using the k -correction by Blanton et al. (2003; v1_11).

Then, we limit galaxies between $-23 < Mr^* < -19.5$ and subtract global galaxy number count adjusted to the angular area that 50 or 75 kpc subtends at the redshift. The faint end of the magnitude limit ($Mr^* = -19.5$) corresponds to $r^* = 22.2$ at the highest redshift ($z=0.3$) of the young E+A sample for galaxies with large k -correction. Although star/galaxy separation become unstable at $r^* > 21.5$, the object detection of the SDSS imaging data is 95% complete at $r^* = 22.2$ (Stoughton et al. 2002). Table B.3 summarizes the number of accompanying galaxies within 50 and 75 kpc for the young E+A, all E+A and 1000 randomly selected galaxy samples. The young E+A galaxies have 0.40 ± 0.12 accompanying galaxies per galaxy on average within 75 kpc, while the 1000 randomly selected galaxies with a similar redshift distribution have 0.16 ± 0.01 accompanying galaxies per galaxy. Thus, the young E+A galaxies have 2.5 times more accompanying galaxies than the randomly selected galaxies with more than two σ significance. A similar result can be obtained when we use 50 kpc radius, where young E+As have accompanying galaxies of 0.24 ± 0.09 , which is eight times more than the random sample of galaxies with 0.03 ± 0.01 accompanying galaxies. In addition, we calculated the number of accompanying galaxies for all the E+A galaxies to be 0.12 ± 0.03 and 0.26 ± 0.04 within 50 and 75 kpc, respectively. It is interesting that the number of accompanying galaxies for all E+A sample is between the young E+A sample and the random sample for both 50 and 75 kpc radii. These results might suggest that accompanying galaxies of the young E+As will be merged into the central E+A galaxy in a few hundred Myrs when it is seen as a normal (older) E+A galaxy. In Figure B.18, we show a preliminary absolute magnitude distribution of accompanying galaxies within 75 kpc radius after fore/background subtraction for young E+As. A slight peak may be found at the faintest magnitude bin ($Mr^* \sim -19.5$), suggesting that accompanying galaxies are fainter than the central E+A galaxies. Thus, the possible origin of E+A galaxies can be called minor (different mass) merger/interaction rather than major (equal mass) merger/interaction. However, since star/galaxy separation and k -correction become uncertain at the faintest magnitude of $r^* \sim 22.2$ ($Mr^* = -19.5$ at $z = 0.3$), Figure B.18 should not be over-interpreted. Follow-up observations are urgently needed.

B.8 Discussion : Origins of E+A Galaxies

B.8.1 Are E+As Cluster Related Phenomena?

In section B.5, we showed that the spatial distribution of E+A galaxies does not depend much on the local galaxy density. There are many E+A galaxies at a local galaxy density of $\ll 1 \text{ Mpc}^{-2}$. Our result is consistent with Zabludoff et al. (1996) and Balogh et al. (1999), where they also found E+A galaxies in the field. Recently Quintero et al. (2003)

reported that E+A galaxies do not lie in high-density regions using a sophisticated K/A ratio method to select ~ 1000 E+A galaxies from the same SDSS data. There is, however, other work which reported that E+A galaxies live preferentially in cluster regions (e.g., Poggianti et al. 1999; Dressler et al. 1999). We would like to stress the high quality of our spectra data. As we showed in Section A.5 of Chapter A, we found a comparable number of HDS+[OII] galaxies to E+A galaxies (52%). Therefore high redshift E+A samples often selected without $H\alpha$ information could be contaminated with HDS+[OII] galaxies up to 52%. Also if errors in measuring EWs of lines were larger in the previous work, the errors could affect the resulting ratio of E+A galaxies. Since E+A galaxies are rare, there are more galaxies scattering into the E+A sample than E+A galaxies slipping out of E+A criteria. We tried to avoid these problems using high quality spectra from the SDSS and a much larger number of 133 E+As than used in previous work. In addition, most of the work reporting an excess of E+A galaxies in cluster regions usually observed only cluster regions, and did not have good field data. All the field survey data (LCRS, CNOC and the SDSS) found E+A galaxies in field regions. Considering all of these, our result indicates that E+A phenomena are common to various environments including the general field region, rather than cluster specific phenomena. At the very least, it is clear that the field E+A galaxies we found can not be explained by cluster related phenomena since there exists no ram-pressure or cluster tidal effects in the field. Additional mechanisms which work in the field is needed.

Historically many people connected the existence of E+A galaxies to the evolution of cluster galaxies such as the Butcher-Oemler effect or the spiral-to-S0 transition. However, our results indicate that E+A galaxies has little to do with these cluster-related phenomena. It seems that we have to search for the physical mechanism responsible for cluster galaxy evolution elsewhere (e.g., Goto et al. 2003d; Chapter 7).

B.8.2 Are E+As Dusty Star-forming Galaxies?

Among the 8 radio detected galaxies of Smail et al. (1999), 5 have strong Balmer absorption and no detectable [OII] emission. Miller & Owen (2002) detected 2 galaxies in radio out of 15 E+A galaxies defined in Zabludoff et al. (1996). These two studies indicate that E+A galaxies might have an on-going star formation, but their star formation might be hidden by dust. However, we would like to point out that E+A galaxies defined in these two samples do not have $H\alpha$ information. In Chapter A, we found that 52% of $H\delta$ -strong galaxies with no [OII] emission do have $H\alpha$ in emission (HDS+ $H\alpha$). Therefore, it is no wonder that 5/8 or 2/15 of their post-starburst galaxies had star formation, and thus radio emission. These galaxies may be HDS+ $H\alpha$ galaxies in our category. Strictly speaking on E+A galaxies in our criteria (HDS with no [OII] or $H\alpha$ in emission), E+A

galaxies are not redder in $r - K$ than other galaxies as shown in Figure B.12. For example, radio detected galaxies in Smail et al. (1999) are redder than other galaxies by ~ 1 mag in $r - H$. Therefore, Figure B.12 suggests that our E+A galaxies are not dust-enshrouded star-forming galaxies. In addition, in Figure B.13, we showed that the upper limit of the radio SFR of the E+A galaxies is around $10 M_{\odot} \text{ yr}^{-1}$. We can not rule out the possibility that E+As might have moderate star formation rates. However, we can conclude that E+As are not dusty starbursting ($\sim 100 M_{\odot} \text{ yr}^{-1}$) galaxies. In the literature, Poggianti & Wu (2000) detected HDS+[OII] galaxies (e(a) galaxies in their criteria) in far-infrared (FIR). However, they did not detect E+A galaxies (k+a/a+k in their criteria) in FIR, suggesting that E+A galaxies do not have dust hidden star formation. Duc et al. (2002) studied mid-infrared emission in the A1689 region and found that none of the galaxies with post-starburst optical spectra is detected in $15 \mu\text{m}$ down to its flux limit, which corresponds to SFR_{IR} of $1.4 M_{\odot} \text{ yr}^{-1}$. This does not support the dust-enshrouded origin of E+A galaxies, either. Furthermore, Quillen et al. (1999) observed 7 E+A galaxies at $12 \mu\text{m}$ using ISO to find that E+A's $12\mu\text{m}$ flux is consistent with that of old stellar populations. They concluded that the E+A phase appears to be truly a post-starburst phase with little on-going star formation. We still can not reject the possibility that some of E+A galaxies might have moderate rate of star formation hidden by dust. However, it is also difficult to explain all of the E+A galaxies as dusty star-forming galaxies. Therefore, the majority of E+A galaxies seems to originate from other physical mechanisms than dust enshrouded star formation.

A selective extinction (Poggianti & Wu 2000) is also capable of explaining the E+A phenomena. In this scenario, O- and B-type stars are embedded in heavily dust obscured star-forming HII regions, and therefore, [OII] and H α emission lines are invisible in optical. However, A-type stars responsible for strong H δ absorption have a longer life time ($10^7 - 1.5 \times 10^9 \text{ yr}$) to drift away from (or disperse) such dusty regions where they were born. In this scenario, the effect of dust is maximum for the youngest generation of stars that provides the ionizing flux responsible for the emission lines, and decreases for older stars. This scenarios is equivalent to a clumpy distribution of dust where the location and thickness of the patches are not random but dependent on the age of the embedded stellar populations. Observationally this scenario is very difficult to verify unless high spatial resolution Mid-/Far-IR observation which can resolve each HII region becomes available. However, we would like to point out that we observed many HDS+em galaxies in which [OII] and H α emission lines are visible in addition to strong H δ absorption. If the selective extinction is the explanation for E+A galaxies, it needs to explain why selective extinction only happens in a certain sub-sample of H δ -strong galaxies, instead of all H δ -strong galaxies.

B.8.3 Merger/Interaction Origin of E+A Galaxies

In Section B.7, we found that the instantaneous burst model can explain the observational properties of E+A galaxies very well, including optical colors (Figure B.11), infrared colors (Figure B.12), H δ strength and stellar population indicators (D4000 in Figure B.14; $u - g$ in Figure B.15). Assuming that this instantaneous burst model is correct, we selected young E+A galaxies (E+A galaxy between 270 and 430 Myrs after the burst; Section B.7). Since these young E+As are closer to the burst epoch than the other E+As, they have stronger H δ absorption and brighter absolute magnitude (Table B.2). In a few hundred Myrs, when H δ absorption becomes a little weaker, these galaxies will be seen as a typical E+A galaxy. In Figure B.17, we examined the image of young E+As and found that these galaxies frequently have accompanying galaxies. In fact, these galaxies have ~ 2.5 times more accompanying galaxies within 75 kpc than 1000 randomly selected galaxies with two σ significance. This statistical result suggests that merger/interaction is the origin of these galaxies (Table B.3).

In the literature, there have been some evidence on a few nearby E+A galaxies, suggesting that interaction/merger between galaxies can trigger starburst. For example, Oegerle, Hill, & Hoessel(1991) observationally found a tidal feature in a nearby E+A galaxy G515 (see also Carter et al. 1988). Belloni et al. (1995) reported the merging origin of E+A galaxies based on the HST image. Schweizer (1996) found several nearby E+As that have highly disturbed morphologies consistent with the products of galaxy-galaxy mergers. Also 5 out of 21 E+A galaxies in LCRS have a tidal feature (Zabludoff et al. 1996). One of two E+A galaxies observed with the HST has an elliptical morphology with extended tidal tails (Zabludoff 1999). One E+A galaxy observed with the VLA has clear tidal tails (Chang et al. 2001), which support the galaxy-galaxy interaction picture for E+A formation. Poggianti & Wu (2000) reported that proportion of close mergers are very high among their e(a) sample (HDS+em in our definition). Liu & Kennicutt (1995a,b) also found E+A galaxies among 40 merging/interacting systems they observed. Bartholomew et al. (2001) and Norton et al. (2001) found that star formation in E+A galaxies is centrally concentrated. They argued that their observational results are consistent with the tidal interaction origin, considering the fact that Moss & Whittle (1993,2000) reported that early-type tidally distorted spiral galaxies are often found with compact nuclear H α emission. Theoretically, Bekki et al. (2001) showed that galaxy-galaxy mergers with high infrared luminosity can produce e(a) spectra which evolve into E+A spectra (See also Shioya et al. 2001,2002).

Since these previous results were based on only a few nearby E+A galaxies, and thus lacked statistical significance, previous authors did not conclude on origins of E+A galaxies. However, considering our findings of excess number of accompanying galaxies around E+As using a much larger sample of 133 E+As, it is likely that these previous

results are truly observing a merger/interaction remnant of E+A galaxies. In the last two subsections, the dusty origin and cluster origin are not all plausible. Therefore, we conclude that the E+A phenomena are most likely to be the results of merger/interaction with accompanying galaxies.

B.9 Summary and Conclusions

E+A spectra (strong H δ absorption with no [OII] nor H α emission) can be only understood with an instantaneous starburst and its truncation. However, the cause of the starburst and its truncation has been unknown for more than 20 years since the discovery of E+As (Dressler & Gunn 1983). We have pursued the origin of this interesting population of galaxies, using the four statistically large subsamples of 3183 H δ -strong (HDS; H δ EW >4 Å) galaxies presented in Chapter A; 133 E+A (H δ -strong with no [OII] nor H α emission), 42 HDS+[OII] (HDS with [OII] and without H α), 108 HDS+H α (H δ -strong with H α and without [OII]), and 2900 HDS+em (H δ -strong with both of [OII] and H α) galaxies. Our findings can be summarized as follows.

- Morphologies of E+A galaxies are elliptical-like, while those of HDS+em galaxies are disk-like (Figure B.5).
- The local galaxy density distribution of E+A galaxies is consistent with that of the field galaxies. And thus, many E+A galaxies are found in field regions. These field E+A galaxies can not be explained with cluster-related phenomena such as ram-pressure stripping or gravitational interaction with cluster potential. Therefore, the origin of E+A galaxies is not likely to be cluster-related.
- Dusty star-forming galaxies are expected to have redder color in $r - K$ by ~ 1 mag. However, $r - K$ colors of E+As (Figure B.12) are not much redder than those of normal galaxies. We derived an upper limit on the dust enshrouded star formation using radio data from the FIRST survey, and found that dust enshrouded star formation rate of E+A galaxies is well below ~ 10 M $_{\odot}$ yr $^{-1}$. Therefore, it is not likely that E+A galaxies are dusty starburst galaxies.
- We compared three typical star formation histories in the GISSEL model with the observational quantities including H δ EW, D4000 and $u - g$ color. As is found in previous work, only the instantaneous burst model can explain unusual properties of E+A galaxies, assuring the post-starburst nature of these galaxies.
- Assuming the instantaneous burst model, we selected young E+A galaxies of an age of 270-430 Myrs after the burst. These young E+As have a stronger H δ absorption and a brighter absolute magnitude than normal (all) E+As. In Figure

B.17, we investigated images of the young E+As and found that they frequently have close accompanying galaxies. Statistically, these galaxies have accompanying galaxies within 75 kpc \sim 2.5 times more frequent than randomly selected galaxies at two σ significance level. Considering that cluster related origins and dusty star formation origins are not all plausible in terms of our data, we conclude that a merger/interaction with closely accompanying galaxies is the most likely mechanism to be responsible for the violent star formation history of E+A galaxies.



Figure B.1: [OII] EWs are plotted against $H\delta$ EWs for four sub-samples of $H\delta$ -strong galaxies. The contours show the distribution of all 94770 galaxies. Large open circles, triangles, squares, and small dots represent E+A, HDS+[OII], HDS+ $H\alpha$ and HDS+em galaxies, respectively.

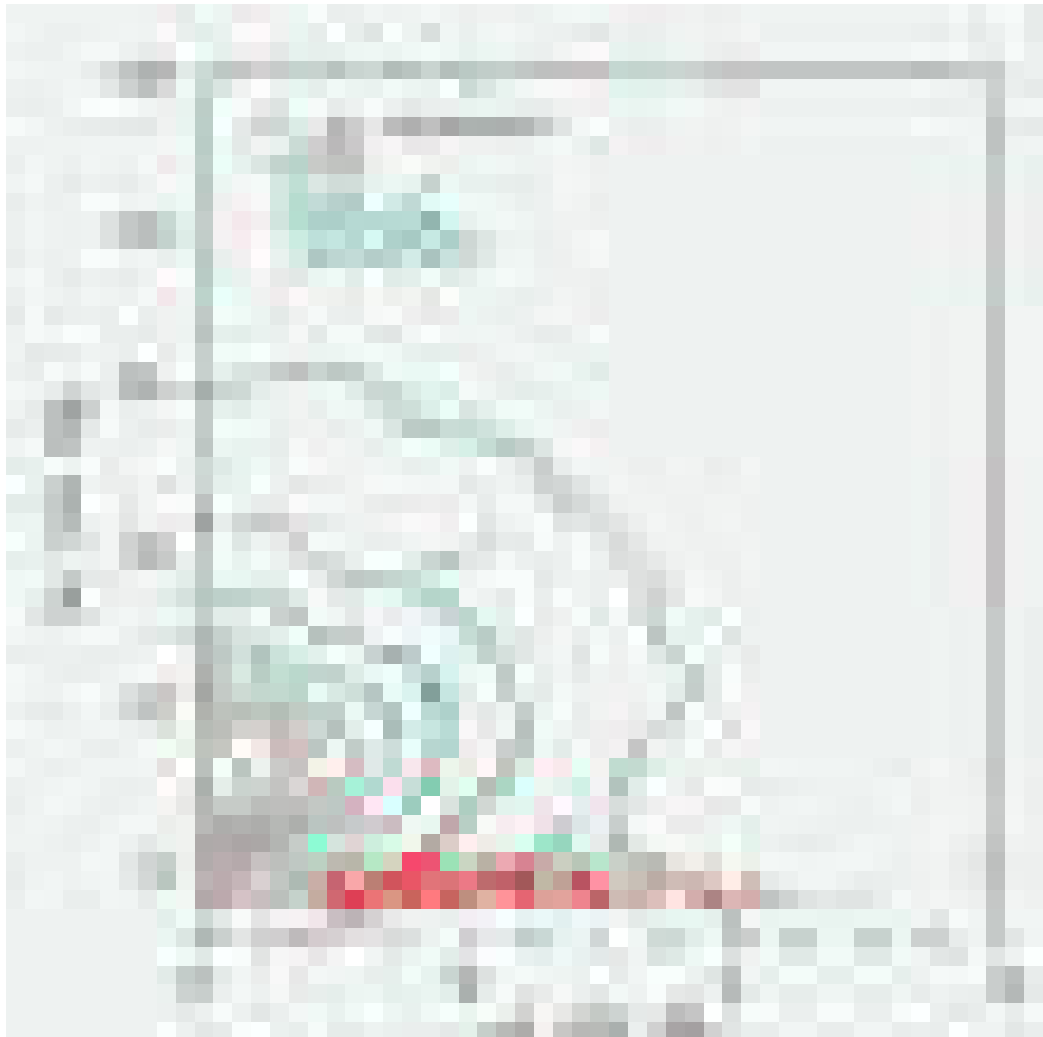


Figure B.2: $\text{H}\alpha$ EWs are plotted against $\text{H}\delta$ EWs for four sub-samples of $\text{H}\delta$ -strong galaxies. The contours show the distribution of all 94770 galaxies. Large open circles, triangles, squares, and small dots represent E+A, HDS+[OII], HDS+ $\text{H}\alpha$ and HDS+em galaxies, respectively.



Figure B.3: Star formation rate estimated using $\text{H}\alpha$ flux for each class of galaxies. The solid line is for all 94770 galaxies. The long dashed, dotted, short dashed and dotted-dashed lines represent E+A, HDS+em, HDS+ $\text{H}\alpha$ and HDS+[OII] samples, respectively.



Figure B.4: Luminosity functions in r band for each subclass of $H\delta$ -strong galaxies. The solid line is for all galaxies in the volume limited sample. The long dashed, dotted, short dashed and dotted-dashed lines represent E+A, HDS+em, HDS+ $H\alpha$ and HDS+[OII] samples, respectively.

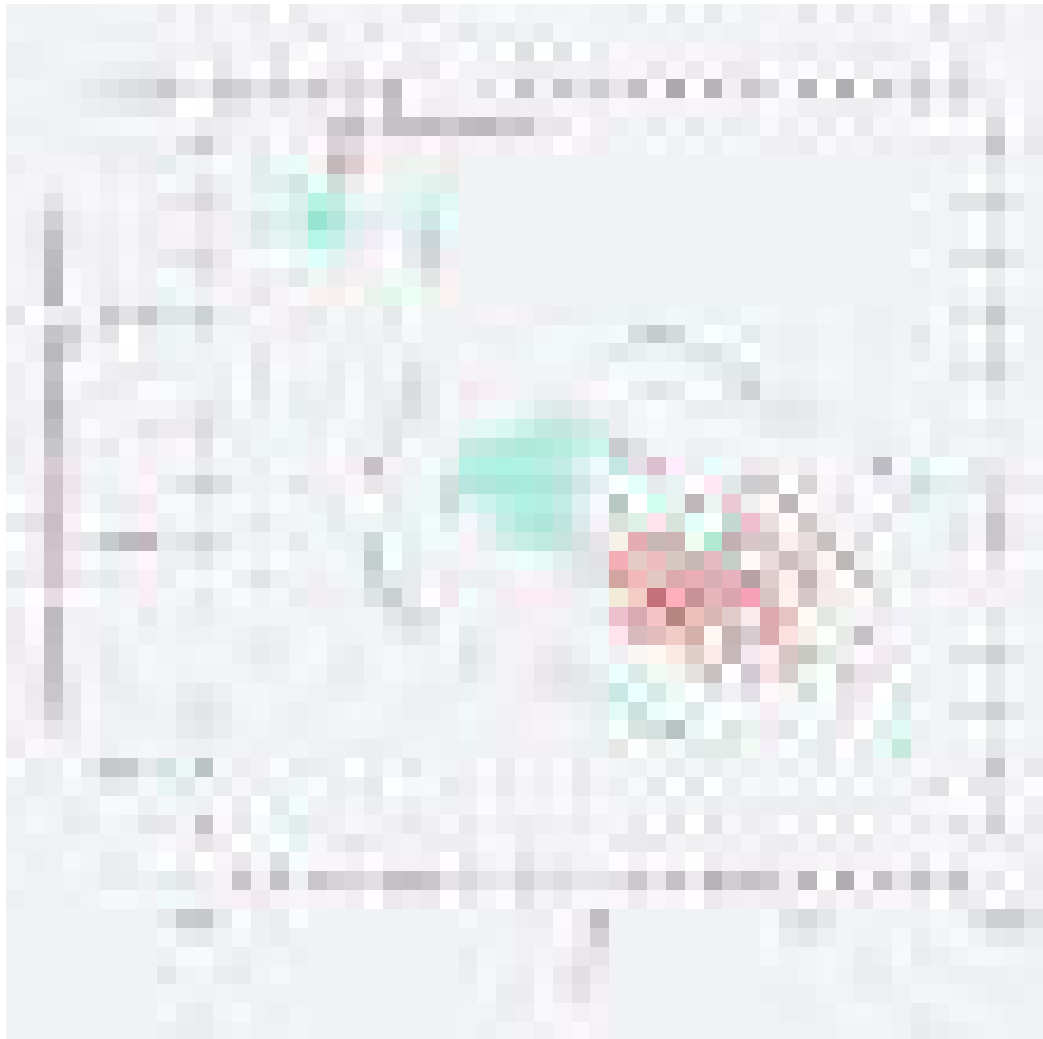


Figure B.5: Distributions of each subclass of galaxies in C_{in} v.s. $u - r$ plane. The contours show the distribution of all 94770 galaxies. The large open circles, triangles, squares, and small dots represent E+A, HDS+[OII], HDS+H α and HDS+em galaxies, respectively.

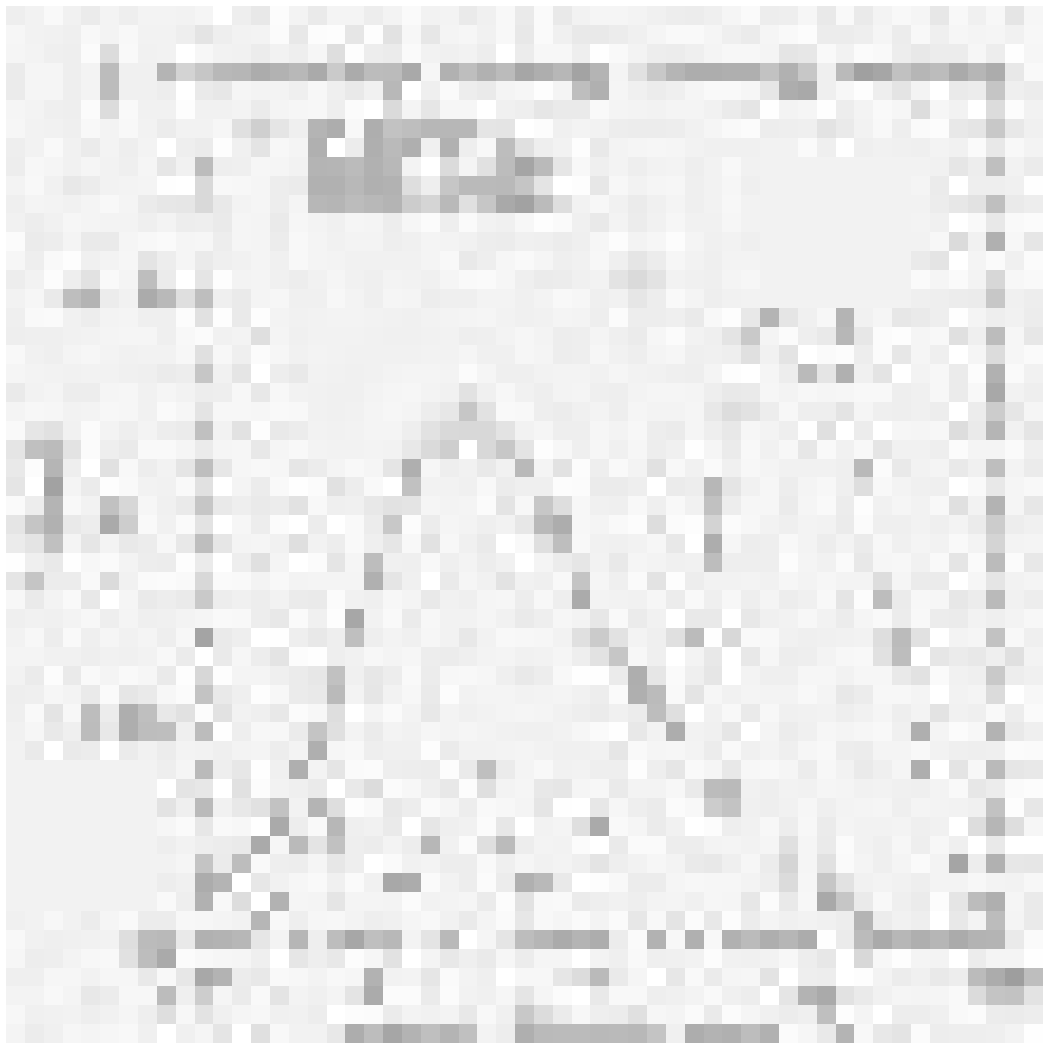


Figure B.6: Distribution of local galaxy density. The solid, dashed and dotted lines show distributions for all 94770 galaxies, galaxies within 0.5 Mpc from the nearest cluster and galaxies between 1 and 2 Mpc from the nearest cluster, respectively.

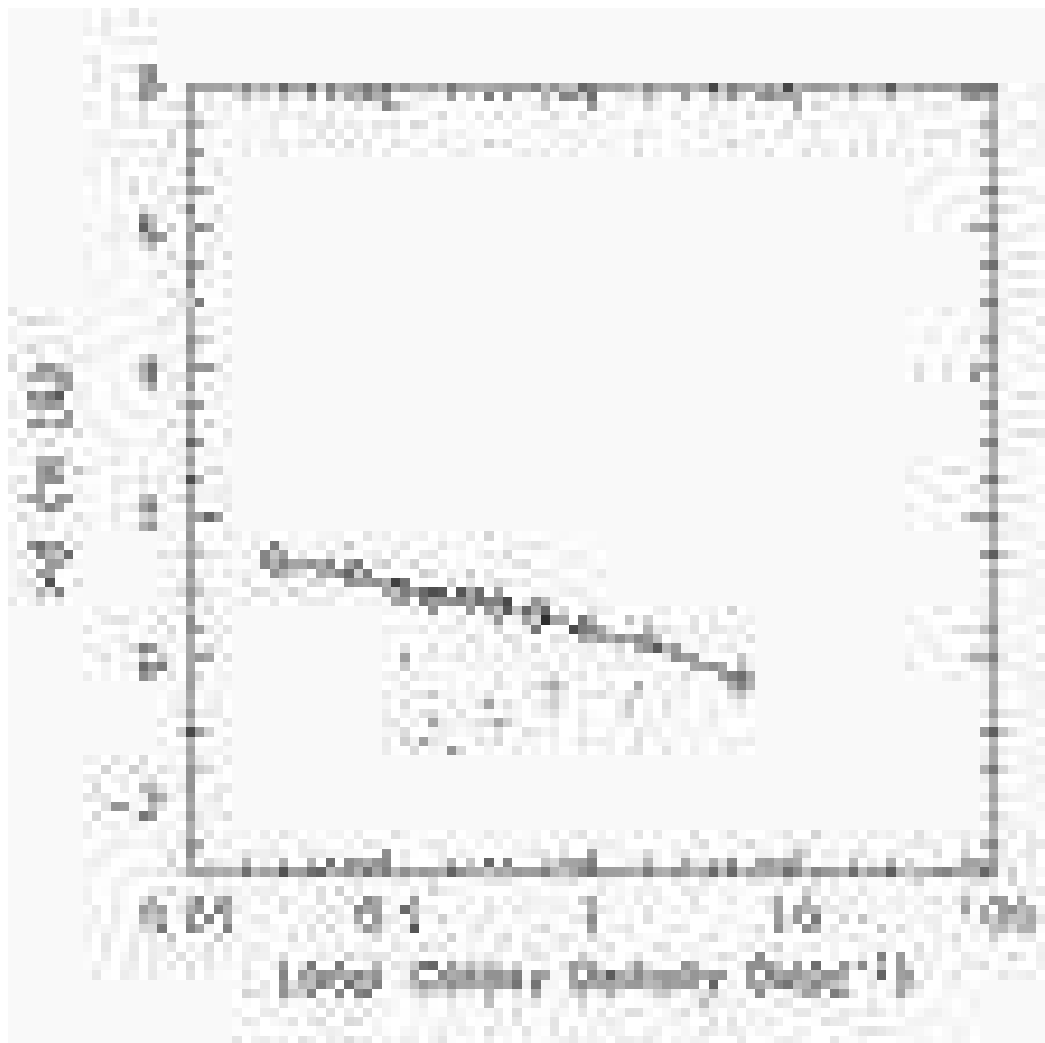


Figure B.7: $H\delta$ EW is plotted against local galaxy density. Negative EWs are absorption lines. The solid line shows the median of the distribution.

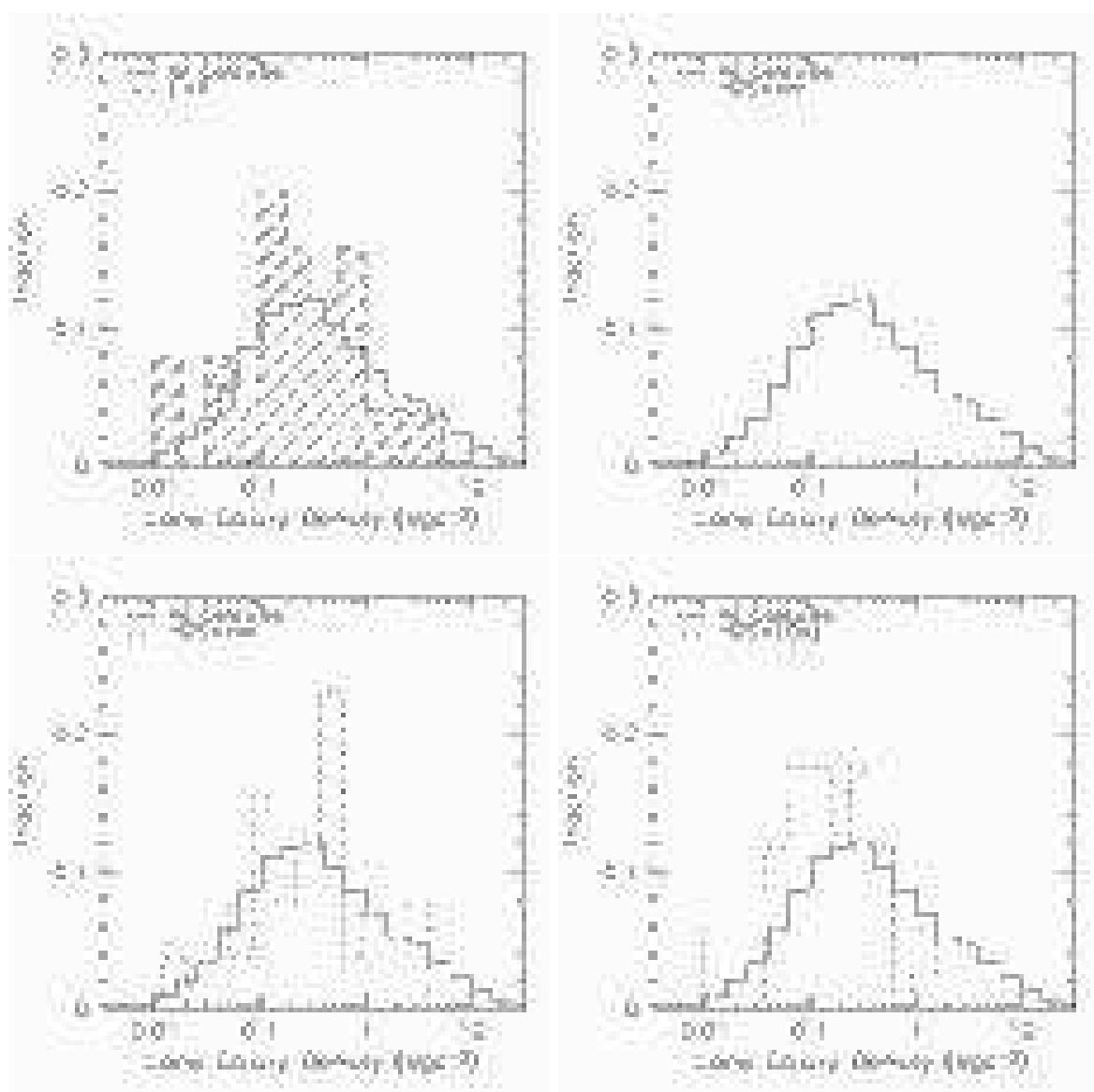


Figure B.8: Distributions of local galaxy density for each subsample of $H\delta$ -strong galaxies and all 94770 galaxies in the volume limited sample. The solid line is for all galaxies. The long dashed, dotted, short dashed and dot-dashed lines represent E+A, HDS+em, HDS+ $H\alpha$ and HDS+[OII] samples, respectively.

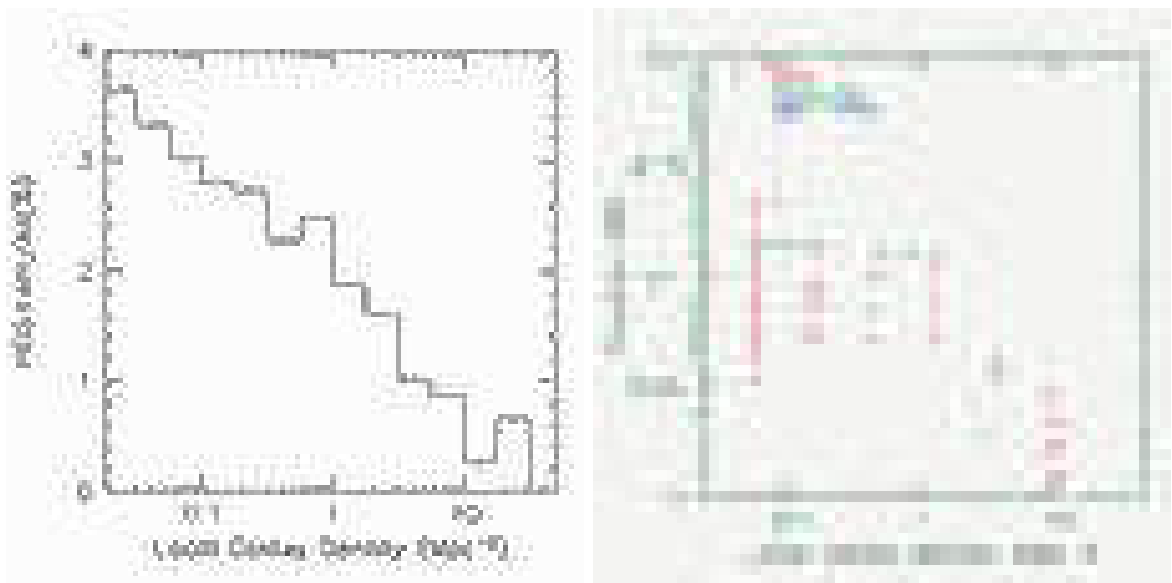


Figure B.9: Ratio of each subclass of H δ -strong galaxies to all galaxies as a function of local galaxy density. The left panel shows ratio for HDS+em galaxies to all galaxies in the volume limited sample. In the right panel, a long dashed, short dashed and dotted-dashed lines represent E+A, HDS+H α and HDS+[OII] galaxies, respectively.

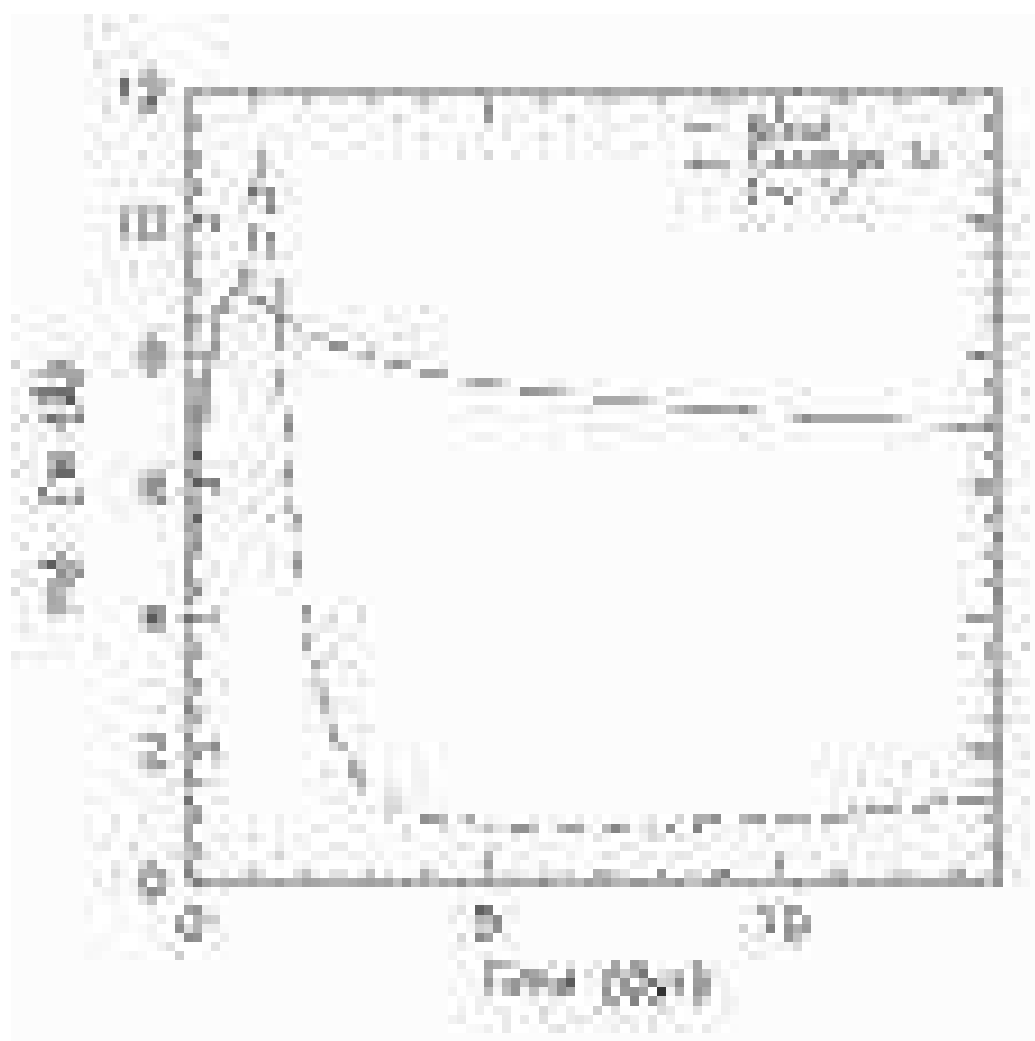


Figure B.10: $H\delta$ EWs are plotted against time (age) for three star formation histories with the GISSEL model. The dashed, solid and dotted lines show the models with instantaneous burst, constant star formation and exponentially decaying star formation rate. The models in this figure assume Salpeter IMF and solar metallicity.

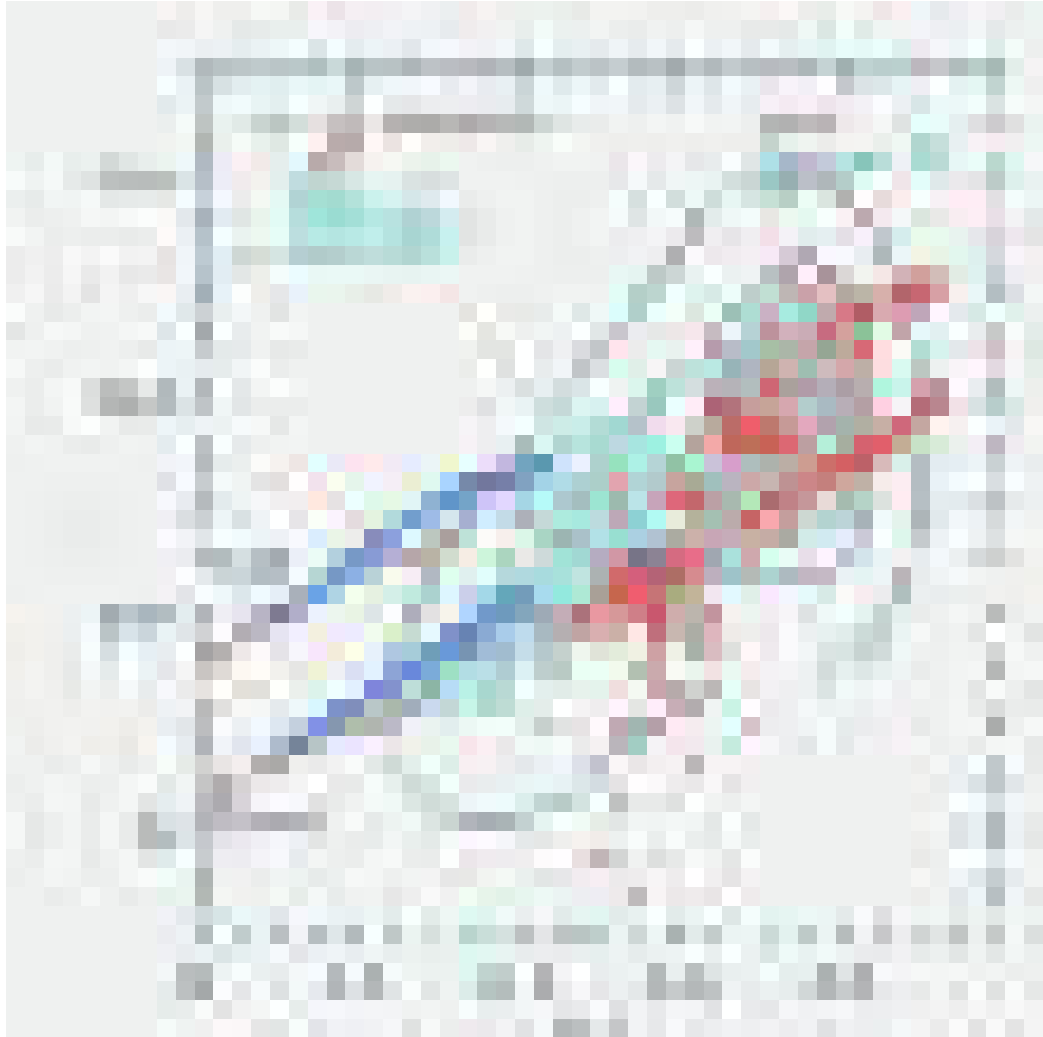


Figure B.11: Restframe $g - r$ color is plotted against $r - i$ color. The dashed, solid and dotted lines show the models with instantaneous burst, constant star formation and exponentially decaying star formation rate. Two sets of the models are present for solar metallicity ($Z=0.02$) and 5 times solar metallicity ($Z=0.1$). Open circles, small dots, triangles and squares represent E+A, HDS+em, HDS+H α and HDS+[OII], respectively.



Figure B.12: $J - K$ is plotted against $r - K$. All magnitudes are in restframe AB system. The contours show distribution of all galaxies in our sample. Open circles, small dots, triangles and squares represent E+A, HDS+em, HDS+H α and HDS+[OII], respectively. The dashed, solid and dotted lines show the models with instantaneous burst, constant star formation and exponentially decaying star formation rate. Three sets of the models are plotted for different metallicities.

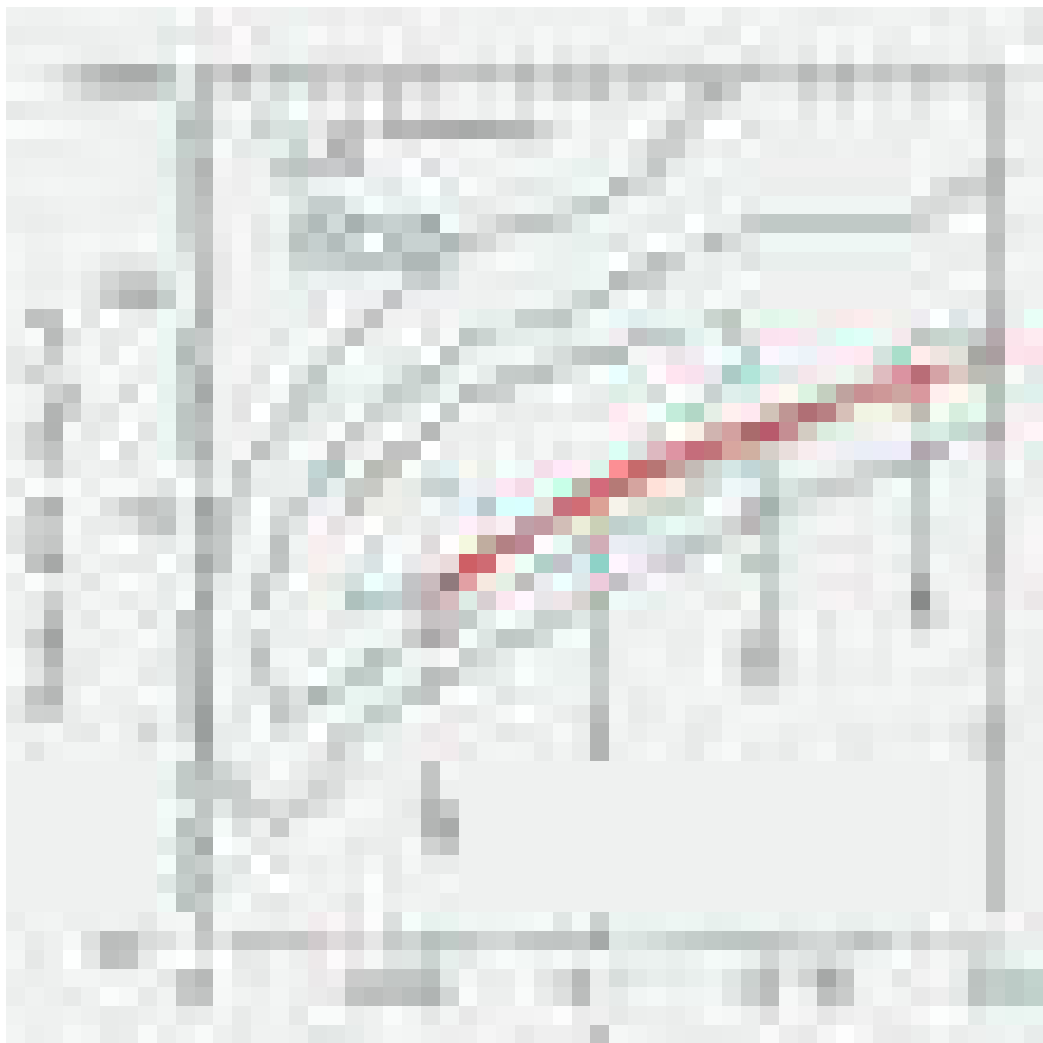


Figure B.13: Radio SFR calculated using the FIRST data is plotted against redshift. The contours show the distribution of all galaxies in our sample. Open circles, small dots, triangles and squares represent E+A, HDS+em, HDS+H α and HDS+[OII], respectively. When a H δ -strong galaxy is not detected in the FIRST data, we assigned 1 mJy as an upper limit of radio flux. Those galaxies with no radio detection appear in the plot as a line around $10 \text{ M}_\odot \text{ yr}^{-1}$ showing the upper limit of radio SFR.

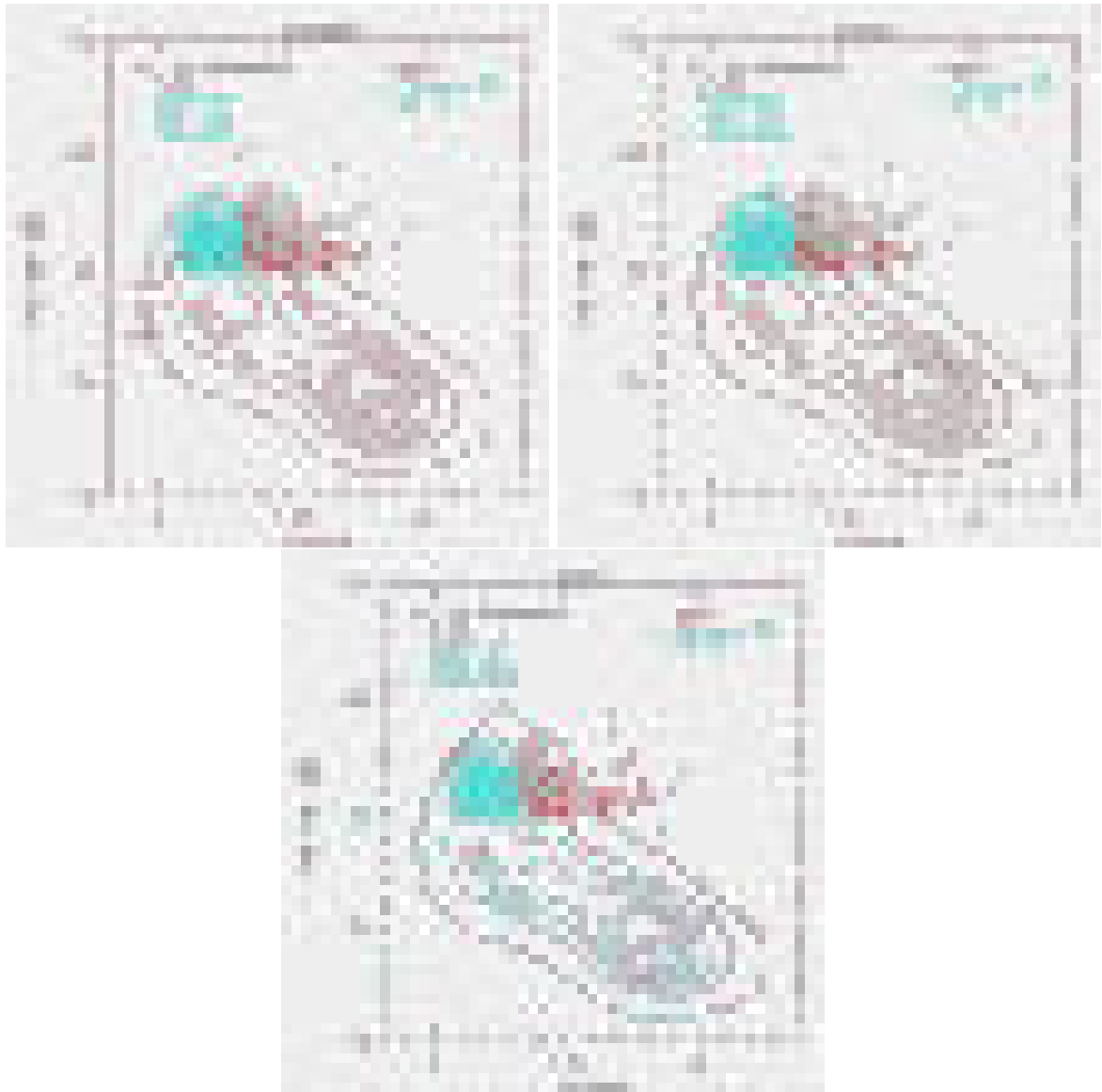


Figure B.14: $H\delta$ EWs are plotted against D4000 for the models with $Z=0.0001$ (0.5% solar), 0.02(solar) and 0.1 (5 times solar) from top to bottom. The dashed, solid and dotted lines are for the models with instantaneous burst, constant star formation and exponentially decaying star formation rate. Observational data are plotted using open circles, small dots, triangles and squares for E+A, HDS+em, HDS+ $H\alpha$ and HDS+[OII], respectively.

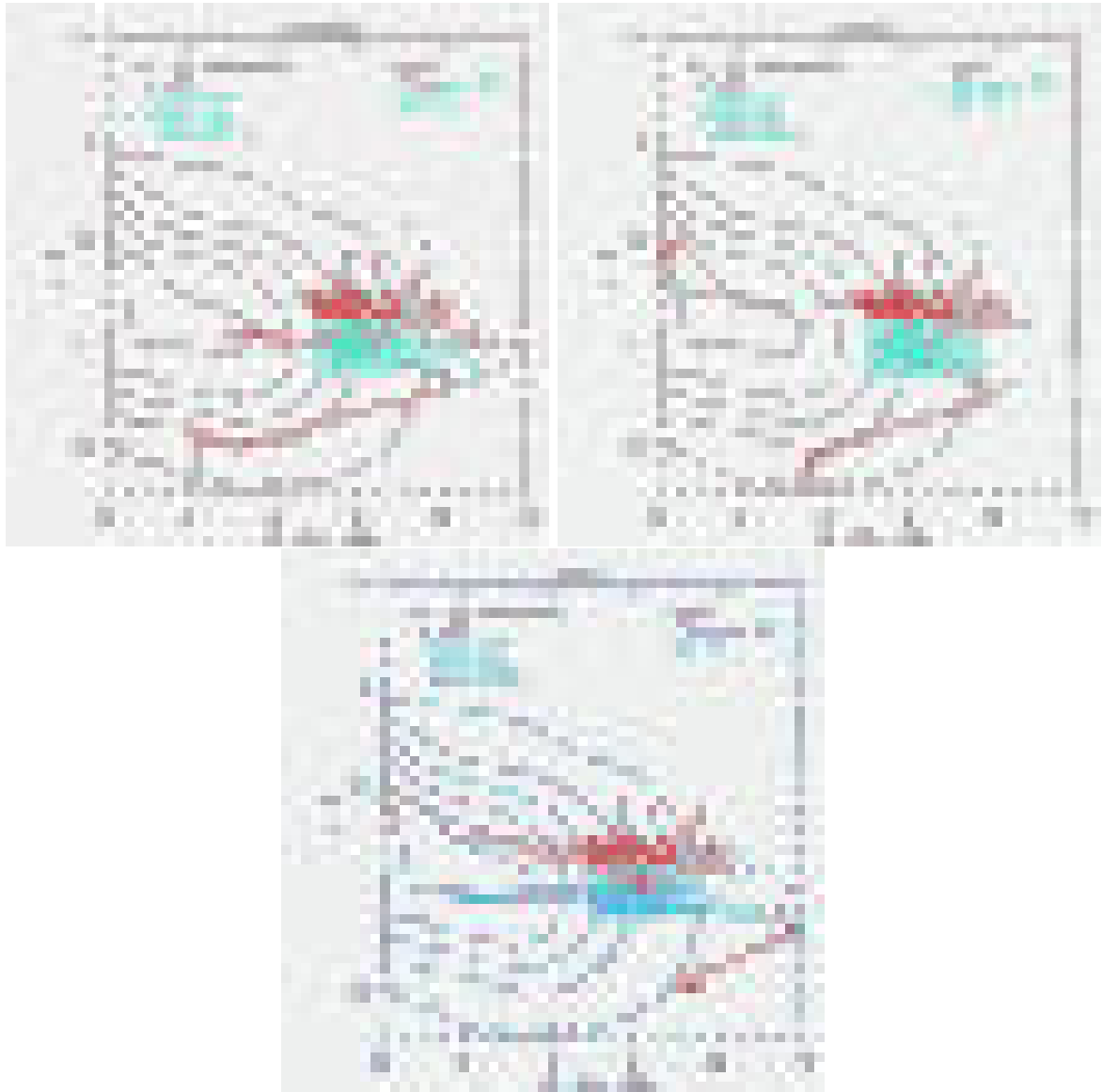


Figure B.15: The $u - g$ color is plotted against $H\delta$ EWs for three metallicity models and three star formation histories. Metallicities are $Z=0.0001$ (0.5% solar), 0.0004 (2% solar), 0.04 (20% solar), 0.02 (solar), 0.10 (5 times solar) from top to bottom. Star formation histories are the burst, constant and exponentially decreasing, shown by the dashed, solid and dotted lines, respectively. Observational data are plotted using open circles, small dots, triangles and squares for E+A, HDS+em, HDS+H α and HDS+[OII], respectively.

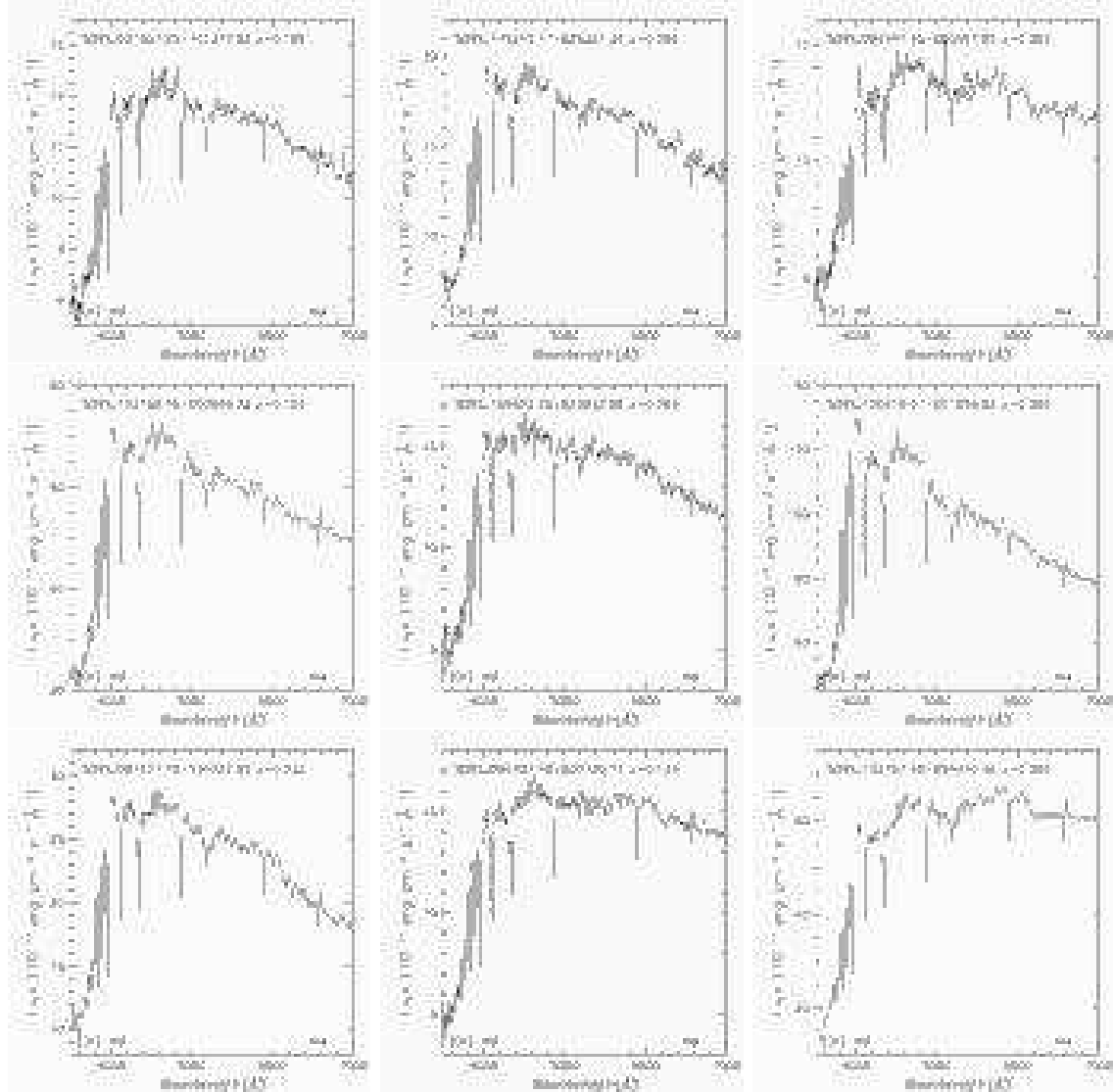


Figure B.16: Nine example spectra of young E+A galaxies (E+As with H δ EW > 7 Å). Spectra are shifted to restframe and smoothed using a 20Åbox.



Figure B.17: Nine example images of young E+A galaxies (E+As with $H\delta$ EW > 7 Å). Image size is $60'' \times 60''$ and north is up. Each panel corresponds to that in Figure B.16.

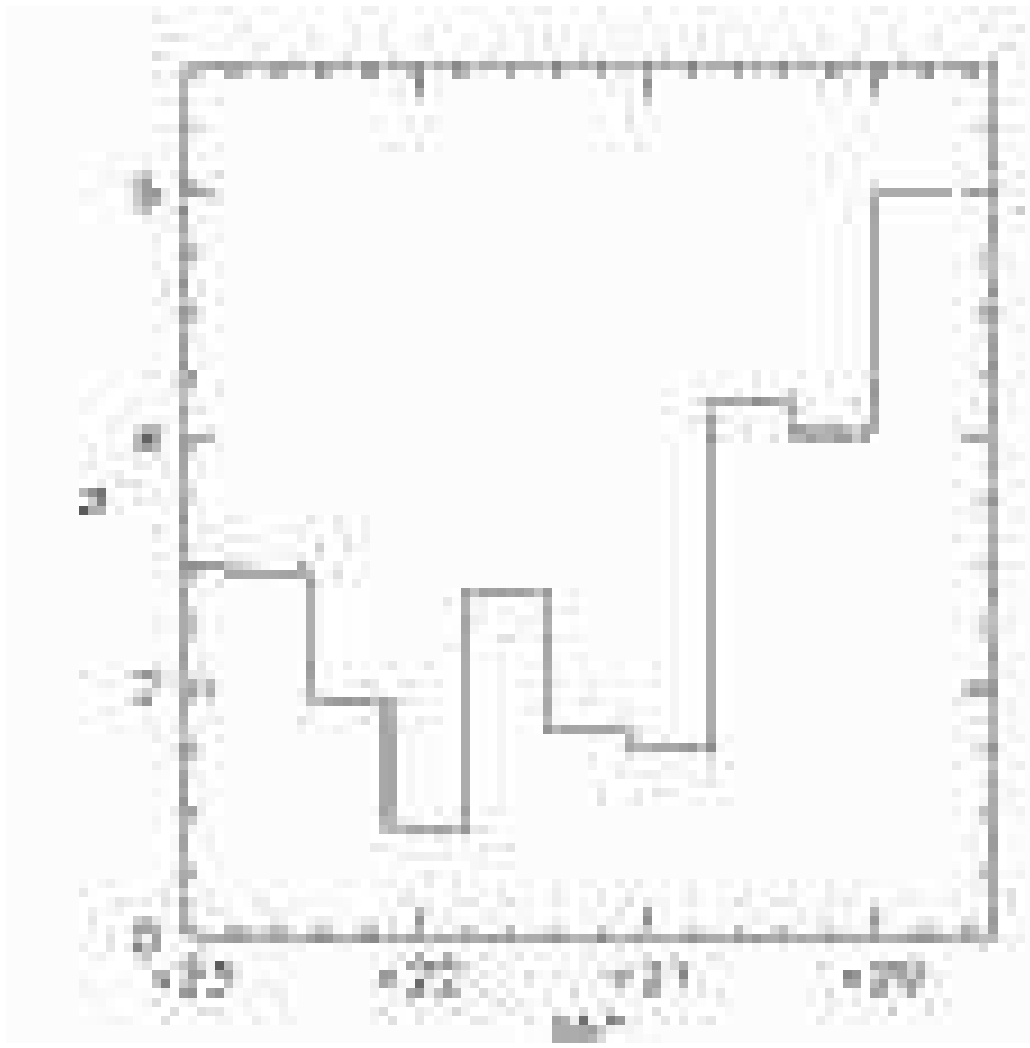


Figure B.18: Absolute magnitude distribution of accompanying galaxies within 75 kpc of young E+A galaxies. Since uncertainty in k -correction and star/galaxy separation of the SDSS increase at $r^* \sim 22.2$ ($M_{r^*} = -19.5$ at $z = 0.3$), this figure should not be over-interpreted.

Table B.1: Number of galaxies in each subsample of H δ -strong galaxies. Galaxies with the line ratios consistent with an AGN are not included in the sample of H δ -strong galaxies .

Category	Number
E+A	133
HDS+em	2900
HDS+H α	108
HDS+[OII]	42
All H δ -strong	3183
All	94770

Table B.2: Median properties of all E+A galaxies and young E+As (with H δ EW>7 Å). Errors are quoted using 75 and 25 percentile.

Parameter	E+As with H δ EW>7 Å	All E+As
H δ EW (Å)	7.67 ^{+0.40} _{-0.34}	5.94 ^{+0.92} _{-0.48}
$u - g$	1.35 ^{+0.28} _{-0.15}	1.37 ^{+0.09} _{-0.07}
$u - r$	2.45 ^{+0.27} _{-0.12}	2.43 ^{+0.27} _{-0.19}
$g - r$	0.57 ^{+0.05} _{-0.04}	0.59 ^{+0.07} _{-0.04}
$r - i$	0.26 ^{+0.08} _{-0.12}	0.25 ^{+0.07} _{-0.05}
D4000	1.41 ^{+0.13} _{-0.04}	1.48 ^{+0.11} _{-0.09}
[OII] EW (Å)	-0.01 ^{+0.72} _{-0.41}	-0.11 ^{+0.92} _{-0.79}
H α EW (Å)	-1.75 ^{+1.10} _{-0.35}	-1.61 ^{+0.46} _{-0.34}
Local Galaxy Density (Mpc $^{-2}$)	0.05 ^{+0.32} _{-0.04}	0.08 ^{+0.23} _{-0.06}
C_{in}	0.36 ^{+0.02} _{-0.02}	0.35 ^{+0.01} _{-0.02}
M_{r^*}	-22.23 ^{+0.85} _{-0.64}	-21.70 ^{+0.45} _{-0.65}

Table B.3: Number of accompanying galaxies around all the E+A galaxies and young E+A galaxies (with $H\delta$ EW>7) are compared with that of 1000 randomly picked galaxies with similar redshift distribution. Numbers of accompanying galaxies are counted using galaxies with $-23.0 < Mr^* < -19.5$ after k -correction within the radius of 50 and 75 kpc. Fore/backgournd galaxy number counts are statistically subtracted.

Sample	$N_{nearby\ galaxy}$ within 50 kpc	$N_{nearby\ galaxy}$ within 75 kpc
Random	0.03 ± 0.01	0.16 ± 0.01
All E+As	0.12 ± 0.03	0.26 ± 0.04
E+A with $H\delta$ EW>7 Å	0.24 ± 0.09	0.40 ± 0.12

List of Figures

1.1	Hubble's tuning fork diagram.	12
1.2	Blue galaxy fraction vs. redshift. Filled circles, compact clusters ($C \geq 0.40$); open circles, irregular clusters.	13
1.3	The S0/E fraction for clusters in the sample as a function of redshift. The open circles are the same as in Figure 1.2.	13
2.1	The Apache Point Observatory in New Mexico, U.S.A.	19
2.2	The SDSS 2.5-meter telescope located at Apache Point Observatory	20
2.3	The imaging camera of the SDSS. The five broadband filters are aligned in an order of <i>riuzg</i>	21
2.4	The SDSS photometric system response as a function of wavelength. The upper curves is without absorption features.	22
2.5	A galaxy cluster Abell 168, observed with the SDSS imaging camera.	23
2.6	A bright spiral galaxy M101, observed with the SDSS imaging camera.	24
2.7	A globular cluster M2, observed with the SDSS imaging camera.	25
2.8	The location of the survey imaging strips plotted in a polar projection for the North (left) and South (right).	26
2.9	Astrophysicist Rich Kron, of the University of Chicago and Fermilab, inserts optical fibers into the fiber-fed spectrograph.	27
2.10	The fiber-fed spectrograph is being installed to the SDSS telescope.	28
2.11	A cone diagram; redshift distribution of galaxies observed with the SDSS spectrograph. The edges of the cone are defined by the radial velocity of the galaxies.	29
3.1	$r - i$ color-magnitude diagram of A168. $r - i$ color is plotted against r magnitude for confirmed member galaxies.	50
3.2	$g - r$ color-magnitude diagram. $g - r$ color cut bins are superimposed on the color-magnitude relation.	50
3.3	$r - i$ color-magnitude diagram. $r - i$ color cut bins are superimposed on the color-magnitude relation.	50
3.4	Same as Figure 3.2, but for $i - z$	51
3.5	$g - r - i$ color-color boxes to find galaxy clusters. The abscissa is the $g - r$ color. The ordinate is the $r - i$ color.	52
3.6	An example of color-cut capturing color-magnitude relation. Galaxies within $1.5 h^{-1}\text{Mpc}$ aperture radius are plotted.	53
3.7	An example of color-cut capturing color-magnitude relation. Galaxies within $1.5 h^{-1}\text{Mpc}$ aperture radius are plotted.	53
3.8	The distribution of galaxies brighter than $r^*=20.0$ around RXJ0256.5+0006. The upper left panel shows the distribution of galaxies brighter than $r^*=20.0$. The upper right panel shows the distribution of galaxies brighter than $r^*=21.5$	54
3.9	Color-color diagram of spectroscopically confirmed member galaxies of A168. The abscissa is $g - r$ color. The ordinate is $r - i$ color.	55
3.10	Color-color diagram of spectroscopically confirmed member galaxies of A168. The abscissa is $r - i$ color. The ordinate is $i - z$ color.	55
3.11	$r - i - z$ color-color boxes to find galaxy clusters. The abscissa is $r - i$ color. The ordinate is $i - z$ color.	56
3.12	The distribution of galaxies brighter than $r^*=21.5$. The upper left panel shows the distribution of galaxies brighter than $r^*=21.5$. The upper right panel shows the distribution of galaxies brighter than $r^*=20.0$	56
3.13	Evaluation of high- z color cut. The filled triangles show the color prediction for elliptical galaxies. The open triangles show the color prediction for spiral galaxies.	57
3.14	The redshift estimation accuracy. The estimated redshifts are plotted against spectroscopic redshifts.	58
3.15	The number of galaxies fed (N_{gal}) v.s. CE richness. The number of galaxies inputted into an analysis as a function of richness.	59

3.16	Recovery rate in Monte Carlo simulation with the real SDSS background. Recovery rate is plotted against the richness of the cluster.
3.17	Positional accuracy with the real SDSS background. The positional accuracy is almost constant.
3.18	Recovery rate in Monte Carlo simulation with the shuffled background. The artificial clusters are randomly distributed.
3.19	Positional accuracy with the shuffled background. The positional accuracy is almost independent of the richness of the cluster.
3.20	False positive tests. Detection tests are performed using 23.75 deg^2 of the SDSS commissioning field.
3.21	False positive tests. Detection tests are performed using 23.75 deg^2 of the SDSS commissioning field.
3.22	A successful detection with the CE method. The image is $6' \times 13'$ true color image of the SDSS cluster.
3.23	A successful detection with the CE method. The image is $6' \times 13'$ true color image of the SDSS cluster.
3.24	Comparison of four catalogs by richness. The abscissa is the richness of the cluster. The ordinate is the fraction of clusters detected.
3.25	Comparison of four catalogs by redshift. The abscissa is the redshift of the clusters. The ordinate is the fraction of clusters detected.
3.26	Comparison of the MF with the CE. The abscissa is the estimated redshift. The ordinate is the fraction of clusters detected.
3.27	Comparison of the CE with the MF. The abscissa is the estimated redshift. The ordinate is the fraction of clusters detected.
3.28	Elongation distribution of the detected clusters. The number of the clusters is plotted against elongation.
3.29	Comparison of the maxBCG clusters with the CE catalog. The abscissa is the color estimated by the CE method.
3.30	Comparison of the CE method with the maxBCG method. The abscissa is the estimated redshift.
3.31	Comparison of the CE method with the VTT method. The abscissa is the estimated redshift.
3.32	Comparison of the VTT method with the CE method. The abscissa is the estimated redshift.
4.1	Composite LF of 204 galaxy clusters from the SDSS CE galaxy cluster catalog in five SDSS bands.
4.2	Composite luminosity functions of de Vaucouleur galaxies and exponential galaxies. The galaxies are selected by their concentration index.
4.3	Composite luminosity functions of high-concentration and low-concentration galaxies. The concentration index is measured by the Petrosian radius.
4.4	Composite luminosity functions of $u - r < 2.2$ (late-type) and $u - r \geq 2.2$ (early-type) galaxies.
4.5	Results of a Monte-Carlo simulation to test the robustness of the weighting scheme. The histograms show the distribution of the estimated redshift.
5.1	Photometric and morphological Butcher-Oemler effect from the 514 SDSS Cut & Enhance clusters.
5.2	Normalized distributions of late type fractions (f_b , f_{Cin} , f_{exp} and f_{u-r}). The dashed lines show the best-fit lines.
5.3	Richness distribution as a function of redshift. Richesses are measured as the number of galaxies.
5.4	The difference of the late type fractions from the best-fit lines as a function of redshift are plotted.
5.5	The difference of late type fractions from the best-fit lines as a function of redshift are plotted.
5.6	The distribution of Cin , the inverse of the concentration index defined as the ratio of Petrosian radii.
5.7	The dependence of f_{Cin} on seeing. The open squares and the solid lines show the distribution and the best-fit line.
5.8	The seeing distribution of all galaxies brighter than $r=21.5$. 87% of all galaxies have seeing better than 1.5 arcseconds.
5.9	The dependence of f_{exp} on seeing. The open squares and the solid lines show the distribution and the best-fit line.
5.10	Various systematic tests. The solid lines show distributions for 2.1-2.21 Mpc annular fore/back.
5.11	Comparison of the late-type fraction from imaging with that from spectroscopy. Late-type fraction is measured by the concentration index.
5.12	Distribution of varying radius to measure blue/spiral fractions. It has a peak at 0.7 Mpc.
5.13	The same as Figure 5.1, but measured with varying radius. 138
5.14	The same as Figure 5.4, but measured with varying radius. 139
5.15	The same as Figure 5.5, but measured with varying radius. 140

- A.6 In the left panel, we present the comparison of our [OII] EW measurements (flux summing) and
- A.7 In the left panel, we present the comparison of our H α EW measurements (flux summing) and
- A.8 The amount of emission filling correction of H δ EW. The solid line is for the iteration method
- A.9 The absolute difference in the measured H δ EW (\AA) for duplicate observations of 11538 SDSS
- A.10 The absolute difference in the [OII] EW (\AA) for duplicate observations of 11538 SDSS galaxies
- A.11 The absolute difference in the H α EW (\AA) for duplicate observations of 11538 SDSS galaxies a
- A.12 We present the distribution of differences for the H δ line from our duplicate observations. The
- A.13 The distribution of differences for the [OII] line from our duplicate observations. The four pane
- A.14 The distribution of differences for the H α line from our duplicate observations. The four panel
- A.15 The fraction of HDS galaxies as a function signal-to-noise ratio in the g band. The error bars
- A.16 Five examples of spectra for the “true E+A” subsample of HDS galaxies discussed in Section A
- A.17 Five example spectra of our HDS galaxies that possess detected [OII] and H α emission lines. T
- A.18 Five example spectra of our HDS galaxies that possess detected [OII] emission lines, but no de
- B.1 [OII] EWs are plotted against H δ EWs for four sub-samples of H δ -strong galaxies. The contours
- B.2 H α EWs are plotted against H δ EWs for four sub-samples of H δ -strong galaxies. The contours
- B.3 Star formation rate estimated using H α flux for each class of galaxies. The solid line is for all 9
- B.4 Luminosity functions in r band for each subclass of H δ -strong galaxies. The solid line is for all
- B.5 Distributions of each subclass of galaxies in C_{in} v.s. $u - r$ plane. The contours show the distri
- B.6 Distribution of local galaxy density. The solid, dashed and dotted lines show distributions for a
- B.7 H δ EW is plotted against local galaxy density. Negative EWs are absorption lines. The solid li
- B.8 Distributions of local galaxy density for each subsample of H δ -strong galaxies and all 94770 gal
- B.9 Ratio of each subclass of H δ -strong galaxies to all galaxies as a function of local galaxy density
- B.10 H δ EWs are plotted against time (age) for three star formation histories with the GISSEL mod
- B.11 Restframe $g - r$ color is plotted against $r - i$ color. The dashed, solid and dotted lines show the
- B.12 $J - K$ is plotted against $r - K$. All magnitudes are in restframe AB system. The contours show
- B.13 Radio SFR calculated using the FIRST data is plotted against redshift. The contours show the
- B.14 H δ EWs are plotted against D4000 for the models with $Z=0.0001(0.5\% \text{ solar}), 0.02(\text{solar})$ and
- B.15 The $u - g$ color is plotted against H δ EWs for three metallicity models and three star formation
- B.16 Nine example spectra of young E+A galaxies (E+As with H δ EW $> 7 \text{ \AA}$). Spectra are shifted to
- B.17 Nine example images of young E+A galaxies (E+As with H δ EW $> 7 \text{ \AA}$). Image size is $60'' \times 60''$
- B.18 Absolute magnitude distribution of accompanying galaxies within 75 kpc of young E+A galaxies

List of Tables

3.1	Tilt and scatter of color-magnitude relation of A1577.	80
3.2	The fraction of galaxies in the color-cut both for galaxies inside of the RXJ0256.5+0006 ($z = 0.15 < z < 0.3$)	
3.3	Sigma cut test. Sigma is a threshold when detecting clusters in the enhanced density map. The test is performed using a 23.75 deg^2 region in the data. A number of clusters detected with the MF, the maxBCG and the VTT to the CE cluster detection method	
3.4	Test of fluxmax cut. The test is performed using a 23.75 deg^2 region in the data. A number of clusters detected with the MF, the maxBCG and the VTT to the CE cluster detection method	
3.5	10 false detections of the CE method. The region examined is RA between 16 and 25.5 deg, Dec between -10° and 10°	
3.6	Ratio of number of clusters detected with the MF, the maxBCG and the VTT to the CE cluster detection method	
3.7	The comparison of the detected clusters with the methods other than the Cut & Enhance method	
4.1	Best-fit Schechter parameters of the composite luminosity function of five SDSS bands. The field sample	
4.2	Best-fit Schechter parameters for de Vaucouleur and exponential galaxies in five SDSS bands. The field sample	
4.3	Best-fit Schechter parameters for low concentration (early-type) and high concentration (late-type) galaxies	
4.4	Best-fit Schechter parameters for $u - r > 2.2$ (early type) and $u - r \leq 2.2$ (late type) galaxies	
4.5	Best-fit Schechter parameters for galaxies using positions of brightest cluster galaxies as a central point	
4.6	Best-fit Schechter parameters for galaxies using global background subtraction in five SDSS bands	
4.7	Best-fit Schechter parameters in the r band for galaxies using richer systems. The best-fit Schechter parameters	
4.8	Comparison with previous studies on the composite luminosity function. The CE composite LF	
5.1	Spearman's correlation coefficients between z and fractions of late type galaxies. 514 clusters with $z < 0.3$	
5.2	Significances in Kolmogorov-Smirnov tests between distributions for $z \leq 0.15$ and $0.15 < z < 0.3$	
5.3	Scatters in late-type fractions around the best-fit line are compared with median errors of late-type fractions	
5.4	Change in the fraction of galaxies with $C_{in} > 0.4$ (late type) in two different filters(g, r). 142	
5.5	Change in the fraction of galaxies with exponential fit likelihood greater than de Vaucouleur likelihood	
6.1	Completeness and contamination rate of our four sample of galaxies classified by T_{auto} are calculated	
6.2	MORPHS cluster sample	175
7.1	Wavelength ranges used to measure the equivalent widths of [OII], H α and H δ lines. 202	
A.1	The wavelength ranges used to measure our H δ , [OII] and H α EWs.	250
A.2	Coefficients of third order polynomial fits to the error distributions shown in Figures A.9, A.10 and A.11	250
A.3	The frequency of finding HDS galaxies.	250
A.4	A comparison of our HDS sample of galaxies to previous work in the literature. 251	

- B.1 Number of galaxies in each subsample of H δ -strong galaxies. Galaxies with the line ratios cons
- B.2 Median properties of all E+A galaxies and young E+As (with H δ EW>7 Å). Errors are quoted
- B.3 Number of accompanying galaxies around all the E+A galaxies and young E+A galaxies (with

Bibliography

- [1] Abadi, M. G., Moore, B., & Bower, R. G. 1999, MNRAS, 308, 947
- [2] Abazajian K. et al. 2003 submitted to AJ
- [3] Abell, G. 1958, APJS, 3, 211
- [4] Abell, G., Corwin, H. & Olowin, R. 1989, APJS, 70, 1
- [5] Abraham, R. G., Valdes, F., Yee, H. K. C., & van den Bergh, S. 1994, ApJ, 432, 75
- [6] Abraham, R. G., van den Bergh, S., Glazebrook, K., Ellis, R. S., Santiago, B. X., Surma, P., & Griffiths, R. E. 1996a, ApJS, 107, 1
- [7] Abraham, R. G. et al. 1996b, ApJ, 471, 694
- [8] Abraham, R. G. & van den Bergh, S. 2001, Science, 293, 1273
- [9] Adami, C., Ulmer, M. P., Durret, F., Nichol, R. C., Mazure, A., Holden, B. P., Romer, A. K., & Savine, C. 2000, AA, 353, 930
- [10] Allen, S. W. & Fabian, A. C. 1998, MNRAS, 297, L57
- [11] Allington-Smith, J. R., Ellis, R., Zirbel, E. L., & Oemler, A. J. 1993, ApJ, 404, 521
- [12] Andreon, S., Davoust, E., & Heim, T. 1997, A&A, 323, 337
- [13] Andreon, S. 1998, ApJ, 501, 533
- [14] Andreon, S. & Ettori, S. 1999, ApJ, 516, 647
- [15] Annis, J. et al. 2003 *in preparation*
- [16] Aragon-Salamanca, A., Ellis, R. S., Couch, W. J., & Carter, D. 1993, MNRAS, 262, 764

- [17] Arnaud, M. & Evrard, A. E. 1999, MNRAS, 305, 631
- [18] Athanassoula, E., Gario, A., & García Gómez, C. 2001, MNRAS, 321, 353
- [19] Bahcall, N. A. 1974, ApJ, 193, 529
- [20] Bahcall, N. A. 1977, ApJL, 218, L93
- [21] Bahcall, N. 1988, ARAA, 26, 631
- [22] Bahcall, N., Fan, X. & Cen, R. 1997, ApJL, 485, 53
- [23] Bahcall, N. et al. 2003, *in preparation*
- [24] Balogh, M. L., Morris, S. L., Yee, H. K. C., Carlberg, R. G., & Ellingson, E. 1997, ApJL, 488, L75
- [25] Balogh, M. L., Schade, D., Morris, S. L., Yee, H. K. C., Carlberg, R. G., & Ellingson, E. 1998, ApJL, 504, L75
- [26] Balogh, M. L., Morris, S. L., Yee, H. K. C., Carlberg, R. G., & Ellingson, E. 1999, ApJ, 527, 54
- [27] Balogh, M. L., Navarro, J. F., & Morris, S. L. 2000, ApJ, 540, 113
- [28] Balogh, M. L., Christlein, D., Zabludoff, A. I., & Zaritsky, D. 2001, ApJ, 557, 117
- [29] Balogh, M., Bower, R. G., Smail, I., Ziegler, B. L., Davies, R. L., Gaztelu, A., & Fritz, A. 2002, MNRAS, 337, 256
- [30] Balogh, M. L., Couch, W. J., Smail, I., Bower, R. G., & Glazebrook, K. 2002, MNRAS, 335, 10
- [31] Barger A. J., Aragon-Salamanca A., Ellis R. S., Couch W. J., Smail I., Sharples R. M., 1996, MNRAS, 279, 1
- [32] Bartholomew L. J., Rose J. A., Gaba A. E., Caldwell N., 2001, AJ, 122, 2913
- [33] Becker R. H., White R. L., Helfand D. J., 1995, ApJ, 450, 559
- [34] Bekki, K. 1998, ApJL, 502, L133
- [35] Bekki, K., Shioya, Y., & Couch, W. J. 2001, ApJL, 547, L17
- [36] Bekki, K., Couch, W. J., & Shioya, Y. 2002, ApJ, 577, 651
- [37] Belloni P., Bruzual A. G., Thimm G. J., Roser H.-J., 1995, A&A, 297, 61

- [38] Benitez, N., Broadhurst, T., Rosati, P., Courbin, F., Squires, G., Lidman, C., Magain, P. 1999, *ApJ*, 527, 31
- [39] Benson, A. J., Frenk, C. S., Baugh, C. M., Cole, S., & Lacey, C. G. 2001, *MNRAS*, 327, 1041
- [40] Bertin, E.& Arnouts, S. 1996, *A&AS*, 117, 393
- [41] Bertin, G. & Romeo, A. B. 1988, *A&A*, 195, 105
- [42] Binggeli, B., Sandage, A., & Tamman, G. A. 1988, *ARAA*, 26, 509
- [43] Binney, J., & Tremaine, S. 1987, *Galactic Dynamics* (Princeton: Princeton Univ. Press)
- [44] Binney, J., Tremaine, S. 1987, *Natur*, 326, 219
- [45] Blanton, M. R., Dalcanton, J., Eisenstein, D., Loveday, J., Strauss, M. A., SubbaRao, M., Weinberg, D. H., Anderson, J. E., et al. 2001, *AJ*, 121, 2358
- [46] Blanton, M. R., Lin, H., Lupton, R. H., Maley, F. M., Young, N., Zehavi, I., & Loveday, J. 2003, *AJ*, 125, 2276
- [47] Blanton M. R., Brinkmann J., Csabai I., et al., 2003a, *AJ*, 125, 2348
- [48] Bode, P. W., Berrington, R. C., Cohn, H. N., & Lugger, P. M. 1994, *ApJ*, 433, 479
- [49] Bode, P., Bahcall, N.A., Ford, E.B., Ostriker, J.P. 2001, *ApJ*, 551, 15
- [50] Bothun, G. D. & Sullivan, W. T. 1980, *ApJ*, 242, 903
- [51] Bothun, G. D. & Dressler, A. 1986, *ApJ*, 301, 57
- [52] Bower, R.G., Luecy, J.R. & Ellis, R.S. 1992, *MNRAS* 254, 601
- [53] Bower, R. G., Lucey, J. R., & Ellis, R. S. 1992, *MNRAS*, 254, 589
- [54] Bower, R. G., Bohringer, H., Briel, U. G., Ellis, R. S., Castander, F. J., & Couch, W. J. 1994, *MNRAS*, 268, 345
- [55] Boyce, P. J., Phillipps, S., Jones, J. B., Driver, S. P., Smith, R. M., & Couch, W. J. 2001, *MNRAS*, 328, 277.
- [56] Bramel, D.A., Nichol, R.C., Pope, A.C. 2000, *ApJ*, 533, 601

- [57] Bravo-Alfaro, H., Cayatte, V., van Gorkom, J. H., & Balkowski, C. 2000, AJ, 119, 580
- [58] Bravo-Alfaro, H., Cayatte, V., van Gorkom, J. H., & Balkowski, C. 2001, A&A, 379, 347
- [59] Broadhurst, T. J., Ellis, R. S., & Shanks, T. 1988, MNRAS, 235, 827
- [60] Bruzual A., G. 1983, ApJ, 273, 105
- [61] Bruzual A., G. & Charlot, S. 1993, ApJ, 405, 538
- [62] Bureau, M. & Carignan, C. 2002, AJ, 123, 1316
- [63] Butcher H., Oemler A., 1978, ApJ, 226, 559
- [64] Butcher, H., Oemler, A.Jr. 1978, ApJ, 219, 18
- [65] Butcher, H., Oemler, A.Jr. 1984, ApJ, 285, 426
- [66] Byrd, G. & Valtonen, M. 1990, ApJ, 350, 89
- [67] Caldwell N., Rose J. A., Sharples R. M., Ellis R. S., Bower R. G., 1993, AJ, 106, 473
- [68] Caldwell N., Rose J. A., Franx M., Leonardi A. J., 1996, AJ, 111, 78
- [69] Caldwell N., Rose J. A., 1997, AJ, 113, 492
- [70] Calzetti D., Kinney A. L., Storchi-Bergmann T., 1994, ApJ, 429, 582
- [71] Carlberg, R.G., Yee, H.K.C., Ellingson, E., Abraham, R., Gravel, P., Morris, S., Pritchett, C.J. 1996, ApJ, 464, 63
- [72] Carter, D., Prieur, J. L., Wilkinson, A., Sparks, W. B., & Malin, D. F. 1988, MNRAS, 235, 813
- [73] Castander, F. J. et al. 2001, AJ, 121, 2331
- [74] Cavaliere, A., Menci, N., & Tozzi, P. 1997, ApJL, 484, L21
- [75] Cayatte, V., van Gorkom, J. H., Balkowski, C., & Kotanyi, C. 1990, AJ, 100, 604
- [76] Cayatte, V., Kotanyi, C., Balkowski, C., & van Gorkom, J. H. 1994, AJ, 107, 1003

- [77] Chang T., van Gorkom J. H., Zabludoff A. I., Zaritsky D., Mihos J. C., 2001, AJ, 121, 1965
- [78] Charlot, S. & Fall, S. M. 2000, ApJ, 539, 718
- [79] Charlot S., Longhetti M., 2001, MNRAS, 323, 887
- [80] Charlot, S. et al. submitted to MNRAS
- [81] Clowe, D., Trentham, N., Tonry, J. 2000, astro-ph/0001309
- [82] Cole, S., Lacey, C. G., Baugh, C. M., & Frenk, C. S. 2000, MNRAS, 319, 168
- [83] Colless, M. 1989, MNRAS, 237, 799
- [84] Condon J. J., 1992, ARA&A, 30, 575
- [85] Couch, W. J. & Sharples, R. M. 1987, MNRAS, 229, 423
- [86] Couch, W. J., Ellis, R. S., Sharples, R. M., & Smail, I. 1994, ApJ, 430, 121
- [87] Couch, W. J., Barger, A. J., Smail, I., Ellis, R. S., & Sharples, R. M. 1998, ApJ, 497, 188
- [88] Couch, W. J., Balogh, M. L., Bower, R. G., Smail, I., Glazebrook, K., & Taylor, M. 2001, ApJ, 549, 820
- [89] Cowie, L. L. & Songaila, A. 1977, Nature, 266, 501
- [90] Cowie, L. L., Songaila, A., & Barger, A. J. 1999, AJ, 118, 603
- [91] da Costa, L., Arnouts, S., Bardelli, S., Benoist, C., Biviano, A., Borgani, S., Boschin, W., Erben, T. et al. 2000, astro-ph/0012254
- [92] David, L. P., Slyz, A., Jones, C., Forman, W., Vrtilek, S. D., & Arnaud, K. A. 1993, ApJ, 412, 479
- [93] Diaferio, A., Kauffmann, G., Balogh, M.L., White, S.D.M., Schade, D. & Ellingson, E. 2001, MNRAS, 323, 999.
- [94] Dickinson, M. 1996, The Universe at High-z, Large-Scale Structure and the Cosmic Microwave Background. Proceedings of an Advanced Summer School Held at Laredo, Cantabria, Spain, 4-8 September 1995. Edited by E. Martinez-Gonzalez and J. L. Sanz. Springer-Verlag Berlin Heidelberg New York. Also Lecture Notes in Physics, volume 470, 1996, p.3, 3

- [95] Doi, M., Fukugita, M., & Okamura, S. 1993, MNRAS, 264, 832
- [96] Domínguez, M. J., Zandivarez, A. A., Martínez, H. J., Merchán, M. E., Muriel, H., & Lambas, D. G. 2002, MNRAS, 335, 825
- [97] Domínguez, M., Muriel, H. ;, & Lambas, D. G. 2001, AJ, 121, 1266
- [98] Dressler, A. 1980, ApJ, 236, 351
- [99] Dressler A., Gunn J. E., 1983, ApJ, 270, 7
- [100] Dressler, A. 1984, ARAA, 22, 185
- [101] Dressler, A., Thompson, I. B., & Shectman, S. A. 1985, ApJ, 288, 481
- [102] Dressler, A. 1987, in Nearly Normal Galaxies, Springer-Verlag, p.276
- [103] Dressler, A. & Gunn, J.E. 1992, ApJS, 78, 1
- [104] Dressler, A., Oemler, A. J., Butcher, H. R., Gunn, J. E., 1994, ApJ, 430, 107
- [105] Dressler, A., Oemler, A.J., Couch, W.J., Smail, I., Ellis, R.S., Barger, A., Butcher, H., Poggianti, B.M. et al. 1997 ApJ, 490, 577
- [106] Dressler, A., Smail, I., Poggianti, B. M., Butcher, H., Couch, W. J., Ellis, R. S., & Oemler, A. J. 1999, ApJs, 122, 51
- [107] Driver, S. P., Couch, W. J., & Phillipps, S. 1998, MNRAS, 301, 369
- [108] Duc P.-A., Poggianti B. M., Fadda D., et al., 2002, A&A, 382, 60
- [109] Edge, A. C. & Stewart, G. C. 1991, MNRAS, 252, 414
- [110] Eisenstein, D. J. et al. 2001, AJ, 122, 2267
- [111] Eke, V.R.; Cole, S., Frenk, C.S. 1996, MNRAS, 282, 263
- [112] Ellingson, E., Lin, H., Yee, H. K. C., & Carlberg, R. G. 2001, ApJ, 547, 609
- [113] Ellis, R. S., Smail, I., Dressler, A., Couch, W. J., Oemler, A. J., Butcher, H., & Sharples, R. M. 1997, ApJ, 483, 582
- [114] Elmegreen, D. M., Elmegreen, B. G., Frogel, J. A., Eskridge, P. B., Pogge, R. W., Gallagher, A., & Iams, J. 2002, AJ, 124, 777
- [115] Evrard, A. E. 1991, MNRAS, 248, 8P
- [116] Evrard, A. E. et al. 2002, ApJ, 573, 7

- [117] Fabricant D. G., McClintock J. E., Bautz M. W., 1991, ApJ, 381, 33
- [118] Fabricant, D., Franx, M., & van Dokkum, P. 2000, ApJ, 539, 577
- [119] Fairley, B. W., Jones, L. R., Wake, D. A., Collins, C. A., Burke, D. J., Nichol, R. C., & Romer, A. K. 2002, MNRAS, 330, 755
- [120] Fan, X. 1999, AJ, 117, 2528
- [121] Farouki R., Shapiro S. L., 1980, ApJ, 241, 928
- [122] Fasano, G., Poggianti, B. M., Couch, W. J., Bettoni, D., Kjærgaard, P., & Moles, M. 2000, ApJ, 542, 673
- [123] Finoguenov, A., Briel, U.G., Henry, J.P., 2003, submitted to A&A
- [124] Fioc, M., & Rocca-Volmerange, B. 1997, A&A, 326, 950
- [125] Fisher D., Fabricant D., Franx M., van Dokkum P., 1998, ApJ, 498, 195
- [126] Franx M., 1993, ApJ, 407, L5
- [127] Frieman et al. 2003, in prep.
- [128] Fujita, Y. 1998, ApJ, 509, 587
- [129] Fujita, Y. & Nagashima, M. 1999, ApJ, 516, 619
- [130] Fujita, Y. 2001, ApJ, 550, 612
- [131] Fujita Y., Takizawa M., Nagashima M., Enoki M., 1999b, PASJ, 51, L1
- [132] Fujita Y. 2003, submitted to ApJ
- [133] Fukugita, M., Shimasaku, K., Ichikawa, T. 1995, PASP, 107, 945
- [134] Fukugita, M., Ichikawa, T., Gunn, J. E., Doi, M., Shimasaku, K., & Schneider, D. P. 1996, AJ, 111, 1748.
- [135] Fukugita, M., Ichikawa, T., Gunn, J. E., Doi, M., Shimasaku, K., Schneider, D.P. 1996, AJ, 111, 1748
- [136] Gal, R. R., de Carvalho, R. R., Brunner, R., Odewahn, S. C., & Djorgovski, S. G. 2000, AJ, 120, 540
- [137] Galaz G., 2000, AJ, 119, 2118
- [138] Garilli, B., Maccagni, D., Andreon, S. 1999, A&A, 342, 408

- [139] Girardi, M., Giuricin, G., Mardirossian, F., Mezzetti, M., & Boschin, W. 1998, ApJ, 505, 74
- [140] Gisler, G. R. 1978, MNRAS, 183, 633
- [141] Gladders, M.D., & Yee, H.K.C. 2000, AJ, 120, 2148
- [142] Glazebrook, K., Ellis, R., Santiago, B., & Griffiths, R. 1995, MNRAS, 275, L19
- [143] Gómez, P. L. et al. 2003, ApJ, 584, 210
- [144] Goto, T., Sekiguchi, M., Nichol, R. C., Bahcall, N. A., Kim, R. S. J., Annis, J., Ivezić, Željko, Brinkmann, J., et al. 2002a, AJ, 123, 1807
- [145] Goto, T. et al. 2002b, PASJ, 54, 515
- [146] Goto, T. et al. 2003a, PASJ, 55, 739
- [147] Goto, T. et al. 2003b, PASJ, 55, 771
- [148] Goto, T. et al. 2003c, in prep.
- [149] Goto, T. et al. 2003d, PASJ, 55, 757
- [150] Gunn, J. E. & Gott, J. R. I. 1972, ApJ, 176, 1
- [151] Gunn, J.E., Hoessel, J.G., & Oke, J.B. 1986, ApJ, 306, 30.
- [152] Gunn, J.E., Carr, M., Rockosi, C., Sekiguchi, M., Berry, K., Elms, B., de Haas, E., Ivezić , Z. et al. 1998, AJ, 116, 3040
- [153] Hammer, F., Flores, H., Lilly, S. J., Crampton, D., Le Fevre, O., Rola, C., Mallen-Ornelas, G., Schade, D., & Tresse, L. 1997, ApJ, 481, 49
- [154] Hashimoto, Y. & Oemler, A. J. 1999, ApJ, 510, 609
- [155] Hattori, M., Ikebe, Y., Asaoka, I., Takeshima, T., Bohringer, H., Mihara, T., Neumann, D.M., Schindler, S. 1997, Nature, 388, 146
- [156] Hausman, M. A., & Ostriker, J. P. 1978, ApJ, 224, 320
- [157] Haynes, M. P. & Giovanelli, R. 1986, ApJ, 306, 466
- [158] Heavens, A. F. 1993, MNRAS, 263, 735
- [159] Helsdon, S. F. & Ponman, T. J. 2003, MNRAS, 339, L29
- [160] Henry, J. P. & Arnaud, K. A. 1991, ApJ, 372, 410

- [161] Henry, J.P. , 1997, ApJ, 489, 1
- [162] Henry, J.P., 2000, ApJ, 534, 565
- [163] Heydon-Dumbleton, N. H., Collins, C. A., & MacGillivray, H. T. 1989, MNRAS, 238, 379
- [164] Hogg, D. W., Finkbeiner, D. P., Schlegel, D. J., & Gunn, J. E. 2001, AJ, 122, 2129
- [165] Hopkins, A. et al. 2003, in prep.
- [166] Huchra, J., Davis, M., & Latham, D. 1983, Cambridge: Smithsonian Center for Astrophysics, 1983
- [167] Ichikawa, S. 1986, Ann. Tokyo Astron. Obs., 21, 77
- [168] Icke, V. 1985, A&A, 144, 115
- [169] Jarrett, T. H., Chester, T., Cutri, R., Schneider, S., Skrutskie, M., & Huchra, J. P. 2000, AJ, 119, 2498
- [170] Jenkins, A., Frenk, C.S., White, S.D.M., Colberg, J.M., Cole, S., Evrard, A.E., Couchman, H.M.P., Yoshida, N., 2001, MNRAS, 321, 372
- [171] Jones, C. & Forman, W. 1978, ApJ, 224, 1
- [172] Jones, C. & Forman, W. 1999, ApJ, 511, 65
- [173] Katgert, P., Mazure, A., den Hartog, R., Adami, C., Biviano, A., Perea, J. 1998, A&AS, 129, 399
- [174] Kauffmann, G. 1995, MNRAS, 274, 153
- [175] Kauffmann G., Heckman T. M., White S. D. M., et al., 2003a, MNRAS, 341, 54
- [176] Kauffmann G., Heckman T. M., White S. D. M., et al., 2003b, MNRAS, 341, 33
- [177] Kawasaki, W., Shimasaku, K., Doi, M., Okamura, S. 1998, ApJ, 500, 173
- [178] Keel, W. C. 1983, ApJ, 269, 466
- [179] Kennicutt, R. C., Roettiger, K. A., Keel, W. C., van der Hulst, J. M., & Hummel, E. 1987, AJ, 93, 1011
- [180] Kennicutt, R. C. 1989, ApJ, 344, 685

- [181] Kennicutt R. C., 1992a, ApJS, 79, 255
- [182] Kennicutt R. C., 1992b, ApJ, 388, 310
- [183] Kennicutt R. C., 1998, ARA&A, 36, 189
- [184] Kennicutt, R. C. 1998, ApJ, 498, 541
- [185] Kent, S. M. 1981, ApJ, 245, 805
- [186] Kepner, J., Fan, X., Bahcall, N., Gunn, J., Lupton, R., Xu, G. 1999, ApJ, 517, 78
- [187] Kewley, L. J., Dopita, M. A., Sutherland, R. S., Heisler, C. A., & Trevena, J. 2001, ApJ, 556, 121
- [188] Kim, R. S. J. et al. 2002, AJ, 123, 20
- [189] King, I.R. 1966, AJ, 71, 64
- [190] Kodama, T., Arimoto, N., Barger, A.J., Arag'on-Salamanca, A. 1998, A&A, 334, 99
- [191] Kodama, T., Smail, I., Nakata, F., Okamura, S., & Bower, R. G. 2001, ApJ, 562, L9
- [192] Kodama, T. & Bower, R. G. 2001, MNRAS, 321, 18
- [193] Kodama, T. & Smail, I. 2001, MNRAS, 326, 637
- [194] Lahav, O. et al. 1995, Science, 267, 859
- [195] Larson, R. B., Tinsley, B. M., & Caldwell, C. N. 1980, ApJ, 237, 692
- [196] Lavery, R. J. & Henry, J. P. 1986, ApJL, 304, L5
- [197] Lavery, R. J. & Henry, J. P. 1988, ApJ, 330, 596
- [198] Lavery R. J., Pierce M. J., McClure R. D., 1992, AJ, 104, 2067
- [199] Lavery R. J., Henry J. P., 1994, ApJ, 426, 524
- [200] Lea, S. M. & Henry, J. P. 1988, ApJ, 332, 81
- [201] Lewis, I. et al. 2002, MNRAS, 334, 673
- [202] Lilly, S. J., Le Fevre, O., Hammer, F., & Crampton, D. 1996, ApJL, 460, L1

- [203] Lilly, S., Schade, D., Ellis, R., Le Fevre, O., Brinchmann, J., Tresse, L., Abraham, R., Hammer, F., et al. 1998, ApJ, 500, 75
- [204] Lin, H., Yee, H. K. C., Carlberg, R. G., Morris, S. L., Sawicki, M., Patton, D. R., Wirth, G., & Shepherd, C. W. 1999, ApJ, 518, 533
- [205] Liu C. T., Kennicutt R. C., 1995a, ApJS, 100, 325
- [206] Liu C. T., Kennicutt R. C., 1995b, ApJ, 450, 547
- [207] Lobo, C., Iovino, A., Lazzati, D., Chincarini, G. 2000, A&A, 360, 896
- [208] Lonsdale, C. J., Persson, S. E., & Matthews, K. 1984, ApJ, 287, 95
- [209] Loveday, J., Peterson, B. A., Efstathiou, G., & Maddox, S. J. 1992, ApJ, 390, 338
- [210] Lubin, L. M., Postman, M., Oke, J. B., Ratnatunga, K. U., Gunn, J. E., Hoessel, J. G., & Schneider, D. P. 1998, AJ, 116, 584
- [211] Lugger, P. M. 1986, ApJ, 303, 535
- [212] Lugger, P. M. 1989, ApJ, 343, 572.
- [213] Lumsden, S. L., Collins, C. A., Nichol, R. C., Eke, V. R., Guzzo, L., 1997, MNRAS, 290, 119
- [214] Lumsden, S. L., Nichol, R. C., Collins, C. A., & Guzzo, L. 1992, MNRAS, 258, 1
- [215] Lupton, R. H., Gunn, J. E., Ivezić, Z., Knapp, G. R., Kent, S., & Yasuda, N. 2001, Astronomical Data Analysis Software and Systems X, ASP Conference Proceedings, Vol. 238. Edited by F. R. Harnden, Jr., Francis A. Primini, and Harry E. Payne. San Francisco: Astronomical Society of the Pacific, ISSN: 1080-7926, 2001., p.269, 10, 269
- [216] Lupton R. H., Gunn J. E., Szalay A. S., 1999, AJ, 118, 1406
- [217] Lupton, R. et al. 2003 *in preparation*
- [218] MacLaren, I., Ellis, R. S., & Couch, W. J. 1988, MNRAS, 230, 249
- [219] Madau, P., Ferguson, H. C., Dickinson, M. E., Giavalisco, M., Steidel, C. C., & Fruchter, A. 1996, MNRAS, 283, 1388
- [220] Makino, J. & Hut, P. 1997, ApJ, 481, 83
- [221] Malumuth, E. M. & Richstone, D. O. 1984, ApJ, 276, 413

- [222] Mamon, G. A. 1992, ApJL, 401, L3
- [223] Mannucci, F., Basile, F., Poggianti, B. M., Cimatti, A., Daddi, E., Pozzetti, L., & Vanzi, L. 2001, MNRAS, 326, 745
- [224] Margoniner, V. E. & de Carvalho, R. R. 2000, AJ, 119, 1562
- [225] Margoniner, V. E., de Carvalho, R. R., Gal, R. R., & Djorgovski, S. G. 2001, ApJL, 548, L143
- [226] Markevitch, M. 1998, ApJ, 504, 27
- [227] Martin, C. L., Lotz, J., & Ferguson, H. C. 2000, ApJ, 543, 97
- [228] Marzke, R. O., Geller, M. J., Huchra, J. P., & Corwin, H. G. 1994, AJ, 108, 437
- [229] Marzke, R. O. & da Costa, L. N. 1997, AJ, 113, 185
- [230] Marzke, R. O., da Costa, L. N., Pellegrini, P. S., Willmer, C. N. A., & Geller, M. J. 1998, ApJ, 503, 617
- [231] Merritt, D. 1984, ApJ, 276, 26
- [232] Metevier, A. J., Romer, A. K., & Ulmer, M. P. 2000, AJ, 119, 1090
- [233] Mihos, J. C. 1995, ApJL, 438, L75
- [234] Miller, C. J. et al. astro-ph/9912362
- [235] Miller, C. J. et al. 2003 *in preparation*
- [236] Miller, G. E. 1983, ApJ, 268, 495
- [237] Miller, N. A. & Owen, F. N. 2001, ApJL, 554, L25
- [238] Miller N. A., Owen F. N., 2002, AJ, 124, 2453
- [239] Mitchell, R. J., Ives, J. C., & Culhane, J. L. 1977, MNRAS, 181, 25P
- [240] Mo, H. J. & Mao, S. 2002, MNRAS, 333, 768
- [241] Moore, B., Katz, N., Lake, G., Dressler, A., & Oemler, A. 1996, nature, 379, 613
- [242] Moore, B., Lake, G., & Katz, N. 1998, ApJ, 495, 139
- [243] Moore, B., Lake, G., Quinn, T., & Stadel, J. 1999, MNRAS, 304, 465
- [244] Morgan, W. W. 1958, PASP, 70, 364

- [245] Morgan, W. W. 1959, PASP, 71, 394
- [246] Morris, S. L., Hutchings, J. B., Carlberg, R. G., Yee, H. K. C., Ellingson, E., Balogh, M. L., Abraham, R. G., & Smecker-Hane, T. A. 1998, ApJ, 507, 84
- [247] Moss C., Whittle M., 2000, MNRAS, 317, 667
- [248] Moss C., Whittle M., 1993, ApJ, 407, L17
- [249] Nakamura, O., Fukugita, M., Yasuda, N., Loveday, J., Brinkmann, J., Schneider, D. P., Shimasaku, K., & SubbaRao, M. 2003, AJ, 125, 1682
- [250] Newberry, M. V., Kirshner, R. P., & Boroson, T. A. 1988, ApJ, 335, 629
- [251] Newberry M. V., Boroson T. A., Kirshner R. P., 1990, ApJ, 350, 585
- [252] Nichol, R. C. et al. 2001, Mining the Sky, 613, astro-ph/0110231
- [253] Norton S. A., Gebhardt K., Zabludoff A. I., Zaritsky D., 2001, ApJ, 557, 150
- [254] Oegerle, W. R., Hill, J. M., & Hoessel, J. G. 1991, ApJL, 381, L9
- [255] Oemler, A. J., Dressler, A., & Butcher, H. R. 1997, ApJ, 474, 561
- [256] Oh, S.P. & Benson, A.J. 2003, submitted to MNRAS
- [257] Ohama, N. 2003, Dissertation, University of Tokyo
- [258] Okamoto, T., & Nagashima, M. 2001, ApJ, 547, 109
- [259] Okamoto, T. & Nagashima, M. 2003, submitted to MNRAS
- [260] Osterbrock, D. E. 1960, ApJ, 132, 325
- [261] Osterbrock, D.E., 1989, Astrophysics of Gaseous Nebulae and Active Galactic Nuclei (University Science Books)
- [262] Ostriker, J. P. 1980, Comments on Astrophysics, 8, 177
- [263] Ostriker, J. P. & Hausman, M. A. 1977, ApJL, 217, L125
- [264] Oukbir, J., Blanchard, A. 1992, A&A, 262, 21O
- [265] Owen F. N., Ledlow M. J., Keel W. C., Morrison G. E., 1999, AJ, 118, 633
- [266] Paolillo, M., Andreon, S., Longo, G., Puddu, E., Gal., R. R., Scaramella R., Djorgovski, S. G., de Carvalho, R. 2001, A&A, 367, 59

- [267] Petrosian, V. 1976, ApJL, 209, L1
- [268] Phillipps, S. 1988, A&A, 194, 77
- [269] Phillipps, S., Driver, S. P., Couch, W. J., & Smith, R. M. 1998, ApJ, 498, L119
- [270] Pier, J. R., Munn, J. A., Hindsley, R. B., Hennessy, G. S., Kent, S. M., Lupton, R. H., & Ivezić, Ž. 2003, AJ, 125, 1559
- [271] Pimbblet, K. A., Smail, I., Kodama, T., Couch, W. J., Edge, A. C., Zabludoff, A. I., & O'Hely, E. 2002, MNRAS, 331, 3
- [272] Poggianti, B. M. & Barbaro, G. 1997, A&A, 325, 1025
- [273] Poggianti, B. M., Smail, I., Dressler, A., Couch, W. J., Barger, A. J., Butcher, H., Ellis, R. S., & Oemler, A. J. 1999, ApJ, 518, 576
- [274] Poggianti, B. M., Wu, H., 2000, ApJ, 529, 157
- [275] Poggianti, B. M., Bridges, T. J., Mobasher, B., et al., 2001, ApJ, 562, 689
- [276] Postman, M. & Geller, M. J. 1984, ApJ, 281, 95
- [277] Postman, M., Lubin, L.M., Gunn, J.E., Oke, J.B., Hoessel, J.G., Schneider, D.P., Christensen, J.A. 1996, AJ, 111, 615
- [278] Quillen A. C., Rieke G. H., Rieke M. J., Caldwell N., Engelbracht C. W., 1999, ApJ, 518, 632
- [279] Quilis, V., Moore, B., & Bower, R. 2000, Science, 288, 1617
- [280] Quintero A. et al. 2003, submitted to ApJL
- [281] Rakos, K. D. & Schombert, J. M. 1995, ApJ, 439, 47
- [282] Rakos, K. D., Schombert, J. M., Odell, A. P., & Steindling, S. 2000, ApJ, 540, 715
- [283] Reichart, D. E., Castander, F. J., & Nichol, R. C. 1999, ApJ, 516, 1
- [284] Reichart, D.E., Nichol, R.C., Castander, F.J., Burke, D.J., Romer, A.K., Holden, B.P., Collins, C.A., Ulmer, M.P. 1999, ApJ, 518, 521
- [285] Richards G. T., Fan X., Newberg H. J., et al., 2002, AJ, 123, 2945
- [286] Romer, A. K., Viana, P. T. P., Liddle, A. R., & Mann, R. G. 2001, ApJ, 547, 594

- [287] Rose J. A., Gaba A. E., Caldwell N., Chaboyer B., 2001, AJ, 121, 793
- [288] Salpeter, E. E. 1955, ApJ, 121, 161
- [289] Sandage, A.&Visvanathan, N. 1978, ApJ, 225, 742
- [290] Sandage, A., Binggeli, B., & Tammann,G. A. 1985, AJ, 90, 1759
- [291] Sanders, D. B., Soifer, B. T., Elias, J. H., Madore, B. F., Matthews, K., Neugebauer, G., & Scoville, N. Z. 1988, ApJ, 325, 74
- [292] Schade, D., Lilly, S. J., Le Fevre, O., Hammer, F., & Crampton, D. 1996, ApJ, 464, 79
- [293] Schlegel, D. J., Finkbeiner, D. P., & Davis, M. 1998, ApJ, 500, 525
- [294] Schuecker, P., Boehringer, H. 1998, A&A, 339, 315
- [295] Schweizer F., 1982, ApJ, 252, 455
- [296] Schweizer F., 1996, AJ, 111, 109
- [297] Scranton, R. et al. 2002, ApJ, 579, 48
- [298] Sellwood, J. A. & Carlberg, R. G. 1984, ApJ, 282, 61
- [299] Sharples, R. M., Ellis, R. S., Couch, W. J., & Gray, P. M. 1985, MNRAS, 212, 687
- [300] Shectman, S.A. 1985, ApJS, 57, 777
- [301] Shectman, S. A., Landy, S. D., Oemler, A., Tucker, D. L., Lin, H., Kirshner, R. P., & Schechter, P. L. 1996, ApJ, 470, 172
- [302] Shimasaku, K., Fukugita, M., Doi, M., Hamabe, M., Ichikawa, T., Okamura, S., Sekiguchi, M., Yasuda, N., et al. 2001, AJ, 122, 1238
- [303] Shioya Y., Bekki K., Couch W. J., 2001, ApJ, 558, 42
- [304] Shioya, Y., Bekki, K., Couch, W. J., & De Propris, R. 2002, ApJ, 565, 223
- [305] Smail, I., Dressler, A., Couch, W. J., Ellis, R. S., Oemler, A. J., Butcher, H., & Sharples, R. M. 1997, ApJS, 110, 213
- [306] Smail, I., Edge, A. C., Ellis, R. S., & Blandford, R. D. 1998, MNRAS, 293, 124

- [307] Smail I., Morrison G., Gray M. E., Owen F. N., Ivison R. J., Kneib J.-P., Ellis R. S., 1999, ApJ, 525, 609
- [308] Smith, J. A., Tucker, D. L., Kent, S., Richmond, M. W., Fukugita, M., Ichikawa, T., Ichikawa, S., Jorgensen, A. M., et al. 2002, AJ, 123, 2121
- [309] Solanes, J. M., Manrique, A., García-Gómez, C., González-Casado, G., Giovanelli, R., & Haynes, M. P. 2001, ApJ, 548, 97
- [310] Soucail, G., Kneib, J.P., Jansen, A.O., Hjorth, J., Hattori, M., Yamada, T. 2000, astro-ph/0006382
- [311] Spitzer, L. J. & Baade, W. 1951, ApJ, 113, 413
- [312] Springel, V., White, S. D. M., Tormen, G., & Kauffmann, G. 2001, MNRAS, 328, 726
- [313] Stanford, S. A., Eisenhardt, P. R. M., & Dickinson, M. 1995, ApJ, 450, 512
- [314] Stanford S.A., Eisenhardt P.R., Dickinson M. 1998, AJ, 492, 461
- [315] Stevens, I. R., Acreman, D. M., & Ponman, T. J. 1999, MNRAS, 310, 663
- [316] Stoughton, C., Lupton, R. H., Bernardi, M., Blanton, M. R., Burles, S., Castander, F. J., Connolly, A. J., Eisenstein, D. J., et al. 2002, AJ, 123, 485
- [317] Strauss, M. A. et al. 2002, AJ, 124, 1810
- [318] Strateva, I., Ivezić, Željko, Knapp, G. R., Narayanan, V. K., Strauss, M. A., Gunn, J. E., Lupton, R. H., Schlegel, D., et al. 2001, AJ, 122, 1861
- [319] Struble, M.F. & Rood, H.J. 1987, ApJS, 63, 555
- [320] Struble, M.F. & Rood, H.J. 1999, ApJ, 125, 35
- [321] Sullivan, M., Treyer, M. A., Ellis, R. S., Bridges, T. J., Milliard, B., & Donas, J. ; 2000, MNRAS, 312, 442
- [322] Terlevich, A. I., Caldwell, N., & Bower, R. G. 2001, MNRAS, 326, 1547
- [323] Thompson L. A., 1988, ApJ, 324, 112
- [324] Toniazzo, T. & Schindler, S. 2001, MNRAS, 325, 509
- [325] Toomre, A. & Toomre, J. 1972, BAAS, 4, 214
- [326] Toomre, A. & Toomre, J. 1972, ApJ, 178, 623

- [327] Trentham, N. 1998, MNRAS, 294, 193
- [328] Treu, T. et al. 2003, ApJ in press, astro-ph/0303267
- [329] Treyer, M. A., Ellis, R. S., Milliard, B., Donas, J., & Bridges, T. J. 1998, MNRAS, 300, 303
- [330] Uomoto, A. et al. 2003, in prep.
- [331] Valotto, C. A., Moore, B., & Lambas, D. G. 2001, ApJ, 546, 157.
- [332] Valotto, C. A., Nicotra, M. A., Muriel, H., & Lambas, D. G. 1997, ApJ, 479, 90.
- [333] Valluri, M. 1993, ApJ, 408, 57
- [334] van den Bergh, S. 1976, ApJ, 206, 883
- [335] van Dokkum, P. G., Franx, M., Kelson, D. D., Illingworth, G. D., Fisher, D., & Fabricant, D. 1998, ApJ, 500, 714
- [336] van Dokkum, P. G., Franx, M., Fabricant, D., Illingworth, G. D., & Kelson, D. D. 2000, ApJ, 541, 95
- [337] Viana, P.T.P., Liddle, A.R. 1996, MNRAS, 281, 323
- [338] Viana, P.T.P., Liddle, A.R., 1999, MNRAS, 303, 535
- [339] Visvanathan, N. & Sandage, A. 1977, ApJ, 216, 214
- [340] Vollmer, B., Marcellin, M., Amram, P., Balkowski, C., Cayatte, V., & Garrido, O. 2000, A&A, 364, 532
- [341] Vollmer, B., Cayatte, V., Balkowski, C., & Duschl, W. J. 2001, ApJ, 561, 708
- [342] Vollmer, B. 2003, A&A, 398, 525
- [343] Wang, Q. D. & Ulmer, M. P. 1997, MNRAS, 292, 920
- [344] White, D. A., Jones, C., & Forman, W. 1997, MNRAS, 292, 419
- [345] Whitmore, B. C., Gilmore, D. M., & Jones, C. 1993, ApJ, 407, 489
- [346] Whitmore, B. C. 1995, ASP Conf. Ser. 70: Groups of Galaxies, 41
- [347] Wilkerson, M. S. 1980, ApJL, 240, L115
- [348] Willick, J.A., Thompson, K.L., Mathiesen, B.F., Perlmutter, S., Knop, R.A., Hill, G.J. 2000, astro-ph/0012119

- [349] Wilson, G., Cowie, L. L., Barger, A. J., & Burke, D. J. 2002, AJ, 124, 1258
- [350] Wu, X., Xue, Y., & Fang, L. 1999, ApJ, 524, 22
- [351] Xue, Y. & Wu, X. 2000, ApJ, 538, 65
- [352] Yagi, M., Kashikawa, N., Sekiguchi, M., Doi, M., Yasuda, N., Shimasaku, K., & Okamura, S. 2002a, AJ, 123, 66
- [353] Yagi, M., Kashikawa, N., Sekiguchi, M., Doi, M., Yasuda, N., Shimasaku, K., & Okamura, S. 2002b, AJ, 123, 87
- [354] Yamauchi, C. et al. 2003. in prep.
- [355] Yee, H. K. C., Ellingson, E., & Carlberg, R. G. 1996, ApJS, 102, 269
- [356] York, D.G., Adelman, J., Anderson, J.E.J., Anderson, S.F., Annis, J., Bahcall, N.A., Bakken, J.A., Barkhouser, R. et al. 2000, AJ, 120, 1579
- [357] Yun M. S., Reddy N. A., Condon J. J., 2001, ApJ, 554, 803
- [358] Zaritsky, D., Zabludoff, A. I., & Willick, J. A. 1995, AJ, 110, 1602
- [359] Zabludoff, A. I., Zaritsky, D., Lin, H., Tucker, D., Hashimoto, Y., Shectman, S. A., Oemler, A., & Kirshner, R. P. 1996, ApJ, 466, 104
- [360] Zabludoff A. I., 1999, IAUS, 186, 125
- [361] Zwicky, F., Herzog, E., Wild, P., Karpowicz, M., Kowal, C. 1961-1968, in Catalog of Galaxies and of Clusters of Galaxies, Vols. 1-6, California Institute of Technology, Pasadena.